Karlsruher Institut für Technologie

# Clumpy Dark Matter Phenomenology: A Study of Axion Miniclusters and Primordial Black Holes

For the Obtention of the Academic Degree of Doctor of Natural Sciences (Dr. rer. nat.) by the Karlsruhe Institute of Technology (KIT) Faculty of Physics

By Virgile Dandoy

November 2020 - November 2023

*Oral Defense:*
27 October 2023

*Supervised by:*
Prof. Dr. T. Schwetz-Mangold

*Co-Supervised by:*
Prof. Dr. J. Jaeckel

Karlsruher Institut für Technologie

# Clumpy Dark Matter Phenomenology: A Study of Axion Miniclusters and Primordial Black Holes

Zur Erlangung des akademischen Grades eines DOKTORS DER NATURWISSENSCHAFTEN (Dr. rer. nat.)

von der KIT-Fakultät für Physik des
Karlsruher Instituts für Technologie (KIT)
genehmigte DISSERTATION
von M. Sc. Virgile Dandoy

Tag der mündlichen Prüfung: 27. Oktober 2023

*Referent:*
Prof. Dr. Thomas Schwetz-Mangold

*Korreferent:*
Prof. Dr. Joerg Jaeckel

# Erklärung

Ich versichere hiermit, dass ich die vorliegende Dissertation selbständig und unter Beachtung der Regeln zur Sicherung guter wissenschaftlicher Praxis im Karlsruher Institut für Technologie (KIT) in der aktuellen Fassung angefertigt habe. Ich habe keine anderen als die angegebenen Quellen und Hilfsmittel benutzt. Wörtlich oder inhaltlich übernommene Stellen sind als solche kenntlich gemacht.

Ort, Datum

Virgile Dandoy

# Abstract

After decades of research, dark matter remains elusive. This has motivated the recent efforts to comprehend the characteristics of dark matter in our neighborhood. In this thesis, we investigate the possibility of dark matter forming gravitationally bound structures. In addition to the inevitable constraints imposed on our techniques for identifying and detecting dark matter, these might also be correlated with distinctive signals. Consequently, they may offer precious insights into specific models of dark matter.

One notable illustration of this phenomenon is given by the axion miniclusters. Emerging within a scenario where axions, hypothetical particles introduced to address the strong CP problem, are produced subsequent to inflation, these structures consist of axions bound by gravitational forces, exhibiting a mass on the order of $\sim 10^{-12} M_{\odot}$. Given their potential to form as early as during the matter-radiation equality epoch, the initial population of axion miniclusters is subjects to many effects that alter, damage and even destroy them. Among these effects, tidal interactions with stars, after becoming gravitationally bound within a galaxy, are particularly noteworthy. Inspired by the critical implications for direct detection – where the presence of a uniform axion background versus bound structures can result in markedly divergent signals – we investigate the survival of the miniclusters when confronted to these tidal interactions. Notably, marking a pioneering step, we undertake this analysis by incorporating the classical wave formalism that is indispensable for comprehending axion miniclusters. Our research conclusively establishes that the survival is profoundly linked to their density profile. However, as we explore various profiles, our study reveals a noteworthy outcome: a substantial proportion of these clusters would survive to the stellar tidal interactions. (a)

In line with this analysis, we then proceed to study the signal an axion minicluster would induce in direct detection experiments and more precisely in haloscope setups similar to ADMX. Since the output signal in the latter experiment is proportional to the product of the density and the axion-photon coupling, $\rho g_{a\gamma\gamma}^2$, we confirm that a minicluster would induce a signal order of magnitudes larger than in an axion background case. More importantly, we show that in the happy event of an encounter, a high-resolution haloscope can unravel the density coupling product by first accessing the gravitational potential of the cluster. (b)

Another part of this thesis is devoted to primordial black holes, long considered to be good candidates for dark matter, even though they are today strongly constrained by observations. They constitute a strong prediction in the case of large scalar (curvature) fluctuations in the early universe and have the interesting phenomenological property of being associated with the production of gravitational waves. Based on the recent potential gravitational wave signal observed among the Pulsar Timing Array communities, we perform a Bayesian search to derive the posterior distributions for the shape of the primordial curvature fluctuations. We demonstrate that, although the signal might, at first sight, be explained by such a process, the associated production of primordial black holes is spoiling the observational constraints. (c)

(a) V.Dandoy, T. Schwetz, and E. Todarello, "*A self-consistent wave description of axion miniclusters and their survival in the galaxy*", JCAP 09 (2022) 081, [2206.04619].

(b) V. Dandoy, J. Jaeckel, and V. Montoya, "*Using Axion Miniclusters to Disentangle the Axion-photon Coupling and the Dark Matter Density*" , [2307.11871] (Prepared for submission to JCAP).

(c) V. Dandoy, V. Domcke, and F. Rompineve, "*Search for scalar induced gravitational waves in the International Pulsar Timing Array Data Release 2 and NANOgrav 12.5 years dataset*", [2302.07901] (Accepted in SciPost).

# Acknowledgement

How to not start these acknowledgments by thanking my supervisor Thomas Schwetz-Mangold. Over the course of three years, the list of things I could be grateful for is extensive. However, if I must highlight the most significant, I will remember how you guided my path without imposing one upon me. In the manner in which, when facing projects, hierarchies seemed to fade away, making room for a simple collaboration among colleagues. I hope to continue collaborating with you.

I would also like to extend my heartfelt gratitude to Joerg Jaeckel for his valuable time and collaboration. It has been one the most peaceful collaboration I had, for sure not because of its simplicity, but rather due to the welcoming work atmosphere you are capable of creating.

I would like to convey my deep appreciation to the theoretical physics community at CERN for their incredibly warm reception. Specifically, I extend my heartfelt thanks to Valerie Domcke and Fabrizio Rompineve for generously dedicating their time and effort to collaborate on a project with me. It is worth emphasizing that this collaboration has played a substantial role in shaping my commitment to continue pursuing an academic career.

Last but not least, I would like to thank all the colleagues I have shared experiences with.

Je me suis souvent demandé ce qui m'a amené ici, aujourd'hui. Quel enchainement de circonstances, de rencontres, d'opportunités et de conseils suivis? Il est certain que mes parents, au travers de leur éducation basée sur la curiosité, m'ont poussé à accomplir des choses dont je ne me serais pas crû capable. Une éducation exigente mais plus que tout impliquée à nous donner l'impulsion nécessaire pour réaliser les rêves que nous chérissions. Ecrire cette thèse était très certainement l'un d'eux. Mon enfance est ainsi tissée de souvenirs qui ont, probablement, contribués à façonner la personne que je suis devenue aujourd'hui. Ce manuscrit leur est dédié.
L'un des êtres les plus chers que j'ai eu à connaître fût sans doute ma grand-mère. Si elle n'est plus là pour lire ces lignes, c'est cependant en grande partie grâce à elle que cette thèse existe.

Il est également important de faire la lumière sur toutes les personnes qui ont joué, dans l'ombre, un rôle indispensable dans cette thèse. Je parle ici, des mes plus chers amis, ils se reconnaitront. De ma famille proche, ma soeur et mes cousins. Je parle également de Sophie, qui n'a jamais été en manque de conseils dans les moments de doute.

Il existe une dernière personne qui merite, elle aussi, son propre paragraphe. Tes encouragements, ta bienveillance et ta douceur ont été, pour sûr, le pansement sur les doutes et les inquiètudes que j'ai pû avoir. Cette dernière année fût l'une des plus belles.

I finally would like to acknowledge the European Union's Horizon 2020 research and innovation programme under the Marie Sklodowska-Curie grant agreement No 860881-HIDDeN

# Contents

# List of Figures

# List of Tables

# Acronyms

**ADMX** Axion Dark Matter Experiment

**AMCs** axion miniclusters

**BH** black holes

**CAST** CERN Axion Solar Telescope

**CMB** cosmic microwave bakcground

**EKG** Einstein-Klein-Gordon

**G** Gaussian

**GWs** gravitational waves

**H** Hernquist

**HD** Hellings-Downs

**HMF** halo mass function

**IAXO** International Axion Observatory

**IPTA** International Pulsar Timing Array

**LE** Lane-Embden

**LIGO** laser interferometer gravitational-wave observatory

**LSS** large scale structure

**MADMAX** Magnetized Disc and Mirror Axion experiment

**NFW** Navaro-Frenk-White

**NG12** NANOgrav 12 years

**OSQAR** Optical Search for QED Vacuum Birefringence

**PBHs** primordial black holes

**PQ** R.Peccei and H.Quinn

**PS** Press-Schechter

**PTA** Pulsar Timing Array

**SGWB** stochastic gravitational wave background

**SIGW** scalar induced gravitational wave

**SMBHBs** super massive black hole binaries

**SP** Schrodinger-Poisson

**TH** top-hat

**TOA** time of arrival

**WKB** Wentzel-Kramers-Brillouin

# Chapter 1

# Introduction

> "We see it as Columbus saw America from the coast of Spain. Its movements have been felt, trembling along the far-reaching line of our analysis with a certainty hardly inferior to that of ocular demonstration".
>
> William Herschel

What course of action should I take if I suddenly discover an exception to a law of nature that has long been accepted by the community as a whole? This question has two radically opposed but equally interesting answers, and has probably guided the generation of modern scientists.

To illustrate the first, we need to go back to the 18th century. At that time, Newton's law of gravity was considered to be one of the most accomplished theory, able to predict the motion of all objects on Earth, as well as all known planets. Nonetheless, as a breakthrough in this peace full timeline, William Herschel showed by observations the evidence of a new planet, Uranus [1]. Soon, astronomers realized that its orbital motion around the sun was incompatible with what was expected and calculated from Newton's theory [2]. Naturally, this matter divided the scientific community in two groups. The first, in favor of a modification of the universal law of gravity proposed by Newton, argued that the latter should be only valid close enough to the sun and would lose its validity as moving away from it. The second, not ready to give up on Newton's laws, proposed to explain the Uranus anomaly by an other planet, yet undiscovered, disturbing the orbital motion of Uranus by gravitational interactions. Eventually, the second group, based on Newton's gravity, calculated the position of the supposed new planet and discovered Neptune, first astrophysical object found only with the use of the laws of physics. Regardless of the outcome, both solutions would have lead to a radical change of perception.

To illustrate the second answer to our question, one of the most striking example has emerged much more recently. Still according to Newton's laws, in a two body system, like a planet-star system, the point of closest approach, the perihelion, is fixed. At the end of the 19th century, Le Verrier, realized that this condition was actually not fulfilled for one planet, Mercury [3]. So, by analogy with what happened over a hundred years ago with Uranus, the scientific community found itself faced with the same two options: Should we modify theory or is there something, that we do not see, that is disturbing the motion of Mercury? Clearly learning from their previous experience, most of them have headed for a new planet, even closer to the Sun than Mercury [4]. None was found, despite the much more advanced technology available at that time. It was not until the 20th century and Einstein's theory of general relativity [5] that it became clear that Mercury's anomaly was due to a lack of validity of Newton's gravity near the Sun. Again, here both options would have lead to a radical change in our perception of the world, but this time, the theory has to be changed.

The aim of this introduction was to present the important context in which the dark matter problem - center of this thesis - arose and to help you understand the possible outcomes.
The story of dark matter began in the same way as previous situations, with an anomaly: In the 20th century, our knowledge on the Universe was already quite broad. We knew, for instance, about the existence of galaxy clusters. They are nothing more than galaxies held together by a perfect balance of gravity and speed. Gravity prevents them from escaping and their speed prevents them from collapsing towards each other. Measuring the speed of galaxies in a stable cluster should therefore give us an idea of the total mass of the cluster. In the 20th century, Fritz Zwicky [6], observing stable clusters of galaxies, hence proceeded to determine the mass of the clusters by measuring the velocity dispersion of the galaxies. He then compared it to the mass he could actually observed from looking directly at the galaxies. The two measurements of the cluster mass did not match. More precisely, he concluded that the mass he directly observed was dramatically lower than the mass needed for the clusters to be stable. According to its calculation, the galaxies were not providing enough mass to generate the gravity required, and the clusters should have been dismantled by now.
After this first anomaly, many others followed (rotational curves [7], bullet clusters [8, 9],...), all pointing to two possible conclusions: either there is some missing mass (today named dark matter), or the theory of gravity needs to be modified, once again. To put concrete numbers on this, we know today that, if dark matter is indeed a unknown component of the universe, it should compose $85\%$ of the latter total mass [10]. Unfortunately, compared to the two previous examples, the answer on the nature of dark matter is yet still unknown.
Of course, this thesis is not intended to provide an answer to this question, as it will probably come from experimental evidence. Nevertheless - taking the assumption that there is indeed a unknown component in the universe - this manuscript aims to address the phenomenological consequences on specific dark matter candidates. This process is in fact inevitable if we want to steer experimental research in the right direction: it seems difficult to search for this hidden part of the Universe if we don't know how it looks like. To give concrete intuition on how the phenomenology of a dark matter candidate could alter the experimental searches, let's imagine that dark matter is a new particle, homogeneously distributed in the galaxy. Naively, an Earth-based direct detection experiment would have a time-independent probability of detecting this dark matter background. On the other hand, if the same new particle is bound in stable structures (small relative to the galaxy), we can only hope to have a signal if one of these dark matter clusters crosses the Earth. The astrophysical structure of dark matter is, therefore, playing a crucial role in the way we should search for it. Motivated by this last example (and others omitted in this introduction), we will be mainly focused, along this manuscript, on the possibility for dark matter to be bound inside stable structures. In addition to provide radically different signal in direct detection experiments, clumped dark matter structures could also be associated with other types of signals, such as the gravitational lensing effects, gravitational waves (GWs), etc,... Observing these effects, would then provide important hints on the nature and the astrophysical structure of dark matter and, on the other hand, their non-observation can constrain some of these clumped structures.
Two distinct dark matter candidates that present clumped structures will be discussed. The first, the *axion* (a new hypothetical particle), has the exotic property, under some scenarios, to be bound in clusters named axion miniclusters (AMCs) . They will be at the center of this thesis and their properties, as well as signatures in experiments, will be extensively discussed. The second, the primordial black holes (PBHs), has the property to be associated with the production of gravitational waves. Using the data from Pulsar Timing Arrays experiments, we will see that existing constraints on PBH abundance may be used to importantly constrain cosmological models.

## 1.1 Axions and Axion Miniclusters

If the dark matter is "simply" composed of particles, what properties should they have? Intuitively, since we are not able to observe them, they can not interact electromagnetically or at most very weakly, same for the weak interaction. On the other hand, they need to interact gravitationally in

order to account for all the observed effects. Last but not least, dark matter must be cold, i.e that the particles are non-relativistic, in order to not spoil structure formation. None of the known particles of the Standard Model meets all these constraints. The way is, therefore, to go beyond Standard Model particle physics as it has for instance been done with Super-Symmetry (SUSY) [11]. In this model, many new elementary particles are added and can then potentially behave as dark matter. We refer to WIMPs (weakly interaction massive particles) for these particles. Unfortunately, despite important effort from the experimental side, no evidence for WIMPS has been found [12, 13, 14].
Another hypothetical new particle - the *axion* - has recently attracted strong attention. Interestingly, the scientists behind the postulation of this new particle were in the process of solving another very important problem in physics, the strong CP problem [15, 16, 17]. Without giving too deep details here (this will be extensively discussed in Chapter 2), the latter is related to the fact that the strong interaction seems to preserve the CP symmetry, whereas it is known that a violating term is actually present in the Lagrangian. This apparent conundrum was solved in the 1970's by Peccei and Quinn [15], who realised that the introduction of a new Goldston boson, later named the axion [18] , could compensate for the CP violating term, thus reconciling theory and experiment. However, they did not realise that this Goldston boson would have the exact properties of the cold dark matter the community was looking for. This conclusion has been later given by Weinberg [18].

The essential idea behind the axion, is that the Standard Model is extended with a global $U(1)$ symmetry. The latter is spontaneously broken at a given scale $f_a$ so that the emerging Goldston boson gets interactions inversely proportional to this scale. We will see in the next chapter that, in order to solve the strong CP problem, the axion has to carry an interaction term with the gluon field. Importantly, this represents a temperature dependent potential for the axion that will, in addition to solve the strong CP problem, induces a temperature dependent mass $m_a(T)$. As soon as the gluon potential develops, the axion field would start to oscillate around the minimum of the potential and provide an energy density in line with was is expected from cold dark matter. This is the so-called misalignment mechanism [19, 20, 21, 22, 23]. Of course, the today's relic abundance depends on the axion mass $m_a$ (or the symmetry breaking scale $f_a$). It will be shown that, for $m_a \sim 10^{-5}\mathrm{eV}$, the total amount of dark matter can be explained by axions [24].
Interest in this particle goes even further than its dark matter interpretation. Soon after its postulation, it has indeed been realized that, in the case of a symmetry breaking occurring after inflation, the field is initially inhomogeneous, taking different initial values in each causal disconnected region. While it does not change the possibility for the axion to account for the whole dark matter relic abundance, it induces phenomenological signatures extremely precious for dark matter searches. In particular, those inhomogeneities are expected to grow and collapse way before usual structure formation into the so-called *axion miniclusters* [25].
Post-inflation axions therefore offer the promise of exotic phenomenoligical signatures and the clumped structures we introduced above. But, what do we know about axion miniclusters?
So far, they have been extensively studied via numerically simulations (see Refs.[26, 27, 28, 29, 30, 31]). It is, however, extremely challenging to understand the whole evolution of these objects, from their creation around matter-radiation equability until our current days. For instance, previously mentioned numerical simulations account for their evolution, through merging and collisions, down to a redshift $z \approx 100$. At that time galaxies have not yet formed. At late times, it is known that axion miniclusters would become the site of galaxy formation [31] and themselves be part of the dark matter halo of those galaxies. This late part of the history of the life of the axion minicusters is, therefore, not understood yet.
Secondly, we may wonder about the way to describe an axion minicluster. A careful analysis would lead to the conclusion that such light particles have extremely high occupation numbers (since they are bosons this is indeed not a problem). Hence, in analogy to the photons that are better described by the Maxwell equations in this limit, the axions will be described via a classical field [32]. It implies for the axion miniclusters to be described, as well, by a classical field rather than via a classical particle description.

The first chapter of this thesis is specifically dedicated to these two previous points: how to describe the late time evolution of the axion miniclusters accounting for their classical wave properties? Solving this question will shed light on the fact that, even if being astrophysical objects, their wave function is still governed by the Schrodinger equation. This interplay between classical behavior and quantum formalism makes the richness of this analysis. In this chapter, the survival of the miniclusters against tidal interactions with galactic stars will be extensively studied.

As mentioned in the first part of this introduction, having clumped structures would induced a radical change in the expected signal on direct detection experiments. This conclusion motivates the second chapter of this thesis, where the haloscope [33, 34] signal in the case of an axion minicuster encounter will be studied.
The latter, designed as a cavity embedded in a strong magnetic field, uses the fact that axions should, in addition to the gluon coupling, inherit a coupling to photons, with a coupling constant $g_{a\gamma\gamma}$ that is naturally unknown. As we are travelling within the dark matter halo, incoming axions in the cavity can then interact with the magnetic field and induce an electromagnetic field. Intuitively, the strength of the output signal can be enhanced by two distinct factors. First, the axion density $\rho$ can simply be increased. This would naturally enhance the electromagnetic power produced within the haloscope cavity. On the other hand, increasing the coupling would increase the axion-photon conversion and contributes as well in enhancing the output power. Doing explicit calculation (see Chapter 4) leads to the conclusion that the electromagnetic power induced in a haloscope experiment is proportional to $\sim g^2_{a\gamma\gamma}\rho$. No separate information on the coupling or the density can apparently be extracted from such measurement.
In this context, the haloscope signal in the case of an encounter with an axion minicluster will be derived. It will be furthermore shown that, in the, lucky, case of such an encounter, the haloscope cavity would be capable of disentangling the axion-photon coupling by having first access to the gravitational potential of the cluster.

## 1.2 Primordial Black Holes and Gravitational Waves

We mentioned that observing particular cosmological/astrophysical signatures may constrain some clumped dark matter candidates, and *vice versa*. This is the case for primordial black holes and gravitational waves.
The Pulsar Timing Arrays (IPTA [35], NANOGrav [36, 37], EPTA [38],...), are experiments observing multiple pulsars and recording the times at which their light pulses are reaching the Earth. For stable pulsars, as the ones they are observing, it is expected for the pulses to be extremely regular in time (up to some known deviations). However, in the case of incoming gravitational waves, the induced space-time distortion would translate into an additional delay between the pulses. Hence, recent data[1] have shown evidence for the presence of a stochastic gravitational wave background. This was naturally followed by a considerable effort to understand its origins. If the most accepted is given to be the coalescence of super-massive balck holes [39, 40], gravitational waves may also be produced in the early universe by exotic phenomena.
One of those assumes large curvature fluctuations at small scales [41, 42, 43, 44, 45, 46]. It indeed constitutes an exotic production mechanism since the curvature fluctuations are know to be extremely small at CMB scales ($\sim 1\mathrm{Mpc}$) [10]. If, for some reasons, large fluctuations are, nonetheless, produced at small scales, the scalar perturbations of the metric would naturally trigger tensor perturbations and induce a gravitational wave background nowadays. The counter part of having large curvature perturbations is that it would unavoidably produce primordial black holes, that will contribute to the dark matter relic density [47, 48]. The fraction of the dark matter in primordial black holes is however strongly constrained by observations (lensing, cosmic microwave bakcground (CMB), laser interferometer gravitational-wave observatory (LIGO),...).

[1] At the time of this project, only data from NANOGrav 12.5 years were available [36]. At the end of this thesis the 15 years data set have been released [37], showing even stronger evidence for a stochastic gravitational wave background.

In Chapter 5, we proceed to analyse the public data from both NANOGrav 12.5 years and IPTA DR2, interpreting the potential gravitational wave signal as coming from large curvature fluctuations. We find that the population of primordial black holes induced by the fluctuations capable of explaining the signal are in strong conflict with the astrophysical constraints.

This manuscript is organized as follows: Starting with the axion part, the Chapter 2 is dedicated to introduce this new particle. We, therefore, discuss the strong CP-problem as well as its solution and the production mechanism for the axion in the early universe. In Chapter 3, we discuss the evolution of the axion miniclusters in the late universe and their survival in the galaxy. We derive as well a general formalism to describe the axion miniclusters in a classical field picture. In Chapter 4, we use this wave function to derive the signal in haloscope experiments an axion minicluster would induce and proceed to describe a method able to disentangle the axion-photon coupling.
In chapter 5, we discuss how primordial black holes can constrain the potential gravitational wave signal observed in pulsar timing arrays.
We finally conclude, discuss the results and future prospects in Chapter 6

# Chapter 2

# Formalism and Phenomenology of Axion Dark Matter

In this chapter the axion will be consistently introduced. In Sec.2.1 and Sec.2.2 we start with the way it brings a solution to the well-known strong CP-problem. The axion interactions in the different models will then be discussed in detail in Sec.2.3 and the current existing limits on axion parameters will be reviewed. Finally, in Sec.2.4, we are going to introduce the different mechanisms able to produce a sizable axion relic abundance today and see how it could behave as cold dark matter. The phenomenological consequences of each mechanism will be discussed and Sec.2.5 will be dedicated to the appearance of axion miniclusters (AMCs).

## 2.1 The Chiral Anomaly and $U(1)_A$ problem

Interestingly, the strong-CP problem was first introduced to solve another well-known puzzle in particle physics, the $U(1)_A$ problem. In order to make sense on why the axion had to be introduced, we must therefore start chronologically (see Ref.[49] for further details calculation on what will follow).
Let's consider the QCD Lagrangian for N quarks:

$$\mathcal{L}_{\text{QCD}} = -\frac{1}{4} G^a_{\mu\nu} G^{a,\mu\nu} + \sum_{i=0}^{N} \bar{q}^i \left(\gamma^\mu D_\mu - m_i\right) q^i, \tag{2.1}$$

with $q^i$ and $G^a_{\mu\nu}$ respectively the quark and gluon fields.
Considering only the three quarks $(u, d, s)$ and neglecting their mass makes this Lagrangian invariant under the global symmetry group $U(3)_V \times U(3)_A = SU(3)_I \times U(1)_B \times SU(3)_A \times U(1)_A$. Intuitively, $SU(3)_I$ and $U(1)_B$ stand for the isospin and baryon numbers. These last two symmetries are indeed well observed in experiments and show up as multiplet arrangements in the hadron spectrum. However, the axial symmetries are spontaneously broken by the QCD vacuum when this one becomes non-zero. This translates into as many massless Goldstone bosons as broken generators, nine in the present case.
Of course, if we now turn on the masses of the quarks, this provides explicit sources of symmetry breaking. Hopefully, since in this case the masses are close to zero, this effect is small enough to be captured perturbatively and it would simply give masses to the produced Goldstone bosons [1]. It is in addition expected that those new particles carry similar masses.
Eight of them have indeed been found in the same mass range, namely the three pions $(\pi^0, \pi^\pm)$, the four kaons $(K^0, \bar{K^0}, K^\pm)$ and the eta $\eta$. However a last one, that may be associated with the $U(1)_A$ symmetry, the $\eta'$, has been found to have a much heavier mass. What could induce such a mass gap if we have claimed earlier that the nine Goldstone bosons were expected to have similar masses? As pointed out by Weinberg in 1975 [17], this gap in mass is the consequence of the fact that the group

[1] We then talk about *pseudo Goldstone bosons*.

$U(1)_A$ is a good symmetry of the classical Lagrangian but is violated in the quantum theory, we say that it is *anomalous* [50, 51]. Therefore, the $U(1)_A$ symmetry has a much stronger source of explicit symmetry breaking, in addition to the one coming from the quark masses. It intuitively explains the much heavier mass of the $\eta'$ and leads to the conclusion that this last one can not be adequately described by the Goldston mechanism.
But what makes the $U(1)_A$ symmetry explicitly broken if the massless QCD Lagrangian is invariant under it? This question is answered by looking at the current $J_5^\mu$ associated to this symmetry. If for a perfect symmetry the divergence of its current is zero, it is known that axial currents suffer from the chiral anomaly [50, 51], returning a non-vanishing divergence. We have here

$$\partial_\mu J_5^\mu = \frac{g^2 N}{32\pi^2} G_a^{\mu\nu} \tilde{G}_{a,\mu\nu}, \tag{2.2}$$

where $N$ is the number of quarks, $g$ the strong coupling and $\tilde{G}_{a,\mu\nu} = \frac{1}{2}\epsilon_{\mu\nu\alpha\beta} G_a^{\alpha\beta}$.
Hence, through a quark $U(1)_A$ transformation

$$q^i \to e^{i\alpha\gamma_5/2} q^i, \tag{2.3}$$

the action is modified as

$$\delta S = \alpha \frac{g^2 N}{32\pi^2} \int d^4x \, G_a^{\mu\nu} \tilde{G}_{a,\mu\nu}. \tag{2.4}$$

Interestingly, it has been first thought that this integral was vanishing making $U(1)_A$ a perfect symmetry again. However, in the specific case of QCD, the complex structure of its vacuum configuration[2] makes this last one non-zero and the $U(1)_A$ symmetry definitely explicitly broken [52].
The complex structure of the QCD vacuum therefore explains that only 8 pseudo Goldston bosons have been found in the same mass range and solves the $U(1)_A$ problem. It, however, has further consequences. Indeed, it directly implies that an additional term must be present in the QCD Lagrangian:

$$\mathcal{L}_\theta = \theta \frac{g^2}{32\pi^2} G_a^{\mu\nu} \tilde{G}_{a,\mu\nu}, \tag{2.5}$$

with $\theta$ a new parameter.
This term carries strong phenomenology implications since it breaks the CP symmetry and induces in the same time a dipole moment for the neutron proportional to the $\theta$ term [53]

$$d_n \approx \frac{e\theta m_q}{m_N^2}. \tag{2.6}$$

The neutron dipole moment is, however, strongly constrained by experiments. Hence, it is known that $d_n < 2.9 \times 10^{-26} e$ cm at 90% CL [54], translating into $\theta < 10^{-9}$. But why $\theta$ would be that small where it could intuitively take any value between $[0, 2\pi]$?

## 2.2 The Strong $CP$ Problem and the Axion solution

Solving the $U(1)_A$ problem has then brought on the table a new critical question referred as the strong CP problem. In this section, we are going to review the possible solutions and in, particular, the axion solution.
Taking a closer look at the new term $\mathcal{L}_\theta$, it could be noticed that a $U(1)_A$ transformation applied on a single quark would modify the $\theta$ term as

$$\theta \frac{g^2}{32\pi^2} G_a^{\mu\nu} \tilde{G}_{a,\mu\nu} \to (\theta - \alpha) \frac{g^2}{32\pi^2} G_a^{\mu\nu} \tilde{G}_{a,\mu\nu}, \tag{2.7}$$

where $\alpha$ is the rotation angle.
Once the quark masses are generated during electroweak symmetry breaking, they appear as a non-diagonal complex matrix $M_{ij}$. We usually diagonalize this matrix by performing a $SU(N)$ rotation

[2] The interested reader is invited to read the more detailed references associated to this topic since it is beyond the scope of this thesis.

(where $N$ is the number of quarks) and then remove the complex phases, $\alpha_i$, with a $U(1)_A$ chiral rotation for each quark. From Eq.(2.7), we see that such a procedure would induce a contribution to the $\theta$ term [49]

$$\theta \frac{g^2}{32\pi^2} G_a^{\mu\nu} \tilde{G}_{a,\mu\nu} \rightarrow (\theta + \arg\det M) \frac{g^2}{32\pi^2} G_a^{\mu\nu} \tilde{G}_{a,\mu\nu}. \tag{2.8}$$

Hence, making the masses real forces us to define the full theory coefficient

$$\bar{\theta} = \theta + \arg\det M. \tag{2.9}$$

All experimental measurements therefore depend on the full theory parameter $\bar{\theta}$ and then the condition on the neutron dipole moment considered earlier must be applied on it as well.
Naively, we could use a chiral rotation to put the new CP violating Lagrangian term to 0. However for such a field redefinition, the basis for the Yukawa matrices would not be the mass basis and the resulting mass matrix would contain an overall CP violating phase $\bar{\theta}$. In conclusion, in the full theory, the CP violating term $\bar{\theta}$ is independent of the basis choice.
So why $\bar{\theta}$ is so small? A first proposed solution was to assume a massless quark in the Lagrangian. Indeed, in such a case, a chiral symmetry applied on it is only anomalous and $\bar{\theta}$ can be shifted away with no physical effect. In the Standard Model the lightest quark is the up one with $m_u = 2.2 \pm 0.5$ MeV, making the latter solution ruled out [55]. However the idea that a $U(1)_A$ global symmetry, explicitly broken only by the anomaly, can washed out the CP violating term is the milestone of the axion solution we are going to discuss now.
Since we cannot allow for massless quarks, we must find a way to implement a $U(1)_A$ global symmetry with a massive one. Based on that, the first idea came from R.Peccei and H.Quinn (PQ) who introduced a new axial symmetry, today called $U(1)_{PQ}$ [15]. In its minimal set up, we only need a quark $q$ and complex scalar $\phi$ field that both transform under it. This symmetry is explicitly broken by the anomaly as it should. Initially the quark does not have any mass term, but carries a Yukawa interaction

$$\mathcal{L}_{\phi qq} = \bar{q}_L \phi q_R + h.c. \tag{2.10}$$

To make this term invariant under the chiral $U(1)_{PQ}$ we need that $\phi$ transforms as

$$\phi \rightarrow e^{i\alpha} \phi, \tag{2.11}$$

where $\alpha$ is the angle of the chiral rotation defined earlier. Similarly to the Higgs mechanism, the scalar field has a potential with a minimum located at $|\phi| = f_a$. Below that scale, the $U(1)_{PQ}$ is spontaneously broken and the quark acquires some mass. However, the $U(1)_{PQ}$ symmetry is still hidden in the theory and it would be possible to wash out the CP violating term. Let's derive that explicitly.
When the theory gets spontaneously broken, the Goldstone formalism can be applied on the complex scalar field $\phi$. Explicitly we can write it as

$$\phi(x) = (f_a + \chi(x))\, e^{ia(x)/f_a}, \tag{2.12}$$

where $\chi(x)$ is the radial mode, often referred as the "saxion", and $a(x)$ is the axion. Under a $U(1)_{PQ}$ symmetry the axion field now translates as

$$a(x) \rightarrow a(x) + \alpha f_a. \tag{2.13}$$

If the $U(1)_{PQ}$ was an exact symmetry of the theory, the axion Lagrangian would include only kinetic terms, derivative interactions suppressed by the scale of the symmetry breaking $f_a$ and the axion would remain massless. However, because of the anomaly, the source of explicit symmetry breaking propagates into the axion Lagrangian and it can be shown that the following axion-gluon interaction term is present [15, 49, 56]

$$\mathcal{L}_{agg} = \frac{g^2}{32\pi^2 f_a} a\, G_a^{\mu\nu} \tilde{G}_{a,\mu\nu}. \tag{2.14}$$

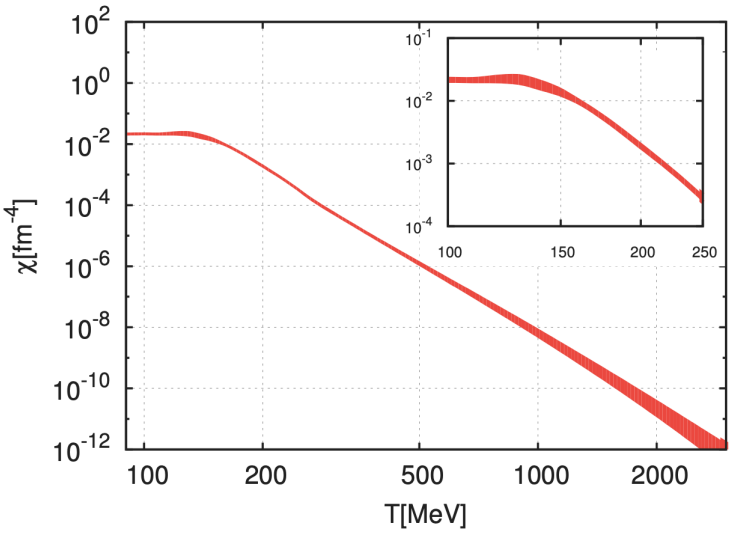


**Figure 2.1:** Evolution of the topological susceptibility of QCD, $\chi(T)$, as a function of the temperature. The original figure can be found in Ref.[59].

This term is essential to the strong CP problem solution since it has a similar shape than the $\theta$-CP violating term. Below QCD phase transition, the axion potential inherited by Eq.(2.14) can be calculated using instantons [57] as well as directly from chiral perturbation theory [58]. It takes the form

$$V(a) = m_\pi^2 f_\pi^2 \frac{m_u m_d}{m_u^2 + m_d^2}\left(1 - \cos\left(\bar{\theta} + \frac{a}{f_a}\right)\right). \tag{2.15}$$

The minimum of this potential is at $\langle a\rangle = -f\bar{\theta}$. Hence in the presence of the potential induced by the anomaly, the axion field will roll down to a minimum that cancels exactly the $\bar{\theta}$ term. The axion field dynamically solves the strong CP problem by settling down to a CP conserving minimum. Using the remaining shift symmetry, we can redefine the axion field as $a_{\text{phys}} \to a + \langle a\rangle$ and observe that the theory has no longer $\bar{\theta}$-CP violating terms. The background contribution of the axion field is therefore CP conserving.

In addition to solving the strong CP problem, the Eq.(2.15) potential induces a mass term for the axion given by

$$\begin{aligned} m_a^2 &= \left.\frac{\partial^2 V}{\partial a^2}\right|_{\text{min}}, \\ &= \frac{m_\pi^2 f_\pi^2}{f_a^2}\frac{m_u m_d}{m_u^2 + m_d^2}. \end{aligned} \tag{2.16}$$

Since the up and down quark masses $m_u$ and $m_d$ as well as the pion mass $m_\pi$ and scale $f_\pi$ are known, the axion mass below QCD confinement depends only on the breaking scale $f_a$ as [59]

$$m_a \approx 5.7\mu\text{eV}\left(\frac{10^{12}\text{GeV}}{f_a}\right). \tag{2.17}$$

It is, however, important to note that Eq.(2.15) is only valid below QCD phase transition, down to zero temperature. The axion gluon term in Eq.(2.14) will indeed provide a more general temperature dependent potential, even above QCD transition. Using instantons [57] or lattice [59] calculations, the temperature dependent potential is given by

$$V(a,T) = m_a^2(T)\left(1 - \cos\left(\frac{a}{f_a}\right)\right), \tag{2.18}$$

where the shift on the axion field has already been performed in this last expression. The temperature dependence of the mass is now given in terms of the topological susceptibility of QCD,

$$m_a^2(T) = \frac{\chi(T)}{f_a^2}, \tag{2.19}$$

which is calculated again using instantons [57] or lattice [59] calculations (see Fig.2.1). As it should, we recover the result in Eq.(2.17) as $T$ goes below the QCD scale ($T_{\rm QCD} \approx 200\,{\rm MeV}$) [57]. Note that $\chi(T)$ decays rapidly beyond the confinement temperature, such that the axion is essentially massless at high temperatures.

## 2.3 Axion Models and Interactions

The strong CP problem is therefore solved by the introduction of the axion as the Goldston boson of the new $U(1)_{PQ}$ symmetry. However, at this stage, we have still not defined the quark and the complex scalar field used in the PQ mechanism. We have stressed earlier that such a set up was actually the minimal ingredients needed to achieve the PQ mechanism. Indeed, more sophisticated realizations, involving sometimes more fields, also exist. Hence, the *KSVZ* model [60, 61] for instance considers a complex scalar field and a quark that do not belong to the Standard Model. Both of them are singlet under $SU(2)_W$ and the quark is charged under $SU(3)_C$ as it should. As it does not belong to the Standard Model the mass of the quark produced by the spontaneous symmetry breaking can take arbitrary large values, so as $f_a$. From the previous expressions we see that a large symmetry breaking scale $f_a$ means that the axion could then reach an extremely small mass and get weakly coupled. The *DFSZ* model [19, 62] introduces on its side a second Higgs doublet, a complex scalar field, and uses the quarks of the Standard Model. All of them transform under $U(1)_{PQ}$.
The important point here is that in any model, the axion-gluon coupling that arises from the spontaneous symmetry breaking is the same and is then model independent[3]. It implies that the mass of the axion behaves as well model independently. Moreover, at low energy, the interaction between axions and pions implies that the axion will inherit from the pion-two photons interaction. It translates into an axion-photon model independent interaction

$$\mathcal{L}_{a\gamma\gamma} \approx \frac{\alpha}{32\pi^2 f_a} a\, F^{\mu\nu}\tilde{F}_{\mu\nu}. \tag{2.20}$$

Those photon and gluon couplings are the only model independent interactions the axion would get (and the only ones at all in the KSVZ model). Beyond those, interactions with quarks as well as contributions to the photon interaction can also emerge in a model dependent way as it is the case for the DFSZ model. To summarize the axion interactions, we write down explicitly the axion Lagrangian with the model independent and dependent interactions as follows:

$$\mathcal{L}_a = \mathcal{L}_{ind.} + \mathcal{L}_{dep.}, \tag{2.21}$$

with

$$\mathcal{L}_{ind.} = \frac{1}{2}\partial_\mu a \partial^\mu a + \frac{g^2}{32\pi^2 f_a} a\, G_a^{\mu\nu}\tilde{G}_{a,\mu\nu} \tag{2.22}$$

and the model dependent part given by

$$\mathcal{L}_{dep.} = \frac{g_{a\gamma\gamma}}{4} a\, F^{\mu\nu}\tilde{F}_{\mu\nu} + \frac{\partial_\mu a}{2f_a}\bar{q}_i\gamma^\mu C^{ij}\gamma^5 q_j, \tag{2.23}$$

where $g_{a\gamma\gamma}$ is the model dependent axion photon coupling and $C^{ij}$ is a diagonal matrix containing the quark couplings. At low energy, the phenomenologically relevant part of the full Lagrangian

[3] It must be as such, since the strong-CP problem is solved by its induced potential.

can be written in terms of interactions with photons, protons, neutrons and electrons:

$$\mathcal{L}_a \supset \frac{g_{a\gamma\gamma}}{4} a\, F^{\mu\nu}\tilde{F}_{\mu\nu} + i\sum_{f=n,p,e} C_{af}\frac{\partial_\mu a}{2f_a}\bar{\Psi}_f\gamma^\mu\gamma^5\Psi_f - i\sum_{f=n,p} C_{af\gamma}\frac{a}{2f_a}F^{\mu\nu}\bar{\Psi}_f\sigma_{\mu\nu}\gamma^5\Psi_f. \tag{2.24}$$

In the KSVZ model the axion-proton, axion-neutron and axion-electron couplings have been found to be [63, 64, 65]

$$\begin{aligned} C_{ap}^{\text{KSVZ}} &= -0.47(3), \\ C_{an}^{\text{KSVZ}} &= -0.02(3), \\ C_{ae}^{\text{KSVZ}} &= \frac{3\alpha^2}{4\pi^2}\left(\frac{E}{N}\log\left(f_a/m_e\right) - 1.92\log(1\text{GeV}/m_e)\right), \end{aligned} \tag{2.25}$$

where $E/N$ is the ratio between the electromagnetic and color anomalies and is usually set to $0$ in the KSVZ model [60, 61] whereas it takes the value $3/8$ in the DFSZ one [19, 62]. However, it has been shown that a broader range of values are possible [66, 67, 68, 69]. In the DFSZ model, the coefficients become [63, 64]

$$\begin{aligned} C_{ap}^{\text{DFSZ}} &= 0.617 + 0.435\sin^2\beta \pm 0.025, \\ C_{an}^{\text{DFSZ}} &= 0.254 - 0.414\sin^2\beta \pm 0.025, \\ C_{ae}^{\text{DFSZ}} &= \frac{\sin^2\beta}{3}, \end{aligned} \tag{2.26}$$

where $\beta$ is an extra parameter related to the ratio of the Higgs vevs.
The axion-photon-nucleon coupling is model independent and gets the same absolute value for the proton and neutron [63, 64]

$$C_{an\gamma} = -C_{ap\gamma} = (3.7 \pm 1.5)\times 10^{-3}. \tag{2.27}$$

Finally, the axion-photon coupling is given as well in terms of the ratio between the electromagnetic and color anomalies $E$ and $N$ as [63, 64]

$$g_{a\gamma\gamma} = \left(0.203(3)\frac{E}{N} - 0.39(1)\right)\frac{m_a}{\text{GeV}^2}. \tag{2.28}$$

The KSVZ and DFSZ theoretical values for this coupling are shown in Fig.2.2 by the yellow band.

Let's have a closer look at the axion-photon coupling and the way it can be probed in experiments. First, this interaction allows for the decay of the axion into two photons. However, for the breaking scale $f_a$ usually considered $f_a \sim 10^{12}$GeV (see Sec.2.4), the lifetime of the axion would reach the lifetime of the universe, making this particle stable. Bad luck for experiments since such a decay would have a clear signature with each photon carrying an energy $E_\gamma = m_a/2$. On the other hand, stability is a necessary condition for being a good dark matter candidate. Secondly, the axion-photon coupling allows for the conversion of an axion into photons in the presence of a strong magnetic field (and vice-versa). This is known as the Primakoff effect [70]. P. Sikivie proposed to use it to detect the axion into several experiments [33]. The first one is the so-called light shining through the wall experiment. A laser embedded in a strong magnetic field is projected toward a wall such that photons could be converted into axions. They would then easily penetrate the wall and be converted again into photons on the other side where a strong magnetic field is still applied. However, no such signal has been ever observed and bounds on the axion photon couplings can be set. The current best limit has been derived by the Optical Search for QED Vacuum Birefringence (OSQAR) collaboration with $g_{a\gamma\gamma} < 3.5\times 10^{-8}\text{GeV}^{-1}$ for $m_a < 0.3\,\text{meV}$ at $95\%$ CL [71].
The second experiment is the so-called axion Haloscope. It uses the assumption that the dark matter halo of the milky way is, at least partially, composed of axions and that the Earth is therefore

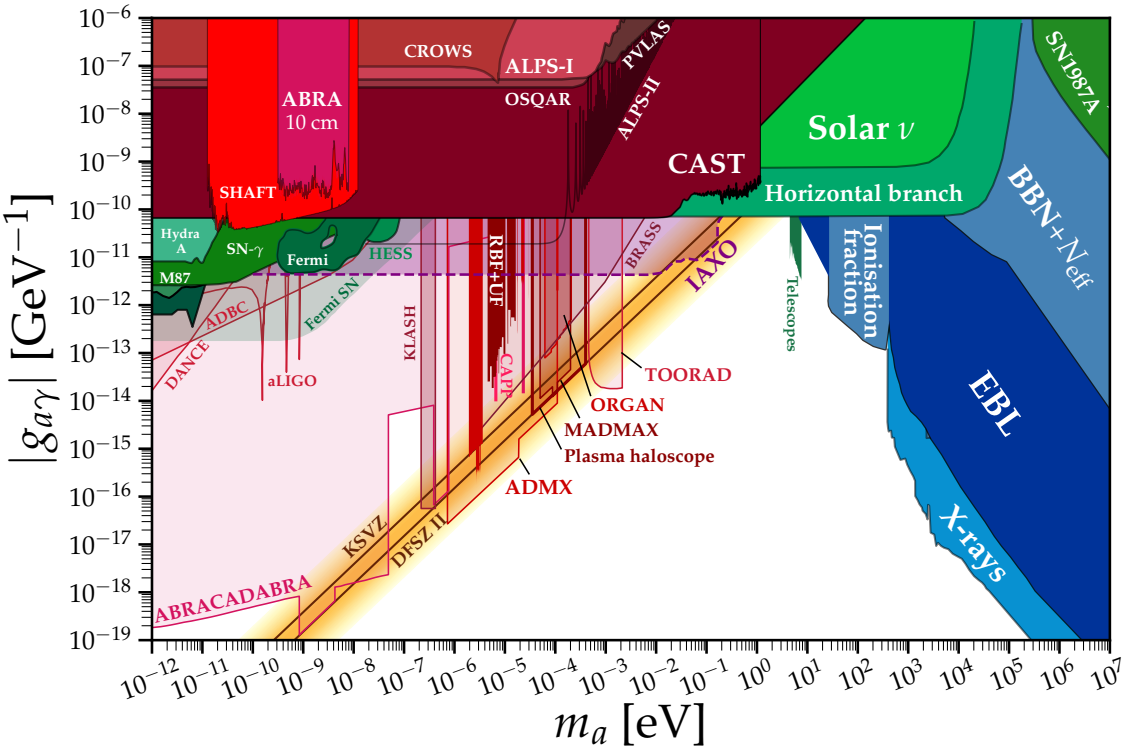


**Figure 2.2:** Upper limits on the axion-photon coupling $g_{a\gamma\gamma}$ from current experiments. The KSVZ and DFSZ theoretical predictions are shown by the two solid black lines. The yellow band represents the extended possible values for the ratio $E/N$ (see main text). The future experiments sensitivities are represented by the light shaded regions. This figure has been taken from Ref.[72]

constantly moving in an axion background. The haloscope experiments are usually designed as cavities embedded in a strong magnetic field. When the axion field penetrates it, it could convert into photons leaving an electromagnetic power that we can measure. More precisely, if the axion field frequency, given roughly by its mass if the axions are non-relativistic, is the same as the one of the main mode of the cavity, resonance happens and the signal is enhanced. The cavity shape is therefore constantly modified in order to modify the main mode and to look for resonance. Doing so, those experiments were able to exclude a large range of the possible axion masses. The Axion Dark Matter Experiment (ADMX), based in the USA, has started to probe the parameter space of the axion-photon coupling predicted by both the KSVZ and DFSZ models and this in the mass range $2.7 - 4.2\,\mu$eV [73, 74, 75, 76]. Other similar experiments also exist and derived upper limits on heavier mass ranges (see Fig. 2.2). Chapter 4 will be specifically dedicated to haloscope experiments and more details will be therefore given in this one.

The last experiment proposed by P. Sikivie is the so-called axion helioscope experiment. The axions produced inside the Sun (they could be for instance produced by the strong magnetic field in the inner parts of the Sun) create an incoming flux of relativistic particles on Earth. The idea here consists in pointing toward the Sun a strong magnetic field to convert this axion flux back to X-ray photons. The strongest upper limit has been derived by the CERN Axion Solar Telescope (CAST) experiment and set $g_{a\gamma\gamma} < 6.6 \times 10^{-11}$ GeV at 95% CL in the mass range $m_a < 0.02$ eV [77]. Limits on masses up to $m_a < 1.17$ eV have also been reached by filling the magnet bores with different gases [78, 79, 80]. As for the axion haloscope, the other experiment upper limits are shown in Fig. 2.2.

Following the same idea, since axions could be produced in hot astrophysical plasma and then easily escape, it would generate an anomalous cooling for stars, reducing their lifetime. Observation of the horizontal branch stars lead to strong constraints on the axion-photon coupling: $g_{a\gamma\gamma} < 6.6 \times 10^{-11}$ GeV at 95% CL on a mass range even broader than the one obtained by CAST [81].

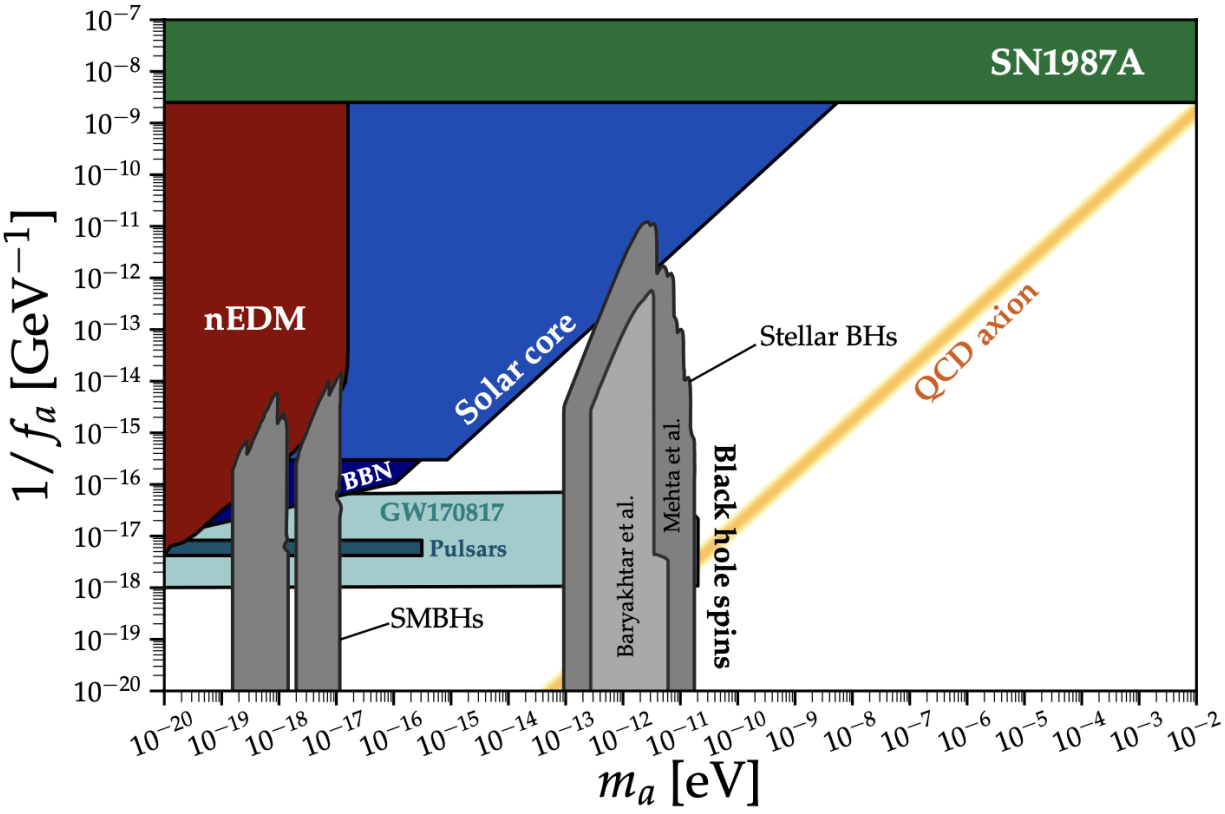


**Figure 2.3:** Limits on the PQ symmetry breaking scale $f_a$ as a function of the axion mass $m_a$. This figure has been taken from Ref.[72]

Other constraints on lighter and heavier mass ranges are presented in Fig. 2.2.
Finally, future experiments are expected to importantly improve the current upper limits. This is for instance the case of ABRACADABRA which should reach a sensitivity able to probe couplings down to $g_{a\gamma\gamma} \approx 10^{-18}$ GeV [82, 83]. Next generation of axion helioscope, the International Axion Observatory (IAXO), should also push the coupling limit down [84]. On the axion haloscope prospects, the next generation of ADMX or the new proposed experiment, the Magnetized Disc and Mirror Axion experiment (MADMAX), should explore broader mass ranges and dig deeper in the KSVZ and DFSZ region [85, 86]. All the future experiment sensitivities are presented in Fig.2.2.
Upper limits also exist for the other couplings of the Lagrangian (2.24) but since this thesis will not dedicate a specific section to those interactions, we redirect the interested reader to Ref.[72] for a summary on their current limits.

## 2.4 Axion as Dark Matter

Let's summarize the chain of events leading to the axion appearance. At some high scale $f_a$ the new $U(1)_{PQ}$ symmetry is spontaneously broken and leads to the axion as the angular degree of freedom of a complex scalar field $\phi$. The axion field $a$ inherits from the $U(1)_{PQ}$ symmetry through a shift symmetry $a \to a +$ const. However the anomaly of the chiral symmetries breaks explicitly $U(1)_{PQ}$ and induces a model independent potential for the axion as well as a mass term depending on the temperature and the symmetry breaking scale $f_a$. Limits from supernova cooling [87, 88] and black holes superradiance [89] have constrained the breaking scale $f_a$ in the range $10^9$ GeV $< f_a < 10^{17}$ GeV (see Fig.2.3).
The axion gets self-interactions and couplings to Standard Model particles suppressed by powers of the scale factor $f_a$. For this reason, the large expected value of the breaking scale implies for the

axion to be long-lived and weakly interacting. In addition, for the QCD axion, since the mass is inversely proportional to $f_a$, the axion is expected to be extremely light. For those reasons, it becomes naturally a good dark matter candidate.
Assuming the axion to be a good dark matter candidate means that an efficient production mechanism is needed in order to produce a sizeable dark matter relic abundance. In this section, we are going to introduce and discuss in detail the so-called misalignment mechanism [20, 21, 22] since it provides an elegant way to produce the observed cold dark matter abundance on a model independent way. The thermal production will be discussed as well at the end of the section.

### 2.4.1 Misalignment Mechanism

The misalignment production [20, 21, 22] relies directly on the spontaneous symmetry breaking of $U(1)_{PQ}$ and provides a model independent mechanism to produce a cold axion relic abundance. As it will be discussed later in this section, axions produced via this mechanism would have a cosmological evolution drastically different depending on whether the symmetry breaking occurres before or after inflation.
Let's start the discussion by considering the equation of motion for the axion field in an expanding universe. The action, neglecting the axion self-interactions and couplings to other particles, is given by

$$S_\theta = f_a^2 \int d^4x \sqrt{-g} \left( -\frac{1}{2}\partial_\mu\theta\partial^\mu\theta - V(\theta, T) \right), \tag{2.29}$$

where $g^{\mu\nu}$ is the Friedman-Robertson-Walker metric and $\theta = a/f_a$. The temperature dependent axion potential induced by the chiral anomaly is written as $V(\theta, T)$ (c.f Eq.(2.18)). Below QCD phase transition, it takes its zero temperature form given by Eq.(2.15).
From this, the equation of motion for the axion can be written as

$$\Box\theta - \frac{\partial V}{\partial\theta} = 0, \tag{2.30}$$

where the d'Alembertian operator depends on the following metric

$$\Box = \frac{1}{\sqrt{-g}}\partial_\mu \left( \sqrt{-g} g^{\mu\nu} \partial_\nu \right). \tag{2.31}$$

For the Friedman-Robertson-Walker metric, the equation of motion becomes

$$\ddot{\theta} + 3H\dot{\theta} - \frac{1}{a^2}\nabla^2\theta + \frac{\partial V}{\partial\theta} = 0, \tag{2.32}$$

with $a$ the scale factor (not to be confused with the axion field denoted $\theta$ in further parts of the section) and the Hubble constant is $H = \dot{a}/a$.
We have already claimed that for the large breaking scales remaining unconstrained, the QCD axion would have an extremely small mass. However, in order to produce a sizable fraction of the dark matter abundance, the occupation number on each energy level should be enormous. For this reason, the axions are described by a classical field rather than by individual quanta. The equation of motion derived for the axion field then has to be understood exactly as when photons are described classically by the Maxwell equations.
In addition, the stress energy tensor is defined for the axion field as

$$T^{\mu\nu} = f_a^2 \partial^\mu\theta\partial^\nu\theta + g^{\mu\nu} f_a^2 \left( -\frac{1}{2}\partial_\sigma\theta\partial^\sigma\theta - V(\theta, T) \right). \tag{2.33}$$

It follows that the energy density $\rho_\theta$ and pressure $P_\theta$ of the axion field are given by

$$\begin{aligned} \rho_\theta &= f_a^2 \left( \frac{1}{2}\dot{\theta}^2 + \frac{1}{2a^2}(\nabla\theta)^2 + V(\theta, T) \right), \\ P_\theta &= f_a^2 \left( \frac{1}{2}\dot{\theta}^2 - \frac{1}{6a^2}(\nabla\theta)^2 - V(\theta, T) \right). \end{aligned} \tag{2.34}$$

These last set of equations are the starting point for the misalignment mechanism. Before going into more details, let's sketch its main ideas.
At early times (large temperatures, much higher than QCD confinement $T_{QCD} = \Lambda_{QCD} \approx 200\,\text{MeV}$), the axion mass and hence the potential are still negligible, $V(\theta) \sim 0$. In that case the equation of motion is simply

$$\ddot{\theta} + 3H\dot{\theta} - \frac{1}{a^2}\nabla^2\theta = 0. \tag{2.35}$$

In order to solve this equation, the initial conditions for the axion field are needed. Since no potential influences the axion so far, $\theta = a/f_a$ can, therefore, get any value between $-\pi$ and $\pi$. We call $\theta_i$ this initial value. Let's for the moment assume that the axion field takes this initial value homogeneously in the whole universe. In that case, the gradient term disappears and we are left with

$$\ddot{\theta} + 3H\dot{\theta} = 0. \tag{2.36}$$

It is then easy to see that the axion field would stay frozen at its initial value $\theta_i$ as long as this equation remains valid.
However, the universe is cooling down and as derived in the previous section, the potential $V(\theta, T)$ (and therefore the axion mass $m_a(T)$) arising from the chiral anomaly becomes eventually relevant. At that stage, using Eq.(2.15), the equation of motion becomes

$$\ddot{\theta} + 3H(T)\dot{\theta} + m_a^2(T)\theta = 0. \tag{2.37}$$

Note that here we have used a Taylor expansion of the potential assuming small displacements of the axion around its minimum, which means that $a \ll f_a$ and that the potential can be written at leading order as $V(\theta, T) \approx \frac{1}{2}m_a(T)^2\theta^2$. The last equation is basically the one of a damped harmonic oscillator. A competition therefore occurs between the oscillation term coming from the mass $m_a(T)$ and the damping from the universe expansion, parameterized by the Hubble constant $H(T)$ decreasing with temperature. Since both of those quantities are functions of the temperature, it is possible to follow the axion field evolution as a function of the temperature as well. Of course we recover that at early times, the axion field is frozen at its initial value $\theta_i$ since $m_a(T) \sim 0$ and the damping dominates. However, at lower temperatures the oscillations can start and eventually dominates when $m_a(T) > H(T)$. As already developed in the previous section, the oscillations occur around a CP conserving minimum, solving the strong CP problem. Those oscillations will in addition, generate an energy density and finally an axion relic abundance today. This is the key of the misalignment mechanism.
An important question still remains. We have so far assumed that the initial value of the axion field was homogeneous and given by $\theta_i$ in the whole universe. Is that true in any case? Actually not really. When symmetry breaking happens, different values of $\theta_i$ would be observed in different causally disconnected regions. However, if the $U(1)_{PQ}$ symmetry gets broken before inflation, each Hubble patch with different values of $\theta_i$ would be stretched out by the fast expansion, so that at the end of inflation our current Hubble volume starts with a homogeneous value of $\theta_i$. This is the so-called *pre-inflation scenario*. On the other hand, if symmetry breaking occurs after the inflation period, each Hubble patch of radius $R \sim 1/H$ would get a random initial field value. This would lead to some exotic phenomenology and eventually the so-called axion miniclusters. This is the *post-inflation scenario*. We are now going to derive explicitly for these two scenarios the dark matter relic abundance and the properties of the axion field.

#### Pre-Inflation Scenario

As explained, in this scenario inflation ends with a single and homogeneous value for the axion field. This value $\theta_i$ is randomly taken between $-\pi$ and $\pi$. It can be seen that the evolution of the axion field is identical to the toy model considered above: the field is initially frozen at the initial value $\theta_i$

as long as $m_a(T) < H(T)$. Hence at that stage, the energy density is given from Eq.(2.34) by

$$\rho_\theta(T) = \frac{f_a^2}{2} m_a^2(T)\theta_i^2 \tag{2.38}$$

Eventually, as the mass keeps increasing up to its zero temperature mass (see Eq.(2.17)) and the Hubble constant keeps decreasing, the mass overtakes the friction term and the axion field starts oscillating.
To capture the cosmological evolution of the axion field at this stage, we solve Eq.(2.37) with the help of the WKB approximation in the limit $H(T) \ll m_a(T)$. It that case, the solution is given by

$$\theta(t) \approx \frac{C}{a^{3/2}\sqrt{m_a(t)}} \cos\left(\int_{t_0}^{t} dt'\, m_a(t')\right), \tag{2.39}$$

where $C$ has to be fixed by the initial condition at a time $t_0$. The detail calculation could be found in [90] for the interested reader.
The energy density in that limit is a fast oscillating function with frequency $\sim m_a$. Hence the density averaged over those fast oscillations is written as

$$\langle \rho_\theta(T) \rangle = \frac{C^2 f_a^2}{2a^3} m_a(T). \tag{2.40}$$

The coefficient $C$ is found by matching together both limits at the time the oscillations start. This takes place at the oscillating temperature $T_{\text{osc}}$ when $3H(T_{\text{osc}}) \sim m_a(T_{\text{osc}})$ and we find

$$C^2 = m_a(T_{\text{osc}}) a^3(T_{\text{osc}}) \theta_i^2. \tag{2.41}$$

When the mass becomes dominant and the oscillations start, the mean energy density is then given by

$$\langle \rho_\theta(T) \rangle = \frac{m_a(T_{\text{osc}}) m_a(T) f_a^2}{2} \left(\frac{a(T_{\text{osc}})}{a(T)}\right)^3 \theta_i^2, \tag{2.42}$$

In addition, the averaged pressure can be calculated in a similar way, leading to

$$\langle P_\theta(T) \rangle = 0. \tag{2.43}$$

The strong conclusion of this result is that as soon as the field starts to oscillate (when $m_a > H$), the energy density starts to decay following $\rho_\theta \sim 1/a^3$ and the equation state has $w_\theta = 0$ independently of whether the background is radiation or matter dominated. This is exactly the same behavior as ordinary matter, and for this reason the axion field behaves as cold dark matter.
In order to calculate the axion relic abundance $\Omega_\theta = \rho_\theta(T_0)/\rho_c$, with $T_0$ and $\rho_c$ respectively the temperature today and the critical density, we must find the oscillating temperature $T_{\text{osc}}$. This one would depend exclusively on the symmetry breaking scale $f_a$. Indeed, using the analytical approximation derived in Ref.[91] for the mass $m_a(T)$ at temperature $T > \Lambda_{QCD}$,

$$m_a^2(T) \approx 0.018 \times m_a^2(T=0) \left(\frac{\Lambda_{QCD}}{T}\right)^4, \tag{2.44}$$

it is found that axions with breaking scale $f_a < 2 \times 10^{15}$GeV have an oscillating temperature $T_{\text{osc}} > \Lambda_{QCD}$. For those, the oscillating temperature is given by

$$T_{\text{osc}} = 150\,\text{MeV} \left(\frac{10^{16}\text{GeV}}{f_a}\right)^{1/6}. \tag{2.45}$$

It is then possible to calculate the axion relic abundance today for $f_a < 2 \times 10^{15}$GeV [91],

$$\Omega_\theta h^2 \sim 2 \times 10^4 \left(\frac{f_a}{10^{16}\text{GeV}}\right)^{7/6} \theta_i^2. \tag{2.46}$$

For larger breaking scales $f_a > 2 \times 10^{15}$GeV, oscillations start with $T_{\rm osc} < \Lambda_{QCD}$. At those temperatures, the mass can be evaluated with its zero temperature value and the axion relic abundance is in that case [91]

$$\Omega_\theta h^2 \sim 5 \times 10^3 \left(\frac{f_a}{10^{16}\text{GeV}}\right)^{3/2} \theta_i^2. \tag{2.47}$$

We observe here that the axion relic abundance depends on the symmetry breaking scale $f_a$ as well as on the random initial value of the field $\theta_i$. It is therefore possible to tune this parameter to reach arbitrary values for the axion relic abundance. The pre-inflation is, for this reason, less predictive than the post-inflation scenario, where we will see, this $\theta_i$ dependence disappears.

So far, only the background axion field contribution has been considered. However, for axions to be fully considered as cold dark matter, its density fluctuations should be investigated as well. In particular, they should follow the same equation as a perfect pressureless fluid, if we want to explain the observed power spectrum. Detailed calculations have been conducted in Refs.[92, 93, 94, 95] and at linear order the density contrast $\delta = (\rho_\theta - \bar{\rho_\theta})/\bar{\rho_\theta}$, with $\bar{\rho_\theta}$ the background density calculated above, follows the equation

$$\ddot{\delta}_{\boldsymbol{k}} + 2H\dot{\delta}_{\boldsymbol{k}} - \left(4\pi G\bar{\rho_\theta} - \frac{1}{4}\frac{k^4}{m_a^2 a^2}\right)\delta_{\boldsymbol{k}} = 0, \tag{2.48}$$

where $\delta_{\boldsymbol{k}}$ is the amplitude of the Fourier mode with momentum $\boldsymbol{k}$.
Interestingly, this equation has an additional pressure term compared to the standard pressureless cold dark matter equation. This so-called quantum pressure[4], explicitly given by

$$\begin{aligned} \mathcal{Q} &= \frac{1}{2a^2 m_a^2}\frac{\Delta_{\boldsymbol{x}}\sqrt{\rho_\theta}}{\sqrt{\rho_\theta}}, \\ &= \frac{1}{2a^2 m_a^2}\frac{\Delta_{\boldsymbol{x}}\sqrt{1+\delta}}{\sqrt{1+\delta}}, \\ &\approx \frac{1}{4a^2 m_a^2}\Delta_{\boldsymbol{x}}\delta, \end{aligned} \tag{2.49}$$

is the direct consequence of the uncertainty principle: as the momentum increases, the delocalization of the particle increases as well [96]. Intuitively, this source of pressure will stand in opposition to gravity (first term in the bracket in Eq.(2.48)). Hence, after matter-radiation equality it is expected for the perturbations to grow at all scales. However, in the specific case of axion dark matter, all the modes with momentum $k > k_J$ would rather oscillate since they are supported by the quantum pressure. We define here the comoving Jean scale $k_J$ as

$$k_J = a\left(16\pi G m_a^2 \bar{\rho_\theta}\right)^{1/4}, \tag{2.50}$$

which corresponds to a physical wavelength

$$\begin{aligned} \lambda_J &= \frac{2\pi a}{k_J}, \\ &= 2\pi\left(16\pi G m_a^2 \bar{\rho_\theta}\right)^{-1/4}, \\ &= 5.4 \times 10^{14}\text{cm}\left(\frac{m_a}{10^{-5}\text{eV}}\right)^{-1/2}. \end{aligned} \tag{2.51}$$

At larger scales, the axion is therefore acting exactly as pressureless dark matter. For smaller scales below $\lambda_J$ , structure formation is, however, compromised by the quantum pressure. Nevertheless, we see that $\lambda_J$ is small compared to the solar system size for masses around $10^{-5}$eV. Only very

[4]The term that appears in the previous equation is the Fourier transform of $\Delta_{\boldsymbol{x}} Q$.

light axions $m_a \sim 10^{-22}$eV would therefore play an observable role on structure formation (see for instance Ref.[97]). We conclude that, as long as we are away from $\lambda_J$, the axions can act as a good cold dark matter candidate.
We now move on to the post inflation scenario.

**Post-Inflation Scenario**

As already stressed above, the pre-inflation scenario has the disadvantage to depend directly on the initial angle $\theta_i$, randomly distributed between $[-\pi, \pi]$. It is therefore difficult to make strong predictions without fine-tuning the value of $\theta_i$. Let's see how the post-inflation scenario evades this issue.
If the PQ symmetry is broken after inflation, the axion field takes a different initial value $\theta_i$ in causally disconnected regions, each of them scaling as the Hubble radius $\sim 1/H$. Since the field has no homogeneous initial condition, the gradient term in Eq.(2.32) can not be dropped out as for the pre-inflation scenario. In addition, these initial inhomogeneities would evolve into large isocurvature density fluctuations. As we will see, those are the seeds of the axion miniclusters we are going to discuss in detail in the next chapters.
Even though, the equation of motion for the axion field gets more complicated in this scenario, the mean density can be estimated rather easily. Indeed, assuming that all the patches with different initial $\theta_i$ are independent, we can simply calculate the energy density in each and finally average over them [21, 20, 98, 23]. The mean density in the post-inflation scenario is therefore given by an average over all the $\theta_i$ on Eq.(2.42),

$$\langle \rho_\theta(T) \rangle = \frac{m_a(T_{\rm osc}) m_a(T) f_a^2}{2} \left( \frac{a(T_{\rm osc})}{a(T)} \right)^3 \int_{-\pi}^{\pi} d\theta_i f(\theta_i) \theta_i^2, \tag{2.52}$$

where $f(\theta_i)$ is the probability distribution of the parameter $\theta_i$. In particular, for a uniform distribution, we get $f(\theta_i) = 1/2\pi$ and then

$$\langle \rho_\theta(T) \rangle = \frac{m_a(T_{\rm osc}) m_a(T) f_a^2}{2} \left( \frac{a(T_{\rm osc})}{a(T)} \right)^3 \frac{\pi^2}{3}. \tag{2.53}$$

Note that all the information about the initial angles $\theta_i$ is lost in the final expression and the background density only depends on the symmetry breaking scale $f_a$ and the mass $m_a$. As for the pre-inflation scenario, we use the temperature dependence of the mass $m_a(T)$ to calculate the oscillation temperature $T_{\rm osc}$. Hence, under this simplified calculation, the today's axion relic abundance $\Omega_\theta = \rho_\theta(T_0)/\rho_c$ is finally found to be [57, 24, 99]

$$\begin{aligned} \Omega_\theta h^2 &\sim 0.1 \left( \frac{f_a}{10^{12}\text{GeV}} \right)^{7/6}, \\ &\sim 0.1 \left( \frac{m_a}{5.7 \times 10^{-6}\text{eV}} \right)^{-7/6}, \end{aligned} \tag{2.54}$$

where, in the last step, we have used the relation between the mass and the breaking scale from Eq.(2.17). Since $\Omega_{\rm DM} h^2 = 0.12$ [10], axions with masses of the order $m_a \sim 10^{-5}$eV could account for the whole dark matter relic abundance. Any mass much smaller than that would overproduce dark matter and then overclose the universe.

A more careful analysis has, however, been achieved in Ref.[100] by solving explicitly Eq.(2.32) and then taking into account the non-zero momentum modes. Following their calculations, the axion field is initially inhomogeneous and we could write it as

$$\theta(\boldsymbol{x}) = \int d\boldsymbol{k}\, \theta(\boldsymbol{k}) e^{i\boldsymbol{k}.\boldsymbol{x}}, \tag{2.55}$$

where $\theta(\boldsymbol{k})$ are the Fourier coefficients. The randomness behavior of this field is captured by its variance and we recover the previous result,

$$\langle\theta^2(\boldsymbol{x})\rangle = \frac{\pi^2}{3}. \tag{2.56}$$

In Fourier space, this translates into the power spectrum definition

$$\langle\theta(\boldsymbol{k})\theta^*(\boldsymbol{k'})\rangle = (2\pi)^3\delta^3(\boldsymbol{k}-\boldsymbol{k'})P_\theta(k). \tag{2.57}$$

The randomness of the axion field is then translated to the Fourier coefficients. In practice the power spectrum can be taken as an Heaviside function encoding the fact that the causally disconnected regions are uncorrelated.
Each Fourier mode evolves independently and the time evolution for each of them is encoded inside the function $f_{\boldsymbol{k}}(t)$, such that $\theta(\boldsymbol{k},t) = \theta(\boldsymbol{k})f_{\boldsymbol{k}}(t)$. This last function has to be found numerically but can be understood easily: for a given mode $\boldsymbol{k}$, $f_{\boldsymbol{k}}(t)$ is frozen at 1 in the early universe. But similarly to the pre-inflation scenario, at a given oscillation temperature, it becomes an oscillating function decaying with power $a^{-3/2}$. The frequency of the oscillation is here given by $\omega_k^2(T) = k^2/a^2(T) + m_a(T)$, where the additional term compared to the pre-inflation scenario is coming from the gradient in (2.32). Therefore the high momentum modes start oscillating earlier and the zero mode is the last one to do so. The mean density is given by (see Ref.[100] for an explicit derivation)

$$\langle\rho_\theta\rangle = \frac{f_a^2}{4\pi^2}\int dk k^2 P_\theta(k)F(k), \tag{2.58}$$

with the function $F(k)$ defined as

$$F(k) = \dot{f}_k^2 + \omega_k^2 f_k^2. \tag{2.59}$$

Let's consider the late time behavior of this solution. When all the modes have become non-relativistic (when the term $k^2/a$ becomes subdominant compared to $m_a$) and when the axion mass has reached its zero temperature value, $f_k$ scales as $a^{-3/2}$ and oscillates with a frequency proportional to $m_a$ for all the modes. We can factorize the only scale factor dependence, $a^{-3}$, out of the function $F(k)$ and average over the fast oscillations as for the pre-inflation scenario,

$$\langle\rho_\theta\rangle = \frac{f_a^2}{8\pi^2 a^3}\int dk k^2 P_\theta(k)\tilde{F}(k), \tag{2.60}$$

where $F = a^{-3}\tilde{F}(k)$.
It may be observed that the background density acts as cold dark matter again, as it should. The only difference with the previous simple estimate is that the contribution from all the modes is now taken into account via the momentum integral. For both a top-hat and a Gaussian window function, Ref.[100] proved that Eq.(2.60) leads to similar abundance as derived in Eq.(2.54).
However, as already emphasized in the introduction of this part, the post-inflation scenario leads to further important phenomenology predictions. The initial large inhomogeneities in the field due to the distribution of the misalignment angle $\theta_i$ make it necessary to use the full potential and not the approximation used so far. The use of the full non-linear expression brings new axion field solutions that will contribute to the relic abundance. In particular, at the locations where the field is surrounded by all possible values of $\theta_i$ between $[-\pi,\pi]$, the complex scalar field (that should produce the axion by spontaneous symmetry breaking) do not know on which vacuum value it should fall down. As long as the axion field is massless it therefore stays on top of the Mexican-hat potential. Those field configurations create topological defects named cosmic strings [101, 102, 103] (see left panel of Fig.2.4). As the universe is cooling down, the axion develops its mass and the strings would decay by emitting relativistic axions. Another topological defect may then also form

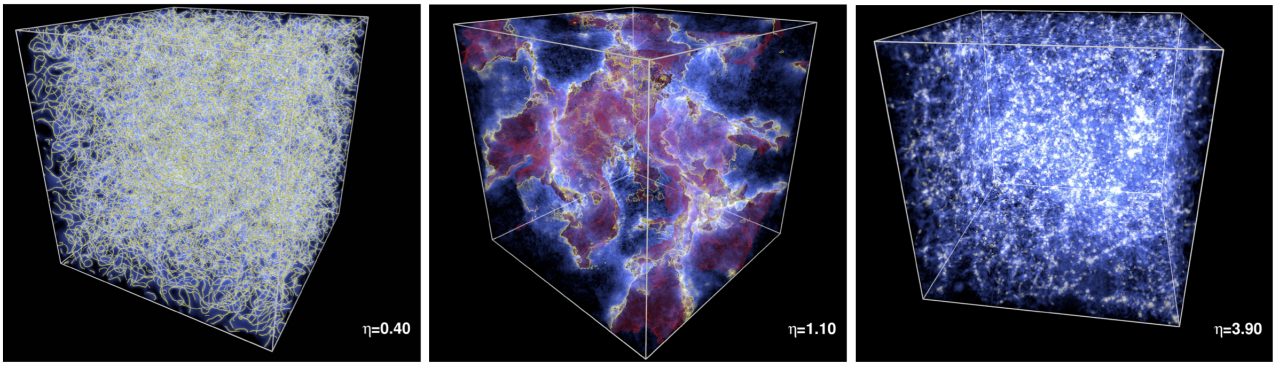


**Figure 2.4:** Simulations from Ref.[29] showing the non-linear evolution of the axion field in the post-inflation scenario. The cosmic strings are represented in yellow, the domain walls in red and the energy density in blue. From left to right, the time is going from before, during and after QCD phase transition.

from the boundaries of the cosmic strings, the domain walls (see middle panel of Fig.2.4). They are, however, unstable as well and contribute to the production of relativistic axions. In practice, only numerical simulations can follow the evolution of the string-domain network as it has been done for instance in Refs.[29, 30]. The relic abundance calculated above must therefore take those contributions into account in order to make correct prediction on the QCD axion mass needed to account for the whole dark matter. It has been found in Ref.[104] that $m_a \sim 20\mu$eV is needed in order to cover the observed dark matter abundance, which is of the same order as what has been found earlier without considering the topological defects.
When all the topological defects have finally decayed (below QCD phase transition, when the axion mass has reached its zero temperature value), some large inhomogeneities remains on the small scale energy density (see right panel of Fig.2.4). Those fluctuations are the seeds of the axion miniclusters and would collapse before matter-radiation equality [25, 105, 106] . It is important to note here that those isocurvature fluctuations differ from the adiabatic fluctuations considered previously in the pre-inflation scenario. In the post-inflation scenario, both types of fluctuations would be present such that

$$\delta_\theta = \delta_\theta^{\text{iso.}} + \delta_\theta^{\text{adi.}}. \tag{2.61}$$

It is usually assumed that adiabatic fluctuations are inherited from inflation and characterized by the curvature power spectrum $P_\zeta(k)$. In particular, this one has been constraint by CMB observations to be of the order $10^{-9}$ at lare scales [10]. The adiabatic fluctuations are transmitted to all the different species (baryons, photons, dark matter,...) and would eventually be responsible for the large-scale structures and the origin of galaxy formation. On the other hand, the isocurvature fluctuations introduced here concern only the axion field and are totally uncorrelated with the curvature fluctuations. Moreover, the overall density fluctuation is zero: $\delta\rho_\theta = 0$.
As we will see in detail in the next section 2.5, those isocurvature fluctuations are large enough to collapse into axion miniclusters way before galaxy formation. The initial population of axion miniclusters will eventually evolve into large dark matter halo, in which the galaxies would form. From that stage, the axion miniclusters would undergo tidal interactions with the galactic stars. The impact of those interactions on the miniclusters will be at the center of the chapter 3.

### 2.4.2 Thermal Production

We have concluded in the previous section that the misalignment mechanism provides an efficient way to produce a cold axion relic abundance and the mass needed to account for the whole dark matter is of the order of $m_a \sim 10^{-5}$eV. However, is it possible to produce a sizable number of axions through thermal production? The interaction involving pions $\pi + \pi \to a + \pi$ is the most efficient

process and when its rate goes below the Hubble rate, an axion relic is expected with a number density given by [107]

$$n_a \approx \frac{83\,\mathrm{cm}^{-3}}{g_*(T_D)/10}, \tag{2.62}$$

where $g_*(T_D)$ is the number of degrees of freedom at the freeze-out temperature $T_D$.
The axions produced would be relativistic, in opposition to the misalignment mechanism, until the temperature drops below the axion mass. Hence, under such a production the axions are expected to act as hot dark matter similarly as neutrinos do.
The axion thermal production gets more efficient as the pion-axion coupling gets larger. Since the axion interactions scale inversely with $f_a$, it means that we need a small breaking scale, meaning a large mass, in order to produce a sizable number of axions. It has been estimated that the thermal population is significant for $m_a > 0.15$eV, corresponding to $f_a \sim 10^7$GeV. However, stellar cooling constraints impose that $f_a > 10^9$GeV. In that range the thermal production is totally negligible.

## 2.5 Production and Evolution of the Axion Miniclusters in the Early Universe

In the previous section, we have briefly introduced the exotic phenomenology proper to the post-inflation scenario. In particular, we have discussed the appearance of large inhomogeneities that would collapse to AMCs in radiation domination era. This section has for purpose to provide more details on their formation in the early universe, according to the current state of the art and has to be seen as the first part of the lifetime of the AMCs. The chapter 3 will be dedicated to their late time evolution in the Milky Way.
Before going throughout a review of the AMC formation and evolution in the early universe, a first estimate of the typical mass and radius of the AMCs at formation can be easily made. Indeed, since the gradient term in the equation of motion will smooth the inhomogeneities on the scales smaller than the Hubble radius, the AMC mass would be roughly the one enclosed in a Hubble radius when the field starts to oscillate. For a typical axion mass $m_a \sim 10^{-5}$eV, the oscillation temperature is of the order of $T_{\rm osc} \sim 1$GeV. Hence the mass within the Hubble radius and the characteristic AMC mass is of the order [108, 109, 106]

$$\begin{aligned} M_{\rm AMC} &\sim \frac{4\pi}{3}\bar{\rho}(T_{\rm osc})\left(\frac{\pi}{H(T_{\rm osc})}\right)^3, \\ &\sim 10^{-12} M_\odot. \end{aligned} \tag{2.63}$$

A first approximation for the radius of the AMCs is to take the Hubble radius at matter-radiation equality [5]

$$\begin{aligned} R_{\rm AMC} &\sim \frac{a_{\rm eq}}{a_{\rm osc} H_{\rm osc}}, \\ &\sim 10^6\,\mathrm{km}. \end{aligned} \tag{2.64}$$

Of course those approximations have to be taken with caution since they do not account for the whole dynamic of the collapse as well as the successive mergers between AMCs. It is therefore expected to have a broader distribution in mass and radius when the axion field evolution is solved consistently.

### 2.5.1 Numerical Simulations

The first attempts to resolve the axion field evolution were made in Refs.[26, 27, 28]. The full non-linear potential was there included, and the appearance of AMCs was clearly observed. However,

[5] Even though, as emphasised already earlier, we will see that the collapse of the first generation of AMCs would occur in radiation domination era.

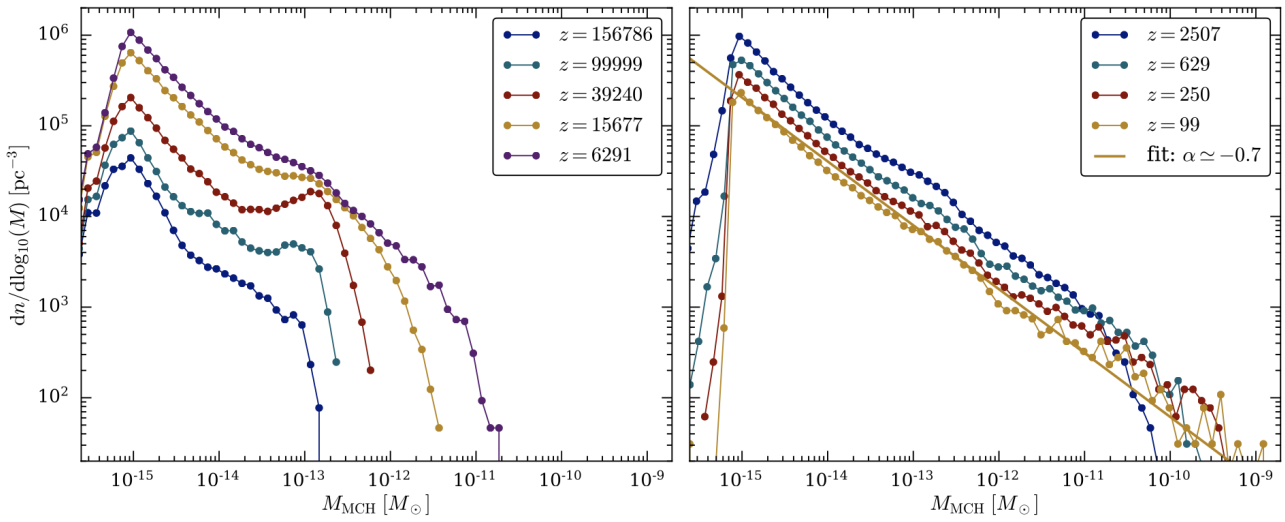


**Figure 2.5:** Evolution of the AMC mass function as a function of the redshift. It can be observed in the left panel that the mass function grows for all masses at high redshift whereas the low redshift dynamics on the right panel is dominated by the mergers and the mass function decreases for low masses to increase the high mass tail. Figure from Ref.[30].

only the real axion field was included in the simulations such that no topological defects, cosmic strings or domain walls, could have been observed. As briefly mentioned in the previous section, those objects arise when the full complex scalar field is considered.
More recently, large simulations have been conducted in Refs.[29, 30] taking into account the complex scalar field before symmetry breaking. They were therefore able to follow the appearance and the decay of the topological structures (see Fig.2.4). The idea of those studies was to characterize the density fluctuations shortly before matter-radiation equality. Their main result is that after the axion gets its zero temperature mass, the density contrast power spectrum gets frozen in time and characterizes overdensities which are already of the order $\mathcal{O}(1)$ in radiation era. Those large overdensities are able to collapse into AMCs if gravitational interactions are turned on.
Only recently, Ref.[31] realized simulations including gravitational interactions. The initial frozen density field derived in [30] was converted into particles and evolved including gravity with N-body simulations. The AMC mass function was then followed as a function of the redshift (see Fig.2.5): At early times, before radiation-matter equality $z \gg z_{\rm eq}$, the mass function is dominated by small mass AMCs corresponding to the small overdensities observed in the initial condition of [30]. As the redshift decreases, a peak starts forming at a mass $M_{\rm AMC} \sim 10^{-13} M_\odot$. This has to be understood has due to the collapse of the largest non-linear fluctuations present at high redshift. The overall AMC mass function keeps growing until radiation-matter equality $z \approx z_{\rm eq}$, washing out progressively the peak. At late time, the mass function is affected by mergers. As it can be observed in the right panel of Fig.2.5, decreasing the redshift indeed leads to a diminution of the number of AMCs in the low mass region and increases the high mass tail. The evolution is pushed down to redshift $z \approx 99$, where at that point numerical tools become inefficient.
Those simulations have finally confirmed the expected Navaro-Frenk-White (NFW) density profile [110] for the AMCs,

$$\rho(r) = \frac{\rho_0}{r/r_s \left(1 + r/r_s\right)^2}, \tag{2.65}$$

with $r_s$ the scale radius and $\rho_0$ a free parameter. However, as pointed out in Ref.[30], more work has to be done in order to follow the density profile evolution in redshift.

Even if numerical simulations provide the ideal and maybe the only way to account for the non-linear effects of the potential and the decay of the topological defects, analytical methods are al-

ways the best option if one needs to understand the underlying physics. For this reason, recent works [100, 111] have studied the formation of AMCs in semi-analytical formalism. For instance, in Ref.[111] the Press-Schechther formalism [112] was applied on the frozen power spectrum obtained in the simulation of Ref.[30] to derive the mass distribution of the AMCs at formation. Similarly, Ref.[100] followed analytically the axion field evolution starting from an initial guess for the power spectrum[6] (see Eq.(2.57)). They obtained that the density contrast power spectrum goes to a time independent function as well and therefore applied the Press-Schechter (PS) formalism at that point. It is, however, important to point out that the mass distributions extracted from those semi-analytical methods do not take into account the successive mergers after formation, as it was conducted in numerical simulations.

[6] As discussed in the previous section, in Ref.[100] the power spectrum is chosen in a way to reproduce correctly the correlation of the axion field.

# Chapter 3

# Axion Miniclusters in the Milky Way

*This Chapter is based on Ref.[113]*

In the previous chapter, we have highlighted the way the post-inflation scenario brings new phenomenological signatures. Among them, the axion miniclusters (AMCs) are a strong prediction of this model and are expected to form from the collapse of the large inhomogeneities already in radiation domination era (see Sec.2.5). As discussed earlier, numerical simulations [30, 111] have pushed the evolution of the first generation of AMCs down to redshift $z \approx 99$ taking into account the mergers in the late times. At lower redshifts, it is expected for the AMCs to become the sit of galaxy formations and to evolve into dark matter halos. This late time evolution is particularly important since interactions with surrounding matter can disturb, damage and even destroy the AMCs. A dominant source of disruption is coming from the tidal interactions with galactic stars. They can indeed strip away parts of the AMCs as they orbit within the dark matter halo leading to the formation of axion streams, particularly important for axion direct detection [114].
If it seems impossible for numerical simulations to push the AMC evolution to those low redshifts, semi-analytical methods have been developed in order to understand how the AMC properties would be modified once they are bound to the dark matter halo and tidally disrupted by stars [114, 115, 116, 117]. Using the well-known formalism directly for tidally shocked galactic clusters [118] (see Sec.3.2), those studies stayed in a picture in which the AMCs are made of classical particles. It is, however, known that for axion mass $m_a < 30\text{eV}$ [1], the averaged number of particles per unit of de Broglie wavelength is extremely large [32] making the axions better described in a classical field picture.

In this context, this chapter has for purpose to account for the wave [2] behavior of the axions in their interactions with galactic stars and their survival in the galaxy. To this point, we start in 3.1 by deriving a solution for the axion field in order to describe the AMCs in a wave picture. In 3.2, we use this solution to see how a tidal interaction with a galactic star would affect the structure of an AMC. Finally, in 3.3, the survival of the AMCs is studied using the formalism of the two previous sections.

## 3.1 Description of Axion Miniclusters in a Wave Formalism

In this section, we derive a wave function for self-gravitating objects made of axion. As emphasized above, it will be used later to describe AMCs, but the formalism described here can be applied to more general structures as well, like dark matter halos. The first step consists in deriving the equation of motion for the axion field: the Schrodinger-Poisson system. This will be discussed in Sec.3.1.1. From it, the wave function for a self-gravitating system will be constructed in Sec.3.1.2. Finally, specific examples of AMC profiles will be discussed in Sec.3.1.3

[1] Remind that the typical QCD axion mass considered in the previous chapter is of the order of $m_a \sim 10^{-5}$eV.
[2] For now on, when talking about "wave" we will always refer to a classical field in the sense of the electromagnetic field for photons.

### 3.1.1 Schrodinger-Poisson System

In order to derive the equations of motion for the axion field in a self-gravitating object, we start from the axion field action already introduced in Eq.(2.29),

$$S_a = \int d^4x \sqrt{-g} \left( -\frac{1}{2}\partial_\mu a \partial^\mu a - V(a,T) + \frac{\mathcal{R}}{16\pi G} \right). \tag{3.1}$$

Note that since we are considering self-gravitating objects, the Ricci scalar $\mathcal{R}$ needs to be included to account for the evolution of the metric. Hence deriving the equations of motion from this action, we get

$$\begin{aligned} &\frac{1}{\sqrt{g}}\partial_\mu \left( \sqrt{-g} g^{\mu\nu} \partial_\nu \right) a + V'(a), \\ &R^{\mu\nu} - \frac{1}{2} g^{\mu\nu} = 8\pi G T_a^{\mu\nu}. \end{aligned} \tag{3.2}$$

The first equation is the evolution of the axion field, as already discussed in the previous chapter. The second one is the Einstein equation, sourced by the stressed energy tensor of the axion field $T_a^{\mu\nu}$ defined in Eq.(2.34). This system is known as the Einstein-Klein-Gordon (EKG) equations.
Let's discuss more in detail the properties of this system. As already stressed earlier, for the standard QCD axion with $m_a \sim 10^{-5}$ eV the occupation number of the axion field is enormous. Indeed, the de Broglie wavelength is given as

$$\begin{aligned} \lambda_{\rm dB} &= \frac{2\pi}{m_a v}, \\ &\approx 1.49\,{\rm km} \times \left( \frac{10^{-6}{\rm eV}}{m_a} \right) \left( \frac{250{\rm km/s}}{v} \right), \end{aligned} \tag{3.3}$$

which leads to the number of axions per de Broglie wavelength [32]

$$N_{\rm dB} \approx \left( \frac{34{\rm eV}}{m_a} \right) \left( \frac{250{\rm km/s}}{v} \right), \tag{3.4}$$

if we consider the dark matter density in the solar system neighborhood $\bar{\rho} \approx 0.4{\rm GeV\ cm}^{-3}$.
Hence, exactly as for the photons that are better described by the classical electric and magnetic fields for high occupation numbers, the axion field is better described by a classical field as well (see [95, 119, 120] for further discussions).
Furthermore, an important simplification of the EKG system can be made in the context of AMCs. Indeed, the escape velocity of such objects is given as $v_{\rm esc} = \sqrt{GM/R}$, with $M$ and $R$ the mass and radius of the AMC. For the characteristic mass and radius found in Sec.2.5, we get $v_{\rm esc} \approx 10^{-9}$ which corresponds to highly non-relativistic particles. In that case, the axion field could be written as

$$a(\boldsymbol{x},t) = \frac{1}{\sqrt{2m_a}} \left( \psi(\boldsymbol{x},t) e^{-im_a t} + \psi^*(\boldsymbol{x},t) e^{im_a t} \right), \tag{3.5}$$

where the fast oscillating mass term has been factorized out such that $\psi$ is the non-relativistic axion field assumed slowly varying in time. Inserting this expansion in the EKG system, and considering the weak gravity limit for the Einstein equation leads to the so-called Schrodinger-Poisson (SP) system [121] (see App.B.1)

$$\begin{aligned} i\partial_t \psi &= -\frac{\nabla^2}{2m_a}\psi + m_a \phi \psi, \\ \nabla^2 \phi &= 4\pi G m_a |\psi|^2, \end{aligned} \tag{3.6}$$

where $\phi$ is the Newton potential of the self-gravitating object.
In the non-relativistic limit, the matter density of the axion field is given by (see App.B.2)

$$\rho = m_a |\psi|^2, \tag{3.7}$$

such that the Poisson equation is sourced by the axion field, as it should. This system describes a self-gravitating object in a wave picture and is the starting point of the next section analysis.
It is important to stress again that even if the axion field is here described via the Schrodinger equation, we are dealing with a classical field and no quantum interpretation has to be given to the wave function $\psi$. Nevertheless, the well-known $U(1)$ symmetry of the equation still has some implications. If in the quantum theory the conserved quantity is the overall probability, here it translates into the conservation of the mass (or the number of particles)

$$M = m_a \int d^3x \, |\psi|^2. \tag{3.8}$$

However, Solving the SP system analytically is challenging. Hence, recent works [122, 123, 124, 125, 126] have opted for numerical simulations in order to analyze structure formation in this wave picture. As pointed out in the previous chapter, it reproduces the cold dark matter behavior exactly at scales larger than the galaxy and deviates from it at scales around the de Broglie wavelength. In the dark matter halos formed in simulations, small-scale granules therefore emerge from the wave interference [122, 127]. We will discuss those granules in the next section more in detail.
However, numerical simulations have limitations as well. For example, even though we are interested in large-scale structures, numerical simulations have to take into account modes with typical wavelength usually much smaller than the scales of interest. The necessity of high resolution becomes then quickly an issue. For this reason, recent studies[121, 127, 128, 129, 130] have been conducted in finding an analytic solution for the wave function of the SP system in the context of dark matter halos and axion background. They are able to nicely reproduce the dark matter halos from simulations, including the small granule interference. Similarly to those works, but adapted to AMCs, we solve in the next section the SP system using the Wentzel-Kramers-Brillouin (WKB) approximation for the wave function [131, 132]. Often referred as the semi-classical approximation in the context of quantum mechanics, the WKB approximation used here for a classical field would offer a well-defined framework to justify the transition to a description of AMCs in terms of particles.

### 3.1.2 Construction of a Self-Gravitating System

#### General Formalism and Random Phase Model

The first step in the construction of the wave function of the self-gravitating AMC is to decompose its wave function on the eigenmode basis of the Schrodinger equation:

$$\left(-\frac{\nabla^2}{2m_a} + m_a\phi(\boldsymbol{x})\right)\psi_i(\boldsymbol{x}) = E_i\psi_i(\boldsymbol{x}), \tag{3.9}$$

where $i$ stands here for the label of the eigenmode $\psi_i$ and $E_i$ is the corresponding eigenenergy.
The wave function can then be written as a superposition of those modes

$$\psi(\boldsymbol{x}, t) = \sum_i a_i\psi_i(\boldsymbol{x})e^{-iE_it}, \tag{3.10}$$

with a corresponding density profile

$$\begin{aligned} m_a|\psi(\boldsymbol{x}, t)|^2 = m_a &\sum_i |a_i|^2|\psi_i(\boldsymbol{x})|^2 \\ &+ m_a \sum_{i\neq j} a_ia_j^*\psi_i(\boldsymbol{x})\psi_j^*(\boldsymbol{x})e^{-i(E_i-E_j)t}. \end{aligned} \tag{3.11}$$

Under this form, it is easy to see that the density profile carries a time independent contribution and an interference term. The latter is responsible for the appearance of the granules mentioned earlier. It can be checked that the characteristic size of those fluctuations is of the order of the de

Broglie wavelength $1/(m_a v)$ and that the typical time scale is $T_{\text{gran.}} = 1/(m_a v^2)$ with $v$ the velocity dispersion of the cluster [97, 133, 134].
An additional key feature of the AMC construction is to assume that the coefficients $a_i$ carry some random phases. Initially proposed by Refs.[121] and then extensively used in the literature for the construction of fuzzy dark matter halos (see for instance Ref.[129, 134, 135]), this assumption can be understood as an analogy to the random phases used to describe the stellar orbits in galaxies. The consequences of these random phases are then quite profound. In Eq.(3.11), they would only affect the interference term, making the small-scale granules randomly distributed. Again, this is in analogy to the stellar motions in the galaxy, where the random phases could cause occasional enhancements of the density of stars [134]. Hence the density profile of the wave function defined in Eq.(3.10) is randomly fluctuating around its mean value

$$\begin{aligned} m_a \langle |\psi(\boldsymbol{x}, t)|^2 \rangle &= m_a \sum_i |a_i|^2 |\psi_i(\boldsymbol{x})|^2, \\ &\equiv \bar{\rho}(\boldsymbol{x}). \end{aligned} \tag{3.12}$$

If each eigenmode coefficient carries a different random phase, it implies for the whole wave function $\psi(\boldsymbol{x}, t)$ to be a Gaussian random field (from central limit theorem). On its side, the random interference term of the density can be written as the sum of two squared Gaussian random fields, such that the overall density follows an exponential distribution [127]

$$P(\rho) = \frac{1}{\bar{\rho}} e^{-\rho/\bar{\rho}}. \tag{3.13}$$

Finally, it also follows from Eq.(3.11) that the variance of the density is given by (see App.B.3)

$$\sigma_\rho(\boldsymbol{x}) = \bar{\rho}(\boldsymbol{x}). \tag{3.14}$$

Hence we already see that such a wave construction can reproduce the characteristic density fluctuations at the de Broglie scales mentioned earlier for the wavy dark matter numerical simulations. However, at this point we have still not specify the value of the coefficients $|a_i|$. To do so, we have to close the SP system and find them by solving the Poisson equation

$$\begin{aligned} \nabla^2 \phi(\boldsymbol{x}) &= 4\pi G m_a |\psi(\boldsymbol{x}, t)|^2 \\ &= m_a \sum_i |a_i|^2 |\psi_i(\boldsymbol{x})|^2 + m_a \sum_{i \neq j} a_i a_j^* \psi_i(\boldsymbol{x}) \psi_j^*(\boldsymbol{x}) e^{-i(E_i - E_j)t}. \end{aligned} \tag{3.15}$$

It is here clear that the solution of the Schrodinger equation leads to a time-dependent density profile as well as a time-dependent gravitational potential. Trying to solve the Poisson equation that way would then induce a different potential than the one used to calculate the modes $\psi_i$. The way to overcome this issue is to assume that the Poisson equation is satisfied on average over the random phases. Hence Eq.(3.16) becomes

$$\begin{aligned} \nabla^2 \bar{\phi}(\boldsymbol{x}) &= 4\pi G m_a \langle |\psi(\boldsymbol{x}, t)|^2 \rangle \\ &= 4\pi G m_a \sum_i |a_i|^2 |\psi_i(\boldsymbol{x})|^2, \end{aligned} \tag{3.16}$$

where the ensemble average over the random phases is explicitly given by

$$\langle a_i a_{i'}^* \rangle = |a_i|^2 \delta_{ii'}. \tag{3.17}$$

Importantly, let's note that this is, of course, an approximation of the true solution. However, the full time dependence of the SP system could only be reached with numerical simulations. It has, however, been shown that the wave function constructed that way reproduces correctly the small-scale structure properties appearing in numerical simulations [134].

In conclusion, the wave function of a self-gravitating AMC with mean density profile $\bar{\rho}(\boldsymbol{x})$ and mean gravitational potential $\bar{\phi}(\boldsymbol{x})$ could be approached analytically under the random phase assumption by finding each eigenmode coefficient according to

$$\begin{aligned}\left(-\frac{\nabla^2}{2m_a}+m_a\bar{\phi}(\boldsymbol{x})\right)\psi_i(\boldsymbol{x})&=E_i\psi_i(\boldsymbol{x}),\\ \nabla^2\bar{\phi}(\boldsymbol{x})&=4\pi G m_a\sum_i|a_i|^2|\psi_i(\boldsymbol{x})|^2.\end{aligned}\tag{3.18}$$

The wave function

$$\psi(\boldsymbol{x},\boldsymbol{t})=\sum_i a_i e^{i\phi_i}\psi_i(\boldsymbol{x})e^{-iE_it}\tag{3.19}$$

reproduces for a given realization of the random phases $\phi_i$ the small scale interference observed in numerical simulations and on average the mean density and gravitational potential.

#### Construction Under WKB Approximation

In practice, it can, however, be challenging to solve the Schrodinger equation, derive the precise energy spectrum and hence an analytical expression for the coefficients $a_i$. For this reason, we derive in the remaining part of the section a formalism based on the WKB approximation for the wave functions $\psi_i$. It would lead to a general expression for the coefficients $a_i$, given a mean density $\rho(\boldsymbol{x})$[3] and potential $\phi(\boldsymbol{x})$.
Let's first assume that the mean gravitational potential $\phi(r)$ and density profile $\rho(r)$ are fixed and spherically symmetric (relevant for AMCs), we then write the eigenmodes in spherical coordinates with the use of the spherical harmonics $Y_{lm}$ as

$$\psi_{nlm}(r,\theta,\phi)=R_{nl}(r)Y_{lm}(\theta,\phi).\tag{3.20}$$

As for the hydrogen atom, $n$ stands for the principal quantum number and $l,m$ respectively for the angular momentum and its $z$ component. The energy levels $E_{nl}$ are independent of the quantum number $m$. The radial part of the wave function is found assuming the semi-classical WKB limit

$$R_{nl}(r)=\frac{1}{\sqrt{\mathcal{N}_{nl}}}\frac{1}{r}\frac{1}{\left[2m_a\left(E_n-V_l(r)\right)\right]^{1/4}}\sin\left(\int^r dr'\sqrt{2m_a\left(E_n-V_l(r')\right)}+\pi/4\right),\tag{3.21}$$

where $V_l(r)$ is the effective potential defined in the limit $l\gg 1$ [4] as

$$V_l(r)=\frac{l^2}{2m_a r^2}+m_a\phi(r),\tag{3.22}$$

and $\mathcal{N}_{nl}$ is a constant to assure the correct normalization

$$\mathcal{N}_{nl}=\frac{1}{2}\int_{r_1(n,l)}^{r_2(n,l)}dr\frac{1}{\sqrt{2m_a\left(E_n-V_l(r')\right)}}.\tag{3.23}$$

In this last equation, we have averaged over the fast oscillating term and introduced the two classical turning points $r_i(n,l)$ defined as $V_l(r_i)=E_{nl}$.
In line with Eq.(3.19), the wave function of the AMC is then

$$\psi(r,\theta,\phi)=\sum_{nlm}a_{nlm}R_{nl}(r)Y_{lm}(\theta,\phi)e^{-iE_{nl}t}.\tag{3.24}$$

[3] From now one we drop out the bar for the mean density/potential notation and we will specifically mention when discussing a specific realization of the density/potential.
[4] We will discuss later why this is in line with the WKB approximation.

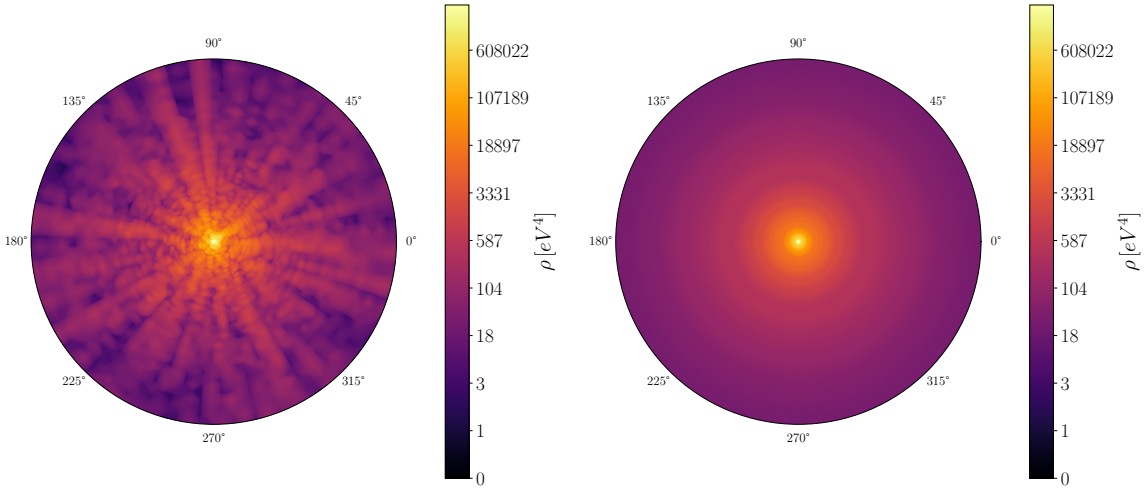


**Figure 3.1:** *Left*: Single realization of an NFW AMC with mass and radius given by $M = 10^{-13}\,M_\odot$, $R = 10^{-7}$ Pc respectively. The concentration is set here to $c = 10$. *Right*: Ensemble average over 40 realizations of the random phases for the same AMC profile. This figure corresponds to Fig.1 in Ref.[138].

In Ref.[113], we found that the coefficients $a_{nlm}$, in order to fulfil the Poisson equation (3.16) (averaged over the random phases), must be given by

$$a_{nlm} = \sqrt{(2\pi)^3 f(E_{nl}) g_l(E_{nl}) \Delta E}\, e^{i\phi_{nlm}}, \tag{3.25}$$

where $g_l(E_{nl}) = 2m_a \mathcal{N}_{nl}/\pi$ is the density of states for a given angular momentum $l$, $\phi_{nlm}$ are the random phases and $f(E_{nl})$ is the distribution function. This last function is directly related to the density and gravitational potential of the AMC through the Eddington formulae [136, 137]

$$f(E) = \frac{1}{2\pi^2 m_a^2} \frac{d}{dE} \int_{E/m_a}^{0} d\phi\, \frac{1}{\sqrt{2m_a(m_a\phi - E)}} \frac{d\rho}{d\phi}\,. \tag{3.26}$$

Let's check that this expression indeed reproduces on average the target density $\rho(r)$:

$$\begin{aligned} \rho(r) &= m_a \langle |\psi(r,t)|^2 \rangle \\ &= m_a \sum_{nlm} |a_{nlm}|^2 R_{nl}^2(r) |Y_{lm}(\theta,\varphi)|^2 \\ &= \frac{4\pi m_a^2}{r^2} \int_{m_a\phi(r)}^{0} dE\, f(E) \int_0^{l_{\max}(E,r)} dl\, \frac{l}{\sqrt{2m_a(E - V_l(r))}}\,, \end{aligned} \tag{3.27}$$

where the ensemble average over the random phases has been performed similarly to Eq.(3.17) and we have also averaged over the fast oscillations in $R_{nl}^2(r)$. In the last line, the continuous limit for the energy levels has been assumed in order to go from the sum to the integral. At a location $r$ and energy $E$, the maximum allowed angular momentum $l_{\max}(E,r)$ is defined by $E = V_{l_{\max}}(r)$. The $l$-integral can be performed and we obtain

$$\rho(r) = 4\pi m_a^2 \int_{m_a\phi(r)}^{0} dE\, f(E) \sqrt{2m_a(E - m_a\phi(r))}\,. \tag{3.28}$$

This expression is the usual relation for the density as a function of the distribution function $f(E)$ and the potential $\phi(r)$ and can be recovered from Eq.(3.26).

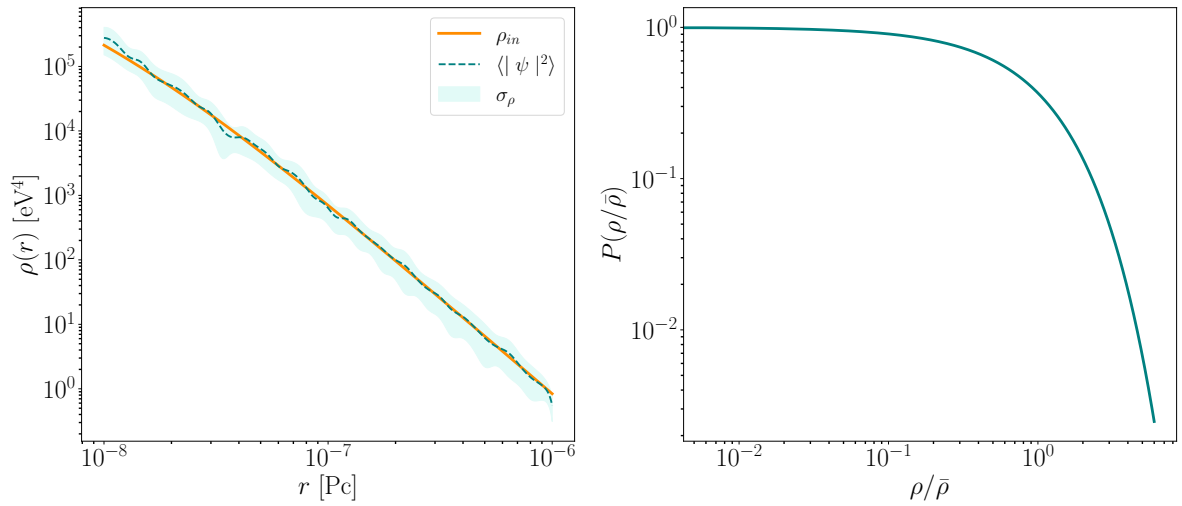


**Figure 3.2:** *Left:* Comparison between the mean density of the AMC considered in Fig.3.1 and the density coming from an average over 40 realizations of the phases. The blue shaded region shows the variance of the density fluctuations. *Right*: Extracted probability distribution for the density.

As already pointed out, the solution (3.24) represents a self-gravitating AMC with mean density $\rho(r)$ and potential $\phi(r)$. However, for a given realization of the phases, the AMC density deviates significantly from $\rho(r)$ with density variance given by $\sigma_\rho = \rho(r)$. For illustrative purposes, we have represented in Fig.3.1 a single realization of the density profile of an AMC with a mean density profile $\rho(r)$ taken to be NFW. Its mass and radius are respectively $M = 10^{-13}\, M_\odot$, $R = 10^{-7}$ Pc and the concentration is set here to $c = 10$. The granules mentioned earlier are clearly visible. On the same figure (right panel), we show how an average over 40 realizations of the phases already converges to a spherically density profile, smoothing out the small-scale granules. In Fig.3.2, we show explicitly how the phase average density profile goes to the mean input density $\rho(r)$. The pale shaded region is the variance calculated from the 40 realizations of the phases. It converges as well to $\sigma_\rho = \rho$ as it should. On the right panel, the probability distribution of the density has been extracted from the 40 realizations. The obtained probability distribution follows the expected one derived in Eq.(3.13).

The WKB solution constructed here is, however, an approximation working only under specific conditions. Indeed the solution (3.21) holds only in the limit where the effective potential $V_l(r)$ varies slowly compared to the de Broglie wavelength. Explicitly, the system needs to satisfy

$$\frac{\lambda}{2\pi} \equiv \frac{1}{\sqrt{2m_a(E_n - V_l)}} \ll \frac{E_n - V_l}{|dV_l/dr|} \sim D\,, \tag{3.29}$$

where $D$ is the characteristic size of the system.
Hence the WKB approximation, used for the modes $\psi_i$, breaks down for energy levels close to the ground states. We will see in the next section that the WKB condition (3.29) translates into the condition $l \gg 1$ on the angular momentum.

### 3.1.3 Lane-Embden and Hernquist Profiles

In the previous chapter we have discussed the recent numerical simulations and how they derived a mass distribution and a characteristic density profile for the AMCs around a redshift $z \approx 99$ [30] (see [139] for a more recent work). Even if a NFW profile seems to be in good agreement with the numerical results, it is difficult to conclude that this would be the density profile of the AMCs within the MW since their properties could be still modified until galaxy formation. It is then fair to assume that the expected shape of the density for the AMCs is not well understood. As we will see in the next section, the density (as well as the gravitational potential and the distribution function) plays

a crucial role in the way the AMCs will react to the interactions with stars. In the remaining parts of this chapter we will then assume two different characteristic profiles for the clusters[5]: the Lane-Embden (LE) [137] and the Hernquist (H) [140] profiles. Their gravitational potential and density are defined as

$$\phi_{\rm LE}(r) = \begin{cases} -\frac{GM}{R}\left(\frac{\pi r}{R}\right) & r < R \\ \frac{GM}{R} - \frac{GM}{r} & r > R \end{cases} \qquad \phi_{\rm H}(r) = -\frac{GM}{(r+r_{\rm H})}\,, \tag{3.30}$$

$$\rho_{\rm LE}(r) = \frac{\pi}{4}\frac{M}{R^3}\left(\frac{\pi r}{R}\right) \qquad r < R \qquad\qquad \rho_{\rm H}(r) = \frac{M}{2\pi}\frac{r_{\rm H}}{r(r+r_{\rm H})^3}\,. \tag{3.31}$$

If the LE profile is not particularly motivated, it still remains a particularly interesting study case since it provides an AMC with a finite radius $R$, i.e. $\rho(r > R) = 0$. On its side, the Hernquist profile presents the same $1/r$ behavior for the density as the NFW profile but falls faster at large radius making its total mass finite. In order to directly compare those two profiles, we define a typical radius $R$ for the Hernquist profile as the radius in which $80\%$ of the mass is enclosed in. Using Eq.(3.30), we get that $R \approx 8.94\, r_{\rm H}$. In the remaining part we will adopt this definition for the radius in the Hernquist case.

In the top panels of Fig.3.3 we compare the gravitational potential and cumulative mass function of those two profiles. For the same mass and radius, it can be observed that the Hernquist profile leads to a much deeper gravitational potential than the Lane-Emden one. In addition, the mass is much tighter in the center of the clump in the Hernquist case.

In order to complement the description of those two AMC profiles, we finally need to specify their distribution functions $f(E)$. As stressed in the previous section, the coefficients of the wave function would be directly proportional to it. We have [140, 141]

$$f_{\rm LE}(E) = \frac{1}{m_a^4}\frac{1}{8\sqrt{2}\pi G R^2}\sqrt{-\frac{m_a}{E}}\,, \tag{3.32}$$

$$f_{\rm H}(E) = \frac{1}{m_a^4}\frac{M}{8\sqrt{2}\pi^3 r_{\rm H}^3 v_g^3}\frac{3\sin^{-1}(q) + q\sqrt{1-q^2}(1-2q^2)(8q^4-8q^2-3)}{(1-q^2)^{5/2}}\,, \tag{3.33}$$

where

$$q = \sqrt{-\frac{r_{\rm H}}{GM}\frac{E}{m_a}}\,, \qquad v_g = \sqrt{\frac{GM}{r_{\rm H}}}\,, \tag{3.34}$$

and $f(E) = 0$ for $E \geq 0$.

At this point it is important to note the difference in behavior of those two distribution functions. In the Lane-Emden case, $f_{\rm LE}(E)$ diverges for $E \to 0$, whereas for the Hernquist profile the strongest contribution comes from the most tightly bound states. This can be observed in the bottom left panel of Fig.3.3, where the contribution of each energy level (integrated over the angular momentum) $dM/d|E|$ is shown. In the LE case, the contribution is dominated by shallower energy modes and diverges for $E = 0$ whereas for the Hernquist profile, important contributions appear from lower energy levels. Of course, this would have important effects during tidal interactions since usually only energy levels close to $E \approx 0$ would be affected.

On the bottom right panel of Fig.3.3, we show the normalized contribution of each angular momentum to the total mass. Since the LE profile has a finite radius, the system has a maximum angular momentum as well. This one is given by

$$l_{\rm max}^{\rm LE} \approx 0.607\, m_a\sqrt{GMR}\,, \tag{3.35}$$

$$\approx 210\,\frac{m_a}{10^{-5}\,{\rm eV}}\sqrt{\frac{M}{10^{-12}M_\odot}}\sqrt{\frac{R}{10^{-6}\,{\rm pc}}}\,. \tag{3.36}$$

[5]Note that the formalism we will develop could be applied to any other type of AMC profile.

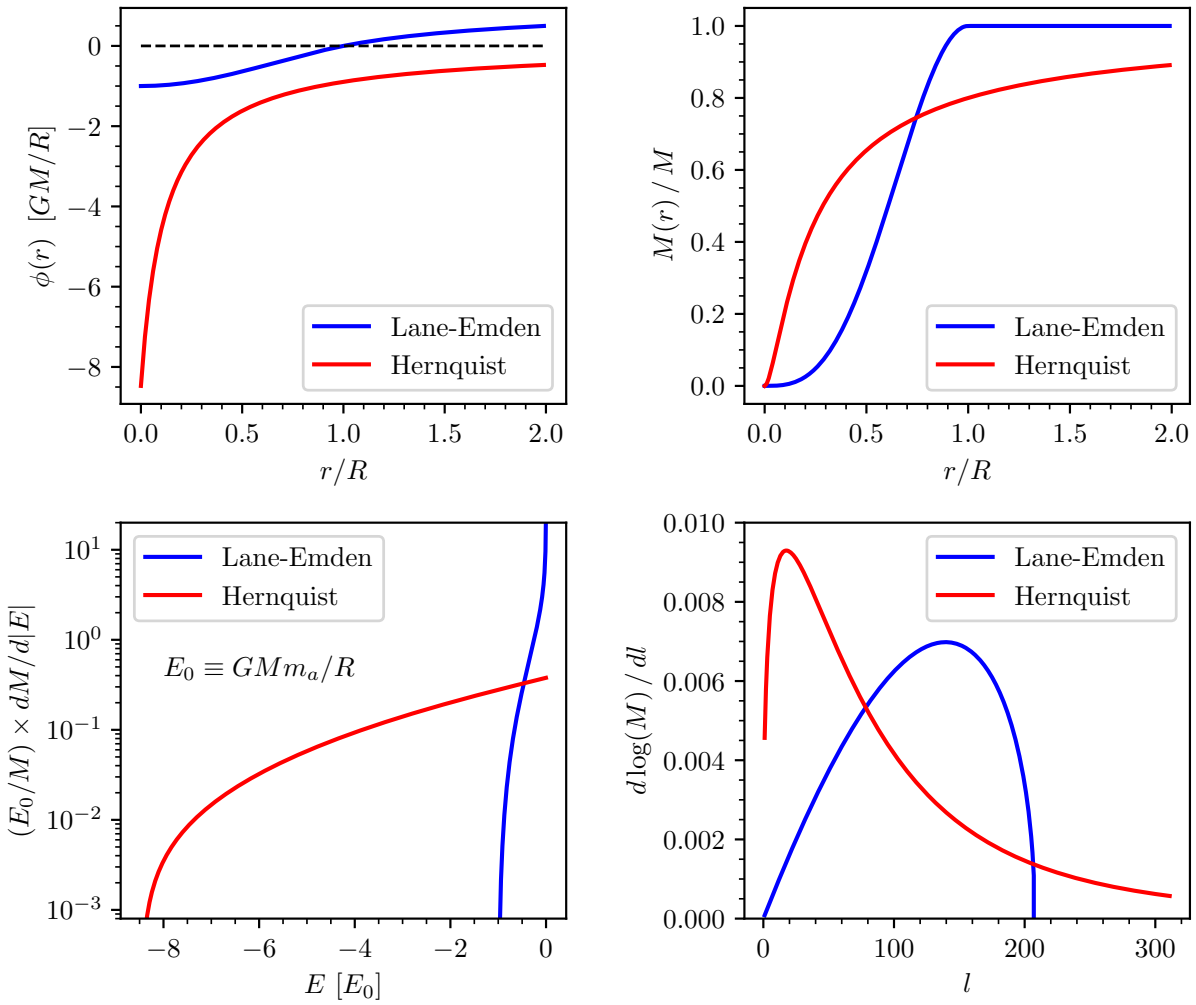


**Figure 3.3:** Comparison of the Lane-Emden (blue) and Herquist (red) profiles. On the top row, the potential $\phi(r)$, as well as the cumulative mass $M(r)$ are shown. The bottom row shows the differential contribution to the total mass of energy states (bottom left) and angular momentum states (bottom right). For all figures, we took a total mass $M = 10^{-12} M_\odot$, $R = 10^{-6}$ pc, $m_a = 10^{-5}$ eV, and for Hernquist we define $R$ such that 80% of the total mass is contained in $r < R$, which implies $R = 8.47\, r_{\rm H}$. The energy unit is $E_0 = GMm_a/R$. This figure corresponds to Fig.1 in Ref.[113]

The LE cluster will then receive contributions from angular momentum between $l = 0$ and $l = l^{\rm LE}_{\rm max}$ with a peak located at around $l_{\rm peak} \approx 0.7\, l^{\rm LE}_{\rm max}$. From that, let's now come back to the WKB approximation. We have stated in Eq.(3.29) that the typical size of the system must be much larger than the typical wavelength. In this case, it translates into

$$\frac{\lambda}{2\pi} \approx \frac{1}{m_a \sqrt{GM/R}} \ll R. \tag{3.37}$$

Using Eq.(3.35), we see that it implies that the WKB approximation holds as long as $l_{\rm max} \gg 1$.
For the Hernquist profile, the shape of the $l$ distribution is rather different, with a peak at significantly lower values, $l^{\rm H}_{\rm peak} \approx 18$ for the parameters chosen in the plot. Numerically we find that the peak value has the same scaling with parameters as given in Eq. (3.35) (which also follows from dimensional arguments). Note also that for Hernquist there is no maximum angular momentum and the distributions continuously go to zero for $l \to \infty$.

Finally, for a self-gravitation object, the gravitational binding energy can be calculated as

$$W = -4\pi G \int_0^\infty dr\, r^2 \frac{\rho(r) M(r)}{r} \quad . \tag{3.38}$$

Using the previous section, we can see that the ensemble averaged AMC is in virial equilibrium such that $E_{\rm tot} = W + K = W/2$ with $K$ being the total kinetic energy. Importantly, we remind that $E_{\rm tot} \neq \langle H_0 \rangle_{ens} = \sum_{nlm} E_n |C_{nlm}|^2$ since the latter quantity corresponds to the energy stored in the field if the potential $\phi$ was a fixed external potential. In contrast, $E_{\rm tot} = W + K$ corresponds to the energy stored in the self-gravitating system, where the potential is provided by the mass distribution itself. In the case of the LE and Hernquist profiles, the gravitational binding energy can be easily expressed in terms of the mass and the radius of the clump

$$W_{\rm LE} = -\frac{3}{4}\frac{GM^2}{R} \quad , \qquad W_{\rm H} = -\frac{1}{6}\frac{GM^2}{r_{\rm H}} \quad . \tag{3.39}$$

## 3.2 Tidal Stripping of Axion Miniclusters

In the previous section we have developed a formalism to derive the wave function of an AMC characterized by a mean density profile $\rho(r)$, gravitational potential $\phi(r)$ and distribution function $f(E)$. Under the random phase assumption, we have seen that a typical minicluster will have small granule fluctuations at scales below the de Broglie wavelength. Only on average over the phases, the cluster reproduces the input density and gravitational potential.
As emphasized in the introduction, we are now going to use this formalism to understand how the AMCs would react to tidal interactions with galactic stars. If this question has already been answered using a classical particle description for the AMCs [114, 115, 116, 117], we are going to propose a generalization for an AMC described by the wave function in Eq.(3.24). To this point, we will briefly recap the tidal stripping in a particle picture in Sec.3.2.1. We will then move to classical field formalism in Sec.3.2.2 and finally apply this one in order to discuss the impact of a single tidal interaction on an AMC.

### 3.2.1 Tidal Stripping in a Particle Picture

In the context of AMC-star encounters, it is fair to assume that the typical interaction time[6] is far shorter than the dynamical time scale of the system. Explicitly, it means that a star with relative velocity $v$ and impact parameter $b$ has an interaction time $\tau_{\rm int.} \sim b/v$ much shorter than the characteristic time $\tau_{\rm cross.} \sim R/\omega$ needed for a particle to cross the cluster (with $\omega = \sqrt{GM/R}$ and $R$ respectively the typical velocity and the radius of the cluster). Under this approximation, refereed as the *impulse approximation* [142, 143, 144, 145], the interaction can be assumed instantaneous and the particles at rest during that time. Hence, only the velocity of the particles would change whereas their position would remain the same.
In addition, the calculation of the stellar interaction is considerably simplified if the size of the perturbed system (here, the minicluster) is much smaller than the impact parameter $b$ through which the perturbator passes. In that case, the gravitational potential applied from the star to the AMC, in a frame where the origin is at the center of the cluster, can be expanded around the origin as

$$\begin{aligned} \phi_*(\boldsymbol{r}, t) &= -\frac{GM_*}{|\boldsymbol{r} - \boldsymbol{r}_*(t)|}, \\ &= -\frac{GM_*}{r_*(t)} - \frac{GM_*}{r_*(t)^2} r\cos(\gamma(t)) - \frac{GM_*}{r_*(t)}\left(\frac{r}{r_*(t)}\right)^2 P_2(\cos\gamma(t)) + \mathcal{O}(r^3/r_*^3(t)), \end{aligned} \tag{3.40}$$

where $\boldsymbol{r}_*(t)$ is the location of the star, $\gamma$ is the angle between $\boldsymbol{r}$ and $\boldsymbol{r}_*(t)$ and $P_2$ denotes the 2nd order Legendre polynomial. In this expression, the first term does not provide any force, the second

[6] Here the time during which the gravitational force is significant.

will induce the Keplerian motion of the clump center of mass and only the third order provides the tidal force we are interested in. Dropping all the terms beyond the second order is called the *tidal approximation*. We then define the tidal potential as

$$\phi_{\rm tidal}(r,t) = -\frac{GM_*}{r_*(t)}\left(\frac{r}{r_*(t)}\right)^2 P_2(\cos\gamma(t)) \ . \tag{3.41}$$

When both the tidal approximation and the impulse approximation hold, we talk about *tidal shocks*.

Let's now discuss the reaction of an AMC under a tidal shock. Starting from the potential in Eq.(3.41), a star with mass $M_*$ flying by with a given relative velocity $\boldsymbol{v}$ and impact parameter $b$ would inject a total energy in the system [137, 142]

$$\Delta\mathcal{E} = \frac{4G^2M_*^2M}{3v^2b^4}\langle r^2\rangle, \tag{3.42}$$

where $\langle r^2\rangle$ is mean squared radius given by

$$\langle r^2\rangle = \left(\frac{\int d^3r\, r^2\rho(r)}{M}\right). \tag{3.43}$$

This total injected energy can be split into individual energy changes in each particle bound to the cluster. On average, each particle located at a location $r$ would experience an energy shift

$$\delta E(r) = \frac{4G^2M_*^2m_a}{3v^2b^4}r^2. \tag{3.44}$$

The AMC response to the tidal shock is then easy to apprehend: all the particles with final positive energy $E_f = E_i + \delta E(r) > 0$ are no longer bound to the clump. Hence, if the mass is initially given by

$$\begin{aligned} M &= 4\pi\int_0^\infty dr\, r^2\rho(r) \\ &= 16\pi^2m_a^2\int_0^\infty dr\, r^2\int_{m_a\phi(r)}^0 dE\, f(E)\,\sqrt{2m_a(E-m_a\phi(r))}, \end{aligned} \tag{3.45}$$

the variation of the mass coming from the ejected particles can then be derived as [116]

$$\begin{aligned} \Delta M &= 4\pi\int_0^\infty dr\, r^2\rho(r) \\ &= 16\pi^2m_a^2\int_0^\infty dr\, r^2\int_{\min[-\delta E(r),m_a\phi(r)]}^0 dE\, f(E)\,\sqrt{2m_a(E-m_a\phi(r))}. \end{aligned} \tag{3.46}$$

Similarly, the total energy variation of the clump can be calculated assuming that the ejected particles carry out a fraction $f_{\rm ej.}$ of the total injected energy $\Delta\mathcal{E}$ given in Eq.(3.42). After the encounter, the final energy of the clump is then given by [116]

$$E_f = E_i + \left(1 - f_{\rm ej.}\Delta\mathcal{E} - E^{\rm ej.}\right), \tag{3.47}$$

where $E^{\rm ej.}$ is the initial energy of the particles that are ejected due to the encounter. This quantity is simply the initial kinetic energy of those particles plus the change in binding energy from ejecting them.

Of course, the system right after the encounter is no longer in virial equilibrium. It means that if $E_i = \alpha GM^2/R$, where $\alpha$ is a coefficient that depends on the density profile, $E_f \neq \alpha G(M-\Delta M)^2/R$. The cluster will then be forced to relax to a new virial configuration. This process is, however, non trivial and still under debate. In Ref.[116], it has been assumed that the AMC will keep the same density profile, hence keeping the coefficient $\alpha$ fixed. The radius would, therefore, change in order to cover the change in mass. Note, however, that in Refs.[145, 146], N-body simulations have been used to derive the density profile after a star encounter and tend to point toward a universal density profile after the first tidal interaction.

### 3.2.2 Tidal Stripping in a Wave Formalism

In the previous section we have discussed the SP system and its solution for the AMCs. It has been mentioned that even if the axion field is described via the Schrodinger equation, no quantum interpretation is given to the wave function $\psi$. We will see now that even if the physical interpretation is not the same, the mathematical properties and tools proper to this equation and more generally to quantum mechanics could be used to understand how an AMC would react to a star tidal interaction.

#### Perturbation of the Axion Field

Let's consider a tidal shock similar to the one described in Sec.3.2.1, the tidal potential induced by the star on the AMC is given by Eq.(3.41)

$$\phi_{\rm tidal}(r,t) = -\frac{GM_*}{r_*(t)}\left(\frac{r}{r_*(t)}\right)^2 P_2(\cos\gamma(t)) \quad . \tag{3.48}$$

Intuitively, this potential has to be added to the Schrodinger equation such that the wave function constructed in Eq.(3.24) is no longer a solution. However, in the case of $\phi_{\rm tidal}(r,t)$ perturbatively small (see App.B.6 for a discussion of the perturbativity in this context), the change in the wave function $\psi$ can be understood analytically. In particular, the consequence of the tidal interaction in the perturbative limit would act on the wave function $\psi$ similarly as a perturbation in quantum mechanics acts on the wave function of a particle. Concretely, it will provide a shift in the energy levels. Therefore, similarly as for the particle picture formalism, since initially all the energy levels of the AMC have a negative energy, those that would become positive after the energy shift would be ejected from the cluster. Let's derive this explicitly.

Under the perturbation (3.48), the new solution for the axion field can be written as a series expansion. Up to the second order, we have

$$|\psi(t)\rangle = |\psi^{(0)}(t)\rangle + |\psi^{(1)}(t)\rangle + |\psi^{(2)}(t)\rangle \quad . \tag{3.49}$$

From now on, we are going to use the quantum mechanical notations keeping in mind that the calculation is still classical.
In the last expression, $|\psi^{(0)}(t)\rangle$ is the wave function of the AMC before the perturbation so that the first correction arises at first order. Each order can be expanded on the unperturbed eigenstate basis defined in Eq.(3.20) and written here $|nlm\rangle$,

$$|\psi^{(i)}(t)\rangle = \sum_{nlm} C^{(i)}_{nlm}(t)\, e^{-iEt}\, |nlm\rangle \quad , \tag{3.50}$$

where the index $(i)$ stands for the order of the expansion, such that $C^{(0)}_{nlm}$ are the coefficients of the unperturbed wave function defined in Eq.(3.25). The coefficients of the next orders are found by solving the differential equation

$$i\partial_t C^{(i)}_{nlm}(t) = \sum_{n'l'm'} C^{(i-1)}_{nlm}\, \langle nlm|\, m_a\phi_{\rm tidal}(r,t)\, |n'l'm'\rangle\ e^{i(E-E')t} \quad , \tag{3.51}$$

where here and in the following we use the short-hand notation $E = E_n$ and $E' = E_{n'}$.
As usually done in quantum mechanics, the idea here is to assume that the interaction starts at $t_{\rm in} = -\infty$ and lasts until $t_{\rm fin} = +\infty$. Initially, the first and second order coefficients are naturally zero since the AMC is described by the unperturbed wave function. The evolution of the coefficients can then be followed be integrating Eq.(3.51) over time. Since we are interested in the AMC after the interaction, we calculate the first and second order coefficients $C^{(1)}_{nlm}$, $C^{(2)}_{nlm}$ at $t = +\infty$. The detailed calculation is made in appendix B.4 and we show here the final result in terms of the averaged[7]

[7] We recall that in this section the average is taken over the random phases that appear in the wave function of the AMC.

variation of the coefficients squared[8],

$$\langle \Delta |C_{nlm}|^2 \rangle = \Delta^{(+)} |C_{nlm}|^2 + \Delta^{(-)} |C_{nlm}|^2, \tag{3.52}$$

with

$$\begin{aligned} \Delta^{(+)} |C_{nlm}|^2 &= \left(\frac{A}{\alpha}\right)^2 \sum_{n',B} |C^{(0)}_{n'lm}|^2 \left| \langle nl | r^2 | n'l \rangle \right|^2 g_{nn'} \\ \Delta^{(-)} |C_{nlm}|^2 &= -|C^{(0)}_{nlm}|^2 \left(\frac{A}{\alpha}\right)^2 \sum_{n'} \left| \langle nl | r^2 | n'l \rangle \right|^2 g_{nn'} \ . \end{aligned} \tag{3.53}$$

The function $g_{nn'}$ is a window function coming from the time integration (see App.B.4 for the exact expression). Naively, the term $\Delta^{(+)}$ corresponds to the transitions from all the states $|n'l'm'\rangle$ toward $|nlm\rangle$. Since initially (at $t = -\infty$) only the bound states have a non-zero coefficient, the sum runs only over them. On the other hand, the term $\Delta^{(-)}$ encodes the transitions from the state $|nlm\rangle$ towards any other states $|n'l'm'\rangle$, bound or unbound. For this reason, the sum is not limited to the bound states as for the $\Delta^{(+)}$. It is easy to see that considering those two contributions assure to have the conservation of the total number of particles.

#### Energy Injected by the Star

The equations (3.53) constitute the starting point of our analysis. We proceed now to apply the above formalism to describe the impact of a single encounter on an AMC. To this point we first derive the total energy injected by the star and then discuss the properties of the AMC after the encounter (final mass, density profile and radius) .
Explicitly, from Eq.(3.53), we obtain two similar expressions for the variation of the energy

$$\Delta E^{(-)} = \sum_{nlm,B} E_{nl} \, \Delta^{(-)} |C_{nlm}|^2 \, , \tag{3.54}$$

$$\Delta E^{(+)} = \sum_{nlm} E_{nl} \, \Delta^{(+)} |C_{nlm}|^2 \, . \tag{3.55}$$

In the first relation, $E_{nl} \, \Delta^{(-)} |C_{nlm}|^2$ corresponds to the amount of energy transferred from the state $|nlm\rangle$. The quantity $\Delta E^{(-)}$ then indicates the total energy transferred by the bound states of the system. Similarly, $\Delta E^{(+)}$ corresponds to the total energy received and since transitions can occur to unbound states, the sum is not limited to the bound states of the system.
The total energy injected in the AMC is then given by the sum of these two contributions

$$\begin{aligned} \Delta \mathcal{E} = 16\pi^2 m_a \int_0^{l_{\max}} dl \, 2l \int_{E_{\min}(l)}^{0} dE \ f(E) \mathcal{N}_{nl} \int_{E_{\min}(l)}^{\infty} dE' \times \\ g_l(E') \, (E' - E) \left(\frac{A}{\alpha}\right)^2 | \, \langle nl | \, r^2 \, | n'l \rangle \, |^2 g_{nn'} \, , \end{aligned} \tag{3.56}$$

where $E_{\min}(l)$ is the minimum value of the effective potential $V_l(r)$ and we have used Eq.(3.53) as well as the explicit expression for the coefficients $|C^{(0)}_{nlm}|^2$ from Eq. (3.25).
This integral can be simplified in the impulse approximation mentioned in Sec.3.2.1. Indeed, we remind that, in the particle picture, if the time scale of the interaction $\sim b/v$ is much shorter than the dynamical time scale of the system, bound particles can be considered "at rest" during the encounter. This approximation has been shown to reproduce quite well the numerical simulation results even for borderline range of impact parameters/velocities [116, 137, 143, 145, 147]. In the wave picture,

[8] From now on the coefficients are always assumed to be evaluated at $t = +\infty$.

this approximation is captured by the function $g_{nn'}$. Indeed, depending on the time scale of the perturbation, the two sudden or adiabatic limits are considered in quantum mechanics. The adiabatic one assumes that the interaction is turned on smoothly and in that case $g_{nn'}$ is well approximated by a Dirac delta. Only transitions to degenerate energy levels are possible in that case. On the other hand, the sudden limit corresponds to the impulse approximation in the sense that the interaction is turned on instantaneously. As naively expected, the function $g_{nn'}$ gets the opposite behavior than in the adiabatic limit and is constant. It could be checked from App.B.4 that in the impulse approximation, $g_{nn'} \approx 1/2$.
The integral in Eq.(3.56) could be finally further simplified using the quantum mechanical sum rules [148, 149] (see App.B.5)

$$\begin{aligned}\int_{E_{\min}(l)}^{\infty} dE'\, g(E')(E'-E)|\langle nl|\, r^2\, |n'l\rangle|^2 = \\ \sum_{n'}(E_{n'}-E_n)|\langle nl|\, r^2\, |n'l\rangle|^2 = \frac{2}{m_a}\langle nl|\, r^2\, |nl\rangle\ ,\end{aligned} \tag{3.57}$$

such that we finally get for the injected energy

$$\Delta\mathcal{E} = 16\pi^2 m_a \int_0^{l_{\max}} dl\, 2l \int_{E_{\min}(l)}^{0} dE\, f(E)\mathcal{N}_{nl}\, \delta E(E,l)\,, \tag{3.58}$$

where we defined

$$\delta E(E,l) = \left(\frac{2GM_*}{b^2 v}\right)^2 \frac{m_a}{4}\langle nl|\, r^2\, |nl\rangle\ . \tag{3.59}$$

This last quantity corresponds to the average energy shift of a state with energy $E$ and angular momentum $l$.
Let's now compare this equation with Eq.(3.44) obtained in the particle picture. Interestingly, they are in very close analogy expected from the radial dependence in Eq.(3.44) replaced by the expectation value $\langle nl|\, r^2\, |nl\rangle$ in the wave formalism. However, similarly to quantum mechanics, where observables are given in terms of expectation values of operators, the term $\langle nl|\, r^2\, |nl\rangle$ has to be seen as the natural generalization of the radial dependence $r^2$ of Eq.(3.44) in a wave formalism.
From Eq.(3.59) it is now possible to study the evolution of the AMC under a single encounter.

#### Properties of the AMC After a Single Encounter

From this point, the properties of the AMC after the encounter can be calculated similarly to the particle picture. Explicitly, under the energy shifts $\delta E(E,l)$, some of the states would transfer their occupation number to unbound states with $E > 0$. Those do not belong to the clump and the associated transferred mass is therefore ejected from the clump. For a given angular momentum $l$, it is then possible to define a critical energy level $\tilde{E}(l)$ such that $\tilde{E}(l) + \delta E(\tilde{E}, l) = 0$. It is easy to see that

$$|\tilde{E}(l)| \equiv \delta E(\tilde{E}, l)\,. \tag{3.60}$$

All the energy states with $|E| < |\tilde{E}(l)|$ would transfer their occupation number to unbound states. Hence, in analogy to Eq. (3.46), we calculate the variation of the density profile as

$$\Delta\rho(r) = 4\pi\frac{m_a^2}{r^2}\int_0^{l_{\max}(r)} dl\, l \int_{-\tilde{E}(l)}^{0} dE\, \frac{f(E)}{\sqrt{2m_a\,(E - V_l(r))}}\,, \tag{3.61}$$

where $l_{\max}(r)$ is the maximum value of the angular momentum $l$ at a given location $r$. The variation of the mass naturally follows from this equation and is given by

$$\Delta M = 4\pi\int_0^{\infty} dr\, r^2\, \Delta\rho(r)\,. \tag{3.62}$$

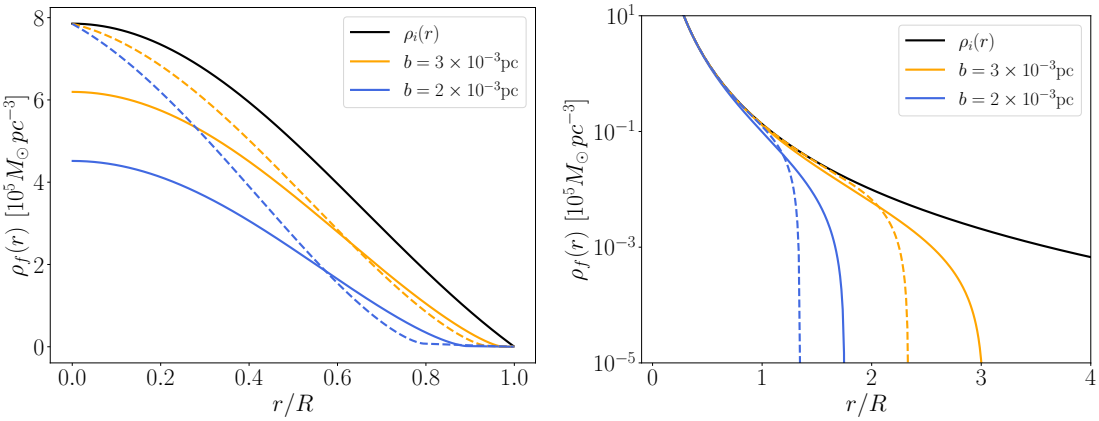


**Figure 3.4:** Variation of the density profile right after the encounter, $\rho_f = \rho_i - \Delta\rho$, where $\rho_i$ (solid black lines) is the density profile before the encounter. We show results for the two studied profiles, Lane-Embden (left) and Hernquist (right). In both cases the initial masses and radii are set to $M = 10^{-12}\, M_\odot$ and $R = 10^{-6}$ pc. The final density profile $\rho_f(r)$ is shown for two different impact parameters: $b = 2 \times 10^{-3}$ pc (blue), $b = 3 \times 10^{-3}$ pc (orange). For both profiles, we have represented with dashed lines the variation of the density calculated in the particle picture. The parameters of the star are set to $M_* = 1\, M_\odot$ and $v = 10^{-4}$. This figure corresponds to Fig.2 in Ref.[113]

In Fig.3.4, we show the impact of a single encounter on AMC with both Lane-Emden and Hernquist density profiles. It is interesting to note the difference between the particle picture (dashed lines) and the wave formalism we have constructed in this section (solid lines). For the particle treatment, the injected energy depends on the radial location $r^2$, such that particles close to the origin of the clump are barely impacted by the interactions. As observed from Fig.3.4, the density profile is then less affected at the center of the cluster. On the other hand, in our formalism the whole energy level is shifted according to Eq.(3.59). It implies that even close to the origin the density profile would feel the tidal interaction of the star. Of course, for the Hernquist minicluster, this effect is less visible since the density diverges at the center. For both profiles, more mass is removed from large radii in the particle compared to the wave treatment.

Hence, the cluster is losing the mass from the states for which the energy shift (3.59) is strong enough to transfer their occupation number to unbound states. For the same reason, the transfer of the occupation number of those states would remove a quantity of energy $\Delta E_{\rm lost}$ from the clump. Following Ref.[116], $\Delta E_{\rm lost}$ is the sum of the kinetic energy initially carried in those states ($\Delta E_K$) and the variation of the binding energy from removing their occupation number ($\Delta E_B$). The first one can be calculated similarly to the Eq.(3.61),

$$\Delta E_K = -16\pi^2 m_a \int_0^\infty dr \int_0^{l_{\rm max}(r)} dl\, l \int_{\tilde{E}(l)}^0 dE\, (E - m_a\phi(r)) \frac{f(E)}{\sqrt{2m_a(E - V_l(r))}}\,, \tag{3.63}$$

whereas the variation of the binding energy is calculated from Eq.(3.38) as

$$\Delta E_B = -4\pi G \int dr\, r\, (\rho_f(r) M_f(r) - \rho(r) M(r))\,, \tag{3.64}$$

where $\rho_f(r) = \rho(r) - \Delta\rho(r)$ and $M_f(r)$ is the enclosed mass according to the density $\rho_f(r)$.
Of course, for the other states, the energy shift is not strong enough to send their occupation number to unbound states but rather to higher bound energy levels. Those transitions do not modify the mass of the clump but only inject some energy. This contribution ($\Delta E_{\rm inj.}$) is calculated via

$$\Delta E_{\rm inj.} = 16\pi^2 m_a \int_0^\infty dr \int_0^{l_{\rm max}(r)} dl\, l \int_{E_{min(l)}}^{-\tilde{E}(l)} dE \frac{f(E)\, \delta E(E,l)}{\sqrt{2m_a\,(E - V_l(r))}}\,. \tag{3.65}$$

The overall energy variation is given by the sum of these last three contributions, such that the final energy of the clump is [9]

$$\begin{aligned} E_f &= E_i + \Delta E_K + \Delta E_B + \Delta E_{\text{inj.}}, \\ &= E_i + \Delta E_{\text{lost}} + \Delta E_{\text{inj.}}, \\ &= E_i + \Delta E\,. \end{aligned} \tag{3.66}$$

Of course, as already emphasized in Sec.3.2.1, right after the encounter the system is no longer in virial equilibrium (see Eq.(3.39) for the virial equations for both the Lane-Emden and the Hernquist density profiles). Hence, we assume, following Ref.[116], that it will relax to a new virialized state by modifying its radius meanwhile conserving its final mass $(M - \Delta M)$ and final energy $E_f$. Furthermore, we assume that the cluster after the encounter will keep the same density profile ( i.e., either the Lane-Emden or the Hernquist profile). In that case the virial relations defined in Eq.(3.39) remains the same and the new radius can be calculated as

$$\begin{aligned} R_f &= -\frac{3}{8}\frac{G\,(M-\Delta M)^2}{E_f} = \kappa R_i\,, \\ r_{H,f} &= -\frac{1}{12}\frac{G\,(M-\Delta M)^2}{E_f} = \kappa r_{H,i}\,, \end{aligned} \qquad \kappa \approx 1 - 2\frac{\Delta M}{M} + \frac{\Delta E}{|E_i|}\,, \tag{3.67}$$

respectively for the LE and H clumps. We remind that we defined the characteristic radius in the case of the Hernquist AMCs as $R \approx 8.94 r_{\text{H}}$.
At this point, it is clear that both cooling and heating effects are in balance after the encounter. The kinetic energy $\Delta E_K$ carried away by the removed modes tends to cool down the system, whereas the variation of the binding $\Delta E_B$ and the injected energy $\Delta E_{\text{inj.}}$ are heating the system. Depending on their relative contribution, the radius will have to grow or shrink in order to recover a virialized configuration. Intuitively, the balance between cooling/heating effects depends on how the matter is distributed within the clump. Hence, it is expected that the behavior of the radius depends on the distribution function of the cluster $f(E)$.

In Fig.3.5 we summarize the formalism constructed in this section by studying how the radius, the energy and the mass change under a single encounter as a function of the impact parameter (top), the minicluster mass (middle) and radius (bottom). As observed, the radius in the LE and H miniclusters react quite differently to small perturbations. This can be understood as, for a small enough tidal interactions, only the loosely bound states are removed from the clump. In the LE case, since the distribution function $f(E)$ is diverging for $E \to 0$, removing those states heats up enough the system to increase the radius. AMCs with this density profile get then more and more venerable after each tidal interaction. This effect is essentially the same as the one observed in the particle picture for NFW AMCs in Ref.[116]. For Hernquist AMCs, the situation is different since the distribution function $f(E) \to 0$ for $E \to 0$. Small perturbations therefore only remove the diffuse outer parts of the cluster, and the injected energy is not important enough to heat up the system. The radius decreases and it becomes more and more difficult to alter the properties of the AMCs. These behaviors found in our wave formalism are in good agreement with the results obtained in Ref.[150] for different density profiles. Hence, LE and H miniclusters react in the opposite way for small perturbations (increasing and decreasing radius respectively). It can, however, be inferred that for specific density profiles, an in-between situation appears where an increase in the radius is followed by a decrease. A study of a broader range of density profiles is left for further work.
For strong perturbations, the system is heated up and both types of AMCs tend to increase their radius. Eventually, they do not form a bound system anymore when $\Delta E/|E_{\text{tot}}| = 1$ and the radius is destroyed (it is manifested by the divergence of the radius in Fig.3.5). Note in particular that the

[9] Note that $\Delta E$ defined in Eq. (3.66) is the energy change of the *bound system*, whereas $\Delta\mathcal{E}$ defined in Eq.(3.58) is the total energy transferred by the star. The latter is shared between states which become ejected with a fraction $f_{\text{ej}}$ and states which remain bound with the fraction $(1 - f_{\text{ej}}) = \Delta E_{\text{inj}}/\Delta\mathcal{E}$. The energy carried away by the ejected part is $f_{\text{ej}}\Delta\mathcal{E} - \Delta E_{\text{lost}}$, such that $E_f + f_{\text{ej}}\Delta\mathcal{E} - \Delta E_{\text{lost}} = E_i + \Delta\mathcal{E}$, which is equivalent to Eq. (3.66). See also Ref. [116].

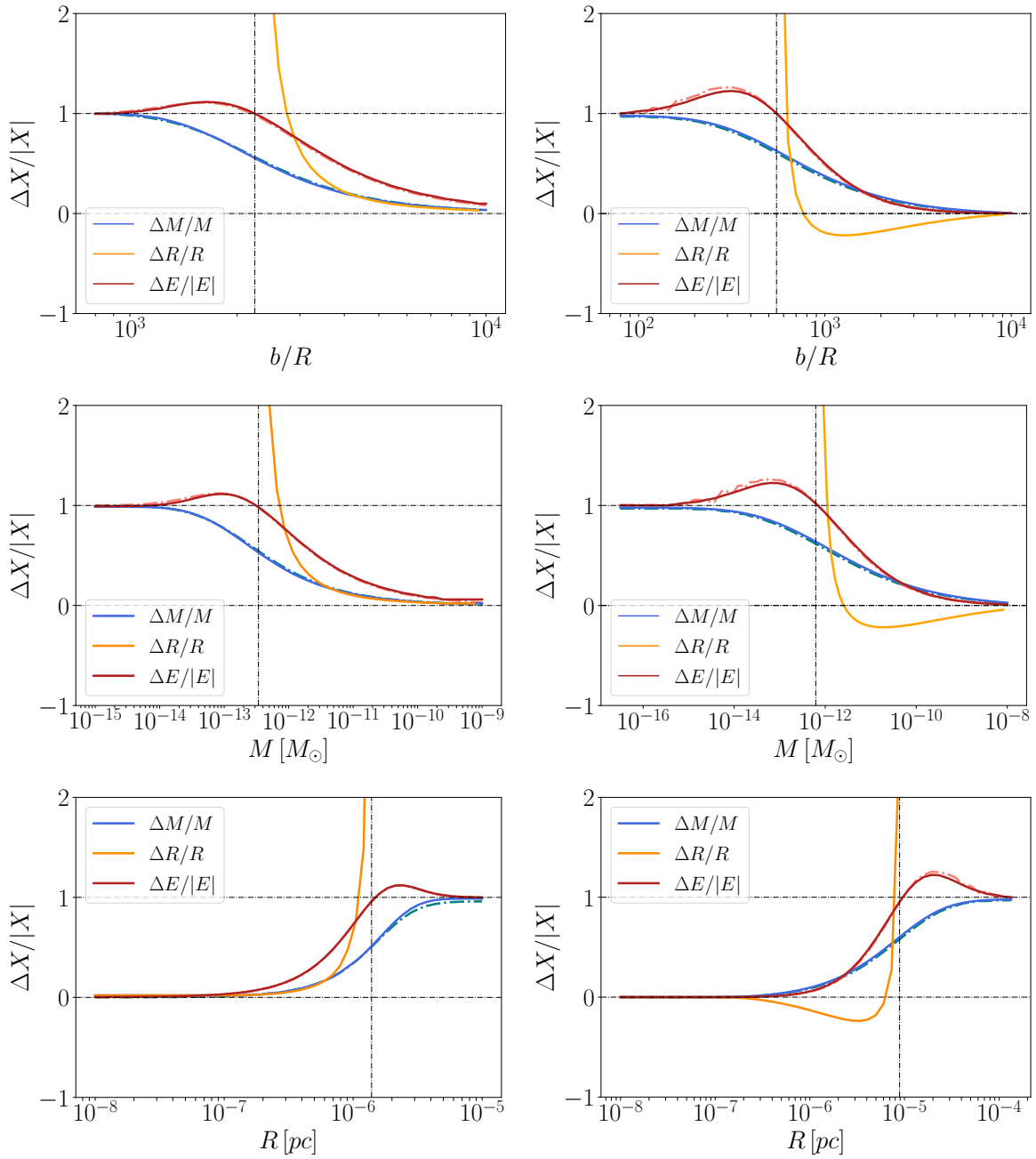


**Figure 3.5:** Perturbation of an AMC under a single star encounter. The change in the mass, radius and energy are shown respectively by the blue, orange and red lines. In each different rows, only one parameters is modified. Hence in the top panels the initial mass and radius are held constant and set to $M = 10^{-12}\,M_\odot$, $R = 10^{-6}$ pc while the impact parameter is modified. In the middle panels, the radius and the impact parameters are kept constant as $R = 10^{-6}$ pc and $b = 3\,(0.5) \times 10^{-3}$ pc for LE (H). In the bottom panels the mass is kept fixed as $M = 10^{-12}\,M_\odot$ and the impact parameter as $b = 3 \times 10^{-3}$ pc. Similar results calculated in the particle picture are shown by the colored dashed lines. The parameters of the star are set to $M_* = 1\,M_\odot$ and $v = 10^{-4}$. In the region to the left (right) of the vertical dashed line in the top, middle (bottom) panels $\Delta E/|E| > 1$, the perturbation is no longer small, and the clump is destroyed; we show these regions only for illustration purposes. This figure corresponds to Fig.3 in Ref.[113]

AMC is destroyed before its total mass gets removed (see dashed vertical line in Fig.3.5)). Furthermore, we confirm the observation made by Ref.[116] that the properties of the AMC after the

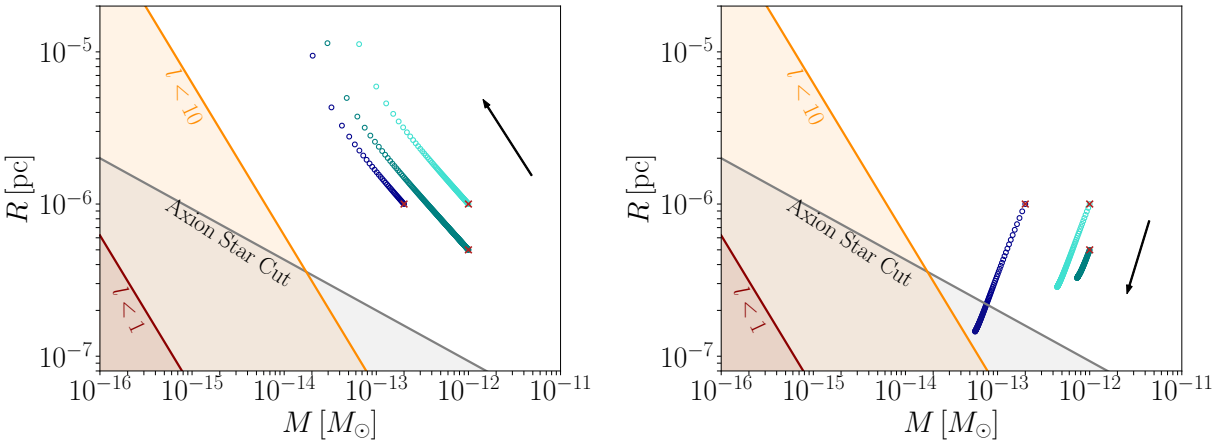


**Figure 3.6:** Progressive evolution of the mass and radius of an AMC under the same repeated perturbation. Results are shown for both Lane-Embden (left) and Hernquist (right) clumps. The perturbation is characterized by $b = 2\,(0.5) \times 10^{-2}$ pc for the LE (H) clump, $v = 10^{-4}$ and $M_* = 1\,M_\odot$. The initial conditions are shown by the red crosses. The total number of perturbations is fixed to $N = 100$ for the H clumps whereas for the LE ones we let the perturbations continue until the cluster is destroyed. The gray, orange and red shaded regions show respectively the axion star cut, the $l_{\rm max} < 10$, and the $l_{\rm max} < 1$ regions. This figure corresponds to Fig.4 in Ref.[113]

interaction depend only on its mean density[10], $\bar{\rho} = 3M/(4\pi R^3)$. In line with that, we can determine the critical density needed to destroy the minicluster in one encounter,

$$\bar{\rho}_{\rm crit} \approx \left(\frac{M_*}{1\,M_\odot}\right)^2 \left(\frac{10^{-3}\,{\rm pc}}{b}\right)^4 \left(\frac{10^{-4}}{v}\right)^2 \times \begin{cases} 0.7 \times 10^{-11}\,M_\odot\,(10^{-6}\,{\rm pc})^{-3} & \text{(Lane-Emden)} \\ 2.1 \times 10^{-14}\,M_\odot\,(10^{-6}\,{\rm pc})^{-3} & \text{(Hernquist)} \end{cases} . \tag{3.68}$$

It is interesting to observe at that point that LE miniclusters are destroyed much more easily than Hernquist ones. This will have important consequences in the next chapter when we are going to consider the survival of those two AMC profiles in the MW.
Comparing the final properties of the AMCs after the encounter in both the particle and the wave formalisms (see dashed colored lines in Fig.3.5), we finally conclude that they agree very well with each other. The question of whether this agreement remains when accounting for a more realistic description of the virialization process of the radius after the encounter is left for further investigation.

In Fig.3.6, we show the evolution of both the radius and the mass under the same repeated tidal encounter (keeping the impact parameter, mass and velocity of the star fixed). As expected from the previous discussion, the LE cluster radius increases for all perturbations. The cluster gets then more a more easily disrupted up to the point where it is completely destroyed. On the other hand, for small perturbations, the Hernquist cluster sees its radius decrease. After each encounter it then gets more and more tightly bound and resistant to further interactions. In the figure we show a finite number of 100 interactions for the Hernquist case.

### 3.2.3 Axion Star and Validity Limits of our Assumptions

The formalism we have constructed is based on the WKB assumption for the wave function of the AMC. However, as already pointed out in Sec.3.1.3, the WKB approximation is expected to break down as the maximum angular momentum gets lower. When the condition $l_{\rm max} \gg 1$ is no longer valid, the typical wavelength of the axion field becomes comparable to the size of the system and the modes of the Schrodinger equation must be found by numerical methods (see Ref.[134] where

[10] We remind the reader that we define $R$ for the Hernquist profile as the radius which contains 80% of the mass, whereas for the Lane-Emden case it contains 100%.

this has been done explicitly). In Fig.3.6 we have represented for both AMC profiles the regions where the maximum angular momentum $l_{\rm max}$ becomes less than $l_{\rm max} = 10$ (orange shaded areas) and $l_{\rm max} = 1$ (red shaded areas). Note that the reaction of an AMC to a tidal disruption in the low angular momentum limit is expected to deviate more significantly from a particle treatment. Indeed, the WKB approximation is a semi-classical description of the axion field. It means that even if the AMC is described by a classical field, the WKB approximation describes a system for which the wavelength of the axion field is short enough to approach a classical particle description. Hence, there is actually no surprise that we find such an agreement between our formalism and the particle picture analysis. On the other hand, in the limit of low angular momentum, the WKB approximation breaks down and the wave construction of the system would have a stronger impact on the tidal respond of the AMC. We leave this interesting question for an incoming study.

The description of AMCs following Sec.3.1 also becomes unphysical in some limits if we include the axion stars (AS) (or soliton) [26, 151] . Those objects have indeed been observed in numerical simulations [152, 153, 154, 155] and would form at the center of the AMC. Recent progress has been recently achieved in the understanding of the relation between the AMC and its axion star. In Refs.[152, 155], the mass of the AS is found to be related to the mass of the AMC via the so-called core-halo relation,

$$M_{\rm AS} \simeq 1.3 \times 10^{-17}\, M_\odot \left(\frac{10^{-5}\,{\rm eV}}{m_a}\right)\left(\frac{M}{10^{-13}\,M_\odot}\right)^{1/3}, \tag{3.69}$$

which can be obtained by assuming that the virial velocities in the star and the halo are equal [155]. The radius of the axion star can be related to the AMC mass as well. In particular, [116, 152, 155]

$$R_{\rm AS} \simeq 3.4 \times 10^{-7}\,{\rm pc} \left(\frac{10^{-5}\,{\rm eV}}{m_a}\right)\left(\frac{M}{10^{-13}\,M_\odot}\right)^{-1/3}. \tag{3.70}$$

In Fig.3.6, the grey shaded region corresponds to the limit beyond which the radius of the minicluster gets smaller than the one of the AS, according to the last equation. In this region, the WKB approximation could not be used any longer to describe the system. On the other hand, far from this limit, the axion star plays a negligible role on the way the AMC would react to a tidal interaction and can therefore be neglected.

Let's finally note that in Refs.[156, 157], the SP system has been solved numerically to extract the mass-radius relation of the AS. This one deviates by more than one order of magnitude from the one extract in Refs.[152, 155]. Moreover, the relation found in Refs.[156, 157] is found to be in good agreement with the $l_{\rm max} = 1$ limit derived from the WKB break down assumption discussed above. Due to these uncertainties on the properties of the AS and to the WKB breakdown, we limit our next section analysis to the white region of Fig.3.6. From this figure, we note that LE clump, if initially in the white region, will always remain inside it. For the Hernquist AMCs, the situation is different, since the decreasing radius might drive the cluster toward the forbidden region. In this scenario, we would consider that the cluster becomes an AS and the tidal interactions do no longer affect it.

## 3.3 Survival of the Axion Miniclusters in the Milky Way

In this final section, we proceed to describe how the axion miniclusters would survive in the Milky Way. As already discussed in the introduction of this chapter, recent progress has been made to describe the first stage of the formation and evolution of the AMCs [29, 100, 30, 25, 106]. In a second stage, the collisions and mergers after matter radiation equality have been considered numerically and the halo mass function (HMF) of the AMCs at late times has been extracted [31, 111, 139, 158, 159, 160]. However, in order to understand the properties of the AMCs today, the simulations need to go down to times when the clusters are bound to the dark matter halo of the galaxy and subject

to tidal interactions with baryonic stars. As already claimed earlier in this chapter, this task is so far inconceivable for numerical simulations.
If recent works [114, 116, 117, 147] have considered the evolution under tidal interactions of the AMC population in the galaxy using semi-analytical treatments, they stayed, however, in a particle description of the clusters and their interactions. For this reason, we propose in this section to study the survival of the AMCs, for both LE and H density profiles, using the wave treatment developed in the previous section. First, in Sec.3.3.1, the survival probability at the sun location as a function of the mass and radius of the cluster will be studied. Since it does not take any information about the initial mass function, those results could be applied to any HMF model. In Sec.3.3.2, we consider a HMF derived from simulations and apply our previous results on this illustrative example to extract an overall survival probability.

### 3.3.1 Survival Probability as a Function of the Mass and the Radius

As emphasised, we first proceed to calculate the survival as a function of the mass and the radius of the minicluster (for both LE and H density profiles). This survival will be calculated at the sun location, but note that the formalism can be applied to any other location.
We assume here that the dark matter halo of the MW is given by an NFW profile,

$$\rho_{\rm NFW}(r) = \frac{\rho_s}{(r/r_s)\,(1+r/r_s)^2}\,, \tag{3.71}$$

with the parameters $\rho_s = 0.014\,M_\odot\,{\rm pc}^{-3}$ and $r_s = 16.1\,{\rm kpc}$ [161].
If this one is entirely composed of AMCs, those must be distributed in a way to reproduce the dark matter halo profile given in Eq.(3.71). Explicitly, it means that specific distributions have to be found for the eccentricity $e$ and the semi-major axis $a$ of the miniclusters. The general way to write a local number density of clusters $n(r)$ in terms of their orbital parameter distributions is given by

$$n(r) = \int da\, 4\pi a^2 n_{\rm amc}(a) \int de\, P(e) \frac{P(r|a,e)}{4\pi r^2}. \tag{3.72}$$

where $P(e)$ is eccentricity probability distribution, $n_{\rm amc}(a)$ is the number density of clusters as a function of the semi-major axis and

$$P(r|a,e) = \frac{2}{T_{\rm orb}} \left(\frac{dr}{dt}\right)^{-1}\,, \tag{3.73}$$

where

$$\begin{aligned} \frac{dr}{dt} &= \sqrt{GM_G(a)\left(\frac{2}{r} - \frac{1}{a} - \frac{a(1-e^2)}{r^2}\right)}\,, \\ T_{\rm orb} &= 2\pi\sqrt{\frac{a^3}{GM_G(a)}}\,, \end{aligned} \tag{3.74}$$

with $M_G(a)$ being the mass enclosed inside a sphere of radius $a$, and $a(1-e) \leq r \leq a(1+e)$. The matter density arising from Eq.(3.72) is defined as $\rho_{\rm amc}(r) = n(r)\langle M_{\rm amc}\rangle$ with $\langle M_{\rm amc}\rangle$ the mean mass of the AMCs.
It is found in Ref.[116] that the NFW density profile (3.71) is obtained from this construction if $n_{\rm amc}(a) = \rho_{\rm NFW}(a)/\langle M_{\rm amc}\rangle$ and if the eccentricity probability distribution is given by $P(e) = 4e(1-e^2)$ [162]. Explicitly,

$$\rho_{\rm NFW}(r) = \int da\, 4\pi a^2 \rho_{\rm NFW}(a) \int de\, 4e(1-e^2) \frac{P(r|a,e)}{4\pi r^2}. \tag{3.75}$$

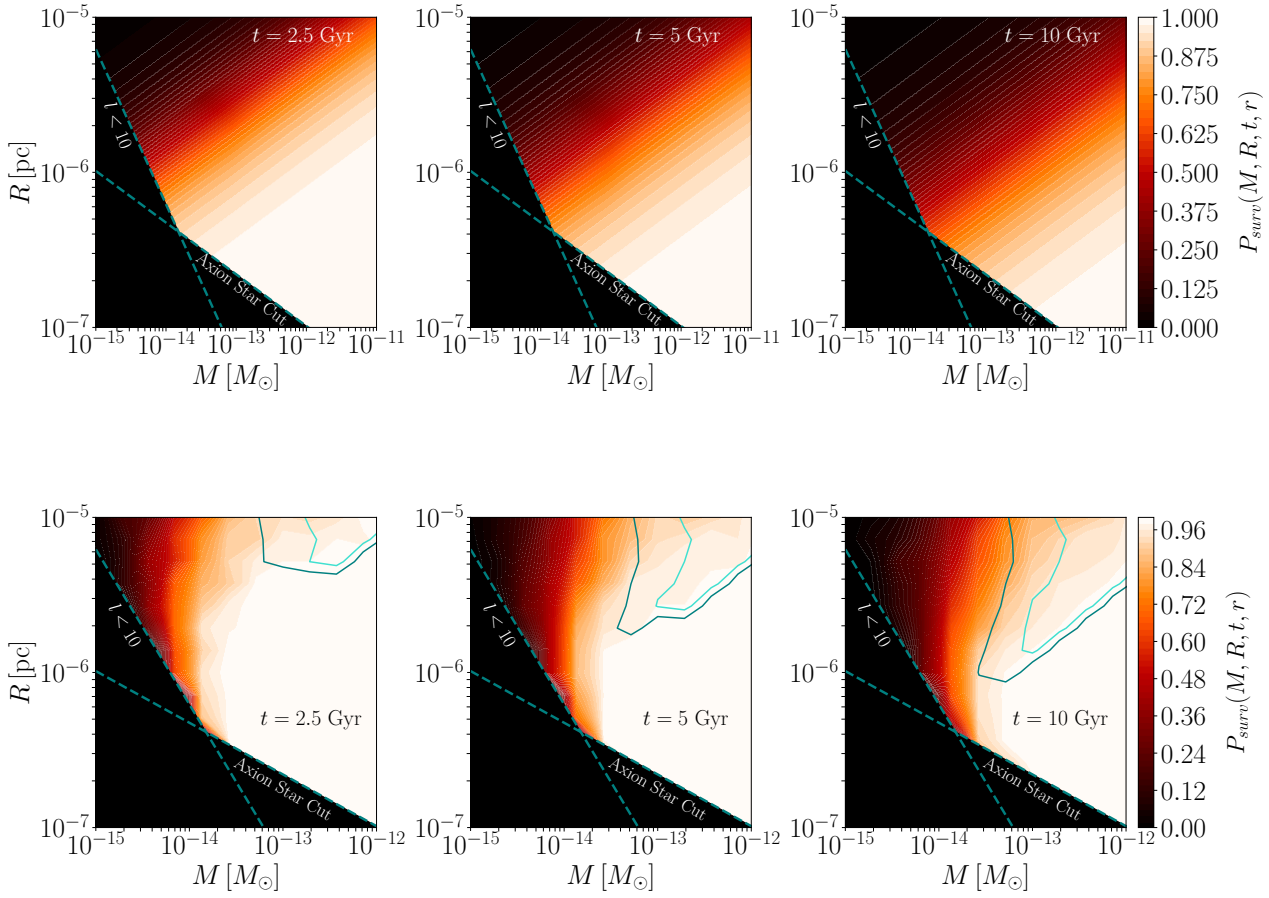


**Figure 3.7:** Local survival probability $P_{\rm surv}(M, R, t, r)$ for the Lane-Emden (top) and Hernquist (bottom) miniclusters at the sun location $r_\odot \approx 8$ kpc. The survival probability is shown for different time snapshots, $t = 2.5$ Gyr, 5 Gyr and 10 Gyr (from left to right). For the Hernquist miniclusters we have included two contours showing the regions where 40% (teal) and 80% (turquoise) of the clusters that did not survive were actually destroyed instead of becoming an axion star. This figure corresponds to Fig.5 in Ref.[113]

From this last equation, we derived in Ref.[113] that at a given location $r$ from the galactic center, the minicluster eccentricity probability distribution is given similarly as before by

$$P(e) = 4e(1 - e^2), \tag{3.76}$$

and the semi-major axis probability distribution given an eccentricity $e$ and location $r$, via

$$P(a|r, e) = P(r|a, e), \tag{3.77}$$

where $P(r|a, e)$ is defined in Eq.(3.73).

In order to calculate the survival probability at the sun location ($r \approx 8$ kpc) as a function of the AMC mass and radius, we are therefore proceeding as follows:

- For a given mass and radius $(M, R)$, we generate a sample of $N_{\rm in}$ initial AMCs. For each of them, the eccentricity and the semi-major axis are chosen according to the probability distributions (3.76) and (3.77), respectively.
- Hence, each of the $N_{\rm in}$ initial AMCs carries a random orbit characterized by the semi-major axis and eccentricity $(a, e)$. Depending on this orbit, the number of star interactions they would

undergo in one period is given by

$$N_{\rm orb}(a,e) = \pi b_{\rm max}^2 \langle v \rangle \int_0^{T_{\rm orb}(a)} dt\, n_*(r(t))\,, \tag{3.78}$$

where $n_*(r(t))$ is the stellar density in the galaxy based on the MW model of Refs. [141, 163, 164, 165, 166] (see App.B.7), $b_{\rm max}$ is the maximal impact parameter chosen such that for any $b > b_{\rm max}$, the impact on the AMC is negligible and $\langle v \rangle$ is the averaged relative velocity of the star. With that the cumulative number of interactions as a function of time is given by

$$N_{\rm tot}(t,a,e) = \frac{t}{T_{\rm orb}(a)}\, N_{\rm orb}(a,e)\,. \tag{3.79}$$

- We simulate each of the $N_{\rm tot}(t,a,e)$ interactions by considering a similar mass of $M_* = 1 M_\odot$ for all the interactions and choosing for each the star velocity and the impact parameter following the probability distributions

$$\begin{aligned} P(v) &= \frac{4\pi v^2}{\left(2\pi\sigma_{\rm rel}^2\right)^{3/2}} \mathrm{e}^{-\frac{v^2}{2\sigma_{\rm rel}^2}}\,, \\ P(b) &= \frac{2b}{b_{\rm max}^2}\,, \end{aligned} \tag{3.80}$$

  with $\sigma_{\rm rel} = \sqrt{2} \times 10^{-3}$ which includes the velocity dispersion of the miniclusters and of the stars.

- At the end of the simulation, we count the $N_{\rm fin}$ surviving AMCs and define the survival probability

$$P_{\rm surv}(M,R,t,r) = \frac{N_{\rm fin}(M,R,r,t)}{N_{\rm in}(M,R,r)}. \tag{3.81}$$

  Importantly, the AMCs that crossed the WKB or AS forbidden region described in Sec.3.2.3 are also removed from the initial sample, since we assume that in that case the system would form a soliton-like object. Note that in the case of a destroyed AMC, it is not clear whether the AS in its center survives. We leave this question to further investigations.

In Fig.3.7, we show the result of the survival $P_{\rm surv}(M,R,t,r)$ at the sun location for three different times $t = 2.5,\ 5,\ 10$ Gyr (from left to right). In the top panels, we simulate the survival from a dark matter halo composed of Lane-Emden AMCs. As already introduced in the previous section, the reaction of the cluster to some tidal interactions depends only on its mean density. Hence, we find that the survival probability of the miniclusters depends only on the mean density, with iso-survival-probability contours following $MR^{-3} = const.$ More specifically, the survival probability is less than $10\%$ for miniclusters with mean density lower than $\bar{\rho} \approx (0.25, 0.5, 1.5) \times 10^2\, M_\odot\,{\rm pc}^{-3}$ for $t = 2.5, 5, 10$ Gyr, respectively. For AMCs with such density profile, the evolution in the Milky Way is then relatively easy to understand. Since their radius is always increased following the interaction, no AMC becomes an AS. They, however, become more and more easily disrupted on further encounters and are eventually destroyed. We show in Fig.3.8 the survival probability of the Lane-Emden AMC as a function of the mean density.
On the bottom panels of Fig.3.7, we study the survival of the Hernquist AMCs. In the previous section we showed that for small perturbations, their radius decreases making them more resistant to further interactions. Hence AMCs with large densities have very low chances to get affected by star interactions. In the upper right corner of the contour plot, we see, however, that the survival is again proportional to the mean density. For those clumps, the density is indeed low enough such that a small portion of the clumps could get destroyed. The area of the destroyed region increased with time as it might be observed from the teal and turquoise contours showing respectively the

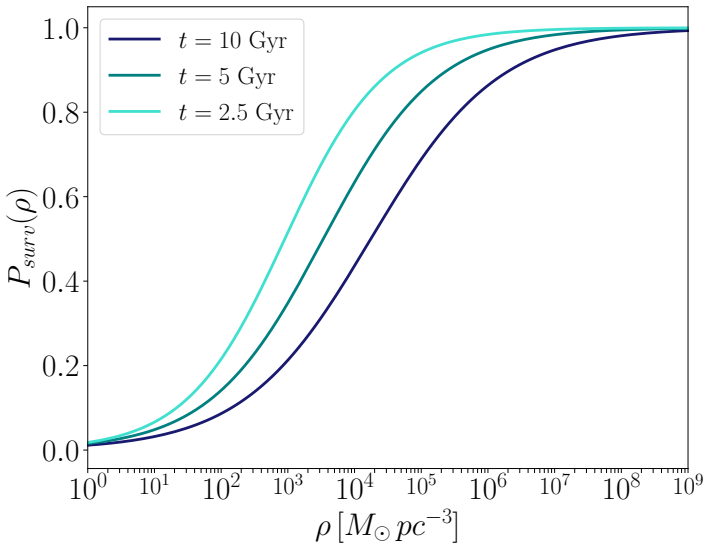


**Figure 3.8:** Local survival probability as a function of the initial mean density $\bar{\rho}$ for the Lane-Emden miniclusters extracted from the previous figure. The three different colored lines show the time evolution of the survival. This figure corresponds to Fig.6 in Ref.[113]

regions where $40\%$ and $80\%$ of the clusters that did not survive were actually destroyed. On the other hand, for AMCs with radius close to the AS limits, the decrease of the radius could drive them into the forbidden region. For this reason, we end up with a final population of AS.

### 3.3.2 Overall Survival for a Specific Mass and Radius Distribution

Let's note that the formalism and results calculated in the previous section do not depend on any mass or radius probability distributions. However, such distributions can be used to calculate the overall survival probability $P_{\rm surv}(r,t)$ (at a location $r$ and time $t$). Indeed we define,

$$P_{\rm surv}(t,r) = \int_{M_{\rm min}}^{M_{\rm max}} dM \int_{R_{\rm min}}^{R_{\rm max}} dR\, P(R,M)\, P_{\rm surv}(M,R,t,r)\,, \tag{3.82}$$

where limits of the integrals correspond to the limits of the mass and radius ranges according to the selected distributions $P(R,M)$. As emphasized in the previous sections, numerical simulations have derived mass and radius distributions at redshift $z = 99$ [30, 153, 159]. We are going to use them to derive values for $P_{\rm surv}(t,r)$. However, it is important to keep in mind that those results might change if the initial probability distributions change as well.
In line with Ref.[153], the mass probability distribution is here assumed to be

$$P(M) = \frac{\gamma}{M_{\rm max}^{\gamma} - M_{\rm min}^{\gamma}} M^{\gamma-1}\,, \tag{3.83}$$

with $\gamma = -0.7$, $M_{\rm min} = 3.3 \times 10^{-19}\,M_\odot$ and $M_{\rm max} = 5.1 \times 10^{-5}\,M_\odot$.
Secondly, a probability distribution $P(\delta)$ for the initial overdensity $\delta$ has been found numerically in Ref. [29]. If the initial overdensity is related to the mean density of the clump by [105]

$$\bar{\rho}(\delta) = 140(1+\delta)\delta^3 \rho_{\rm eq}\,, \tag{3.84}$$

where $\rho_{\rm eq}$ is the average matter density at matter-radiation equality, for a given mass of the clump $M$, the radius is then given by

$$R(M,\delta) = \left(\frac{3M}{4\pi\bar{\rho}(\delta)}\right)^{1/3}. \tag{3.85}$$

Then, combining this with Eq. (3.83), we obtain a joint distribution in mass and radius, $P(R,M)$. The resulting distribution is also in rough agreement with the distributions derived in Ref.[100]

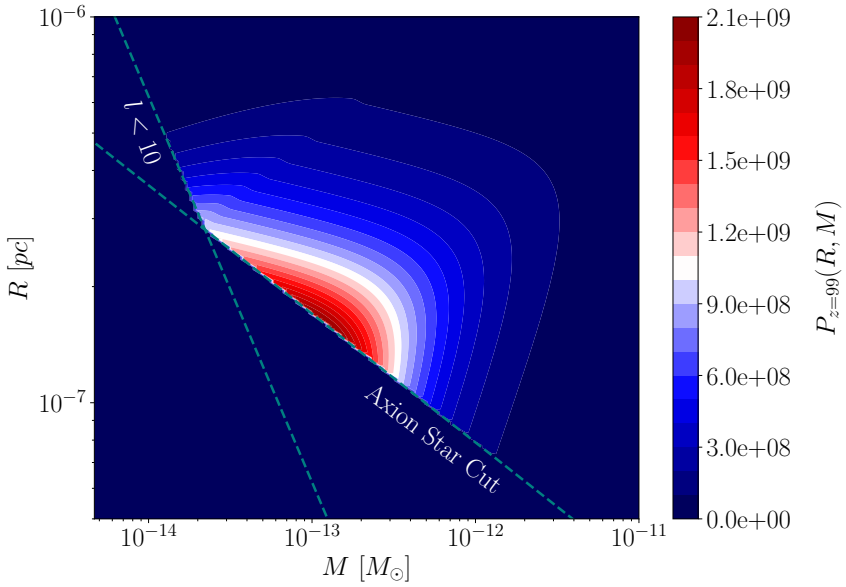


**Figure 3.9:** AMC mass and radius distribution according to Refs. [31, 29] after having applied both the AS cut and the WKB condition. This figure corresponds to Fig.7 in Ref.[113]

| Density profile | $t = 2.5$ Gyr | $t = 5$ Gyr | $t = 10$ Gyr |
|---|---|---|---|
| Lane-Emden | $P_{\rm surv} = 94\%$ | $P_{\rm surv} = 90\%$ | $P_{\rm surv} = 82\%$ |
| Hernquist | $P_{\rm surv} = 99\%$ | $P_{\rm surv} = 98\%$ | $P_{\rm surv} = 94\%$ |

**Table 3.1:** Extracted survival probability from numerical simulations for the two different density profiles, Lane-Emden and Hernquist, at the Sun's location in the Galaxy at the three considered times. This table corresponds to Tab.1 in Ref.[113].

based on semi-analytic methods. Note that here we assume that the mass $M$ and the overdensity $\delta$ are independent, similarly to Ref.[55].
According to this prescription for the mass and radius probability distribution, it turns out that $P(R, M)$ is peaked at the lower cut-off $M_{\rm min}$. Hence a large fraction of the miniclusters would violate the WKB/AS condition discussed in Sec.3.2.3. In order to restrict the analysis to objects for which our approach applies, we renormalize the distribution after applying both the AS and WKB cuts. The renormalized distribution $P_{z=99}(R, M)$ is shown in Fig.3.9.

The overall survival of the Lane-Emden and Henrquist AMCs is finally calculated from Eq.(3.82) and the results are shown in Tab.3.1. It can be appreciated that the Lane-Emden clumps have an overall lower survival probability at our location. Naively, this can be understood since from Sec.3.2.2 we concluded that each perturbation increases their radius, leaving a more vulnerable clump afterward. After 10 Gyr, we observed that $18\%$ of the LE miniclusters are destroyed.
On the other hand, the Hernquist clusters decrease their radius after each interaction, making them more resistant to further ones. As detailed in the previous section, the clumps are therefore less impacted by the star encounters. However nearby the WKB/AS region, the cluster could become an AS object following enough interactions. In the $6\%$ of destroyed Hernquist cluster, we find that $95\%$ actually formed an AS-like object. Hence, it is expected that star tidal interactions in the galaxy generate a population of AS for Hernquist clumps.

### 3.3.3 Limitations and Future Prospects

The results obtained in this section are, however, subjects to some assumptions.
First, along this section we characterized the stellar population by the stellar density $n_*(r)$, considered time independent. This is, of course, an approximation, since it neglects the star evolution. In

Ref.[167], it has been shown that the rate at which the stars are created is higher than the one at which they die. According to that result, using the today's value of $n_*(r)$ for the early times of the galaxy would over-estimate the number of interactions. In addition, we assumed a common mass of $1M_\odot$ for all the stars. It is clear that a realistic mass distribution should be taken into account in the numerical simulation. Note, however, that the mass variation would be degenerated with the impact parameter $b$ and velocity $v$ variations.
Similarly, the evolution of the dark matter halo needs to be taken into account. If we described it as an NFW profile in this work, it is known that the concentration (related to the scale radius $r_s$) is time dependent [168, 169]. In line with the description we made of the miniclusters in the galaxy in Sec.3.3.1, taking into account this dark matter halo time dependence is expected to affect their orbital properties. Of course, since part of the AMCs are destroyed by tidal interactions, the feed-back effect on the dark matter halo profile should be accounted for as well.
Along this work, we also considered that the AMCs would relax toward the same type of density profile. This is of course a strong assumption since we know from Refs.[145, 146] that the density profile would converge toward a universal type of density profile after perturbations.
Furthermore, only a single type of interaction has been considered here. However, it is known that other types of interaction may happen. For instance, crossing the galactic disk generates a tidal source of stripping. This effect has been compared to the stellar tidal interactions considered in this work and has been found subdominant. Tidal interactions between two AMCs could in the same way lead to some stripping. However, since the effect of the tidal interactions scales as the perturbing object mass squared, it is expected that perturbations induced by encounters among AMCs are $10^{-24}$[11] times smaller than by a star with $1M_\odot$.
Finally, we did not consider the tidal disruption of the AS. Indeed, those objects can not be described by the WKB solution constructed in this work and hence the whole formalism of tidal interactions described in Sec.3.2.2 does not apply either. In order to understand how such an object would react to stellar interactions, we need to solve the SP system explicitly for energy levels close to the ground state. As already discussed, larger deviations from the particle picture results are expected if we then apply a tidal perturbation on such a solution.

[11] For an AMC with mass $10^{-12}M_\odot$.

# Chapter 4

# Reconstructing the Axion-Photon Coupling with Axion Miniclusters

*This Chapter is based on Ref.[138]*

In Sec.2.3, we introduced the axion-photon interaction as a model independent result of the PQ solution to the strong CP-problem. Nowadays, as discussed in the same section, this coupling is constrained by several experiments: haloscope experiments, with for instance ADMX [73], helioscope experiments with CAST [77] or again via the light shinning through the wall experiment with OSQAR [71] (see Fig.2.2 for a summary of all the existing constraints).
However, at this stage, an important point has to be made on the assumptions taken to derive those constraints. If we conclude, after some experiment runs, that no signal is observed, two conclusions could indeed be reached. The first one is that the coupling must be objectively small in order to account for the non-event observation. Whereas, the second explanation is that this dark matter candidate constitutes only a small fraction of the local dark matter density so that it prevents a sizable event rate. In the haloscope experiments, the bounds on the axion-photon coupling have been derived assuming the first scenario, considering that the axion constitutes the whole local dark matter abundance.
We can also reverse the previous situation and assume the hypothetical scenario in which a direct or indirect detection is made. Again, it would be impossible to conclude on whether the signal is coming from a dominant form of dark matter or if it comes from a sub-dominant one but more strongly coupled. In other words, these experiments suffer from a coupling-density degeneracy and are only sensitive to a power of the coupling and the dark matter density, $g^n_{a\gamma\gamma}\rho$.
So, how do we disentangle the axion-photon coupling to the axion density? Naively, the degeneracy can be lifted out if we couple the results of two experiments with different sensitivities on the coupling and density. For instance, considering a first one depending only on the coupling (this could be achieved via colliders) and a second one being a direct detection experiment. Unfortunately, it is very challenging for axion searches to have such double experiments.

In this chapter we develop a method able to disentangle the axion-photon coupling to the density via a single experiment, in particular the axion haloscope. This experiment, designed as a cavity embedded in a strong magnetic field, uses the axion-photon coupling to convert the incoming axions from the dark matter halo into photons. Concretely, the incoming axion field acts as a source to induce an electromagnetic field inside the cavity. The electromagnetic power extracted in the case

of a homogeneous axion field with density $\rho$ is [76]

$$\begin{aligned} P &= 6.3 \times 10^{-22}\mathrm{W} \\ &\times \left(\frac{g_{a\gamma\gamma}}{10^{-15}\mathrm{GeV}^{-1}}\right)^2 \left(\frac{\rho}{0.3\mathrm{GeVcm}^{-3}}\right) \\ &\times \left(\frac{B}{8\mathrm{T}}\right)^2 \left(\frac{V}{220\mathrm{l}}\right) \left(\frac{C_{nlm}}{0.69}\right) \left(\frac{Q}{70000}\right) \left(\frac{3\mu\mathrm{eV}}{m_a}\right), \end{aligned} \tag{4.1}$$

where $B$ is the magnetic field inside the cavity, $V$ the cavity volume, $Q$ the quality factor, and $C_{nlm}$ depends on the mode considered for the induced electromagnetic field (see Sec.4.1). As previously advertised, this quantity is the product of the density and the coupling squared and as it is, no independent information is available.
Nonetheless, the current (see for instance Ref.[76]) and future generations (see for instance Ref.[85]) of haloscopes are able to additionally extract the energy spectrum of the axion field with great precision. In recent works, the latter has for instance been used to extract the momentum distribution of the axion field [128, 170, 171]. In this chapter, we show that in the case [1] of an encounter with an axion minicluster, the energy spectrum might be used to extract the gravitational potential of the cluster. This is, of course, an extremely valuable information since, with the use of the Poisson equation, the potential leads to an independent measurement of the cluster density. Together with the power defined in Eq.(4.1), this allows to determine the axion-photon coupling $g^2_{a\gamma\gamma}$. With this knowledge, we are, furthermore, able to extract the fraction of the dark matter background density made of axions, once the AMC has passed and that we measure the signal from the axion field background.

This chapter is decomposed as follows: In Sec.4.1 we review in more details the axion haloscope principles and comment on the way the momentum distribution of the axion field may be extracted from the energy spectrum. In Sec.4.2 we derive the properties of the signal induced in the haloscope in the case of an encounter with an AMC. Finally, in Sec.4.3, we develop a method to reconstruct the axion-photon coupling and apply it to realistic simulated signals.

## 4.1 Haloscope Experiments

### 4.1.1 General Formalism

We thus proceed to start this chapter by recalling the main points of the haloscope operation.
For a setup similar to ADMX [76], the latter is essentially designed as a small (around 1m long) cylinder cavity embedded in a strong magnetic field (around $8\mathrm{T}$ for ADMX). In presence of an axion field[2], the axion-photon coupling induces a source term in the Maxwell equations. These become [33, 16]

$$\begin{aligned} \nabla.\boldsymbol{E} &= 0, \\ \nabla.\boldsymbol{B} &= 0, \\ \nabla \times \boldsymbol{E} &= -\frac{\partial \boldsymbol{B}}{\partial t}, \\ \nabla \times \boldsymbol{B} &= \frac{\partial \boldsymbol{E}}{\partial t} - g_{a\gamma\gamma}\boldsymbol{B}\frac{\partial a}{\partial t}, \end{aligned} \tag{4.2}$$

where in the last set of equations, the axion field has been assumed homogeneous in the cavity volume (this is relevant since the de Broglie wavelength is much longer than the cavity length) and no electromagnetic charge or current is considered. Note that in the precise case of a haloscope experiment, the axion field $a$ is expected to take its origin from the dark matter halo, whether it is

[1] Let's already precise that this is the *extremely lucky case*.
[2] Note that here and from now on, we will always talk about "axion field" in the sense of a classical field. This is in line with the previous chapters where we confirmed that the axions are better described as such.

the dominant part or not.
If the cavity is embedded in an external magnetic field $\boldsymbol{B}_0$, the modified Maxwell equations induce an electric field $\boldsymbol{E}_{\text{ind}}$ given by [172]

$$(\partial_t^2 - \nabla^2)\boldsymbol{E}_{\text{ind}}(\boldsymbol{x}, t) = -g_{a\gamma\gamma}\boldsymbol{B_0}(\boldsymbol{x})\partial_t^2 a(\boldsymbol{x}, t). \tag{4.3}$$

Assuming, for the moment, no specific geometry for the resonant cavity, it is common to expand the electric field on the cavity modes $\boldsymbol{E}_j(\boldsymbol{x})$ [173],

$$\boldsymbol{E}_{\text{ind}}(\boldsymbol{x}, t) = \sum_j \alpha_j(t)\boldsymbol{E}_j(\boldsymbol{x}), \tag{4.4}$$

where $\alpha_j(t)$ are the time dependent coefficients of the modes.
In the absence of sources, the amplitude of each electric modes oscillate at a proper frequency $\omega_j$. In addition, the modes decay at a rate $\exp(-\Gamma_j t/2)$, where $\Gamma_j = \omega_j/Q$ and $Q$ is the quality factor of the cavity. The latter is of the order $\mathcal{O}(10^5)$ for current active cavities [73, 74, 75, 76].

Applying the mode expansion on Eq.(4.3), the equation of motion for the mode coefficients becomes

$$(\partial_t^2 + \omega_j^2 + \Gamma_j\partial_t)\alpha_j(t) = -g_{a\gamma\gamma}\eta_j\partial_t^2 a(\boldsymbol{x}, t), \tag{4.5}$$

where we introduced explicitly the mode decay, and with $\omega_j$ the frequency associated to the mode $\boldsymbol{E}_j(\boldsymbol{x})$, and $\eta_j$ an overlapping function decreasing with the wavelength of the mode, explicitly,

$$\eta_j = \frac{\int_V \mathrm{d}^3x \boldsymbol{E}_j^*.\boldsymbol{B_0}}{\int_V \mathrm{d}^3x |E_j|^2}. \tag{4.6}$$

In order to provide more insights on the physics behind these previous lines, let us first consider a simple situation in which the axion field is given by a homogeneous field oscillating at a frequency $\omega \approx m_a$,

$$a(t) = a_0 e^{-im_a t}. \tag{4.7}$$

In that case the solution for the electric field mode coefficient is trivial and is given by

$$\alpha_j(t) = a_0 g_{a\gamma\gamma}\eta_j \frac{m_a^2}{\left(m_a^2 - \omega_j^2\right) - im_a\omega_j/Q} e^{-im_a t}, \tag{4.8}$$

Intuitively, the cavity mode $\boldsymbol{E}_j$ can get significantly enhanced if its frequency, $\omega_j$, is equal to the axion mass. In that case, its coefficient gets increased by a factor proportional to the cavity quality factor. The latter determines the width of the resonant peak.
The resulting power extracted from the cavity is given in terms of the electric field and the quality factor of the cavity $Q$ [174],

$$\begin{aligned} P &= \frac{\omega_j}{Q}\frac{1}{2}\int_V \mathrm{d}^3x\, |\alpha_j(t)|^2 |\boldsymbol{E}_j(\boldsymbol{x})|^2, \\ &= \frac{\omega_j}{Q}\frac{1}{2} a_0 \left(g_{a\gamma\gamma}B_0\right)^2 V\mathcal{G}\frac{m_a^2}{\left(m_a^2 - \omega_j^2\right)^2 + \left(m_a\omega_j/Q\right)^2}, \end{aligned} \tag{4.9}$$

where $V$ is the cavity volume and we have introduced the form factor of the cavity $\mathcal{G}$,

$$\mathcal{G} = \frac{|\int_V \mathrm{d}^3x \boldsymbol{E}_j^*.\boldsymbol{B_0}|^2}{B_0^2 V \int_V \mathrm{d}^3x |E_j|^2}. \tag{4.10}$$

This last one depends on the cavity geometry and is usually of order $\mathcal{O}(1)$.
It is expected that the power, given in Eq.(4.9), is drastically reduced outside of the resonant region

(determined by the quality factor $Q$). For this reason, in the usual axion searches in haloscope experiments, the cavity shape is progressively modified, leading to a modification of the cavity mode frequency $\omega_j$ as well. Eventually, it is expected to find a large enhanced power in a scenario in which the cavity frequency hits the axion mass. From Eq.(4.9), it can be appreciated that in that case the power is given by

$$P = \frac{\rho_{\rm DM}}{m_a} \left(g_{a\gamma\gamma} B_0\right)^2 V \mathcal{G} Q, \tag{4.11}$$

where we took the usual definition, $a_0^2 = 2\rho_{\rm DM}/m_a^2$, with $\rho_{\rm DM} \sim 0.45\,{\rm GeV/cm^3}$ the local dark matter density.
The last few equations constitute the starting point of the strategy to search for the axion. As stressed in the introduction of the chapter, it is usually assumed that the local dark matter density is fully composed of axions. In the current situation, where no power excess is detected as we progressively changing the frequency $\omega_j$, we are then able to derive constraints in the mass-coupling plane.

### 4.1.2 Haloscope Signal for a Realistic Homogeneous Axion Field

However, as emphasised previously, the axion field considered in the previous example is only barely reflecting the true physical situation. In the previous chapters we have stressed that recent numerical simulations have for instance demonstrated that, because of its wave behavior, the axion density gets granular textures at scales around the de Broglie wavelength. Furthermore, in chapter 3, we discussed that the so-called random phase model was able to recreate those granules, hence preserving the statistics of the axion field while providing a good analytical treatment. It follows that, in order to correctly account for the axion properties, the field that must be considered takes the form [121, 128, 170]

$$a(\boldsymbol{x}, t) = \frac{\sqrt{2\rho_{\rm DM}}}{m_a} \sum_{\boldsymbol{k}} \sqrt{f(\boldsymbol{k})\Delta^3 k} \cos\left(\omega_k t - \boldsymbol{k}\boldsymbol{x} + \phi_{\boldsymbol{k}}\right), \tag{4.12}$$

where $f(\boldsymbol{k})$ is the momentum distribution, $\omega_k \approx m_a + k^2/(2m_a)$ the mode frequency and $\phi_{\boldsymbol{k}}$ the random phases. It could be checked that this last expression returns a Gaussian random field with mean density $\rho_{\rm DM}$.
The signal in haloscopes for such axion field has been recently considered in Refs.[128, 170]. Intuitively, because the axion field is composed of a superposition of momentum modes, the electric field coefficients will get contributions from each of them following [170]

$$\alpha_j(t) = \frac{\sqrt{2\rho_{\rm DM}}}{2m_a} g_{a\gamma\gamma}\eta_j \sum_{\boldsymbol{k}} \frac{\omega_k^2}{\left(\omega_k^2 - \omega_j^2\right) - i\omega_k\omega_j/Q} \sqrt{f(\boldsymbol{k})\Delta^3 k} \left(e^{-i(\omega_k t + \phi_{\boldsymbol{k}})} + c.c\right). \tag{4.13}$$

In the present situation, the equation for the power gets slightly modify compared to Eq.(4.1). Indeed, since taking only the modulus squared of $\alpha_j(t)$ would not lead to a time independent quantity, we proceed to an additional time average over the measurement period,

$$P = \frac{\omega_j}{Q}\frac{1}{2}\int_V {\rm d}^3x \left\langle |\alpha_j(t)|^2 \right\rangle |\boldsymbol{E}_j(\boldsymbol{x})|^2. \tag{4.14}$$

Interestingly, because of the axion field statistics, the power is randomly distributed as well. This is, of course, an important difference compared to the simplified version we considered in Eq.(4.9). Intuitively, the power is still measuring the quantity $\sim \rho_{\rm DM} g_{a\gamma\gamma}^2$, but since the axion density carries randomly distributed granules, the latter now fills these random variations of density.
A usual way to rewrite the power is done via its frequency decomposition. Namely, if the coefficient $\alpha_j(t)$ is measured during a period $T$ at frequency $f$ (such that $N_T = fT$ measurements are made),

we get

$$\begin{aligned} P &= \frac{\omega_j}{2Q}\int_V \mathrm{d}^3x\,\frac{1}{N_T}\sum_{n=0}^{N_T-1}|\alpha_j(t_n)E_j(\boldsymbol{x})|^2, \\ &= \frac{\omega_j}{2Q}\frac{1}{N_T^2}\sum_{d=0}^{N_T-1}|\alpha_j(w_d)|^2\int_V \mathrm{d}^3x\,|E_j(\boldsymbol{x})|^2, \\ &= \frac{\omega_j}{Q}\frac{1}{4\pi}\sum_{d=0}^{N_T-1}\Delta\omega\frac{T}{N_T^2}|\alpha_j(w_d)|^2\int_V \mathrm{d}^3x\,|E_j(\boldsymbol{x})|^2. \end{aligned} \tag{4.15}$$

In the second line, the Parseval theorem has been used to relate the time average with a sum over the Fourier modes of the electric field amplitude. For a finite measurement time $T$, only discreet frequencies enter in the sum and we have $\Delta\omega = 2\pi/T$.
The argument of the sum is defined as the spectral power and is explicitly given by

$$S(\omega_d) \equiv \frac{T}{N_T^2}|\alpha_j(w_d)|^2\int_V \mathrm{d}^3x\,|E_j(\boldsymbol{x})|^2. \tag{4.16}$$

For good enough resolution, the power can be approximated by an integral and we have

$$P \approx \frac{\omega_j}{Q}\frac{1}{4\pi}\int d\omega S(\omega). \tag{4.17}$$

The spectral power for the axion field defined in Eq.(4.12) has been extensively studied in Refs.[128, 170]. As stressed in these works, still as consequence of the axion field statistics, the spectral power is randomly distributed. In particular, it is found that it follows an exponential distribution[3],

$$P(S(\omega_d)) = \frac{1}{\bar{S}(\omega_d)}e^{-S(\omega_d)/\bar{S}(\omega_d)}. \tag{4.18}$$

where $\bar{S}(\omega_d)$ stands for the mean value of the spectral density. From Eq.(4.12) we get after applying a random phase average [128, 170] (see App.C.1 for similar calculation),

$$\bar{S}(\omega_d) = \pi\frac{\rho_{\mathrm{DM}}}{m_a^2}(g_{a\gamma\gamma}B_0)^2 V\mathcal{G}\left(f(\omega_d)\frac{dk}{d\omega}\right). \tag{4.19}$$

It finally follows from the last expression that the mean power is given by

$$\bar{P} \approx \frac{g_{a\gamma\gamma}^2\rho_{\mathrm{DM}}}{4m_a}B_0^2\mathcal{G}\,VQ. \tag{4.20}$$

Note that in this last expression, it has been assumed that the width of the resonant peak $\sim m_a/Q$ was much larger than the width of the axion momentum distribution $\sim (m_a\sigma_v^2)$ with $\sigma_v \sim 10^{-3}$. This is usually the case for setups like those proposed by ADMX with $Q \sim 10^5$ [76] and an axion mass $m_a \sim 10^{-5}\mathrm{eV}$.

The spectral power is at the center of this whole chapter. In the situation we are investigating here, it is for instance clear that it brings additional information about the momentum distribution $f(k)$. Assuming a generic shape for this one (for instance a Maxwellian distribution), Refs.[128, 170] used the spectral power to extract the parameters of the distribution; velocity dispersion, system solar velocity in the galactic frame,... Of course, this is effectively possible only for haloscopes with high enough frequency resolution such that the output signal can be Fourier transformed.
However, at this stage, it is clear that only the product $g_{a\gamma\gamma}^2\rho_{\mathrm{DM}}$ can be extracted from either the power or the spectral power. Based on a similar approach, we show in the next section that the spectral power in the case of an AMC encounter would allow for a disentanglement of the latter product.

[3]This can be easily concluded from noticing that the spectral power is the sum of two Gaussian random fields squared. It follows that it is described by an exponential distribution similarly to the density discussed around Eq.(3.13).

## 4.2 Axion Miniclusters in Haloscope Experiments

From the previous section, it is clear that a homogeneous axion field is not able to provide any information on the axion-photon coupling. Following the example of the works done by Refs.[128, 170], where it is has been shown that the velocity distribution parameters can be inferred from the spectral power, we are going to prove in this section that in the lucky case of an AMC encounter with the Earth, the spectral power can provide information on the gravitational potential of the cluster. This would be, of course, crucial since, with the use of the Poisson equation, the gravitational potential may lead to the density, which then disentangles the quantity $g_{a\gamma\gamma}^2\rho$.

In the appendix C.1, we provide a detailed calculation of the power spectral density induced in the case of an axion minicluster encounter. In particular, we take the axion field to be expressed via the WKB approximation given in Eq.(3.24) and extended to a real field as

$$a_{\rm AMC}(\boldsymbol{x},t) = \frac{1}{\sqrt{2m_a}}\left(\psi(\boldsymbol{x},t)e^{-im_at} + \psi(\boldsymbol{x},t)^* e^{im_at}\right), \tag{4.21}$$

where $\psi$ is the WKB wave function used throughout chapter 3.
In that case, we show that the spectral power is given by

$$\begin{aligned} S(\omega_d) \;\approx\; & T\frac{\left(g_{a\gamma\gamma}B_0\right)^2\mathcal{G}\,V}{2m_a} \\ & \times\left|\sum_{nlm}\frac{\omega_{nlm}^2}{\left(\omega_j^2-\omega_{nlm}^2-i\omega_j\omega_{nlm}/Q\right)}a_{nlm}\psi_{nlm}(\boldsymbol{x})\,\mathrm{sinc}\left(\left(\omega_{nlm}-\omega_d\right)\frac{T}{2}\right)\right|^2, \end{aligned} \tag{4.22}$$

where $a_{nlm}$ are the wave function coefficients derived in Eq.(3.25), $T$ is the measurement period and $\omega_{nlm} = E_{nlm} + m_a + \omega_{\rm amc}$ with respectively the (non-relativistic) binding energy of the axion in the cluster, the axion mass and its kinetic energy due to the cluster velocity. As for the smooth axion field background discussed in the previous section, because of the finite measurement time, only discreet frequencies are resolved by the spectral density and the bin width is given by $\Delta\omega = 2\pi/T$. Finally, note that the location $\boldsymbol{x}$ stands for the location of the earth in a frame where the origin is at the cluster center.

Similarly as in the previous section, since the axion field is a Gaussian random field, the spectral power will be exponentially distributed according to Eq.(4.18). In App.C.1, we derived the mean value of the spectral power in the limit of a narrow sinc function (which is a good approximation for most of the clusters we are going to consider in this chapter). We obtain,

$$\begin{aligned} \bar{S}(\omega_d) \approx 4\pi^2\left(g_{a\gamma\gamma}B_0\right)^2\mathcal{G}\,V & \frac{\omega_d^4}{\left(\omega_j^2-\omega_d^2\right)^2+\left(\omega_j\omega_d/Q\right)^2}f(\omega_d - m_a - \omega_{\rm amc}) \\ & \times\sqrt{\left(2m_a\left(\omega_d - m_a - \omega_{\rm amc} - m_a\phi(r)\right)\right)}, \end{aligned} \tag{4.23}$$

with $\phi(r)$ and $\rho(r)$ the mean potential and density of the cluster. We recall that $f(E)$ is the distribution function and can be obtained from the last two functions via the Eddington formula [175]. From this last equation, it is clear that the spectral power has non-zero value only in the range $[m_a + \omega_{\rm amc} + m_a\phi(r)\,,\; m_a + \omega_{\rm amc}]$ [4]. Hence measuring its width directly provides the gravitational energy $m_a\phi(r)$. Interestingly, the width of the spectral power does not suffer from the statistical fluctuations of the axion field. The reason comes from the fact that, at a given location $\boldsymbol{x}$, only the modes that have a non-zero wave function at this location contribute to the spectral power. All the modes for which this location is in their classical "forbidden" region are therefore not contributing. Since the random phases are only affecting the occupation number of the modes, they would then

[4] Of course, this result does not take into account the deviations from the sinc function in a short measurement time limit (see App.C.1). It is therefore important to keep in mind that the following results account for a large measurement time.

| Haloscope/Axion Parameters | |
|---|---|
| Axion | $m_a = 50\mu$eV<br>$g_{a\gamma\gamma} = 10^{-15}$GeV$^{-1}$ |
| Experiment | $B_0 = 8$T<br>$V = 220$l<br>$Q = 10^5$<br>$\mathcal{G} = 0.69$ ($\mathrm{TM}_{010}$ mode)<br>$\omega_j = m_a$ |

**Table 4.1:** List of the axion/experiment parameters used for the following figures and numerical calculations. We consider a cylinder cavity, as well as the transverse magnetic mode, $\mathrm{TM}_{010}$ [76]. We assume that the cavity is tuned in a way to have the frequency of mode $\omega_j = m_a$. This table corresponds to Tab.1 in Ref.[138].

not alter the width of the spectral power but rather its amplitude.
However, the finite binning of the spectral density will inevitably generate errors in the determination of the gravitational energy $m_a\phi(r)$. We will discuss this matter later in this chapter.

Accordingly, the mean power is found to be given by the same expression as Eq.(4.24)[5],

$$\bar{P} \approx \frac{g_{a\gamma\gamma}^2 \rho(r)}{4m_a} B_0^2 \mathcal{G}\, VQ, \tag{4.24}$$

where the density $\rho(r)$ is the mean density of the cluster at the radius $r$.
As already mentioned, the power is also randomly distributed. In particular, for a given realization of the random phases, the latter will feel the granular structures of the AMC density and will be $\sim g_{a\gamma\gamma}^2 \rho_T$ where $\rho_T$ is the local density averaged over the measurement time $T$ [6].
In Chapter 3, we discussed that, in the random phase model, the variance of the AMC density was given by the mean density, $\sigma_\rho = \rho(r)$. If a time average is additionally applied, we checked numerically that the power variance is given by

$$\begin{aligned} \frac{\sigma_P}{\bar{P}} &\sim \sqrt{\frac{2\pi}{T}\frac{1}{m_a\phi(r)}}, \\ &\sim \sqrt{\frac{T_{\text{gran}}}{T}}. \end{aligned} \tag{4.25}$$

We recall that the time scale of the granules was defined as $T_{\text{gran}} \sim 1/(m_a v^2) \sim 1/(m_a\phi)$ where $v$ is the velocity dispersion in the cluster at radius $r$. Hence, the longer is measured the signal, the smaller the fluctuations in the power we will get. Naively, this effect can be understood as a consequence of the fact, for long measurement sessions, we will go through many granular structures, so that the signal feels the density averaged over them. However, we stress out here that the latter expression holds in the limit of large measurement time $T$. As $T \to 0$, we should recover the usual relation for the variance $\sigma_P = \bar{P}$.

We show in Fig. 4.1 an illustrative example of mean spectral power (left) and integrated power (right) for axion and haloscope parameters described in Tab.4.1. This signal is for an NFW cluster (see Eq. (2.65)) with mass, radius and concentration respectively given by $(10^{-5}M_\odot, 10^{-5}\mathrm{Pc}, 10)$. In the left panel, each colored line represents the mean spectral power at a different location inside the cluster (from blue to red). At each location, the measurement time is taken to be $T = 5 \times 10^4$s, leading to a bin width $\Delta\omega \approx 10^{-19}$eV. In the right panel, the corresponding mean power has been calculated at each location (colored dots). Note that, since the cluster we have considered has a

[5] Where we again assumed that the width of resonance is broad compared to the width of the signal.
[6] Remember that we consider here the time averaged power so that it becomes proportional to the time averaged density as well.

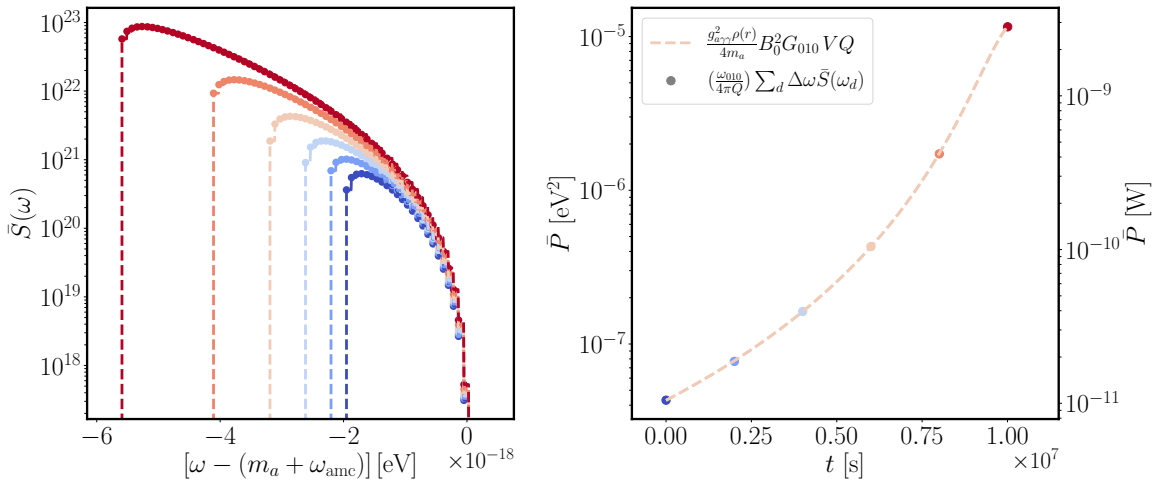


**Figure 4.1:** Averaged spectral power (left) and power (right). In this example the AMC has a mass $M = 10^{-5}\,M_\odot$, radius $R = 10^{-5}$ Pc, concentration $c = 10$ and velocity $v = 10^{-4}c$. We are crossing it with an impact parameter $b = 10^{-6}$ Pc. Each measurement period is $T = 5 \times 10^4$s. Each measurement location is depicted by different colored lines (dots) in both the left (right) panels (from blue to red as we are moving toward the cluster center). The axion and cavity parameters are taken from Tab.4.1. This figure corresponds to Fig.2 in Ref.[138].

density more than 10 orders of magnitude larger than the expected dark matter density background, it is not surprising to find that the power gets the same scale difference compared to the background axion field power $P_{\rm background} \sim 10^{-22}$W [33, 76, 171]. For the same reason the noise will always be irrelevant in our study and will be neglected in the next sections.

## 4.3 Reconstruction of the Axion-Photon Coupling

As it is, the spectral decomposition of the power induced by an axion minicluster allows us to determine the gravitational energy $m_a\phi(r)$ at the location of the measurement (up to some binning erros). The overall power, on its side, provides the usual coupling squared density product $\sim g^2_{a\gamma\gamma}\rho$ (including the granular fluctuations discussed in the last section).
Intuitively, in a hypothetical scenario in which the axion mass has been found after some scan over a wider mass range, the density of the cluster can be extracted from the gravitational potential $\phi(r)$ via the Poisson equation,

$$\nabla^2\phi(r) = 4\pi G\rho(r), \tag{4.26}$$

so that the coupling-density is no longer entangled in the power measurements.
Based on this statement, we provide in this section a detailed method able to indeed extract the coupling $g_{a\gamma\gamma}$ from the simultaneous use of the power and its spectral decomposition.

### 4.3.1 General Method

Let's first emphasized that our formalism applies to a post-axion discovery scenario, meaning that its mass has already been found and is no longer an unknown parameter. Without this assumption, the gravitational potential can not be extracted from the spectral power. Moreover, from the discussion initiated in the previous section, we are neglecting the different noise sources, both thermal and quantum [176, 177].
If a signal is detected, measurements would be performed as we are moving within the cluster. Similarly to Fig.4.1, the spectral power will therefore be obtained at $N$ different locations corresponding to $N$ different measurement times $t_i$, where $t = 0$ is the time at which the first measurement is

performed. Intuitively, what is then obtained from the spectral power is actually not the gravitational potential as a function of the radius but rather of the measurement time $t_i$. It follows that the Poisson equation cannot be used under its usual form. We instead consider a change of coordinates, from space to time (see App.C.2),

$$\frac{\ddot{\phi}(t)}{\dot{r}(t)^2} + \frac{2\dot{\phi}(t)}{\dot{r}(t)r(t)} - \frac{\ddot{r(t)}\dot{\phi}(t)}{\dot{r}(t)^3} = 4\pi G\rho(t), \tag{4.27}$$

where $r(t)$ is the radial motion of the Earth within the cluster, and $\phi(t) = \phi(r(t))$ is the time dependent potential extracted from the spectral power. The radial motion of the Earth is, furthermore, parameterized as

$$r(t) = \sqrt{b^2 + \left(vt - \sqrt{R^2 - b^2}\right)^2}. \tag{4.28}$$

From these last two equations, we proceed to detail the reconstruction method in the following steps:

- The gravitational potential $\phi_{\text{out}}(t_i)$ and the density-coupling product $(g^2_{a\gamma\gamma}\rho(t_i))_{\text{out}}$ are extracted from the spectral power and the power, respectively, at the $N$ different measurement times $t_i$. Moreover, the velocity $v$ of the AMC can be determined from the power spectral density as well, since the signal is non-zero only in the range $[m_a + \omega_{\text{amc}} + m_a\phi(r)\,,\, m_a + \omega_{\text{amc}}]$. As the mass is known, the cut on the right of the signal provides the velocity of the AMC.

- Via the Poisson equation in time coordinates, we construct the function, $\mathcal{F}(g_{a\gamma\gamma}, b, R; t)$,

$$\mathcal{F}(b, R, g_{a\gamma\gamma}; t_i) = \frac{g^2_{a\gamma\gamma}}{4\pi G}\left(\frac{\ddot{\phi}_{\text{out}}(t_i)}{\dot{r}(t_i)^2} + \frac{2\dot{\phi}_{\text{out}}(t_i)}{\dot{r}(t_i)r(t_i)} - \frac{\ddot{r(t_i)}\dot{\phi}_{\text{out}}(t_i)}{\dot{r}(t_i)^3}\right). \tag{4.29}$$

  As a function of the chosen impact parameter, radius and coupling in the last equation, $\mathcal{F}(b, R, g_{a\gamma\gamma}; t_i)$ would return different profiles of $g^2_{a\gamma\gamma}\rho(t_i)$.

- Finally, the parameters $b$, $R$ and $g_{a\gamma\gamma}$ are reconstructed by maximizing the function

$$\mathcal{L}(b, R, g_{a\gamma\gamma}) = \sum_i \log\left(\frac{(g^2_{a\gamma\gamma}\rho(t_i))_{\text{out}}}{|(g^2_{a\gamma\gamma}\rho(t_i))_{\text{out}} - \mathcal{F}(b, R, g_{a\gamma\gamma}; t_i)|}\right). \tag{4.30}$$

  Note that the choice of the maximizing function is not unique and different choices may alter the reconstruction of the parameters. The degeneracy in the determination of the parameters $b$,$R$ and $g_{a\gamma\gamma}$ is discussed in App.C.2.

Let's finally stress that this reconstruction method suffers from both statistical and system errors. As already pointed out, the spectral power is affected by the finite bin width, $\Delta\omega = 2\pi/T$, and the reconstructed gravitational energy, $m_a\phi_{\text{out}}(t_i)$ is therefore extracted with an uncertainty proportional to $\Delta\omega$. Intuitively, this error propagates to the first and second derivatives used to define the function $\mathcal{F}$, so that the reconstruction of the axion-photon coupling applying Eq. (4.30) suffers from a systematic error which gets stronger as $\Delta\omega/(m_a\phi(r)) \gg 1$.
Secondly, we already claimed earlier that the power suffers from the statistical fluctuations of the axion field and directly feels the effect of the granular substructures of the AMC. Hence, using the formalism constructed in this section, the granule structures would affect the quantity $(g^2_{a\gamma\gamma}\rho)_{\text{out}}$ extracted from the power measurement and lead to statistical fluctuations on the reconstructed axion-photon coupling.
An important point is that both the statistical and systematic errors decrease as the averaged ratio $\Delta\omega/(m_a\phi(r)) \to 0$. This last ratio constitutes the main parameter that controls the precision of

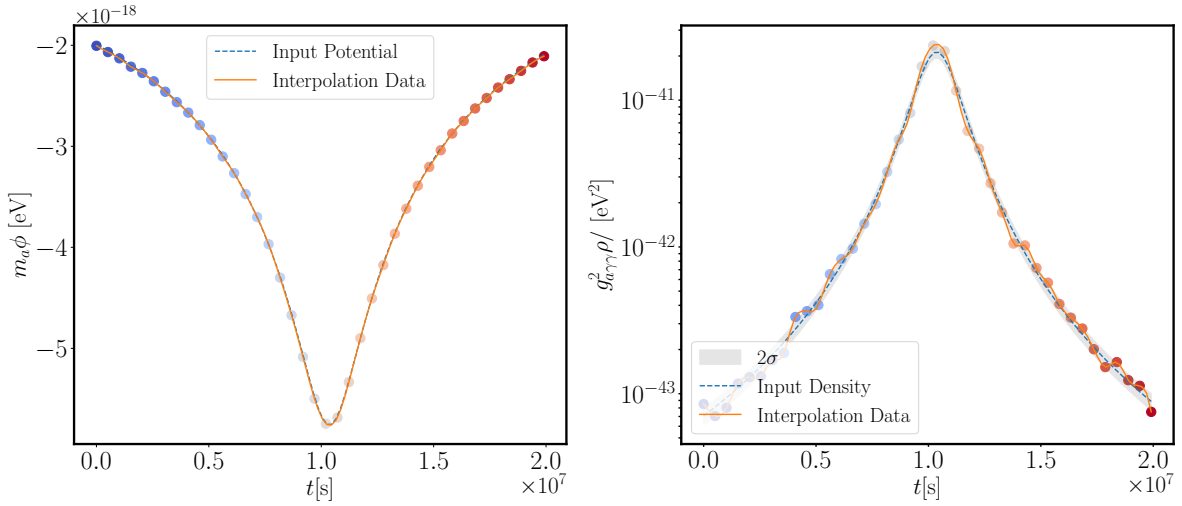


**Figure 4.2:** Gravitational energy (left) and $g^2_{a\gamma\gamma}\rho(r)$ (right) for a simulated signal with a bin width $\Delta\omega/(m_a\phi) \sim 10^{-2}$. The total number of time data points is here $N = 40$. In the left panel, the shaded gray region shows the expected variance $\sigma_P$ of the power due to the granules of the AMC. This figure corresponds to Fig.3 in Ref.[138].

the axion-photon coupling reconstruction. It is, however, expected that the number $N$ of time data points $t_i$ provides another source of systematic error. Indeed in the limit of small $N$, the potential is only reconstructed at few locations, hence its first and second derivatives get less accurately reconstructed, leading to the same conclusion as before.

### 4.3.2 Reconstruction from Simulated Data

We now proceed to apply this method on data obtained from simulated signals. Ultimately, the goal would be to estimate for what range of AMC parameters (i.e mass, radius, impact parameter,...) this reconstruction method is the most efficient.
In our simulations, we practically consider AMCs with an NFW profile. Of course the whole set-up is expected to be insensitive to the density profile choice. From the experiment perspective, the velocity, impact parameter, radius and mass of the cluster are naturally assumed unknown.
Concretely, the spectral power is simulated at each measurement time $t_i$, with $i = 0, ..., N$, according to the probability distribution (4.18) for each discreet frequency defined by the measurement period $T$. For each simulated spectral power, the induced power is finally calculated according to Eq. (4.15). The data are at the end composed of $N$ successive measurements of $\{S(\omega; t_i), P(t_i)\}$ for $i = 0, ...N$.

As an illustrative example of how the extracted gravitational energy and coupling-density product are extracted from the data, we show in Fig.4.2 the output quantities $(m_a\phi)_{\text{out}}$ and $(g^2_{a\gamma\gamma}\rho)_{\text{out}}$ obtained from a simulated signal. More precisely, the data are the ones of a cluster with mass $M = 10^{-5}\text{M}_\odot$, radius $R = 10^{-5}$ Pc and concentration $c = 10$. The impact parameter and the cluster velocity are $b = 10^{-6}$ Pc and $v = 10^{-4}c$. At each location the measurements are taken during $T = 2 \times 10^5$s and we collect data in total at $N = 40$ locations. The input axion mass and coupling, as well as the experiment parameters, are taken from Tab.4.1.
Let's briefly comment on the fluctuations appearing in both the gravitational potential and coupling-density products. For the first one, $(m_a\phi)_{\text{out}}$ is matching extremely well the input potential. In this example, $\Delta\omega/(m_a\phi) \sim \mathcal{O}(10^{-2})$, hence the relative deviations from the finite binning were indeed expected to be small. On the other hand, larger fluctuations appear on the right panel for the coupling-density product. This has to be understood as coming from the granular structures in the density. We indeed proved in Chapter 3 that for a given realization of the phases, the density suffers from fluctuations proportional to the mean density. In the present case, because the power is cal-

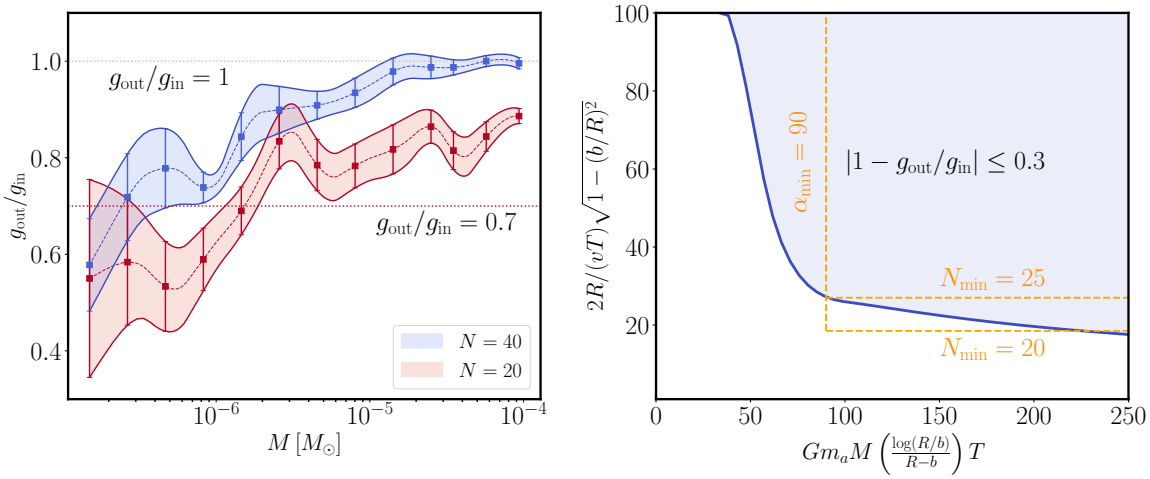


**Figure 4.3:** *Left*: Reconstruction of the axion-photon coupling as a function of the AMC mass. For each mass, the signal has been simulated 10 times. The shaded region shows the dispersion on the reconstruction. The dashed lines show the average over the 10 simulated signals. The radius of the cluster is fixed to $R = 10^{-5}$ Pc, and its velocity to $v = 10^{-4}$c. The measurement time is fixed to $T = 10^5$s. We show the results for both 40 (blue) and 20 (red) time data points. *Right*: Parameter space for which the coupling is reconstructed with 30% accuracy. The dashed orange lines show the rectangle approximations used to infer the rate of encounters in Sec.4.4. This figure corresponds to Fig.4 in Ref.[138].

culated via a time averaged, an extra factor $\sim \sqrt{\Delta\omega/(m_a\phi)}$ effectively reduces the variance of the power. It might additionally be observed that the variance on the right panel (gray shaded region) is larger at early and late times (meaning large radius). This is a direct effect of this last factor which is naturally increasing at larger radii.

As mentioned, we aim to study the dependence of the coupling reconstruction on the AMC parameters. For this reason, we show on the left panel of Fig.4.3 the ratio between the reconstructed coupling, $g_{\rm out}$, and the input one, $g_{\rm in}$, as a function of the AMC mass. The other parameters $(v, R, b, T)$ are respectively fixed to be $(10^{-4}c, 10^{-5}\text{Pc}, 10^{-6}\text{Pc}, 10^5\text{s})$. For each mass, the AMC signal has been simulated 10 times and the coupling has been reconstructed according to our formalism for each of them. Therefore, the dashed lines show the average reconstructed coupling whereas the solid lines stand for the variance over the 10 signal realizations. It can be appreciated that the ratio $\Delta\omega/(m_a\phi)$ decreases with the mass, hence leading to a less efficient reconstruction, as expected. In addition, the statistical error gets as well larger as we go to lower masses. This reflects the larger fluctuations induced in the power measurement. Finally, the red and blue curves show how the number of time data points alter the reconstruction. In particular, the red and blue lines have been simulated for $N = 20$ and $N = 40$ points, respectively.
Since it is expected from the reconstruction to mainly depend on the ratio $\Delta\omega/(m_a\phi)$ and the number of time data points $N$, we use the left panel plot to derive on the right one the parameter space for which the reconstruction is at least 70% accurate. On the horizontal axis, we show the averaged ratio expressed as $\Delta\omega/(m_a\phi) \approx [TGm_aM/(2\pi)]^{-1}\,(\log(R/b)/(R-b))$ [7] and on the vertical one, we express the number of data points as $N \approx 2R/(vT)\sqrt{1-(b/R)^2}$. We checked that our formalism, applied to signals simulated from AMCs with parameters inside the shaded blue region, is able to return the axion photon coupling with $|1 - g_{\rm out}/g_{\rm in}| \leq 0.3$.

[7] The average has been considered because this ratio depends naturally on the location $r$. Taking the average allows to take into account all the locations from the impact parameter $b$ to the radius $R$.

## 4.4 Rate of Encountering Suitable AMCs

In the previous section, we have checked the efficiency of our coupling reconstruction method. Furthermore, we have extracted from simulated data the parameter space that allows for a reasonable reconstruction for both the experiment (measurement time) and the AMC (radius, mass, velocity, impact parameter). But how often could we hope to have an encounter with an AMC with parameters allowing for a good reconstruction or, in other words, falling in the blue shaded region of Fig.4.3?
Assuming an ideal picture where all the clusters have the same mass and radius, the total rate follows

$$\Gamma = n_{\rm AMC}(r)\langle\sigma v\rangle, \tag{4.31}$$

with

$$n_{\rm AMC}(r) = f_{\rm AMC}\frac{\rho_{\rm DM}(r)}{M}. \tag{4.32}$$

In this last equation, $\rho_{\rm DM}$ is the local dark matter density. $f_{\rm AMC}$ stands for the fraction of axion bound in AMCs. Refs. [31, 111] find from numerical simulations that the fraction of axions bound in AMCs is $\sim 0.75$ at redshift around $z \sim 100$. However, it is quite uncertain how this evolves until today. In any case, the numerical values in our figures show rates divided by $f_{\rm AMC}$. But to give rough and optimistic numbers we assume $f_{\rm AMC} \sim 1$. Finally, $M$ is the AMC mass.

A good approximation consists in assuming that the cross section depends exclusively on the impact parameter, $\sigma(b) = \pi b^2$. With that, the differential rate becomes

$$\begin{aligned}\frac{d\Gamma}{db} &= n_{\rm AMC}(r)\left\langle v\frac{d\sigma}{db}\right\rangle \\ &= n_{\rm AMC}(r)\int_{v_i}^{v_f} v f(v)\frac{d\sigma}{db}dv,\end{aligned} \tag{4.33}$$

where $f(v)$ is the DM velocity distribution. In the laboratory frame, it is common to assume the following form,

$$f_{\rm lab}(v) = \frac{2v}{\sqrt{\pi}v_0 v_{\rm lab}}e^{-v_{\rm lab}^2/v_0^2}\sinh\left(\frac{2v_{\rm lab}}{v_0^2}v\right)e^{-v^2/v_0^2}, \tag{4.34}$$

with $v_0 \approx v_{\rm lab} \approx 220{\rm km/s}$ being respectively the velocity dispersion and the laboratory velocity, both in the galactic frame [178].

The rate defined above consists in the total rate, hence taking account clusters for which the reconstruction is not efficient. In order to extract the rate for suitable AMCs (in the sense that they provide a reasonable coupling reconstruction), we use a rectangular approximation for the blue shaded region of Fig.4.3, represented by the orange dashed lines in the latter figure (we show two choices for the rectangular region). This approximation simplifies the parametrization of the parameter space. We now have that clusters within the following range allow for a reasonable coupling reconstruction,

$$\begin{aligned}\alpha_{\rm min} &\leq Gm_a M\frac{\log\left(R/b\right)}{(R-b)}T, \\ N_{\rm min} &\leq \frac{2R}{vT}\sqrt{1-(b/R)^2},\end{aligned} \tag{4.35}$$

where in the most conservative choice[8] , we have $\alpha_{\rm min} \approx 90$ and $N_{\rm min} \approx 25$.
Since the first inequality depends on the measurement period $T$, we optimized it with the use of

[8]Note that these values account for a conservative description of the blue shaded region in the left panel of Fig. 4.3. This "rectangular" approximation provides easy-to-handle calculations and constitutes a first estimate for the rate. Considering the exact shape of this surface is expected not to alter the results drastically and would lead to an increase of the encounter rate.

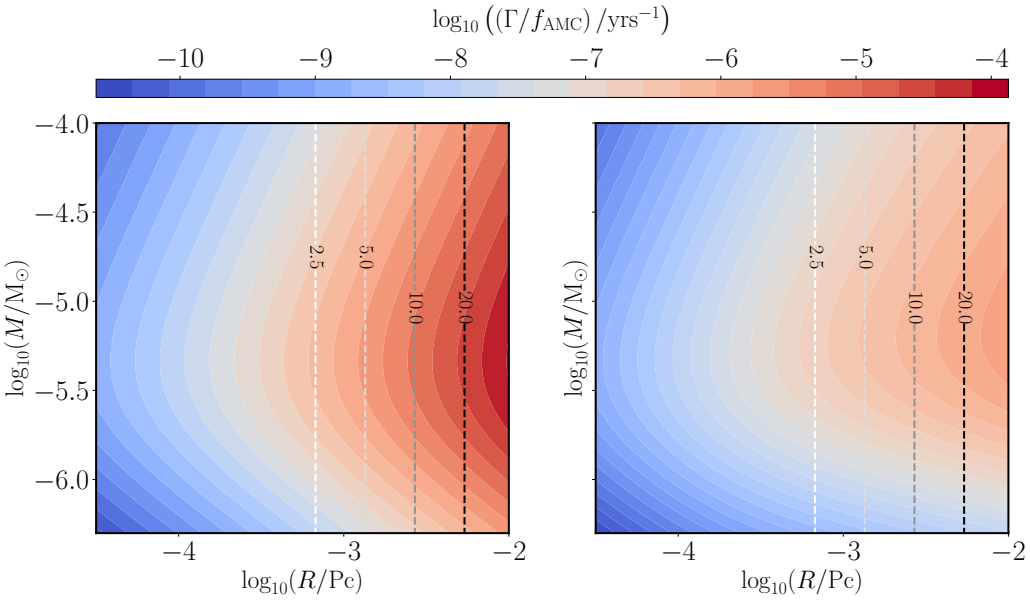


**Figure 4.4:** *Left*: Two-dimensional rate of AMC encounters for which the coupling can reasonably be reconstructed. *Right*: Similar but taking into account the survival probability (given in Ref. [113]). In both panels, the vertical dashed lines show the number of years needed to cross the cluster for a relative velocity given by the mean velocity of the considered distribution. This figure corresponds to Fig.6 in Ref.[138].

the second inequality. Explicitly, for a given radius, impact parameter and velocity, the maximal measurement period is $T_{\rm max}(b,R,v) = 2R/(vN_{\rm min})\sqrt{1-(b/R)^2}$. The condition for a suitable reconstruction therefore becomes

$$\alpha_{\rm min}N_{\rm min} \leq 2\frac{Gm_aM}{v}\frac{\sqrt{1-\kappa^2}}{\kappa-1}\log(\kappa), \tag{4.36}$$

where we have defined $\kappa \equiv b/R$.

For a fixed mass, the last inequality allows to define a maximal value, $\kappa_{\rm max}$ (note that this inequality is solved numerically). Hence applying this constraint on the differential rate defined in Eq.(4.33), we get that the rate for suitable AMC encounters is given by,

$$\Gamma(M,R) = n_{\rm AMC}(r)\pi R^2\int_{v_i}^{v_f}\kappa_{\rm max}(M,v)^2 v f(v)dv. \tag{4.37}$$

The rate, as a function of the mass and the radius, is shown on the left panel of Fig.4.4. Let's first comment on the mass dependency. Intuitively, for increasing mass, the number density of AMCs is decreasing (as observed from Eq.(4.32)). Therefore, it implies a decreasing rate as well. On the other hand, decreasing the mass induces a lower ratio $\Delta\omega/(m_a\phi)$, so that it prevents from a good coupling reconstruction. In the low mass region, it is therefore expected that the rate (for suitable AMC encounters) decreases as well. This is indeed what can be observed from the left panel of Fig.4.4 with a maximal rate around $M \sim 10^{-5}{\rm M}_\odot$.
It can be appreciated from Eq.(4.36) that $\kappa_{\rm max}$ does not depend on the radius. Hence it implies, from Eq.(4.37), that the rate grows as $\sim R^2$, as it can be checked from Fig.4.4.
It has, however, been demonstrated in chapter 3 (see also recent works, [114, 116, 117, 147]) that the survival of the AMCs in the galaxy was decreasing as their mean density increases. Although the survival strongly depends on the density profile of the cluster, we show on the right panel of Fig.4.4 the rate accounting for the survival. In particular we took the survival, derived from a Lane-Emden

profile [137], from Ref.[113].
Accounting for the tidal stripping in the galaxy, we obtain that the rate for suitable AMC encounters, could reach $\Gamma \sim 10^{-6}\mathrm{yrs}^{-1}$. Of course increasing the radius would still increase this rate but, we decide to stop the rate analysis around a crossing time of about 20 years (see dashed black lines).

# Chapter 5

# Primordial Black Holes and Gravitational Waves from Large Curvature Fluctuations

*This Chapter is based on Ref.[179]*

Sizable gravitational waves (GWs) may only be produced by violent enough events in the Universe. Hence the first detection, in September 2015 at the LIGO observatory [180], came from two black holes (BH) that merged around two billion years ago. Such kind of astrophysical signal are today well confirmed individual sources of GWs. On the other hand, it is expected that unresolved super-positions of GWs generate a stochastic gravitational wave background (SGWB). It is, for instance, known that super massive black hole binaries (SMBHBs) should act as a source for this background [181, 182, 183, 184] [1]. Beyond this astrophysical origin [2], the SGWB is expected to be sourced by any violent process that occurred in the early Universe (inflation [186], enhanced small scale perturbations [187], phase transitions [188], cosmic strings [189],...). It might, therefore, be seen as a way to probe physics phenomena that happened at energy scales much higher than CMB. Its detection is one of the main targets of the future and present GW observatories [190, 191, 192, 193, 194, 195, 196].

In particular, one of the early universe mechanism able to induce such a gravitational wave background is realized via the fluctuations inherited by inflation. If it is known that the scalar (or curvature) perturbations evolve independently from the tensor perturbations at linear order, at second order, the tensor modes are sourced by the curvature ones [42, 43, 44, 45, 46, 197, 198], those are the so-called scalar induced gravitational wave (SIGW). We will discuss in detail this production mechanism in Sec.5.1. The important point is that the GWs produced that way are nothing but the consequence of General Relativity and do not constitute any new physics phenomena. Nevertheless, a sizeable amount of GWs is produced only in the scenario of large fluctuations, in order for the second order perturbation theory to be relevant. It translates into the necessity to have large amplitudes for the primordial curvature power spectrum $P_\zeta$. However, CMB and large scale structure (LSS) observations both indicate that $P_\zeta \sim 10^{-9}$ at scales larger than 1 Mpc [10], which implies that only a very small amount of GW is produced at those scales. At scales much smaller than 1 Mpc, the curvature power spectrum is however still very weakly constrained and nothing prevents it from having a significantly larger amplitude. Refs.[199, 200, 201] for instance derived ultra-slow roll inflation models able to enhance the amplitude of the scalar power spectrum. Small scales curvature perturbations are therefore an open window for the production of a SGWB.

The hypothesis of having large amplitudes for the curvature power spectrum at small scales is all the more interesting as it provides a natural mechanism to form Primordial Black Holes (PBH) in addition to GWs [48]. Indeed, the small scale density fluctuations $\delta$ inherited by the curvature perturbations $\zeta$ (the latter being constant at super horizon scales) would reenter the horizon during

[1] SMBHBs, with mass $M = 10^5 - 10^{10}\, M_\odot$ form after galaxy mergers, each galaxy bringing their own central BH in the system [185].

[2] The SMBHB are often referred to astrophysical origin for the gravitational wave background. This is in opposition to the cosmological origin discuss later in this chapter.

radiation domination era. At this point, gravitational force may compete the radiation pressure for large enough perturbations [202]. In particular, the usual Jeans length argument allows to estimate that fluctuations that exceed at horizon reentry the critical overdensity $\delta_c \sim 1/3$ [48] collapse into a black hole. Since the abundance of PBHs today depends crucially on this last quantity, it is important to go beyond this simple approximation. The precise value of this threshold is, however, still under debate and will be discussed in detailed in Sec.5.1. It is nevertheless estimated that PBHs produced from the large curvature fluctuations would constitute a sizeable amount of the dark matter relic abundance if the amplitude of the curvature power spectrum at small scales is $P_\zeta > \mathcal{O}(0.01)$. Being able to detect the SGWB produced by large curvature fluctuations would then be the hint of the existence of an exotic inflation period as well as the existence of PBHs.

Interestingly, a potential new signal of GWs has been recently observed in all Pulsar Timing Array (PTA) communities (we will mainly focus in this chapter on NANOgrav 12 years (NG12)[191] and the International Pulsar Timing Array (IPTA) [35], see Sec.5.2 for detailed discussion on those). What are the PTAs? In short, it is known that pulsars generate electromagnetic pulses with an extremely regular period. In this context, these experiments are observing an array of pulsars with known periods and record the time of arrival (TOA) of their pulses. Many things can, however, alter the regularity of the TOAs and, more interestingly in our case, an incoming GW would generate a common time delay in the pulsar array in addition to a characteristic correlation between the pulsars, named Hellings-Downs (HD) correlation [203]. The current PTAs are, however, still not sensitive enough to draw conclusions on the existence of this correlation and only concluded on the existence of a common process [3]. A signal in the frequency range (1-10 nHz) of those experiments is actually expected from the SGWB of the SMBHBs [39, 40]. Nonetheless, if future generations of PTAs show evidence of Hellings-Downs correlations in this signal, it would be crucial to understand if any cosmological origin might be contained in the signal as well. So could this signal come from the GWs produced by large fluctuations discussed above? To bring light on this question, we perform in this chapter a Bayesian search in the NG12 and IPTA data interpreting the signal as coming from GWs produced by large amplitude curvature fluctuations parameterized by a lognormal power spectrum

$$P_\zeta(k) = \frac{A_\zeta}{(\sqrt{2\pi}\Delta)} \exp\left[-\frac{\log^2(k/k_\star)}{(2\Delta^2)}\right] \tag{5.1}$$

where $(A_\zeta, k_\star, \Delta)$ are parameters. As discussed earlier, for $k_\star$ peaked at small scales, this power spectrum avoids constraints from CMB and LSS.
We will then study the posterior distributions in order to determine the range of parameters $(A_\zeta, k_\star, \Delta)$ able to explain the observed signal. Finally, a careful study of the PBH population induced by such curvature power spectrum will be discussed and compared to the existing constraints on PBH abundance.

This chapter will be decomposed as follows: In Sec.5.1 we derive in detailed the GW spectrum as well as the PBH abundance induced by large curvature fluctuations. The existing PBH constraints will be reviewed as well. In Sec.5.2, we proceed to analyze the data of NG12 and IPTA assuming both SMBHBs and SIGWs. We finally discuss in this section the posterior distributions.

## 5.1 Phenomenology of a Large Curvature Power Spectrum

In this section, we review the GW and PBH production induced by the lognormal curvature power spectrum defined in Eq.(5.1). It is, however, important to keep in mind that both the PBH abundance and GW spectrum would depend drastically on the shape of the chosen power spectrum (see for instance Refs.[204, 205] for similar study on a flat and power law power spectrum, respectively).

[3] As it will be commented at this end of this section, few months after this work has be released, the NANOGrav community released data from 15 years of observation. Whereas in this analysis, we used the 12.5 years data, the new data show a more significant evidence for HD correlation.

The spectrum in Eq.(5.1) is normalized such that $A_\zeta$ is the amplitude of the momentum integrated power spectrum and not the peak amplitude. Note that the latter is instead given by $A_\zeta/(\sqrt{2\pi}\Delta)$ and then diverges for $\Delta \to 0$. Studying such power spectrum shape is therefore particularly interesting since in the limit of $\Delta \ll 1$, we recover the Dirac delta case, $P_\zeta = A_\zeta \delta_D[\log(k/k_\star)]$. A study of the GWs and the PBHs induced by such power spectrum has recently been conducted in the case of the NANOgrav 11 years (NG11) data in Ref.[206]. On the other hand, the limit for $\Delta \gg 1$ corresponds to a broad power spectrum tending to similar flat spectrum considered in Ref.[205]. We can then conclude that the lognormal spectrum in Eq.(5.1) is able to cover a wide range of possible shapes.

### 5.1.1 Scalar Induced Gravitational Waves

As mentioned in the introduction of this chapter, it is expected from cosmological perturbation theory to induce tensor perturbations. However, as we will see only at second order will those GWs be sourced by the scalar perturbations and then have potentially a sizable effect.
We start this discussion by considering the perturbed metric. As usually done, the perturbations in the metric are written in terms of scalars, vectors and tensors components. In the Newton gauge, only a single scalar perturbation, $\Psi$ [4], usually appears. The vector and tensor perturbations are actually decaying at linear order and are therefore most of the time not considered. However, since we explicitly discuss the production of GWs, we include here the transverse traceless tensor $h_{ij}$. The perturbed metric in Newton gauge is then,

$$ds^2 = a^2(\eta)\left[-(1+2\Psi)\,d\eta^2 + ((1-2\Psi)\,\delta_{ij} + h_{ij})\,dx^i dx^j\right], \tag{5.2}$$

where $\eta$ is the conformal time.
The scalar perturbation $\Psi$ can be related in radiation domination to the primordial curvature perturbation $\zeta$ generated during inflation by

$$\Psi(\boldsymbol{k},\eta) = \frac{2}{3}T(k,\eta)\zeta(\boldsymbol{k}), \tag{5.3}$$

where $T(k,\eta)$ is the usual transfer function:

$$T(k,\eta) = 3\left[\frac{\sin\left(k\eta/\sqrt{3}\right) - \left(k\eta/\sqrt{3}\right)\cos\left(k\eta/\sqrt{3}\right)}{\left(k\eta/\sqrt{3}\right)^3}\right]. \tag{5.4}$$

It implies that the scalar perturbations are frozen initially at super-horizon scales and its power spectrum is given in terms of the curvature power spectrum in radiation via $P_\Psi(k) = \frac{4}{9}P_\zeta(k)$.
In Eq.(5.2), the tensor perturbations can be decomposed in terms of the usual $+$ and $\times$ components and the Fourier modes $h_{\boldsymbol{k},\lambda}(\eta)$

$$h_{ij}(\eta,\boldsymbol{x}) = \int \frac{d^3k}{(2\pi)^{3/2}} \sum_{\lambda=+,\times} e^\lambda_{ij}(k) h_{\boldsymbol{k},\lambda}(\eta) e^{i\boldsymbol{k}.\boldsymbol{x}}, \tag{5.5}$$

where $e^\lambda_{ij}(k)$ are the two orthonormal polarization tensors. The equation of motion for the Fourier modes is written at second order in perturbation theory as

$$h''_{\boldsymbol{k},\lambda}(\eta) + 2\mathcal{H}h'_{\boldsymbol{k},\lambda}(\eta) + k^2 h_{\boldsymbol{k},\lambda}(\eta) = \mathcal{S}_\lambda(k,\eta), \tag{5.6}$$

where $\mathcal{S}_\lambda(k,\eta)$ is the source term vanishing at linear order. At second order, it is proportional to the scalar modes $\Psi(k,\eta)$,

$$\mathcal{S}_\lambda(k,\eta) = \int d^3l\, e^\lambda_{ij}(k) l^i l^j f(\boldsymbol{k},\boldsymbol{l},\eta)\psi_{\boldsymbol{l}}\psi_{\boldsymbol{k}-\boldsymbol{l}}, \tag{5.7}$$

[4] Note that there are actually two scalar perturbations, $\Psi$ and $\Phi$. Only in the case of a negligible anisotropic stress we have $\Phi = -\Psi$.

with $\Psi(k,\eta) = T(k\eta)\psi(k)$ so that all the time dependence is contained inside the function $f(\boldsymbol{k},\boldsymbol{l},\eta)$ (see App.D.1 for an explicit expression of this function).
Again, it is important to stress here that only for large scalar (curvature) perturbations the source term $\mathcal{S}_\lambda(k,\eta)$ is large enough to trigger a sizeable GW production. Since the curvature power spectrum has been constrained to be of the order $P_\zeta \sim \mathcal{O}(10^{-9})$ at scales larger than 1 Mpc [10], the power spectrum we consider in Eq.(5.1) must be peaked at scales much smaller in order to allow for larger amplitudes. It naturally implies that all the wavelengths of interest would reenter the horizon in radiation domination era.
We finally define the tensor power spectrum $P_h(k,\eta)$ via

$$\sum_{\lambda=+,\times} \langle e^\lambda_{ij} e^{ij}_\lambda h_{\boldsymbol{k},\lambda} h_{\boldsymbol{q},\lambda}\rangle = \frac{2\pi^2}{k^3} P_h(k,\eta)\delta^{(3)}(\boldsymbol{k}+\boldsymbol{p}). \tag{5.8}$$

The GWs produced through this mechanism are usually characterized in terms of their contribution to the relic abundance $\Omega_{\rm gw}(f)$ [207],

$$\begin{aligned}\Omega_{\rm gw}(f,\eta) &= \frac{1}{\rho_c}\frac{d\rho_{\rm gw}}{d\log f},\\ &= \frac{k^2}{12H^2a^2}P_h(k,\eta),\end{aligned} \tag{5.9}$$

where $f$ is the frequency of the gravitational wave and $\rho_{\rm gw}$ is the total gravitational wave energy density.
As introduced earlier, the aim of the next section would be to understand if the GWs produced that way could have induced the potential signal observed in PTAs. For that, we must, of course, have an easily handling expression of the GW spectrum $\Omega_{\rm gw}(f,\eta_0)$ at our current days, $\eta_0$. To this point, we first calculate the spectrum in radiation domination era, $\Omega_{\rm gw,r}(k)$,when all the wavelengths are deep in the horizon and average over the oscillations, we get [208, 209, 210] (see details in App.D.1)

$$\Omega_{\rm gw,r}(k) = 3\int_0^\infty dv \int_{|1-v|}^{1+v} du \frac{\mathcal{T}(u,v)}{u^2v^2} P_\zeta(uk)P_\zeta(vk), \tag{5.10}$$

with the transfer function $\mathcal{T}$ given by,

$$\begin{aligned}\mathcal{T}(u,v) =& \frac{1}{4}\left[\frac{4v^2-(1+v^2-u^2)^2}{4uv}\right]^2\left(\frac{u^2+v^2-3}{2uv}\right)^4\\ &\times\left[\left(\log\frac{|3-(u+v)^2|}{|3-(u-v)^2|}-\frac{4uv}{u^2+v^2-3}\right)^2+\pi^2\Theta\left(u+v-\sqrt{3}\right)\right].\end{aligned} \tag{5.11}$$

Then, since the GW energy density decays as radiation after equality, the GW spectrum today is obtained just be re-scaling Eq.(5.10) [210, 211],

$$\Omega_{\rm gw}h^2(f,\eta_0) \simeq 10^{-5}\left(\frac{g_*(T_\star)}{17.25}\right)\left(\frac{g_{*s}(T_\star)}{17.25}\right)^{-\frac{4}{3}}\left(\frac{\Omega_{r,0}h^2}{4\times10^{-5}}\right)\Omega_{\rm gw,r}(f). \tag{5.12}$$

In practice it is, however, challenging to obtain an analytical solution for Eq.(5.10) and most of the time only a numerical integration can solve it. However, as we will see in the next section, the computation time of the Bayesian search used to analyze the PTA data is dramatically increased if we go for this last option. Hopefully, Ref.[211] derived an analytical estimated solution of Eq.(5.10) for the lognormal power spectrum considered in Eq.(5.1) in the narrow ($\Delta \ll 1$) and broad ($\Delta \geq \mathcal{O}(1)$) regimes. We confirmed that such analytical estimates are in good agreement with an exact numerical calculation in most of the frequency range. However, we pointed out that in the narrow spectrum limit, the low frequency tail is actually not well fitted by the approximation proposed in Ref.[211].

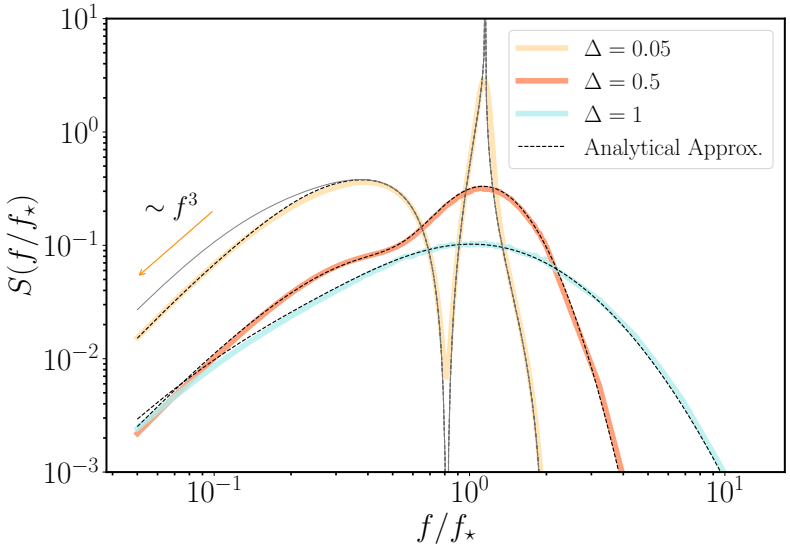


**Figure 5.1:** Gravitational wave spectrum induced by large scalar perturbations parameterized by a lognormal curvature power spectrum. The colored lines have been obtained via numerical integration for different spectrum widths $\Delta$, whereas the black dashed lines correspond to the analytical approximation (see Eq.(5.14),(5.13)). The gray solid line shows the analytical approximated given in Ref.[211]. This figure corresponds to Fig.1 in Ref.[179].

For this reason we adapted the analytical estimation in order to fully match the numerical results. We obtain that the GW spectrum in Eq.(5.10) is given by:

*Narrow peak*

$$\frac{\Omega_{\rm gw,r}(f/f_\star,\Delta)}{A_\zeta^2} \approx 3\alpha^2 e^{\Delta^2}\left[\text{erf}\left(\frac{1}{\Delta}\text{arcsinh}\frac{\alpha e^{\Delta^2}}{2}\right) - \text{erf}\left(\frac{1}{\Delta}\text{arcosh}\frac{\alpha e^{\Delta^2}}{2}\right)\right]\left(1-\frac{1}{4}\alpha^2 e^{2\Delta^2}\right)^2$$
$$\times\left(1-\frac{3}{2}\alpha^2 e^{2\Delta^2}\right)^2\left\{\left[\frac{1}{2}\left(1-\frac{3}{2}\alpha^2 e^{2\Delta^2}\right)^2\log\left|1-\frac{4}{3\alpha^2 e^{2\Delta^2}}\right|-1\right]^2\right.$$
$$\left.+\frac{\pi^2}{4}\left(1-\frac{3}{2}\alpha^2 e^{2\Delta^2}\right)^2\Theta\left(2-\sqrt{3}\alpha e^{\Delta^2}\right)\right\} \tag{5.13}$$

*Broad peak*

$$\frac{\Omega_{\rm gw,r}(f/f_\star,\Delta)}{A_\zeta^2} \approx \frac{4}{5\sqrt{\pi}}\alpha^3\frac{e^{\frac{9\Delta^2}{4}}}{\Delta}\left[\left(\log^2 K+\frac{\Delta^2}{2}\right)\text{erfc}\left(\frac{\log K+\frac{1}{2}\log\frac{3}{2}}{\Delta}\right)-\frac{\Delta}{\sqrt{\pi}}\exp\left(-\frac{\left(\log K+\frac{1}{2}\log\frac{3}{2}\right)^2}{\Delta^2}\right)\right.$$
$$\left.\times\left(\log K-\frac{1}{2}\log\frac{3}{2}\right)\right]+\frac{0.0659}{\Delta^2}\alpha^2 e^{\Delta^2}\exp\left(-\frac{\left(\log\alpha+\Delta^2-\frac{1}{2}\log\frac{4}{2}\right)^2}{\Delta^2}\right)$$
$$+\frac{1}{3}\sqrt{\frac{2}{\pi}}\alpha^{-4}\frac{e^{8\Delta^2}}{\Delta}\exp\left(-\frac{\log^2\alpha}{2\Delta^2}\right)\text{erfc}\left(\frac{4\Delta^2-\log\alpha/4}{\sqrt{2}\Delta}\right), \tag{5.14}$$

where $\alpha = f/f_\star$ and $K = \alpha\exp(3\Delta^2/2)$.
In Fig.5.1, we show the GW spectrum of the lognormal power spectrum defined in Eq.(5.1) for three different choices of width $\Delta$. We could see that the numerical calculated spectrum (colored thick

lines) is in good agreement with our analytical approximation (dashed gray lines). The solid gray line represents the approximation of Ref.[211] and deviates at lower frequencies. The general features of this spectrum are actually simple to understand. First, it is peaked closed to $f_\star = k_\star/(2\pi)$. Around the peak, it increases as $f^3$ for $f \ll f_\star$, as dictated by causality, and decreases exponentially for $f \gg f_\star$ following the decrease of the curvature power spectrum. The precise location of the peak and the behavior around it depends on the width of the power spectrum $\Delta$ [211]. Hence, for $\Delta > 1$, there is a lognormal peak at $f = f_\star$, with a width $\Delta/\sqrt{2}$ whereas for $\Delta < 0.2$, a double peak structure appears [212]. First a sharper peak at $f/f_\star = (2/\sqrt{3})e^{-\Delta^2}$ and secondly a broader one at $f/f_\star = 1/e$. Moreover, they are separated by a dip at $f/f_\star = (\sqrt{2/3})e^{-\Delta^2}$. The presence of the sharp peak is due to resonant amplification of tensor modes, see [212]. Notice that as $\Delta \to 0$, the amplitude of the IR tail of the GW signal, arising from scalar perturbations with anti-aligned wave vectors generating an IR GW, is independent of $\Delta$. We note that in this case, there is an intermediate region with slope $f^2$ for $f_\star > f > 2\Delta e^{-\Delta^2}$.

### 5.1.2 Primordial Black Holes

NANOGrav 12.5 years and IPTA data released 2 have detected a potential GW signal with spectrum amplitude $\Omega_{\rm gw}(f) \geq 10^{-10}$ in a frequency range $f \sim 10^{-9} - 10^{-8}$ Hz. Considering the lognormal spectrum in Eq.(5.1), it implies for it to be peaked around $k_\star \sim 10^5 - 10^8\,{\rm Mpc}^{-1}$ and to have an amplitude of the order $A_\zeta \sim \mathcal{O}(10^{-2})$. As mentioned in the introduction of this chapter, such large amplitudes would naturally induce the formation of PBHs when the associated density fluctuations reenter the horizon during radiation domination. Hence, it is fair to claim that any significant production of GWs via the above formalism would imply a, potentially, non-negligible PBH population. The fraction of PBHs in the total amount of dark matter, $f_{\rm PBH} = \Omega_{\rm PBH}/\Omega_{\rm DM}$ with $\Omega_{\rm DM} = 0.26$, is, however, strongly constrained. In Fig.5.2, we show a complete list of the existing ones. As we will see later in this section, the lognormal curvature power section in Eq.(5.1) with values of $k_\star$ in the appropriate range of detection on NG12 and IPTA would produce solar mass PBHs. The most important constraints are coming (from left to right in Fig.5.2) from microlensing [213, 214, 215, 216, 217], PBH merger rates as deduced by LIGO-VIRGO collaboration [218] and from accretion signatures in CMB [219, 220]. In the remaining parts of this section, we therefore proceed to calculate the PBH fraction, $f_{\rm PBH}$, as a function of the curvature power spectrum parameters $(A_\zeta, k_\star, \Delta)$. To this point, we will first discuss the general formation of PBHs in the early universe. We then proceed to derive the PBH abundance using the Press-Schechter formalism. Finally, we will translate the existing bounds of Fig.5.2 into constraints on $(A_\zeta, k_\star, \Delta)$.

#### Primordial Black Hole Formation

Lets consider a spherically symmetric density perturbation $\delta$ in the early universe. Locally, the perturbed region is usually described via the metric [221]

$$ds^2 = -dt^2 + a(t)^2 e^{2\zeta(\hat{r})}\left(d\hat{r}^2 + \hat{r}^2 d\Omega^2\right), \tag{5.15}$$

where the radial coordinate $\hat{r}$ is related to the comoving radius as $r = \hat{r}e^{\zeta(\hat{r})}$, and to the physical radial coordinate as $R = a(t)\hat{r}e^{\zeta(\hat{r})}$[5]. Finally, $\zeta(\hat{r})$ represents the curvature perturbation.
In these coordinates, density perturbation $\delta(\hat{r})$ is related to the curvature as [222]

$$\begin{aligned}\delta(\hat{r},t) &= -\frac{4(1+\omega)}{5+3\omega}\left(\frac{1}{aH}\right)^2 e^{-5/2\zeta(\hat{r})}\nabla^2 e^{\zeta(\hat{r})/2}, \\ &= -\frac{4}{3}\Phi(t)\left(\frac{1}{aH}\right)^2 e^{-5/2\zeta(\hat{r})}\nabla^2 e^{\zeta(\hat{r})/2}.\end{aligned} \tag{5.16}$$

where in the last line we have defined the function $\Phi(t)$ that encodes the time dependence of the equation of state $\omega$ such that in radiation domination, $\Phi = 2/3$.

[5] In this section, capital letters will refer to physical coordinates, whereas $r$ and $\hat{r}$ will be respectively for comoving and comoving slicing gauge.

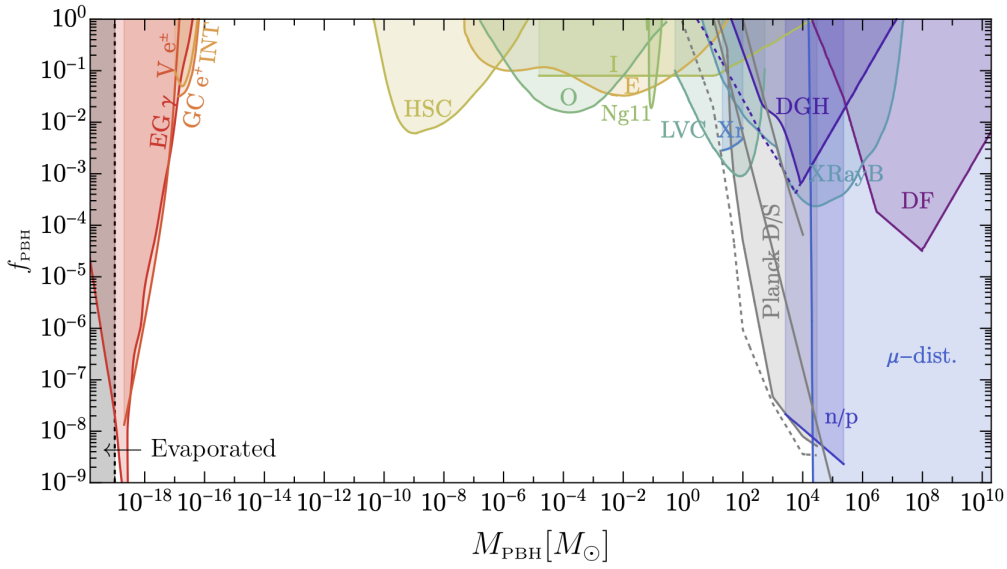


**Figure 5.2:** Observational constraints on the primordial black hole abundance $f_{\rm PBH}$. The curvature power spectrum able to fit NG12 and IPTA data would induce PBH in the mass range $M \sim 10^{-3} - 10^2 \mathrm{M}_\odot$. In such a range the strongest constraints are coming from microlensing [213, 214, 215, 216, 217], PBH merger rates as deduced by LIGO-VIRGO collaboration [218] and from accretion signatures in CMB [219, 220]. Figure taken from Ref.[202].

This perturbation is furthermore characterized by its physical radius $R_m$ and is assumed to be initially at super-horizon scales. At horizon crossing, if the volume averaged perturbation $\delta_m$ at that time exceeds the critical threshold $\delta_c$ (see below for discussion of its numerical value), gravity overcomes pressure forces and the perturbation collapses into a black hole [223, 221, 222]. The mass of the PBH has been found to be proportional to the horizon mass $M_H$ [224, 225],

$$M(\delta_m) = \kappa M_H(r_m)\,(\delta_m - \delta_c)^\gamma\,, \tag{5.17}$$

with the horizon mass at a given scale $k$ given by [204],

$$M_H(k) \equiv 4\pi \frac{M_p^2}{H} \simeq 20\ M_\odot \left(\frac{k}{10^6\ \mathrm{Mpc}^{-1}}\right)^{-2} \left[\frac{g_{*,s}^4(T_k) g_*^{-3}(T_k)}{17.25}\right]^{-1/6}, \tag{5.18}$$

in the previous expression, $\kappa \approx 4$ [223] and $\gamma \approx 0.36$ [225] are fixed parameters and $r_m$ the comoving radius of the perturbation. Note that the value of $\kappa$ is considered in some references to have slightly larger values $\kappa \approx 3 - 10$. We discuss in the next parts how this affects our results.
As we will see, the way to calculate the volume averaged density contrast $\delta_m$ is not unique and leads to important deviations in the PBH abundance between the different formalism. In particular, the volume averaged density contrast is usually calculated with the use of a window function, $W(R; R_m)$, smoothing over the perturbation scale [221]

$$\delta_m \equiv \int_0^\infty dR\, 4\pi R^2 \frac{\delta\rho}{\rho_b}(R, t_H) W(R; R_m), \tag{5.19}$$

where the radial integral is performed over the physical radial coordinate $R$. This last quantity is calculated at horizon crossing, characterized by the time $t_H$.
It might be hoped that different choices of window functions do not affect significantly the properties of the PBH population. But, as it will be checked, different choices bring instead drastic differences. For this reason, we will display our results for two different window functions: a real space top-hat (TH) $W_{\rm TH}$ and a Gaussian (G) window function $W_{\rm G}$. In Fourier space, they are respectively written

[226]

$$W_{\rm TH}(k,k') = 3\frac{\sin\left(k/k'\right) - k/k'\cos\left(k/k'\right)}{\left(k/k'\right)^3},$$
$$W_{\rm G}(k,k') = \exp\left(-\frac{\left(k/k'\right)^2}{4}\right), \tag{5.20}$$

where $k' = 1/r_m$, stands for the comoving scale of the perturbation.

What about the statistics of $\delta_m$? If it is known that small perturbations, i.e at linear order, are Gaussian, it must be expected that in the present case, $\delta_m$ is large in order to form PBHs and hence non-linear and non-Gaussian [223, 227, 228]. Nevertheless, $\delta_m$ can be expressed as a combination of a linear Gaussian component, $\delta_l$, that follows a Gaussian distribution $P(\delta_l) \sim \exp(-\delta_l^2/(2\sigma^2))$ (more details in the following section)[222, 229, 230].
To see this (see App.D.2 for further details), let's use the linearized Eq.(5.16) in order to solve Eq.(5.19). We get at linear order, using the top-hat window function,

$$\delta_m = -2\Phi \hat{r_m}\zeta'(\hat{r_m}) \equiv \delta_l, \tag{5.21}$$

where by definition, $\delta_l$ is a Gaussian variable.
Finally, using the full Eq.(5.16) the non-linear expression for $\delta_m$ is given in terms of $\delta_l$ as

$$\delta_m = \left(\delta_l - \frac{1}{4\Phi}\delta_l^2\right). \tag{5.22}$$

Hence, although $\delta_m$ is not longer described by a Gaussian distribution, it can be statistically characterized by $\delta_l$ which, on its side, is Gaussian distributed (see App.D.2).
With that, we find that the PBH mass formed from a perturbation characterized by the linear Gaussian component $\delta_l$ is given by

$$M(\delta_l) = \kappa M_H(r_m)\left(\delta_l - \frac{1}{4\Phi}\delta_l^2 - \delta_c\right)^\gamma. \tag{5.23}$$

The non-linear effects might therefore be seen as decreasing the production of PBH. Indeed, if at linear order perturbations with $\delta_l > \delta_c$ would collapse, we now have that a PBH would be formed only for perturbations with $\delta_l > 2\left(\Phi - \sqrt{\Phi^2 - \Phi\delta_c}\right)$.
If one uses the Gaussian window function to define the average density contrast instead, it has been shown in Ref.[221, 231] that it implies a change for the critical threshold $\delta_c$ and parameter $\kappa$,

$$(\delta_c)^{\rm TH} \approx 2.17 \times (\delta_c)^{\rm G},$$
$$(\kappa)^{\rm TH} \approx \frac{4}{2.74^2 \times 2.17^\gamma}(\kappa)^{\rm G}, \tag{5.24}$$

where "TH" stays for top-hat and "G" for modified Gaussian. We will see that even taking into those adapted parameters, the PBH abundance would appear to show important differences whether the Gaussian or the top-hat is used.
So what about the critical threshold $\delta_c$? Simple computation in Newton gravity allows to estimate that perturbations with density contrast greater than $\delta_c \approx 1/3$ [6] would be sufficient to cause the collapse [48]. Incorporating general relativity corrections allow to refine this last value and give $\delta_c \approx 0.4$ [233] (for top-hat window function). Recently, the collapse of large perturbations has been studied via numerical simulations. It has been found that the critical threshold is actually dependent on the shape of the curvature power spectrum and falls in the range $0.4 < \delta_c < 2/3$ [222, 234]. Finally, in Ref.[235], the results of the numerical simulations have been used to derive a simple prescription to relate the power spectrum shape and its associated critical threshold. In the left panel of

[6] This value is actually the speed of sound in a radiation fluid.

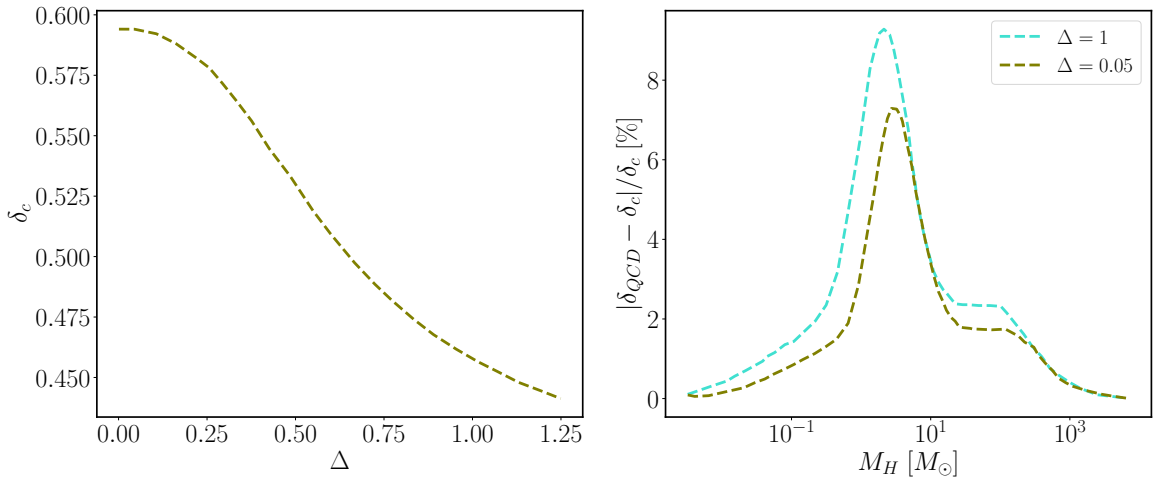


**Figure 5.3:** *Left*: Evolution of the critical threshold $\delta_c$ as a function of the lognormal spectrum width $\Delta$ (for a TH window function) (see Ref. [202]). *Right*: Variation of the critical threshold around QCD phase transition as a function of the horizon mass $M_H$ [232]. This figure corresponds to Fig.8 in Ref.[179].

Fig.5.3, we show the evolution of the critical threshold as a function of the width $\Delta$ of the lognormal curvature power spectrum defined in Eq.(5.1). The interpretation given in Ref.[235] is the following: as the spectrum gets broader, more modes are involved in the collapse. This essentially decreases the gradient pressure and facilitate the collapse by decreasing the critical threshold $\delta_c$. For $\Delta \approx 0 - 1$ we obtain $\delta_c \approx 0.6 - 0.4$.
Moreover, as already briefly mentioned, it is expected for the equation of state to be time dependent. In particular, during QCD phase transition, the change in the number of degrees of freedom introduces a decrease from the initial value of $w = 1/3$ during that period. This translates into a decrease of the pressure and thus favors the collapse. The natural consequence is a diminution of the critical threshold at that time. We show in the right panel of Fig.5.3 the numerical results from Ref.[232] (see also Ref.[236]) for the variation of the critical threshold as a function of the horizon mass[7] for both $\Delta = 0.05$ and $\Delta = 1$.
Finally, it is important to highlight here that the previous results have been derived using a top-hat window function. The threshold values used in line with a Gaussian window function are simply found by means of Eq.(5.24).

#### PBH Abundance from Press-Schechter Formalism

We now proceed to calculate the PBH abundance induced by the primordial curvature power spectrum via the Press-Schechter formalism [56].
In the previous part, we have stated that a perturbation with comoving size $r_m$ can collapse when reentering the horizon if the linear density contrast satisfies $\delta_l > 2\left(\Phi - \sqrt{\Phi^2 - \Phi\delta_c}\right)$. But what is the probability to have such large density contrast? Assuming Gaussian statistics for $\delta_l$, we get that the probability distribution for overdensities with comoving scale $k = 1/r_m$ at the time when this one reenters the horizon is given by

$$P_k(\delta_l) = \frac{1}{\sqrt{2\pi}\sigma_k} \exp\left(\frac{-\delta_l^2}{2\sigma_k^2}\right), \tag{5.25}$$

[7] The horizon mass could be easily translated into a temperature or comoving scale dependence.

where $\sigma_k$, the variance of the distribution, is directly related to the primordial curvature power spectrum via [204, 223, 221]

$$\begin{aligned}\sigma_k^2 &= \langle \delta_l^2 \rangle, \\ &= \int_0^\infty \frac{\mathrm{d}k'}{k'} W^2(k';k) P_\delta(k', t_H), \\ &= \frac{4}{9}\Phi^2 \int_0^\infty \frac{\mathrm{d}k'}{k'} (k'/k)^4 T^2(k', k) W^2(k';k) P_\zeta(k').\end{aligned} \tag{5.26}$$

In the last expression, $P_\delta(k', t_H)$ is the density power spectrum evaluated at the horizon-crossing time $t_H$ of the scale $k = 1/r_m$. Furthermore, $T(k', k)$ is the transfer function taking into account the damping of the modes at sub-horizon scales and in the last line, we have used the relation between the density power spectrum $P_\delta$ and the curvature power spectrum [221]. Note that the window function, $W(k', k)$, used to smooth the power spectrum over the scale of interest must be the same as the one used to derive the volume averaged overdensity in Eq.(5.19). Furthermore, from now on, the critical threshold and other parameters of the mass function Eq.(5.23) must be chosen in line with the window function used in Eq.(5.26) as well.
From this probability distribution, it is possible to calculate the fraction of the total energy density, $\beta_k(M)$, that collapses into a PBH of mass $M$ at a scale $k$ [48]

$$\beta_k(M) = \int_{\delta_c}^\infty \mathrm{d}\delta_l \, \frac{M(\delta_l)}{M_H(k)} P_k(\delta_l) \, \delta_D \left[ \ln \frac{M}{M(\delta_l)} \right]. \tag{5.27}$$

With that, the PBH abundance $\Omega_{\rm PBH} = \rho_{\rm PBH}/\rho_c$ today is nothing but the integral of the density fraction $\beta_k(M)$ over all the possible collapse scales $k$ and mass $M$. Furthermore, We must take into account the fact that during radiation domination, the PBH number density evolves as matter. It means that the number density of PBHs increases proportionally to the scale factor until matter-radiation equality and stays constant afterwards [237]. We then get,

$$\begin{aligned}\Omega_{\rm PBH} &= \int d\log(k)\, d\log(M) \beta_k(M) \left( \frac{M_{\rm eq}}{M_H(k)} \right)^{1/2}, \\ &= \int d\log(M)\, \psi(M),\end{aligned} \tag{5.28}$$

where the factor $(M_{\rm eq}/M_H(k))^{1/2}$ takes into account the increase of the density during radiation. In the last line we have introduced the function $\psi(M)$, such that the quantity $\psi(M)/(M\Omega_{\rm PBH})$ can be interpreted as the mass distribution.

In Fig.5.4, we show an explicit example of the PBH mass function extracted from the lognormal power spectrum defined in Eq.(5.1). In particular, we show results for a power spectrum peaked at $k_\star = 10^6\,\mathrm{Mpc}^{-1}$ and for both $\Delta = 0.05$ (cyan lines) and $\Delta = 1$ (olive lines). The amplitude $A_\zeta$ is chosen in order to have $f_{\rm PBH} = \Omega_{\rm PBH}/\Omega_{\rm DM} = 1$. For both choices of spectrum width, we computed the mass function using the top-hat window function (solid lines) and the Gaussian window function (dashed lines). It can be appreciated that, if the choice of the window function is followed by an appropriate choice of collapse parameters (see discussion of the previous section), the mass function is only barely affected by it. Finally, we obtain from the mass functions that the mean mass for $\Delta = 1(0.05)$ is $M \approx 60(100)\, M_\odot$. It is interesting to note that, despite the usual naive estimation of the mean PBH mass being given by the horizon mass at the scale $k_\star$ ($M_H(k_\star = 10^6\,\mathrm{Mpc}^{-1}) \approx 20\,\mathrm{M}_\odot$), we obtain here larger mean masses. This behavior has already been observed in recent works, see for instance Refs.[226, 238], and could be explained by the fact that $\sigma_k$ is actually peaked at smaller values of $k$. It means that for a curvature power spectrum peaked at a scale $k_\star$, the typical fluctuations would have a larger characteristic scale and then naturally produce heavier PHBs since they collapse at times when the horizon mass is larger as well.

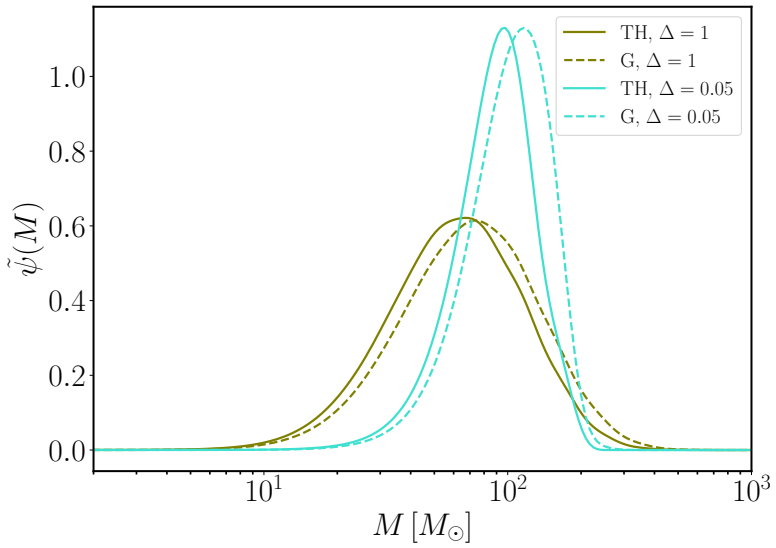


**Figure 5.4:** PBH mass function $\tilde{\psi}(M) = \psi(M)/\Omega_{\rm PBH}$ for a log-normal curvature power spectrum peaked at $k_\star = 10^6$ Mpc$^{-1}$ ($M_H \approx 20 M_\odot$) (note that the amplitude has negligible impact on the normalized mass function). Note that the mean mass is shifted to higher values for decreasing spectrum width [226] (the turquoise and olive lines are respectively for $\Delta = 0.05$ and $\Delta = 1$). Moreover, unlike the PBH abundance, for consistent choice of thresholds and window functions, the mass distribution looks similar for both the TH and G window function. This figure corresponds to Fig.7 in Ref.[179].

Let's conclude this part by discussing the sensitivity of the PBH abundance on the different parameters. From the probability distribution introduced at the beginning of this section in Eq.(5.25), we note that PBHs are actually produced from the tail of the distribution. Hence even a small change in the critical threshold induces exponential effects on the PBH abundance [204]. For the same reason, $f_{\rm PBH}$ is exponentially sensitive to modifications on the variance $\sigma_k$. Such change is for instance induced when changing the window function. We found that even when adapting the critical threshold $\delta_c$ to the choice of window function (see Eq.(5.24)), the PBH abundance still depends drastically on which window function is used. For this reason, we will display our results using both the Gaussian and the top-hat window function. The variance $\sigma_k$ is also affected by the curvature power spectrum itself. Hence, we observe that $f_{\rm PBH}$ is exponentially sensitive to the amplitude $A_\zeta$. In line with that, it is expected that different power spectrum shapes lead to different PBH abundance as well.

#### From PBH Abundance to Constraints on Curvature Power Spectrum

As already mentioned, the PBH abundance $f_{\rm PBH}$ is relatively strongly constrained (see Fig.5.2). From the last section, it implies that for some range of the lognormal curvature power spectrum parameters $(A_\zeta, \Delta, k_\star)$ the induced PBH abundance might spoil existing constraints. Hence, since the purpose of the next section will be to identify the range of parameters $(A_\zeta, \Delta, k_\star)$ able to produce the GW signal potentially identified in PTA experiments, it is important to first clearly determine the parameter space which is in agreement with the PBH constraints. Explicitly, we proceed now to translate the constraints $f_{\rm PBH}(M_{\rm PBH})$ of Fig.5.2 into constraints on the power spectrum amplitude as a function of the peak location, $A_\zeta^{\rm max}(k_\star)$, for a fixed width $\Delta$.
The usual way to achieve this task is to find for a given point $f_{\rm PBH}(M_{\rm PBH})$, the pair $(A_\zeta^{\rm max}, k_\star)$ for

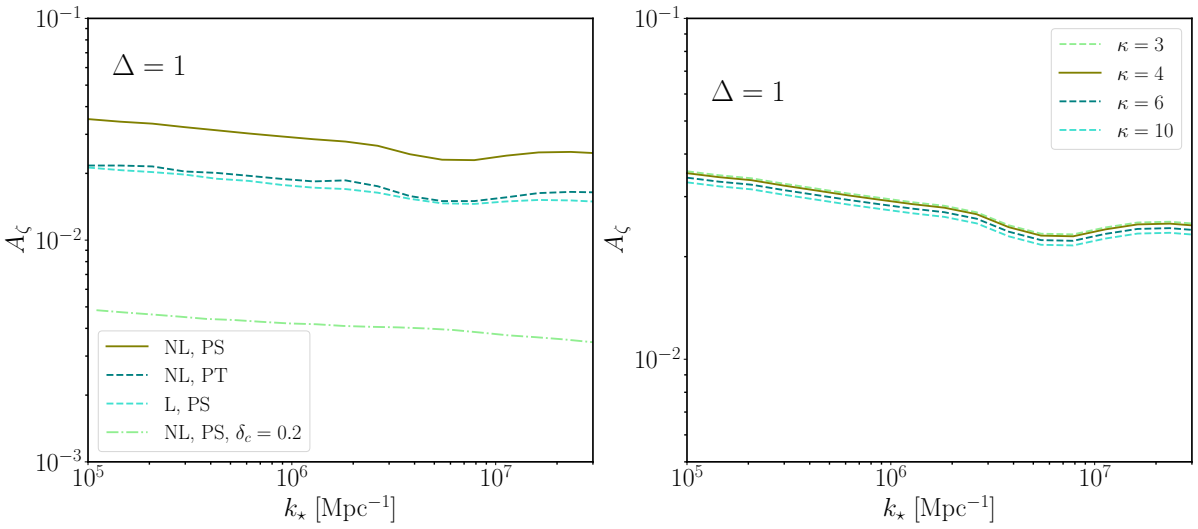


**Figure 5.5:** Limit $f_{\rm PBH} = 1$ translated into constraints on $A_\zeta(k_\star)$ for $\Delta = 1$. *Left*: Effect on the limit $f_{\rm PBH} = 1$ considering the Press-Schecter formalism (PS) with the non-linear (NL) and linear (L) relation for the density. Results using Peak Theory (PT) and with a lower threshold ($\delta_c = 0.2$) are also shown. *Right*: Similar but changing this time only the parameter $\kappa$ . Both are calculated for a lognormal power spectrum with top-hat window function. This figure corresponds to Fig.9 in Ref.[179].

which,

$$\begin{aligned} \frac{1}{\Omega_{\rm DM}} \int d\log(M)\, \psi(M; A_\zeta^{\rm max}, k_\star, \Delta) = f_{\rm PBH}, \\ \frac{1}{\Omega_{\rm PBH}} \int dM\, \psi(M; A_\zeta^{\rm max}, k_\star, \Delta) = M_{\rm PBH}, \end{aligned} \tag{5.29}$$

for a fixed value of the width $\Delta$.
Unfortunately, using this method does not incorporate the extended mass distribution of the PBHs produced via the curvature power spectrum since it only takes into account the mean mass. Hence, we instead follow the recent work of Ref.[239] which allows to find the value of $A_\zeta^{\rm max}$ as function of $k_\star$ (still for fixed $\Delta$) solving the function

$$\frac{1}{\Omega_{\rm DM}} \int d\log(M)\, \frac{\psi(M; A_\zeta^{\rm max}, k_\star, \Delta)}{f_{\rm PBH}(M)} \leq 1. \tag{5.30}$$

As it should, this integral imposes that the extended PBH mass distribution produced by the power spectral density does not spoil the constraints defined by $f_{\rm PBH}(M)$. Of course, the absolute limit $f_{\rm PBH} = 1$ can be simply obtained by setting the denominator to 1 in the last equation.
In Fig.5.5 we show the limits from $f_{\rm PHB} = 1$ translated on the amplitude $A_\zeta$ as a function of the peak location $k_\star$ for the width $\Delta = 1$. Note that the range of $k_\star$ has been chosen in order for the produced GWs to fall in the frequency range of NG12 and IPTA (see Sec.5.2). All the lines have been calculated using a top-hat window function. In the left panel, we show explicitly how our results change depending on the PBH formation mechanism used to calculate the abundance. As it can be observed, the Press-Schechter formalism combined with the appropriate threshold (see above discussion) and taking into account the non-linear relation for the volume average density (see Eq.(5.19)), leads to the weakest constraints on the amplitude (olive solid line). The dark dashed blue line and the light dashed green line show respectively how the limits are affected depending on whether the Peak Theory [240] is used instead of the Press-Schechter or if we do choose a much lower threshold $\delta = 0.2$. Finally, the cyan dashed line shows the limits when the non-linear relation for the volume averaged density contrast is not considered. As expected, considering only the linear relation increase the production of PBHs and naturally leads to stronger constraints. It can be

appreciated that in each case (expected for the line with $\delta_c = 0.2$), the limits are not straight lines but show instead a dip around $k_\star = 10^6 - 10^7 \mathrm{Mpc}^{-1}$. This corresponds to curvature power spectra where the typical fluctuations reenter the horizon during QCD phase transition. Hence, the critical threshold is decreased with respect to its initial value. This effect favors the production of PBHs and then leads to stronger constraints on the amplitude.
On the right panel, we show how the olive line from the left one changes as the parameter $\kappa$ in Eq.(5.23) deviated from $\kappa = 4$ (used in the left plot). As briefly mentioned earlier, this parameter is estimated from numerical simulations to fall in the range $\kappa \approx 3 - 10$ (even if most of the literature uses $\kappa = 4$). We see, however, that changing $\kappa$ has a minor impact on the limit $f_{\rm PBH} = 1$.

## 5.2 Curvature Power Spectrum Probed by Pulsar Timing Arrays Data

In this section, we interpret the NG12 and IPTA excess as coming from scalar induced GWs. To this point, we perform a Bayesian search over their data and study the posterior distributions for the parameters $(A_\zeta, k_\star, \Delta)$. Secondly, we interpret the parameter space able to explain the signal in terms of PBHs, following the calculation of Sec.5.1. Interestingly, we come to the conclusion that the evidence region of the IPTA experiment might lead to an overproduction of black holes.
Before going into the Bayesian analysis, we first discuss the pulsar timing arrays and the way they recorded their data. We also derive the usual likelihood function used in the further Bayesian analysis.

### 5.2.1 Pulsar Timing Arrays

Pulsar timing arrays use the high regularity of the millisecond pulsars to detect any kind of phenomena able to alter the predictable period of those pulsars [241]. In practice, the observatory records the periodic electromagnetic pulses emitted by the pulsar, which are usually named times of arrivals (TOAs). In an ideal scenario, mathematical models are constructed to accurately predict the future TOAs of the pulses. Those models carefully take into account all the known delays induced for instance by the mass distribution in the solar system or the interstellar medium [241]. The timing models are usually optimised to find the best fitting solution but still remains some deviations between the observed and predicted TOAs. Those deviations are collected in a time residual array $\delta \boldsymbol{t}_{\rm mod}$ expressed as

$$\delta \boldsymbol{t}_{\rm mod} = \boldsymbol{M}\boldsymbol{\epsilon}, \tag{5.31}$$

with $\boldsymbol{M}$ and $\boldsymbol{\epsilon}$ respectively the timing model design matrix and the vector encoding the deviation between the model and the observation.
In addition to the error on the TOA modeling, many astrophysical mechanisms, such as spin noise or pulse profile changes, can induce a time-correlated stochastic red noise in the time residuals [242, 243, 244]. In the usual situation where an array of pulsars is observed, those red noises sources show up as unique sources for each pulsars. The usual way to parameterize the residuals for time-correlated red noise is via a decomposition on Fourier modes [245]

$$\begin{aligned} \delta \boldsymbol{t}_{\rm RN} &= \sum_{j=1}^{N_{\rm modes}} \left[ a_j \sin\left(\frac{2\pi j t}{T}\right) + b_j \sin\left(\frac{2\pi j t}{T}\right) \right], \\ &= \boldsymbol{F}\boldsymbol{a} \end{aligned} \tag{5.32}$$

with $T$ the total observation time and $N_{\rm modes}$ the number of modes [8]. We also introduced the Fourier design matrix $\boldsymbol{F}$ which contains alternate sine and cosine functions for each modes and $\boldsymbol{a}$ the mode coefficients. The statistics of the red noise is characterized by its covariance matrix,

$$\langle \boldsymbol{a}_i \boldsymbol{a}_j \rangle = P(f_i)\delta_{ij}, \tag{5.33}$$

[8] This last one will be discussed more in detail later in this section.

In practice, the power spectrum $P(f)$ is taken according to a power law model with two distinct parameters $(A_{\rm RN}, \gamma_{\rm RN})$ for each pulsar [191],

$$P(f) = \frac{A_{\rm RN}^2}{12\pi^2}\left(\frac{f}{f_{\rm yr}}\right)^{-\gamma_{\rm RN}} f_{\rm yr}^{-3}. \tag{5.34}$$

Finally, three white noise sources are usually considered in pulsar timing arrays. They take into account a scale parameter on the TOA uncertainties (EFAC), an additional variance (EQUAD) and a per-epoch variance (ECORR) for each backend. Their time residuals are characterized by the covariance matrix $\boldsymbol{C}_{\rm WN}$ that can be found in Ref.[246].
Hence, so far, the time residuals captured by PTAs are modeled by time model errors and random Gaussian intrinsic red noise and intrinsic white noise,

$$\delta\boldsymbol{t} = \delta\boldsymbol{t}_{\rm mod} + \delta\boldsymbol{t}_{\rm RN} + \delta\boldsymbol{t}_{\rm WN}. \tag{5.35}$$

Nevertheless, it is expected that in the presence of a SGWB, an additional time delay is induced in the TOAs [247, 248]. Unlike the previously considered cases for which the noise sources were intrinsic to each pulsar, a SGWB would induce a common red noise to all pulsars. In addition, for an isotropic GW background it is expected for this red noise to observe a specific correlation between pulsars, this correlation is called "Hellings-Downs" (HD) [203] or quadrupolar correlation. The time delay induced by the SGWB, $\delta\boldsymbol{t}_{\rm gw}$, can be written similarly to the previous intrinsic red noise, as decomposition on Fourier modes. The cross-power spectral density $S_{ab}(f)$, characterizing the process, is expressed in terms of the GW spectrum $\Omega_{\rm gw}(f)$ [249],

$$S_{ab}(f) = \Gamma_{ab}(f)\frac{H_0^2}{16\pi^4 f^5}\Omega_{\rm gw}(f). \tag{5.36}$$

In this last equation, $\Gamma_{ab}(f)$ are the HD coefficients encoding the correlation between the pulsar $a$ and $b$. If no cross-correlation is observed, this equation simply reduces to common red noise and $\Gamma_{ab}(f) = \delta_{ab}$.
The total time delay in the presence of a SGWB is then given by

$$\begin{aligned}\delta\boldsymbol{t} &= \delta\boldsymbol{t}_{\rm mod} + \delta\boldsymbol{t}_{\rm RN} + \delta\boldsymbol{t}_{\rm WN} + \delta\boldsymbol{t}_{\rm gw},\\ &= \delta\boldsymbol{t}_{\rm mod} + \delta\boldsymbol{t}_{\rm Gauss}\end{aligned} \tag{5.37}$$

where in the last line $\boldsymbol{t}_{\rm Gauss}$ contains all the Gaussian process.
With that, the usual way to analyze the PTA data, is done via the likelihood [250]

$$\mathcal{L} = \frac{1}{\sqrt{\det\left(2\pi\boldsymbol{\Sigma}\right)}}\exp\left(-\frac{1}{2}\boldsymbol{R}^T\boldsymbol{\Sigma}^{-1}\boldsymbol{R}\right), \tag{5.38}$$

where we define $\boldsymbol{R} \equiv \left[\delta\boldsymbol{t}^1_{\rm Gauss}, \delta\boldsymbol{t}^2_{\rm Gauss}..., \delta\boldsymbol{t}^N_{\rm Gauss}\right]$ with $N$ the number of pulsars in the array, and $\boldsymbol{\Sigma} \equiv \langle\boldsymbol{R}\boldsymbol{R}^T\rangle$ the covariance matrix. Note that this likelihood is usually marginalized over the model parameter $\boldsymbol{\epsilon}$ [245, 251].

In their last data released, both NG12 and IPTA [36, 252], have claimed strong evidence for a common process in their sensitivity frequency range, $f = 1 - 10\,{\rm nHz}$. Even if no evidence for HD cross-correlation has been found, numerous number of studies have been done interpreting this signal as a SGWB detection. In particular, it is expected for SMBHBs to produce a SGWB at those frequencies [39, 40]. In that case, the cross power spectral density defined in Eq.(5.40) is modeled as a power law similar to the one used in Eq.(5.34) [191],

$$S_{ab}^{\rm SMBHB}(f) = \Gamma_{ab}(f)\frac{A_{\rm SMBHB}^2}{12\pi^2}\left(\frac{f}{f_{\rm yr}}\right)^{-\gamma_{\rm SMBHB}} f_{\rm yr}^{-3}, \tag{5.39}$$

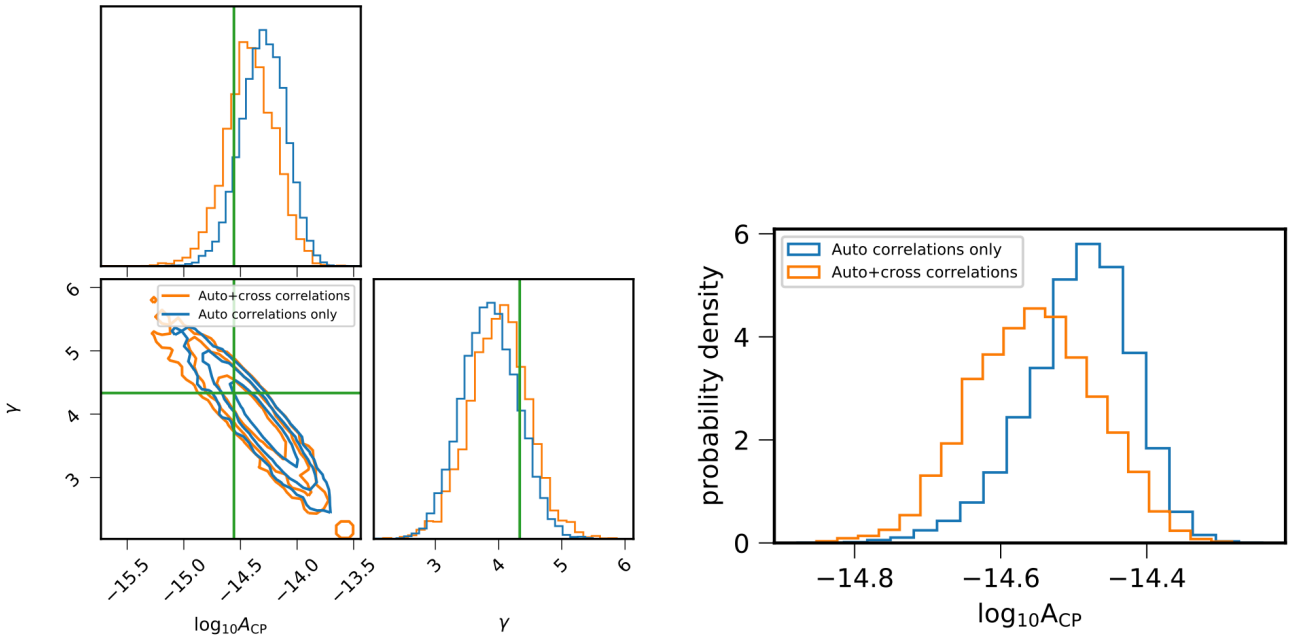


**Figure 5.6:** *Left*: Posterior distribution from Ref.[35] for the SMBHB parameters $(A_{\rm SMBHB}, \gamma_{\rm SMBHB})$. The green line shows the location predicted by theoretical model [256]. *Right:* Probability distribution of $A_{\rm SMBHB}$ with $\gamma_{\rm SMBHB}$ fixed to its expected theoretical value $\gamma = 13/3$. In both panels, the orange and blue lines show the difference when the cross HD correlation is added to the analysis. This figure is taken from Ref.[35].

with this time the same parameters $(A_{\rm SMBHB}, \gamma_{\rm SMBHB})$ for all pulsars since it is a common process. In Refs.[191, 35], a Bayesian search has been performed implementing such SGWB from SMBHBs. In particular, the likelihood defined in Eq.(5.38) has been evaluated using the public codes `enterprise`, `enterprise_extensions` [253] and PTMCMC [254] to obtain Monte Carlo samples. The white noise sources were fixed according to their maximum likelihood a posteriori values from single pulsar analyses without GW parameters such that we are left with two red noise parameters per pulsar $(A_{\rm red}, \gamma_{\rm red})$ and a pair of GW parameters from Eq.(5.39) $(A_{\rm SMBHB}, \gamma_{\rm SMBHB})$ for the whole set of pulsars. Finally, the posterior distributions for those parameters are obtained with `GetDist` [255]. Note that in Refs.[191, 35] this analysis has been performed with and without HD correlations, meaning considering or not the function $\Gamma_{ab}$ in Eq.(5.39). The posterior distributions obtained in Ref.[35] are shown in Fig.5.6 for the parameters $A_{\rm SMBHB}$ and $\gamma_{\rm SMBHB}$. It can be appreciated that the theoretical values predicted by Ref.[256] (green lines in the left panel) are falling in the $3\sigma$ C.L. region. Note that the posterior distributions are not depending strongly on whether the HD correlation is added in the analysis. It implies that there is for the moment no evidence in favor nor against HD correlations.
With those results, the SMBHB interpretation of the NG12 and IPTA potential signal seems to be an attractive solution. If the signal gets confirmed by the future experiments and data, it is, however, crucial to understand if other interpretations could be given. In particular, we are now going to use the gravitational spectrum derived in Sec.5.1 for large curvature fluctuations to see if, for some parameters $(A_\zeta, k_\star, \Delta)$ of the curvature power spectrum (5.1), it may have contributed to the NG12 and IPTA signal.

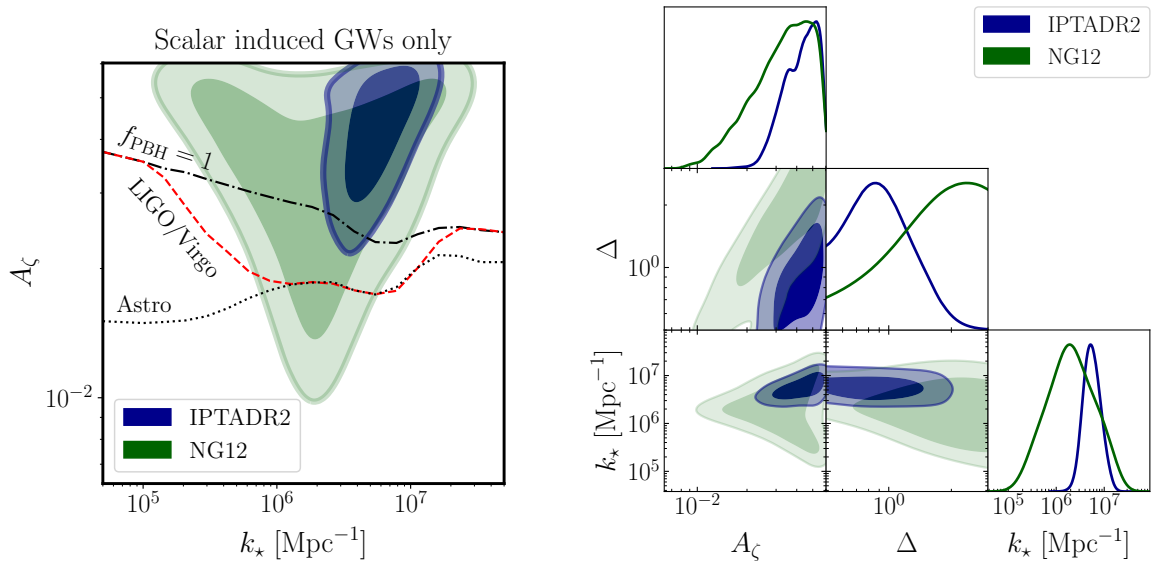


**Figure 5.7:** *Left*: One-dimensional posterior distribution for the amplitude $A_\zeta$ and momentum $k_\star$ (marginalized over the width $\Delta$). The prior for $A_\zeta$ has been chosen to avoid PBH overproduction: $\log_{10} A_\zeta \leq -1.22$, see text for details. The dark (light) shaded regions show 68% and 95% C.L. regions respectively. We, additionally, show for $\Delta = 1$ the astrophysical constraints on PBH overproduction as the gray dotted line. The region above the dashed red curve is constrained by LIGO/Virgo for $\Delta = 1$, see [218]. All the constraints in the plot are obtained using a top-hat window function. They would be stronger (weaker) for smaller (larger) $\Delta$. *Right*: Two-dimensional posterior distributions. This figure corresponds to Fig.3 in Ref.[179].

### 5.2.2 Bayesian Search in the IPTA data released 2 and NANOgrav 12.5 years

#### Detection Analysis

Similarly to the analysis done in the case of SMBHB, we proceed now to a Bayesian search in the NG12 and IPTA data including GWs from large curvature fluctuations. We remind that for common processes the cross-power spectral density is described via

$$S_{ab}(f) = \Gamma_{ab}(f) \frac{H_0^2}{16\pi^4 f^5} \Omega_{\rm gw}(f), \tag{5.40}$$

where here the GW spectrum $\Omega_{\rm gw}(f)$ is taken from Eq.(5.12) in line with the analytical approximations Eq.(5.13)-(5.14). Note that we properly account for the temperature dependence of the number of relativistic degrees of freedom $g_*$, using results of Ref.[59], since the frequency range of NG12 and IPTA would correspond to $k_\star$ values around the QCD scales where $g_*$ changes significantly.

Exactly as for the SMBHB analysis done in Ref.[35, 191], we consider three white noise sources with parameters fixed according to their maximum likelihood for a single pulsar analysis. In addition, the intrinsic red noises are parameterized by the correlation function defined in Eq.(5.34) and the parameters $(A_{\rm RN}, \gamma_{\rm RN})$, proper to each pulsar and free during the Bayesian search. Finally, we have the three parameters of the GW spectrum, $(A_\zeta, k_\star, \Delta)$.
As mentioned in the previous section, it is expected for sizable productions of GWs to induce a significant population of PBHs. For this reason, the priors for the amplitude $A_\zeta$ must be chosen in way to assure that the resulting PBH population is not spoiling any existing constraints. Hence, we choose logarithmic priors $\log_{10}\Delta \in [\log_{10}(0.5), \log_{10} 3], \log_{10} A_\zeta \in [-3, -1.22], \log_{10} k_\star/{\rm Mpc}^{-1} \in [4, 9]$ such that the upper limit on the curvature power spectrum amplitude is dictated by the $f_{\rm PBH} \leq 1$ constraint for $\Delta = 3$ and $k_\star = 10^5$ Mpc$^{-1}$ (for top-hat window function). This is indeed a conservative prior choice since the constraint for PBH overproduction on the amplitude $A_\zeta$ gets stronger

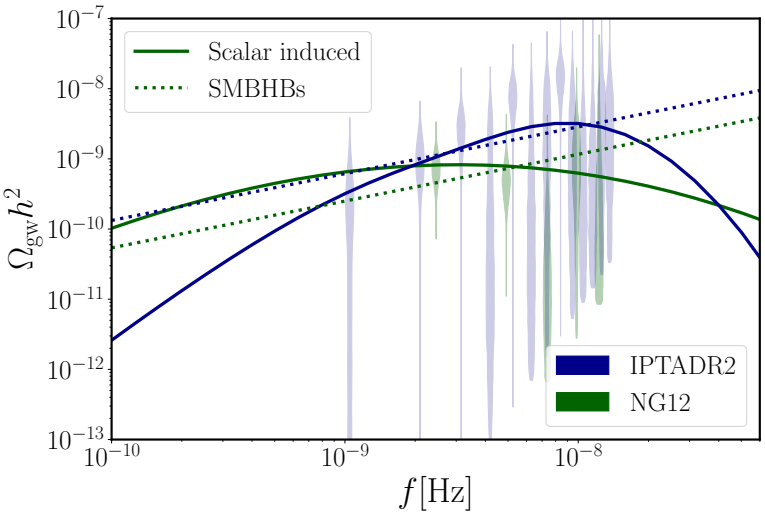


**Figure 5.8:** GW spectra obtained after maximizing the likelihood. We compare the scalar induced GW spectrum, according to our "Scalar induced GW only" search (solid curves), obtained with the parameters $A_\zeta \simeq 0.04\ (0.04), k_\star \simeq 5.5\ (2.2) \cdot 10^6\ \mathrm{Mpc}^{-1}, \Delta \simeq 0.9\ (2.1)$ for IPTA DR2 (NG12) to the GW spectrum obtained from SMBHBs (dotted lines), setting $A_{\rm SMBHBs} \simeq 3\ (2) \cdot 10^{-15}$ for IPTA DR2 (NG12).The free spectrum posteriors obtained by converting the results of [191] (NG12) and [35] (IPTA DR2) are also shown (violin shapes, lower limits due to prior choices). This figure corresponds to Fig.4 in Ref.[179].

as the width $\Delta$ decreases. Moreover, even stronger constraints would be obtained if instead of imposing $f_{\rm PBH} \leq 1$, we would translate the astrophysical constraints (see Fig.5.2) on the amplitude $A_\zeta$ with the use of Eq.(5.30). The different sources of noise as well as all the parameters and their priors are summarized in App.E.1.

In the right panel of Fig.5.7, we show the posterior distributions for the curvature power spectrum parameters $(A_\zeta, k_\star, \Delta)$ for both the IPTA (dark-blue contours) and NG12 (green contours) data including HD correlation. It can be appreciated that, as expected, both NG12 and IPTA are indicating a curvature power spectrum with $k_\star \sim 10^5 - 10^7 \mathrm{Mpc}^{-1}$. This indeed corresponds to a GW spectrum peaked in the frequency range of the PTA experiments. We note that NG12 data accommodates with the whole range of widths $\Delta$, even if it prefers larger values. This was expected since the GW spectrum observed in NG12 is essentially flat and then well fitted by a broad $\Delta \geq 1$ power spectrum. On the other hand, IPTA tends to prefer smaller width $\Delta \leq 1$. As mentioned, since for smaller values of $\Delta$ the $f_{\rm PBH} \leq 1$ constraint on the amplitude $A_\zeta$ gets stronger, it is important to investigate whether the IPTA evidence region is spoiling it. Hence, in the left panel of Fig.5.7, we show the $2\sigma$ C.L. region for the parameters $A_\zeta$ and $k_\star$ with the $f_{\rm PBH} \leq 1$ constraint for $\Delta = 1$ shown explicitly (dashed-dotted line). It can be concluded that most of the IPTA evidence region is excluded by PBH overproduction. Moreover, since most of the IPTA posteriors sit in the $\Delta \leq 1$ region and because lower values of $\Delta$ lead to even stronger constraints on $A_\zeta$, we conclude that the large curvature GW interpretation of the IPTA signal is strongly affected by PBH overproduction constraints. On the same panel is also shown the astrophysical PBH constraints translated on the amplitude $A_\zeta$ for $\Delta = 1$ (black dotted lines). The red dashed line represents in particular the limits coming from LIGO/Virgo BH merger rates [218]. Of course, considering those limits further reinforces our previous assertion.

In Fig.5.8 we show the maximum likelihood GW spectra from both large curvature fluctuations (solid lines) and SMBHBs (dotted lines) together with the free spectrum obtained from IPTA (blue violins) and NG12 (green violins). As already concluded from Fig.5.7, IPTA data are better fitted by smaller width and larger amplitude than those of NG12. Interestingly, we see from Fig.5.8 that the IPTA (NG12) excess is fitted by the small (high) frequency tail of the spectrum.

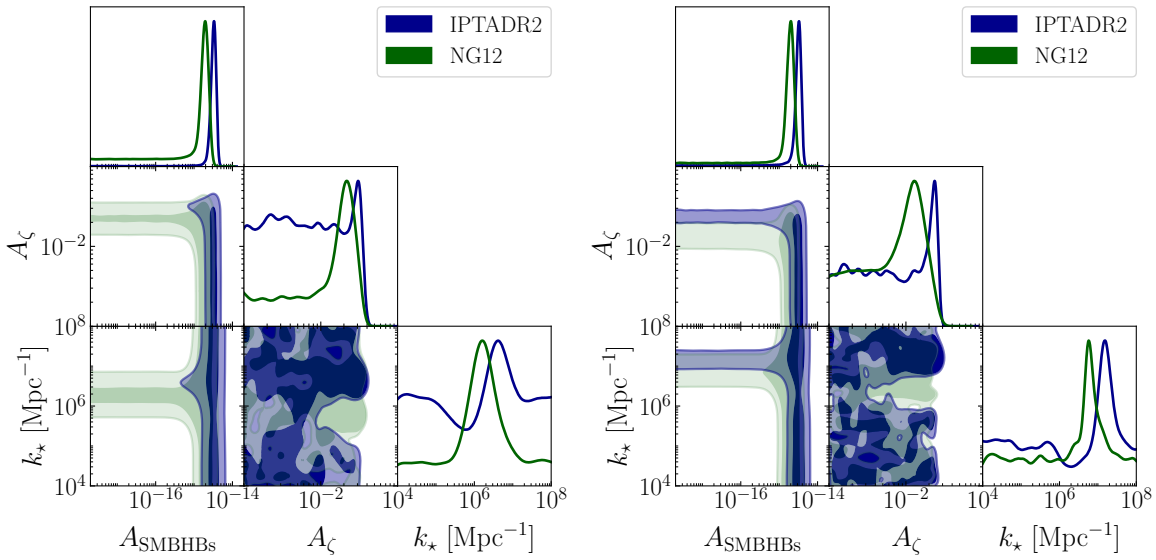


**Figure 5.9:** One- and two-dimensional posterior distributions of our analysis including a SGWB from both SIGW and SMBHB. As before, the upper prior on $A_\zeta$ is chosen to avoid PBH overproduction. The dark (light) shaded regions show 68% and 95% C.L. regions respectively. *Left*: $\Delta = 1$, with upper prior $\log_{10} A_\zeta \leq -1.44$. *Right*: $\Delta = 0.05$, with upper prior $\log_{10} A_\zeta \leq -1.57$. This figure corresponds to Fig.5 in Ref.[179].

At the end of this first analysis, it is possible to conclude that both SMBHBs and scalar induced GWs are able to generate the excess observed in PTA experiments, although the latter might be in conflicts with PBH overproduction. In order to capture which model is the most favored by the data, we continue our analysis by considering both sources of GWs in the likelihood defined in Eq.(5.38). The stochastic GW background would then be characterized by four parameters: three coming from the scalar induced GWs, $(A_\zeta, k_\star, \Delta)$, and one coming from the SMBHB $A_{\rm SMBHB}$ if we assume that the power $\gamma_{\rm SMBHB}$ is fixed to $13/3$ according to the Ref.[40]. In this analysis we do not include the HD correlation since including them do not alter the posteriors strongly but reduces the computational time considerably. Since the PBH overproduction limit depends strongly on the width $\Delta$, we chose to perform the Bayesian search for two specific choices, $\Delta = 1$ and $\Delta = 0.05$. For the priors, we proceed as for the previous analysis and impose that $\log_{10}(A_\zeta) \leq -1.44(-1.57)$ for $\Delta = 1(0.05)$. Those values correspond to the limit $f_{\rm PBH} \leq 1$ at $k_\star = 10^5 {\rm Mpc}^{-1}$ and then to the weakest limit in the scale range of interests (the $f_{\rm PBH} \leq 1$ limit decreases as $k_\star$ increases as it might be seen in Fig.5.5). We finally impose logarithmic priors on the remaining parameters: $4 \leq \log_{10}(k_\star/{\rm Mpc}^{-1}) \leq 9$, $-18 \leq \log_{10}(A_{\rm SMBHBs}) \leq -13$.

The posterior distributions are shown in Fig.5.9 for both $\Delta = 0.05$ (left panel) and $\Delta = 1$ (right panel). We start by considering the results for NG12 (green curves). In both panels, we see that the posteriors $(A_\zeta, A_{\rm SMBHB})$ cover two distinct regions. The first one is centered around $A_{\rm SMBHB} \approx 10^{-15}$ and spans all the values up to $A_\zeta \leq 10^{-2}$. This region has to be understood as the range of parameters for which the NG12 excess is modeled by the SMBHB GWs only. On the other hand, the second region is centered around $A_\zeta \approx 0.02(0.015)$ for $\Delta = 1(0.05)$ and covers the whole range up to $A_{\rm SMBHB} \leq 10^{-14}$. In that region, the signal can be modeled only by the scalar induced GWs. Naively, in the intersection region, the excess is well modeled by a combination of both sources. Similar behavior is observed in the posteriors $(k_\star, A_{\rm SMBHB})$: for the region centered around $A_{\rm SMBHB} \approx 10^{-15}$, $k_\star$ is outside of the PTA range such that there is no contribution in the signal from scalar induced GWs.

For IPTA (blue curves), the situation is significantly different. As already mentioned, IPTA data require a larger amplitude $A_\zeta$, making it challenging to not spoil the PBH overproduction constraint. In the posteriors $(A_\zeta, A_{\rm SMBHB})$ of the left panel ($\Delta = 1$) we see that only the region centered around $A_{\rm SMBHB} \approx 10^{-15}$ is modeling at $2\sigma$ the IPTA excess correctly . Scalar induced GWs are here not

| Bayes Factors | | |
|---|---|---|
| **Experiments** | $\boldsymbol{\Delta = 0.05}$ | $\boldsymbol{\Delta = 1}$ |
| NG12 | $\log_{10}(B_{\zeta,\mathrm{SMBHB}}) = 0.05$ | $\log_{10}(B_{\zeta,\mathrm{SMBHB}}) = 0.3$ |
| IPTA | $\log_{10}(B_{\zeta,\mathrm{SMBHB}}) = 0.9$ | $\log_{10}(B_{\zeta,\mathrm{SMBHB}}) = 2.2$ |

**Table 5.1:** Bayes Factors computed assuming that the PTA excess is either only scalar induced GW or only SMBHB.

able to explain the signal because of the prior choice and hence PBH overproduction. For $\Delta = 0.05$, similar trends exist even if the scalar induced region is disfavored only at $1\sigma$.
Even if this last analysis gives a first insight on which model provides the best explanation for the PTA excess, the best way to determine any preference for one model or the other is to calculate the Bayes factors assuming the stochastic GW background to be either purely scalar induced or coming from SMBHBs. From Tab.5.1, we see that, as expected from the previous analysis, IPTA tends to prefer a scenario where the excess is caused by SMBHB GWs. This is particularly clear in the case $\Delta = 1$, where the Bayes factor is given by $\log_{10}(B_{\zeta,\mathrm{SMBHB}}) = 2.2$. For NG12, we find no substantial evidence for one model against the other as already concluded in Fig.5.9.

The conclusion of this whole analysis is therefore that the scalar induced GW interpretation of the IPTA excess is disfavored compared to the SMBHB one, and this because of the strong constraints coming from PBH overproduction. NG12 is on its side fitted equally well by both models. It is, however, important to keep in mind that only the constraint $f_{\mathrm{PBH}} \leq 1$ has been used. Using the astrophysical constraints (see Fig.5.2) would have a stronger impact on the possible parameter space for the amplitude $A_\zeta$ and eventually disfavor even more the scalar induced GW interpretation. Those conclusions therefore motivate to look for upper limits on the amplitude $A_\zeta$ instead of evidence regions.

#### Upper Limit Analysis

Supported by the previous conclusions, we assume here that the signal is not coming for scalar induced GWs and thus proceed to derive upper limits on the amplitude of the curvature power spectrum $A_\zeta$.
We follow the following strategy to derive upper limits on the amplitude $A_\zeta$ : We first fix the parameter $A_{\mathrm{SMBHB}}$ inferred from the SMBHB analysis only of the NG12 and IPTA collaborations. For each value of the $k_\star$ in the range considered above, we derive the upper limit on the parameter $A_\zeta$. The width $\Delta$ is kept fixed for this analysis. Note that the SMBHB parameter $A_{\mathrm{SMBHB}}$ is given within a $2\sigma$ interval: $\log_{10}(A_{\mathrm{SMBHBs}}) \in [-14.86, -14.57]$ for NG12 [191] and $\log_{10}(A_{\mathrm{SMBHBs}}) \in [-14.7, -14.4]$ for IPTA [35]. For this reason, we derived our upper limits taking both the lower and upper bounds of those intervals. In order to derive upper limits, note that we do not impose any prior for the amplitude $A_\zeta$ (see App.E.2 for the explicit list of parameters in the case of the upper limit search).
In Fig.5.10, we show such upper limits for both $\Delta = 0.05$ (right panel) and $\Delta = 1$ (left panel). Two main features are clearly visible. First, the constraints are stronger for $\Delta = 0.05$. This was indeed expected since, for the same amplitude, the GW spectrum presents a larger peak for a narrower spectrum. Secondly, the upper limits are broader for $\Delta = 1$. This can be understood as a consequence of the exponential decay for frequencies larger than $f_\star$ (see Fig.5.1). In the case of the narrow spectrum, $\Delta = 0.05$, if the spectrum peak $f_\star$ is displaced at a smaller frequency than the first data bin, the exponential decay would prevent any signal in the frequency range of the experiment. For this reason we do not have any upper limit in the low frequencies. Naturally, for the broader spectrum, $\Delta = 1$, even if the spectrum peak is displaced at smaller frequencies than the first bin, the exponential decay is less important and a signal can be obtained, therefore leading to constraints in

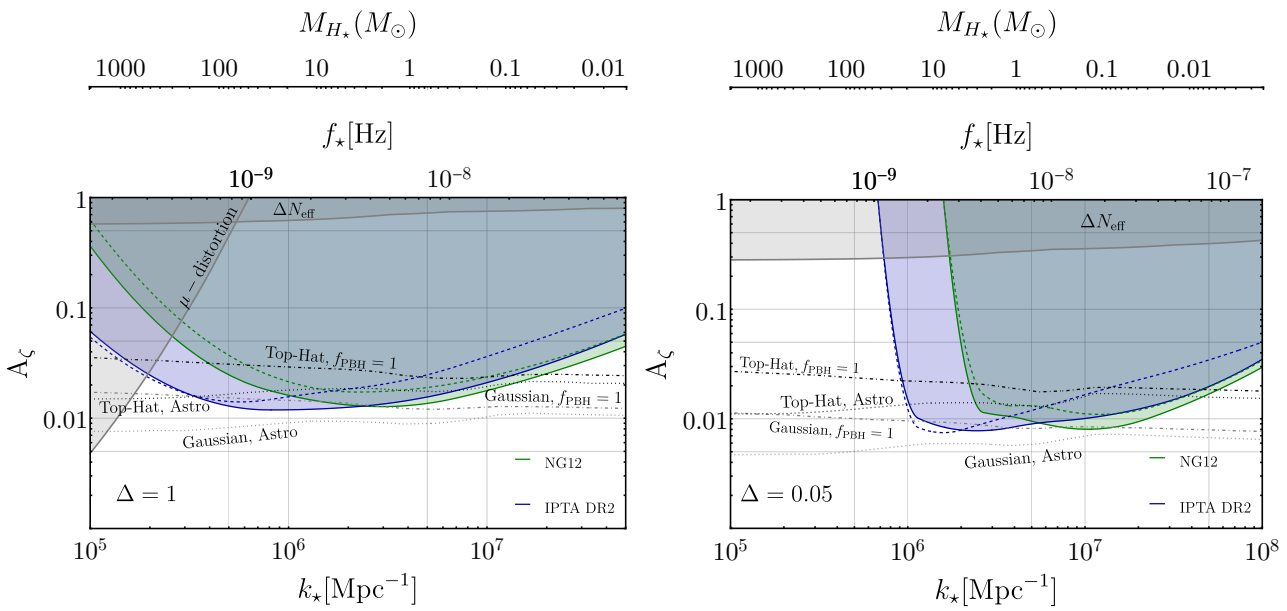


**Figure 5.10:** 95% C.L. upper limits on the amplitude $A_\zeta$, considering the presence of an astrophysical GW background with $\log_{10} A_{\rm SMBHBs}$ (fixed according to the posteriors of [191, 35]). *Left*: $\Delta = 1$. *Right*: $\Delta = 0.05$. The blue (green) shaded regions are constrained by IPTA DR2 (NG12), assuming the upper 95% C.L. posterior value $\log_{10} A_{\rm SMBHBs} = -14.4(-14.57)$. The dashed curves are obtained assuming the lower 95% C.L. posterior value $\log_{10} A_{\rm SMBHBs} = -14.7(-14.86)$ for IPTA DR2 (NG12) instead. Constraints from PBH overproduction are shown as black (gray) dot-dashed curves for a top-hat (Gaussian) window function, and have been obtained using $\delta_c = 0.46(0.59), \kappa = 4$ for the Top-Hat, and $\delta_c = 0.21(0.27), \kappa = 10$ for the modified Gaussian, for $\Delta = 1(0.05)$. Constraints from astrophysical observations are shown as black (gray) dotted curves for a top-hat (Gaussian) window function. The two gray-shaded regions are constrained by CMB observations: the upper region because GWs contribute to the effective number of neutrino species ($\Delta N_{\rm eff} \leq 0.28$ at 95% C.L. from Planck18+BAO [10]); the left corner region in the left panel because curvature perturbations cause $\mu$-distortions (constrained by COBE/FIRAS [257]). The frequency of GWs corresponding to $k_\star$ is shown in the first upper x-axis. The horizon mass at re-entry of the mode $k_\star$ is shown in the second upper x-axis. This figure corresponds to Fig.6 in Ref.[179].

the present analysis. We remind that we performed this analysis fixing $A_{\rm SMBHB}$ to both the upper and lower limits of the $2\sigma$ intervals derived in Refs.[35, 191]. This is depicted in Fig.5.10 by the solid and dashed colored lines.

Finally, we have added in Fig.5.10 the upper limits from PBH overproduction, $f_{\rm PBH} \leq 1$, calculated using both the top-hat and Gaussian window functions (see Sec.5.1 for a detailed discussion on the window function choice). It can be appreciated that the upper limits on $A_\zeta$ calculated from NG12 and IPTA are significantly stronger than those from PBH overproduction in the case of the top-hat window function. There are however similar in the case of the Gaussian window function. In addition, the astrophysical constraints have been translated to constraints on the amplitude $A_\zeta$ following the last section formalism. We find that those are competitive with our upper limits. Other constraints, such as scalar induced GW contribution to the number of degrees of freedom [10] as well as from $\mu$-distortion [257], are shown as grey shaded regions.

Last but not least, we have represented on the upper-x axis the horizon mass when at re-entry of the mode $k_\star$. Since the mean PBH mass has been found in the previous section to be only slightly larger than the horizon mass, the scales constrained by PTAs correspond to PBH with average masses $0.05\ M_\odot \leq M_{\rm PBH} \leq 10^3\ M_\odot$ for broad spectra and $0.01\ M_\odot \leq M_{\rm PBH} \leq 20\ M_\odot$ for narrow spectra.

### 5.2.3 Comparison with Previous Works and Future Expectations

In this section we comment on the previous works relative to scalar induced GWs and PBHs.
First, we discuss the constraints on the curvature power spectrum and the PBH abundance derived from PTA observations. In Ref.[206], upper limits have been derived on the 11-year data of NANOGrav for a power spectrum parameterized by a Dirac delta. Since this power spectrum is recovered in the limit $\Delta \to 0$, their results are similar to ours derived for $\Delta = 0.05$. Additionally, they translated those upper limits on the amplitude $A_\zeta$ into upper limits on the PBH abundance $f_{\rm PBH}$. As mentioned, in Sec.5.1, this last quantity suffers from exponential sensitivities related mainly to the choice of the threshold $\delta_c$ and the window function. In ref.[206], the threshold has been fixed to $\delta_c = 1$ [9] which naturally decreases considerably the abundance of PBHs. Hence, very strong constraints on $f_{\rm PBH}$ have been derived from the upper limits on the amplitude $A_\zeta$ (see similar effects in Ref.[258]).
More recently, Ref.[259] has studied the implications of NG12 for scalar induced GWs. However, instead of performing a Bayesian search in the data set, they used the five bins of the free spectrum to derive posteriors of a curvature power spectrum parameterized by a broken power law. This last one is similar to ours in the case $\Delta \geq 1$. The posterior distribution for the amplitude of their power spectrum is in line with what we find. Moreover, they compared their $2\sigma$ evidence region for the amplitude to the upper limits coming for PBH astrophysical constraints. On this point, we find a deviation compared to our results. This one is most probably caused by their use of a critical threshold $\delta_c$ appropriate for a modified Gaussian window function whereas the rest of their calculation is made with a standard Gaussian window function.
In Ref.[260], similar Bayesian search has been performed on the NG12 data using similar lognormal power spectrum. However, we note that the number of frequency modes used in Eq.(5.32) has been set to $30$ whereas indications from Ref.[191] indicates that $5$ must be used. Indeed, it has been proven that too large a number of modes would induce a coupling between red and white noises and leads to very different posteriors. In addition, they chose too large a threshold $\delta_c$ leading as before to very aggressive upper limits on $f_{\rm PBH}$.
In Ref.[238], a lognormal power spectrum with $\Delta = 1$ has been considered and it was found that the signal could be explained by a curvature power spectrum amplitude $A_\zeta \sim 0.02 - 0.04$ which is in line we what we found in our work. They conclude that this corresponds to a solar mass PBH population. Again, this is in line with the analysis made in this work even if a broader range of masses could be reached. They nevertheless used too large a threshold and did not consider the non-linear relation for the volume averaged density (see Sec.5.1) which naturally leads to deviations on the PBH abundance.

Let's finally mention that few months after this work has been published, the NANOGrav collaboration [37, 261] (as well as the EPTA [38]) released their new data, corresponding to 15 years of observation. Interestingly, whereas previous data were neither for nor against HD correlation, the new version of the data tends to prefer a correlated spectrum with a Bayes factor $\sim 200 - 1000$ to a common uncorrelated spectrum. In the same time, they analysed the possibility that this signal came from large curvature fluctuations. Their evidence analysis show posterior distributions compatible with our IPTA DR2 evidence regions. This might be understood by the fact that IPTA, since regrouping all the different PTA communities, is always more sensitive than the NANOGrav data only published at the same period. Hence, it is expected for IPTA data release 3 (IPTA DR3) to be even more sensitive than NG15 and therefore might be able to decide on the HD correlation issue. In conclusion, the new PTA data are excluding even more the SIGW interpretation of the signal since, following the results presented in this thesis, IPTA DR2 was already strongly in tension with PBH overproduction constraints.

[9] In comparison for $\Delta = 0.05$ we choose $\delta_c = 0.59$.

# Chapter 6

# Conclusion and Outlook

This thesis had for main purpose to study the phenomenology of clustered dark matter structures. In particular, the present work was dedicated to both axion miniclusters and primordial black holes.

The first part of this thesis was dedicated to axions. After a review of the strong CP-problem and the PQ solution, we discussed in chapter 2, the main production channel: the misalignment mechanism. We highlighted that, in the post-inflation scenario, the axions would collapse already around matter-equality into axion miniclusters. As mentioned, the evolution of these clusters have been studied numerically, but the late times - when the clusters are already part of the Milky Way - are not reachable with current numerical methods. In order to fill this gap, we studied the impact of tidal interactions with galactic stars on the axion miniclusters.
The first step was to account for the classical wave treatment of the axion field. In order to construct the wave function of an axion minicluster, we solved the Schrodinger-Poisson system with the use of the random phase anzats for the amplitude of each modes. The consequence of this assumption, is that the cluster wave function would describe a spherically symmetry density profile only on average over the random phases. For a given realization of those, the latter will feature some granular density fluctuations.
Because the wave function is described by the Schrodinger equation (although there is no quantum interpretation for the wave function), the tidal interactions with stars can be described using the well-known formalism of perturbation theory in quantum mechanics (assuming a small enough interaction). Hence, based on this formalism, we studied the impact of a galactic stellar encounter on the mass, radius and energy of the minicluster. We demonstrated that our results are in line with what would have been obtained if the cluster was described in a classical particle picture (as for instance obtained in Refs.[116]). This conclusions might have been expected since, for the clusters considered in this work (with mass $M \sim 10^{-12}\mathrm{M}_{\odot}$ and radius $R \sim 10^{-5}\mathrm{Pc}$), the de Broglie wavelength is small compared to the cluster itself (making the particle picture legit). Nonetheless, for much lighter clusters or ultra light axions ($m_a \sim 10^{-20}\mathrm{eV}$), for which this last statement is no longer correct, it is expected to observe stronger deviations from the particle picture. A natural extension to our work would therefore be to apply this formalism to these objects.
We concluded this work by confirming that the survival of the miniclusters in the galaxy strongly depends on their density profile and the way the energy levels are populated (i.e the shape of the distribution function). Moreover, a dedicated study must be conducted on how the clusters would relax after a tidal interaction. If in this work we assumed that they would keep the same density profile (hence only modifying the radius and the mass), this assumption seems unphysical and may lead to some uncontrolled errors in the overall calculated survival. Although, our results confirmed what has been obtained for different studied density profiles, and show that a significant fraction of the miniclusters would survive in the Milky Way.

In line with this analysis, we then performed a study on haloscope signals induced by an encounter with an axion minicluster. Motivated by the known degeneracy between density and axion-

photon coupling appearing in the measured power in such haloscope experiments, we showed that in the lucky case of an encounter, the power spectral decomposition may lead to a measure of the gravitational potential of the cluster. Hence with the use of the Poisson equation, relating the potential to the density, we can disentangle the coupling-density product in the power.
Therefore, in Chapter 4, we have constructed a method able to extract the axion-photon coupling from the induced electric field generated by the minicluster when crossing the haloscope. We studied in details the different sources of errors and established a parameter space region (for the cluster mass, radius and velocity, as well as the measurement time, and number of data points taken along the cluster crossing) for which the coupling is recovered with reasonable accuracy. We have finally deduced the rate at which a suitable minicluster (i.e with parameters allowing for a good coupling reconstruction) would cross the Earth. Taking into account the result for the survival derived in the previous chapter, we obtain that the rate is around one cluster per $10^6$ years.

In the second part of the manuscript, we studied the recent gravitational wave signal observed in both IPTA DR2 and NANOGrav 12 years. In particular, we have investigated the possibility for the latter to be caused by scalar induced gravitational waves, i.e from large curvature fluctuations at scales unconstrained by CMB observations.
Assuming that the curvature fluctuations at small scales are described by a lognormal power spectrum, parameterized by a peak location in momentum space $k_\star$, a width $\Delta$ and an amplitude $A_\zeta$, we performed a Bayesian evidence search on the public available data from NANOGrav 12.5 years and IPTA DR2 and extracted the $1$ and $2\sigma$ C.L regions for these parameters. As expected the amplitude required to induce a sizeble GW spectrum is of the order of $A_\zeta \sim \mathcal{O}(10^{-2})$ at scales around $k_\star \sim 10^6 \mathrm{Mpc}^{-1}$.
While from this part of the analysis, it might be concluded that the the PTA signal can be explained by scalar induced gravitational waves, we proved that, in addition of inducing a SGWB, such large fluctuations would naturally generate primordial black holes. Using the Press-Schechter formalism, we have consistently calculated the PBH abundance associated with a given set of curvature power spectrum parameters and concluded that the parameter space able to explain the signal is in tension with known observational constraints on PBH abundance. This conclusion is therefore strongly limiting the scalar induced hypothesis for the PTA signal.
At the time this analysis was performed, only the 12.5 years data from NANOGrav were available. However, shortly before the submission of this thesis the new data set (15 years) has been released. Interestingly, it shows even stronger evidence for a GW background. In the same time, similar analysis of the scalar induced hypothesis has been performed by the NANOGrav collaboration and converged to similar conclusion, i.e the population of primordial black holes produced along to the GWs are still in tension with the current observational constraints.

# Appendix A

# Units

If not explicitly mentioned, the natural units are used by default along this thesis, i.e $c = \hbar = 1$. This unit system has the useful advantage to express all quantities in energy units. This appendix lists the conversions most frequently used throughout this thesis.

Using that, in SI units system, $c = 3 \times 10^8\,\mathrm{m/s}$ and $\hbar = h/(2\pi) = 1.05 \times 10^{-34}\,\mathrm{kg\,m^2/s}$, we get for the fundamental units,

$$\begin{aligned} 1\,\mathrm{m} &= 5.0 \times 10^6\,\mathrm{eV}^{-1}, \\ 1\,\mathrm{s} &= 1.5 \times 10^{-15}\,\mathrm{eV}^{-1}, \\ 1\,\mathrm{kg} &= 5.63 \times 10^{35}\,\mathrm{eV}. \end{aligned} \tag{A.1}$$

Throughout this thesis, the gravitational constant G has been extensively used. Its SI value is $G = 6.67 \times 10^{-11}\mathrm{m^3\,kg^{-2}\,s^{-2}}$, which leads in natural units to

$$G = 6.71 \times 10^{-57}\,\mathrm{eV}^{-2}. \tag{A.2}$$

Finally, since we are also dealing with astrophysical units, we translate them here in natural units:

$$\begin{aligned} 1\,M_\odot &= 1.99 \times 10^{30}\,\mathrm{kg}, \\ &= 1.11 \times 10^{66}\,\mathrm{eV}. \end{aligned} \tag{A.3}$$

$$\begin{aligned} 1\,\mathrm{pc} &= 3.1 \times 10^{16}\,\mathrm{m}, \\ &= 1.52 \times 10^{23}\,\mathrm{eV}^{-1}. \end{aligned} \tag{A.4}$$

# Appendix B

# Tidal Interactions in Wave Picture

## B.1 Derivation of the Schrodinger-Poisson System

In this appendix, we proceed to give more insights on how, from the relativistic axion field, described by the Klein-Gordon equation coupled to Einstein gravity, we arrive to the Schrodinger-Poisson system in the non-relativistic limit.

Let's start with the general axion field action coupled to gravity considered in Eq.(3.1),

$$S_a = \int d^4x \sqrt{-g} \left( -\frac{1}{2} g_{\mu\nu} \partial_\mu a \partial^\nu a - V(a,T) + \frac{\mathcal{R}}{16\pi G} \right). \tag{B.1}$$

The equations of motion derived from this action are the usual Klein-Gordon equation in a curved background (characterized by the metric $g_{\mu\nu}$ and the Ricci scalar $\mathcal{R}$) and the Einstein equation sourced by the energy tensor of the axion field $T_a^{\mu\nu}$ (see Eq.(3.2)),

$$\begin{aligned} &\frac{1}{\sqrt{g}} \partial_\mu \left( \sqrt{-g} g^{\mu\nu} \partial_\nu \right) a + V'(a), \\ &R^{\mu\nu} - \frac{1}{2} g^{\mu\nu} = 8\pi G T_a^{\mu\nu}. \end{aligned} \tag{B.2}$$

We are interested in evaluating this set of equations in two limits: the weak gravitational field and the non-relativistic axion limits. The first allows to consider small perturbations around a flat metric (neglecting here the expansion of the universe). In the Newton Gauge, the metric becomes [1],

$$ds^2 = (1 + 2\Phi)\, dt^2 - (1 - 2\Phi)\, \delta_{ij} dx^i dx^j, \tag{B.3}$$

where in this expression the scalar perturbation $\Phi$ must be interpreted as the usual gravitational potential. With this assumption, the metric determinant becomes $\sqrt{-g} \approx 1 - 2\Phi$ and the Ricci scalar $\mathcal{R} \approx 2\,(\nabla\phi)^2$.
The second limit allows to rewrite the axion field in terms of a complex non-relativistic field $\psi$,

$$a(\boldsymbol{x}, t) = \frac{1}{\sqrt{2m_a}} \left( \psi(\boldsymbol{x}, t) e^{-i m_a t} + \psi^*(\boldsymbol{x}, t) e^{i m_a t} \right), \tag{B.4}$$

where $\psi$ is slowy oscillating in time compared to the fast mass oscillation: $\dot{\psi} \ll m\psi$, $\ddot{\psi} \ll m^2 \psi$.
With that, the initially considered action becomes

$$S_\psi = \int d^4x \left( \frac{(\nabla\Phi)^2}{8\pi G} - m_a \Phi \psi\psi^* + i/2 \left( \dot{\psi}\psi^* - \psi\dot{\psi} \right) - \frac{(\nabla\psi)\,(\nabla\psi^*)}{2m_a} \right). \tag{B.5}$$

Finally, varying this action with respect to $\Phi$ and $\psi$ gives respectively the Poisson and the Schrodinger equation.

[1] Note that the complete expression in Newton gauge also include vector and tensor modes. Moreover, this expression assumes no anisotropy stress so that the two usual scalar perturbations $\Phi$ and $\Psi$ are equal.

## B.2 Density of the Non-Relativistic Axion Field

In this appendix, we derive the usual expression for the non-relativistic axion density $\rho = m_a|\psi|^2$. Let's start with the real axion field $a(\boldsymbol{x}, t)$ written as a function of the non-relativistic field $\psi(\boldsymbol{x}, t)$,

$$a(\boldsymbol{x}, t) = \frac{1}{\sqrt{2m_a}} \left(\psi(\boldsymbol{x}, t)e^{-im_a t} + \psi^*(\boldsymbol{x}, t)e^{im_a t}\right). \tag{B.6}$$

In the mean text, we found for the 00 component of the stress-energy tensor

$$T_{00} = \rho = \left(\frac{1}{2}\dot{a}^2 + \frac{1}{2}m_a^2 a^2\right). \tag{B.7}$$

Note that in this last expression, the gradient term, initially present, brings a term $\sim k^2a^2$. In the non-relativistic limit, this is by definition much smaller than the two other terms that are $\sim m_a^2a^2$. Plugging Eq.(B.6) in the latter expression for the energy density, we get,

$$\begin{aligned}
\frac{1}{2}\dot{a}^2 &= \frac{1}{4m_a}\left(\dot{\psi}e^{-im_a t} - im_a\psi e^{-im_a t} + \dot{\psi}^* e^{im_a t} + im_a\psi^* e^{im_a t}\right)^2, \\
&\approx \frac{1}{4m_a}\left(-im_a\psi e^{-im_a t} + im_a\psi^* e^{im_a t}\right)^2, \\
&\approx \frac{m_a}{2}|\psi|^2,
\end{aligned} \tag{B.8}$$

where in the second line, $\dot{\psi} \ll im_a\psi$ still because of the non-relativistic approximation. In the last line, the remaining terms oscillating with the mass have been averaged to zero.
Similarly,

$$\frac{1}{2}m_a^2a^2 \approx \frac{m_a}{2}|\psi|^2. \tag{B.9}$$

Summing both contributions, we finally obtain

$$\rho = m_a|\psi|^2. \tag{B.10}$$

## B.3 Statistics of the Axion Field

In this appendix, we show that the variance of the density is given by $\sigma_\rho = \bar{\rho}$, where $\bar{\rho}$ is the mean density of the minicluster.

Let's assume that the axion field is given by

$$\psi(\boldsymbol{x}, t) = \sum_i a_i e^{i\phi_i}\psi_i(\boldsymbol{x})e^{-iE_i t}, \tag{B.11}$$

where $i$ labels the eigenmodes $\psi_i$, $\phi_i$ are the random phases, $a_i$ the mode coefficients and $E_i$ the eigenenergies.
As mentioned in the main text, the axion density associated with this field is

$$\begin{aligned}
\rho(\boldsymbol{x}, t) &= m_a|\psi(\boldsymbol{x}, t)|^2, \\
&= m_a\sum_{ij} a_i a_j^* e^{i\phi_i}e^{-i\phi_j}\psi_i(\boldsymbol{x})\psi_j^*(\boldsymbol{x})e^{-i(E_i-E_j)t},
\end{aligned} \tag{B.12}$$

with mean value,

$$\bar{\rho}(\boldsymbol{x}) = m_a\sum_i |a_i|^2|\psi(\boldsymbol{x})|^2. \tag{B.13}$$

Furthermore, by definition, the variance of the density is given by

$$\begin{aligned}\sigma_\rho^2 &= \langle\rho\rho\rangle - \bar{\rho}^2, \\ &= m_a^2 \sum_{ij}\sum_{kl} a_i a_j^* a_k a_l^* \langle e^{i\phi_i} e^{-i\phi_j} e^{i\phi_k} e^{-i\phi_l}\rangle \psi_i(\boldsymbol{x})\psi_j^*(\boldsymbol{x})\psi_k(\boldsymbol{x})\psi_l^*(\boldsymbol{x}) e^{-i(E_i-E_j+E_k-E_l)t} - \bar{\rho}^2.\end{aligned} \tag{B.14}$$

Using the usual properties of the random phases, we get,

$$\langle e^{i\phi_i} e^{-i\phi_j} e^{i\phi_k} e^{-i\phi_l}\rangle = \delta_{ij}\delta_{kl} + \delta_{il}\delta_{jk}. \tag{B.15}$$

Inserting the latter relation in the variance we find the final result,

$$\begin{aligned}\sigma_\rho^2 &= 2\bar{\rho}^2 - \bar{\rho}^2, \\ &= \bar{\rho}^2.\end{aligned} \tag{B.16}$$

## B.4 Calculation of the Perturbed Coefficients

In this appendix we derive the variation of the coefficients $|C_{nlm}^{(0)}|$ at second order in perturbation theory. Explicitly, the variation is given by

$$\Delta|C_{nlm}|^2 = |C_{nlm}(\infty)|^2 - |C_{nlm}^{(0)}|^2, \tag{B.17}$$

where $|C_{nlm}(\infty)|^2 = |C_{nlm}^{(0)} + C_{nlm}^{(1)}(\infty) + C_{nlm}^{(2)}(\infty)|^2$. As discussed in the main text, the coefficients are calculated at $t = \infty$ when the interaction term is turned off. For the remaining calculations, we will always refer to the coefficient at that time.
Expanding the modulus square and keeping only the terms up to second order we get

$$\Delta|C_{nlm}|^2 = |C_{nlm}^{(1)}|^2 + \left(C_{nlm}^{(0)} C^{(1)*}{}_{nlm} + c.c.\right) + \left(C_{nlm}^{(0)} C^{(2)*}{}_{nlm} + c.c.\right). \tag{B.18}$$

Let's derive those different contributions by solving Eq.(3.51).

The perturbing star is assumed to have a velocity $v$, impact parameter $b$ and mass $M_*$. We also choose our frame such that its trajectory lies in the $x, y$ plane. The motion of the star is then given by

$$\begin{aligned}\boldsymbol{r_*}(t) &= (r_*(t), \theta_*, \phi_*(t)), \\ &= (\sqrt{b^2 + (vt)^2}, \pi/2, \arctan(vt/b)) \ .\end{aligned} \tag{B.19}$$

The effect of the star on the AMC appears as a time dependent perturbation in the Schrodinger equation and is defined from Eq.(3.48),

$$\begin{aligned}H_1(t) &= m_a \phi_{\text{tidal}}(r, t), \\ &= m_a \frac{GM_*}{r_*(t)} \left(\frac{r}{r_*(t)}\right)^2 P_2(\cos\gamma(t)) \ .\end{aligned} \tag{B.20}$$

The first step in the calculation of the perturbed coefficients is to derive explicitly the matrix element, $\langle nlm|\, H_1(t)\, |n'l'm'\rangle$, that appears in Eq.(3.48). Expanding the Legendre polynomial in $H_1(t)$, we get

$$\langle nlm|\, H_1(t)\, |n'l'm'\rangle = \frac{A}{\alpha} \langle nl|\, r^2\, |n'l'\rangle \sum_{m''=0,\pm 2} I_{m''}^{lm,l'm'} T_{nn'm''}(t) \ , \tag{B.21}$$

where we defined the functions

$$\begin{aligned}\langle nl|r^2\,|n'l'\rangle &= \int dr\, r^4 R_{nl}(r) R_{n'l'}(r) \\ I_{m''}^{lm,l'm'} &= \sqrt{\frac{4\pi}{5}} \int d\Omega\, Y_{lm}^*(\theta,\phi) Y_{l'm'}(\theta,\phi) Y_{2m''}(\theta,\phi) \\ T_{nn'm''}(t) &= \sqrt{\frac{4\pi}{5}} \frac{\alpha}{(1+(\alpha t)^2)^{3/2}} Y_{2m''}(\theta_*,\phi_*(t)) \quad .\end{aligned} \tag{B.22}$$

and $A = -\frac{GM_* m_a}{b^3}$ and $\alpha = \frac{v}{b}$.
As usually done in quantum mechanics, the calculation of the matrix element brings explicit selection rules. In our case, the integral over $I_{m''}^{lm,l'm'}$ could be carried out analytically and leads to

$$m'' - m + m' = 0 \qquad |l-2| \leq l' \leq l+2 \qquad l + l' = \text{even} \quad . \tag{B.23}$$

In addition, we remind that the WKB approximation imposes that $l \gg 1$. In that case the transition in angular momentum are negligible such we assume $l \approx l'$ and $m \approx m'$. We will consider this approximation in the remaining calculations expected in the Winger functions (see below) and Kronecher deltas. The selection rules translate into

$$I_{m''}^{lm,l'm'} \approx \delta_{m',m-m''}(\delta_{l',l-2} + \delta_{l',l} + \delta_{l',l+2})\; d^2_{0,l-l'}(\pi/2)\; d^2_{m'',l-l'}(\arccos(m/l)) \quad , \tag{B.24}$$

where $d^a_{b,c}(\theta)$ are the Wigner functions.
The first order coefficient $C^{(1}_{nlm}$ could be calculated by integrating Eq.(3.51) from $t = -\infty$ to $t = +\infty$ and including the expression found for the matrix element in Eq.(B.21), it leads to

$$\begin{aligned}C^{(1)}_{nlm} \approx -i\frac{A}{\alpha} \sum_{n'} \sum_{l'=l,l\pm2} \sum_{m'=0,\pm2} C^{(0)}_{n',l',m-m'} \langle nl|\, r^2\, |n'l'\rangle \;\; d^2_{0,l-l'}(\pi/2) \\ \times\, d^2_{m',l-l'}(\arccos(m/l))\; \tau_{n,n',m'} \quad ,\end{aligned} \tag{B.25}$$

where the function $\tau_{n,n',m'}$ comes from the time integral and is defined as

$$\tau_{nn'm} = \int_{-\infty}^{\infty} dt\; T_{nn'm}(t)\; e^{i\Delta E_{nn'}t} \quad . \tag{B.26}$$

As expected the coefficients $C^{(1)}_{nlm}$ are expressed as a sum over the unperturbed coefficients $C^{(0)}_{nlm}$. As mentioned in the main text, those ones carry a random phase for each different mode $|nlm\rangle$ such that the coefficients $C^{(1)}_{nlm}$ are by nature random as well. However, in the further steps, we will interested about the mean reaction of the AMC to a tidal interactions, for this reason, Eq.(B.32) will be evaluated on average over the random phases. It leads to

$$\langle |C^{(1)}_{nlm}|^2 \rangle \approx \left(\frac{A}{\alpha}\right)^2 (4\pi)^2 m_a \sum_{n',B} dE_{n'}\; \mathcal{N}_{n'l}\, f(E_{n'})\; \langle nl|\, r^2\, |n'l\rangle^2\; g^{lm}_{nn'} \quad , \tag{B.27}$$

where we have replaced the coefficient $C^{(0)}_{nlm}$ by their value defined in Eq.(3.25) and the function $g^{lm}_{nn'}$ is given by

$$g^{lm}_{nn'} = \left(1 - \frac{3m^2}{2l^2}\right)^2 \tau^2_{n,n',0} + \frac{3}{8}\frac{m^4}{l^4}(\tau^2_{n,n',2} + \tau^2_{n,n',-2}) \quad . \tag{B.28}$$

The index $B$ if the sum of Eq.(B.27) stands for bound states since only those ones have a non zero $C^{(0)}_{nlm}$ coefficient.
Eq.(B.27) is however still fairly complicated and in the purpose to use it in the main text calculation,

we perform an additional simplification by averaging over the anugular momentum $m$,

$$\begin{aligned}\langle|C^{(1)}_{nlm}|^2\rangle &= \frac{1}{2l+1}\sum_{m=-l}^{l}|C^{(1)}_{nlm}|^2{}_{ens}\\ &\approx \left(\frac{A}{\alpha}\right)^2(4\pi)^2 m_a \sum_{n'} dE_{n'\ n'l}\, f(E_{n'})\ \langle nl|\, r^2\,|n'l\rangle^2\, g_{nn'}\ ,\end{aligned} \tag{B.29}$$

where

$$\begin{aligned}g_{nn'} &= \frac{1}{2l+1}\sum_{m=-l}^{l} g^{lm}_{nn'}\\ &\approx \frac{3}{20}\left(3\tau^2_{n,n',0}+\frac{1}{2}(\tau^2_{n,n',2}+\tau^2_{n,n',-2})\right),\\ &\approx \frac{19}{40}\,e^{-\left(\frac{|\Delta E_{nn'}|}{c\alpha}\right)^a},\end{aligned} \tag{B.30}$$

with $a = 1.304$ and $c = 1.426$.
The coefficient calculated in Eq.(B.29) constitutes the first term of Eq.(B.32). Using again the average over the random phases, it is possible to see that the second term in bracket would vanish. We then move on directly to the third term of Eq.(B.32).
Following the same steps as for the first order coefficients, we obtain

$$\langle {C^{(0)}_{nlm}}^* C^{(2)}_{nlm} + c.c.\rangle \approx -\left(\frac{A}{\alpha}\right)^2(4\pi)^2 m_a\, dE_n \mathcal{N}_{nl}\, f(E_n)\sum_{n'}\langle nl|\, r^2\,|n'l\rangle^2\, g^{lm}_{nn'}\ , \tag{B.31}$$

where the sum over $n'$ runs now over both bound and unbound states and similar average over the angular momentum $m$ could be performed.

Hence the variation of the coefficients following the tidal interaction could be finally estimated as

$$\langle\Delta|C_{nlm}|^2\rangle = \Delta^{(+)}|C_{nlm}|^2 + \Delta^{(-)}|C_{nlm}|^2, \tag{B.32}$$

with

$$\begin{aligned}\Delta^{(+)}|C_{nlm}|^2 &= \left(\frac{A}{\alpha}\right)^2(4\pi)^2 m_a \sum_{n'} dE_{n'}\,\mathcal{N}_{n'l}\, f(E_{n'})\ \langle nl|\, r^2\,|n'l\rangle^2\, g_{nn'}\\ &= \left(\frac{A}{\alpha}\right)^2\sum_{n'}|C^{(0)}_{n'lm}|^2\ \langle nl|\, r^2\,|n'l\rangle^2\, g_{nn'}\\ \Delta^{(-)}|C_{nlm}|^2 &= -\left(\frac{A}{\alpha}\right)^2(4\pi)^2 m_a\, dE_n\,\mathcal{N}_{nl}\, f(E_n)\sum_{n'}\langle nl|\, r^2\,|n'l\rangle^2\, g_{nn'}\\ &= -\left(\frac{A}{\alpha}\right)^2|C^{(0)}_{nlm}|^2\ \sum_{n'}\langle nl|\, r^2\,|n'l\rangle^2\, g_{nn'}\ .\end{aligned} \tag{B.33}$$

## B.5 Details on the Sum Rules

In order to solve the integral for the energy injected by the star, in Eq.(3.56), we used the quantum mechanical sum rule. In this appendix we re-derive this relation based on Refs.[148, 149].

Let's consider the following Hamiltonian,

$$H = \frac{P^2}{2m_a} + V(\boldsymbol{r}), \tag{B.34}$$

where $P^2$ and $V(\boldsymbol{r})$ are respectively the momentum operator and a arbitrary potential. We define the eigenstates of this Hamiltonian as $|n\rangle$, with corresponding energy levels $E_n$, so that $H\,|n\rangle = E_n\,|n\rangle$. The summation for which we would like to obtain an easily-handled expression is given by

$$\sum_n (E_n - E_m)\,|\langle m|\,F(\boldsymbol{r})\,|n\rangle|^2 = \langle m|\,[F(\boldsymbol{r}), H]F(\boldsymbol{r})\,|m\rangle|^2, \tag{B.35}$$

where $F(\boldsymbol{r})$ is an arbitrary operator and $[.,.]$ stands for the usual commutator. To obtain the rhs term, the completeness of the eigenstate basis is essentially used: $\sum_n |n\rangle\,\langle n| = 1$. Furthermore, if $F$ is a Hermitian operator, we additional get,

$$\sum_n (E_n - E_m)\,|\langle m|\,F(\boldsymbol{r})\,|n\rangle|^2 = -\,\langle m|\,F(\boldsymbol{r})[F(\boldsymbol{r}), H]\,|m\rangle|^2, \tag{B.36}$$

so that, using both relations,

$$\sum_n (E_n - E_m)\,|\langle m|\,F(\boldsymbol{r})\,|n\rangle|^2 = \frac{1}{2}\,\langle m|\,[F(\boldsymbol{r}), [F(\boldsymbol{r}), H]]\,|m\rangle|^2. \tag{B.37}$$

From the previously defined Hamiltonian, we get for the commutator,

$$[F(\boldsymbol{r}), [F(\boldsymbol{r}), H]] = \frac{1}{m_a}\,(\nabla F(\boldsymbol{r}))\,.\,(\nabla F(\boldsymbol{r}))\,. \tag{B.38}$$

Using this last relation to re-write the sum, we get,

$$\sum_n (E_n - E_m)\,|\langle m|\,F(\boldsymbol{r})\,|n\rangle|^2 = \frac{1}{2m_a}\,\langle m|\,(\nabla F(\boldsymbol{r}))\,.\,(\nabla F(\boldsymbol{r}))\,|m\rangle\,. \tag{B.39}$$

In the situation considered in the main text, $F(\boldsymbol{r}) = r^2$ so that $\nabla F(\boldsymbol{r}).\nabla F(\boldsymbol{r}) = 4r^2$. For the set of eigenfunctions derived for the minicluster, $|nlm\rangle$, the sum rule therefore becomes,

$$\sum_{n'l'm'} (E_{n'l'm'} - E_{nlm})|\,\langle nlm|\,r^2\,|n'l'm'\rangle\,|^2 = \frac{2}{m_a}\,\langle nlm|\,r^2\,|nlm\rangle\,. \tag{B.40}$$

Moreover, since the $r^2$ acts as an operator only the radial part of the eigenfunction, this expression simplifies

$$\begin{aligned}
\sum_{n'l'm'} (E_{n'l'm'} - E_{nlm})|\,\langle n|\,r^2\,|n'\rangle\,|^2\,\delta_{ll',mm'} &= \frac{2}{m_a}\,\langle nlm|\,r^2\,|nlm\rangle\,, \\
\sum_{n'} (E_{n'lm} - E_{nlm})|\,\langle n|\,r^2\,|n'\rangle\,|^2 &= \frac{2}{m_a}\,\langle nlm|\,r^2\,|nlm\rangle\,, \\
\approx \int_{E_{min}(l)}^{\infty} dE'\,g_l(E')(E' - E)|\,\langle nlm|\,r^2\,|n'lm\rangle\,|^2 &= \frac{2}{m_a}\,\langle nlm|\,r^2\,|nlm\rangle\,,
\end{aligned} \tag{B.41}$$

where in the last expression we have used the density of states $g_l(E)$ to transform the sum into an integral. In the continuum limit we have expressed the energy levels of the modes $|nlm\rangle$ and $|n'lm\rangle$ respectively as $E$ and $E'$.

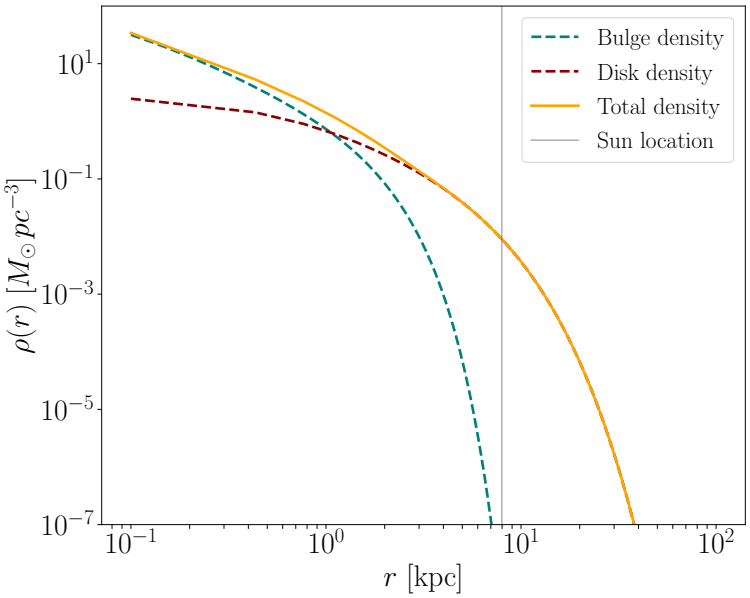


**Figure B.1:** Density distribution of stars in the Milky Way from both the bulge (dashed blue) and the disk (dashed red) regions. The sum of the two contributions is shown by the solid orange line. This figure corresponds to Fig.10 in Ref.[113].

## B.6 Comment On Perturbativity

We stressed in the main text that, in order for the perturbation theory to be valid, we need to have small enough perturbations. Practically, it means that we need to require that the variation of the initial coefficients $|C^{(0)}_{nlm}|^2$ is small. This gives us roughly the condition

$$\frac{A}{\alpha}\, R^2 = \frac{G M_* m_a R^2}{b^2 v} < 1\,. \tag{B.42}$$

For $M_* = M_\odot$ and $m_a = 10^{-5}$ eV, the condition becomes

$$\frac{R}{b} < 5 \times 10^{-3}\, v^{1/2}\,. \tag{B.43}$$

Of course, for some encounters in the galaxy, the latter relation might be violated. However, most of the interactions are extremely small and therefore satisfy the perturbativity condition. Moreover, in numerical simulations, when $\Delta E/|E|$ becomes of order one, the cluster is assumed to be destroyed and removed from the initial sample.

## B.7 Stellar Density in the Milky Way

In Sec.3.3, an explicit stellar distribution is needed in order to accurately predict the number of interactions the axion miniclusters will get in their lifetime. We detail in this appendix the model of stellar distribution used in the main text numerical simulations.

The star distribution in the galaxy can be decomposed into a high-density and quickly decaying central bulge and a more extended disk. The bulge can be approximated by an axisymmetric profile [262]

$$\rho^{\text{bulge}}(r_c, z) = \rho_0 \frac{\mathrm{e}^{-(r'/r_{\text{cut}})^2}}{(1 + r'/r_0)^\lambda}, \tag{B.44}$$

with $r_{\text{cut}} = 2.1$ kpc, $\lambda = 1.8$, $r_0 = 0.075$ kpc, $\rho_0 = 99.3\, M_\odot\, \text{pc}^{-3}$, $r' = \sqrt{r_c^2 + (2z)^2}$, and $r_c$ denotes the radial coordinate in cylindrical coordinates. Note that, in the main text, we have averaged over

the angle in order to obtain a spherically symmetric distribution.

On its side, the disk is modeled as two sub-disks, thin (t) and thick (T) disks, each of them described by an axisymmetric double exponential model [166]:

$$\rho^{\rm disk}(r_c, z) = \frac{\Sigma_d}{2z_d} \exp\left( -\frac{r_c}{r_d} - \frac{|z|}{z_d} \right), \tag{B.45}$$

with $\Sigma_d^t = 816.6\, M_\odot\,{\rm pc}^{-2}$, $\Sigma_d^T = 209.5\, M_\odot\,{\rm pc}^{-2}$, $r_d^t = 2.90\,{\rm kpc}$, $r_d^T = 3.31\,{\rm kpc}$, $z_d^t = 0.3\,{\rm kpc}$, $z_d^T = 0.9\,{\rm kpc}$ [116]. As before, during the numerical simulations, we perform an average over angles in order to have a spherically symmetric profile.

We show in Fig. B.1 the full distribution accounting for the two previous contribution (after the angular average). Finally, to obtain the number density of stars, we assumed in our simulations a unique mass of $1\,M_\odot$ for all stars so that the number density is given by

$$n_*(r) = \frac{1}{1\,M_\odot} \left( \rho^{\rm disk}(r) + \rho^{\rm bulge}(r) \right) . \tag{B.46}$$

# Appendix C

# Axion Miniclusters in Haloscope Experiments

## C.1 Power Spectral Density

In this appendix we proceed to extract the spectral power in the case of an encounter with an AMC. The axion field that enters as a source for the Maxwell equation is taken from the WKB approximation constructed in Eq.(3.24). In addition, since we have to consider the real axion field, we have

$$a_{\rm AMC}(\boldsymbol{x},t) = \frac{1}{\sqrt{2m_a}}\left(\psi e^{-im_a t} + \psi^* e^{im_a t}\right), \tag{C.1}$$

where $\psi$ is given by Eq.(3.24). With this, the power spectral density is by definition calculated as [128, 170]

$$\begin{aligned} S(\omega_d) &= \frac{(\Delta t)^2}{T}\left|\sum_{nlm} C_{nlm}\sum_{n=0}^{N_T-1} e^{i\omega_d n\Delta t}\left(a_{nlm}\psi_{nlm}(\boldsymbol{x})e^{-i\omega_{nlm}n\Delta t} + c.c.\right)\right|^2, \\ &= \frac{1}{T}\left|\sum_{nlm} C_{nlm}\sum_{n=0}^{N_T-1} \Delta t\, e^{i\omega_d n\Delta t}\left(a_{nlm}\psi_{nlm}(\boldsymbol{x})e^{-i\omega_{nlm}n\Delta t} + c.c.\right)\right|^2, \\ &\approx \frac{1}{T}\left|\sum_{nlm} C_{nlm}\int_{-T/2}^{T/2} dt\, e^{i\omega_d t}\left(a_{nlm}\psi_{nlm}(\boldsymbol{x})e^{-i\omega_{nlm}t} + c.c.\right)\right|^2, \end{aligned} \tag{C.2}$$

where $\Delta t = T/N_T$, with $N_T$ the number of time data points taken during the measurement, and we have introduced the coefficients $C_{nlm}$ as

$$C_{nlm} = \sqrt{(g_{a\gamma\gamma}B_0)^2\,\mathcal{G}_j\,V}\,\frac{\omega_{nlm}^2}{\sqrt{2m_a}\left(\omega_j^2 - \omega_{nlm}^2 - i\omega_j\omega_{nlm}/Q\right)}. \tag{C.3}$$

In this last equation $\mathcal{G}_j$ is the usual form factor and is of the order $\mathcal{O}(1)$, $V$ is the cavity volume and $\omega_{nlm} = E_{nlm} + m_a + \omega_{\rm amc}$ respectively the (non-relativistic) binding energy of the axion in the cluster, the axion mass and its kinetic energy due to the cluster velocity. Note that the wave functions $\psi_{nlm}(\boldsymbol{x})$ depends on the location $\boldsymbol{x}$ (in a frame centered at the origin of the cluster) at which we are doing the measurement in the cluster. We assumed in the main text that the cluster is moving slowly enough so that its motion is neglected during the measurement period $T$.
The time integral can be solved easily and we obtain

$$S(\omega_d) \approx T\left|\sum_{nlm} C_{nlm}a_{nlm}\psi_{nlm}(\boldsymbol{x})\,\mathrm{sinc}\left(\left(\omega_{nlm}-\omega_d\right)\frac{T}{2}\right)\right|^2. \tag{C.4}$$

The average value of the power spectral density is derived by taking the average over the random phases. Explicitly,

$$\begin{aligned}\bar{S}(\omega_d) &= T\left\langle \left| \sum_{nlm} C_{nlm} a_{nlm} \psi_{nlm}(\boldsymbol{x}) \left( (\omega_{nlm} - \omega_d) \frac{T}{2} \right) \right|^2 \right\rangle, \\ &= T \sum_{nlm} \left| C_{nlm} a_{nlm} \psi_{nlm}(\boldsymbol{x}) \right|^2 \mathrm{sinc}^2 \left( (\omega_{nlm} - \omega_d) \frac{T}{2} \right).\end{aligned} \tag{C.5}$$

Finally, with the definition of the coefficients $a_{nlm}$ given in Eq. (3.25) and the assumption that the distribution function $f(E)$ is constant in the width of the sinc, we get

$$\begin{aligned}\bar{S}(\omega_d) \approx 4\pi^2 \left(g_{a\gamma\gamma} B_0\right)^2 \mathcal{G}\, V \frac{\omega_d^4}{\left(\omega_j^2 - \omega_d^2\right)^2 + \left(\omega_j \omega_d / Q\right)^2} f(\omega_d - m_a - \omega_{\mathrm{amc}}) \\ \times \sqrt{\left(2 m_a \left(\omega_d - m_a - \omega_{\mathrm{amc}} - m_a \phi(r)\right)\right)}.\end{aligned} \tag{C.6}$$

## C.2 Comment on the Poisson Equation in Time Coordinate

In Sec.4.3, we discussed how, from the gravitational potential obtained from the spectral power width, the Poisson equation can be used to have access to the density and hence disentangle the coupling-density degeneracy. However, the potential is only obtained as a function of time (times at which the induced electric field is measured). In this appendix, we show how the Poisson equation has to be modified in order to be described in time coordinate.

In spherical coordinates, $(r, \theta, \phi)$ the Poisson equations reads,

$$\frac{1}{r^2} \frac{\partial}{\partial r} \left( r^2 \frac{\partial}{\partial r} \right) \phi(r) = 4\pi G \rho(r), \tag{C.7}$$

where $\phi(r)$ and $\rho(r)$ are respectively the gravitational potential and density of the minicluster. Let's parameterize arbitrarily the radial motion of the cluster through the Earth as $r = r(t)$. We then have the differential relation between both variables,

$$\begin{aligned}\frac{\partial}{\partial r} &= \frac{\partial t}{\partial r} \frac{\partial}{\partial t}, \\ &= \frac{1}{\dot{r}(t)} \frac{\partial}{\partial t},\end{aligned} \tag{C.8}$$

where the dot stands for the time derivative.
With that, we get

$$\begin{aligned}\frac{1}{r^2} \frac{\partial}{\partial r} \left( r^2 \frac{\partial}{\partial r} \right) \phi(r) &= \frac{1}{r^2(t)\dot{r}(t)} \partial_t \left( \frac{r^2(t)}{\dot{r}(t)} \dot{\phi}(t) \right) \\ &= \frac{1}{r^2(t)\dot{r}(t)} \partial_t \left( \frac{2r(t)\dot{r}(t)}{\dot{r}(t)} \dot{\phi}(t) + \frac{r^2(t)}{\dot{r}^2(t)} \ddot{\phi}(t) - \frac{r^2(t)\ddot{r}(t)}{\dot{r}^2(t)} \dot{\phi}(t) \right), \\ &= \frac{\ddot{\phi}(t)}{\dot{r}(t)^2} + \frac{2\dot{\phi}(t)}{\dot{r}(t) r(t)} - \frac{r(t)\ddot{\phi}(t)}{\dot{r}(t)^3}.\end{aligned} \tag{C.9}$$

This last expression is the Poisson equation in time coordinate we used in Eq.(4.27).

Let's, finally, briefly comment on the degrees of freedom appearing in the time Poisson equation if we impose a specific parametrization as the one in Eq.(4.28),

$$r(t; b, R, v) = \sqrt{b^2 + \left( vt - \sqrt{R^2 - b^2} \right)^2}, \tag{C.10}$$

with $b$, $R$ and $v$ respectively the impact parameter, the radius of the cluster and the Earth velocity in a frame centered at the origin of the cluster.
As mentioned in the main text, the velocity of the cluster can be obtained from the right cut in the spectral power. This one is therefore no longer an unknown parameter in the parametrization of the radial motion. Moreover, the time dependent potential $\phi(t)$ is limited in a specific time range, corresponding to the time needed for the Earth to cross the cluster. This, in addition to the knowledge on the velocity allows us to further constrain the parameter space. More concretely, defining the ratio of the impact parameter and the radius $(b/R)^2 \equiv \chi$, we have the following constraint,

$$\chi = 1 - \left(\frac{T_{1/2} v}{R}\right)^2 , \tag{C.11}$$

where $T_{1/2}$ is the time at which $r(t) = b$ corresponding to the minimum of the function $\phi(t)$.
With that the radial motion of the Earth throughout the minicluster is given by

$$r(t; R) = R\sqrt{\chi(R) + \left(vt/R - \sqrt{1-\chi(R)}\right)^2}, \tag{C.12}$$

where only the radius remains as free parameter.
With this conclusion, the maximization of the function $\mathcal{L}(b, R, g_{a\gamma\gamma})$ defined in Eq.(4.30) is actually made only over two parameters: the radius and the axion-photon coupling. The impact parameter being fixed by Eq.(C.11). We have checked that the determination of both was not associated to any degeneracy, since the axion-photon coupling appears as an overall factor whereas the radius influence the shape of the returned density by means of Eq.(C.9).

# Appendix D

# Phenomenology of Large Curvature Fluctuations

## D.1 Scalar Induced Gravitational Waves

In this appendix we proceed to give more detailed calculation on the scalar induced gravitational wave spectrum introduced in Sec.5.1.
Let's start by recalling the GW equation of motion,

$$h''_{\boldsymbol{k},\lambda}(\eta) + 2\mathcal{H}h'_{\boldsymbol{k},\lambda}(\eta) + k^2 h_{\boldsymbol{k},\lambda}(\eta) = \mathcal{S}_\lambda(k,\eta), \tag{D.1}$$

with the source term given by

$$\mathcal{S}_\lambda(k,\eta) = \int d^3l\, e^\lambda_{ij}(k) l^i l^j f(\boldsymbol{k},\boldsymbol{l},\eta)\psi_{\boldsymbol{l}}\psi_{\boldsymbol{k}-\boldsymbol{l}}. \tag{D.2}$$

In both equations, $\lambda$ stands for the polarisations $+$ and $\times$, $\eta$ is the conformal time and $\Psi(\boldsymbol{k},\eta) = T(k\eta)\psi(\boldsymbol{k})$ is the scalar perturbation in the Newton gauge. Finally, the function $f(\boldsymbol{k},\boldsymbol{l},\eta)$ encodes the time dependence of the latter perturbation and is given by [211]

$$f(\boldsymbol{k},\boldsymbol{l},\eta) = 6T(|\boldsymbol{k}-\boldsymbol{l}|\eta)T(l\eta) + 3\eta\left(\partial_\eta T(|\boldsymbol{k}-\boldsymbol{l}|\eta)\right)T(l\eta) + 2\eta^2\partial_\eta T(|\boldsymbol{k}-\boldsymbol{l}|\eta)\partial_\eta T(l\eta). \tag{D.3}$$

Eq.(D.1) can be solved with the use of the Green's function. In particular, we find

$$h_{\boldsymbol{k},\lambda}(\eta) = \frac{1}{a(\eta)}\int_{\eta_0}^{\eta} d\bar{\eta}\, G_k(\eta,\bar{\eta})a(\bar{\eta})\mathcal{S}(\boldsymbol{k},\bar{\eta}), \tag{D.4}$$

with $\eta_0$ some initial time and the Green's function satisfying the equation

$$G''_k(\eta,\bar{\eta}) + \left(k^2 - \frac{a''(\eta)}{a(\eta)}\right) = \delta(\eta-\bar{\eta}). \tag{D.5}$$

In a radiation dominated universe, this last equation has the simple solution,

$$G_k(\eta-\bar{\eta}) = \frac{\sin(k(\eta-\bar{\eta}))}{k}. \tag{D.6}$$

From this solution, the GW power spectrum is calculated as

$$\sum_{\lambda=+,\times}\langle e^\lambda_{ij}e^{ij}_\lambda h_{\boldsymbol{k},\lambda}h_{\boldsymbol{q},\lambda}\rangle = \frac{2\pi^2}{k^3}P_h(k,\eta)\delta^{(3)}(\boldsymbol{k}+\boldsymbol{p}), \tag{D.7}$$

with

$$\langle e^\lambda_{ij}e^{ij}_{\lambda'}h_{\boldsymbol{k},\lambda}h_{\boldsymbol{q},\lambda'}\rangle = \delta^{(3)}(\boldsymbol{k}+\boldsymbol{q})\delta_{\lambda\lambda'}e^\lambda_{ij}(\boldsymbol{k})e^{ij}_\lambda(\boldsymbol{q})\int_{\eta_0}^{\eta}d\bar{\eta}_1\frac{a(\bar{\eta}_1)}{a(\eta)}\int_{\eta_0}^{\eta}d\bar{\eta}_2\frac{a(\bar{\eta}_2)}{a(\eta)}G_k(\eta,\bar{\eta}_1)G_q(\eta,\bar{\eta}_2)$$
$$\times\left(\frac{4}{9}\right)^2 8\pi^4\int\frac{d^3l}{(2\pi)^{3/2}}\,l^i l^j f(\boldsymbol{k},\boldsymbol{l},\bar{\eta}_1)\int\frac{d^3p}{(2\pi)^{3/2}}\,p_i p_j f(\boldsymbol{q},\boldsymbol{p},\bar{\eta}_2)\frac{P_\zeta(l)P_\zeta(|\boldsymbol{k}-\boldsymbol{l}|)}{l^3|\boldsymbol{k}-\boldsymbol{l}|^3}\delta^{(3)}(\boldsymbol{l}+\boldsymbol{p}). \tag{D.8}$$

In Ref.[210], the time integrals have been performed analytically. More precisely, the solution of these integrals can be further simplified by considering the late time behavior (taking the limit $k\eta \gg 1$) and an oscillation average (see Eq.(26) of Ref.[210]).
Using the explicit expression for the polarisation tensor, $e_{ij}(\boldsymbol{k})l^i l^j = l^2\sin^2(\theta)$ with $\theta$ the angle between the vectors $\boldsymbol{l}$ and $\boldsymbol{k}$ and defining the new variables, $u = |\boldsymbol{k}-\boldsymbol{l}|/k$ and $v = l/k$ we finally get for the GW power spectrum in radiation,

$$\Omega_{\rm gw,r}(k) = 3\int_0^\infty d\,v\int_{|1-v|}^{1+v} d\,u\frac{\mathcal{T}(u,v)}{u^2v^2}P_\zeta(uk)P_\zeta(vk), \tag{D.9}$$

with the transfer function $\mathcal{T}$ given by,

$$\begin{aligned}\mathcal{T}(u,v) =& \frac{1}{4}\left[\frac{4v^2-(1+v^2-u^2)^2}{4uv}\right]^2\left(\frac{u^2+v^2-3}{2uv}\right)^4\\ &\times\left[\left(\log\frac{|3-(u+v)^2|}{|3-(u-v)^2|}-\frac{4uv}{u^2+v^2-3}\right)^2+\pi^2\Theta\left(u+v-\sqrt{3}\right)\right].\end{aligned} \tag{D.10}$$

## D.2 The Non-Linear Relation of the Density Constrast

As mentioned in the main text, a density fluctuation characterized by its volume averaged density contrast $\delta_m$ would collapse into a black hole if $\delta_m > \delta_c$, with $\delta_c$ the critical threshold. This, somehow, requires to have large overdensities. If at linear level, the density fluctuations are Gaussian random variables, this is non longer true when they are large enough to consider their non-linear evolution. In other words, the probability distribution for the density contrast $\delta_m$ is expected to not follow a Gaussian distribution. Nevertheless, we show in this appendix that $\delta_m$ can be expressed as a combination of its linear component which is, on its side, described by a Gaussian distribution.

Let's star by recalling the definition of the volume averaged density contrast,

$$\delta_m \equiv \int_0^\infty dR\,4\pi R^2\frac{\delta\rho}{\rho_b}(R,t_H)W(R;R_m), \tag{D.11}$$

where, in this appendix, the window function will be chosen to be the top-hat one. The previous equation becomes

$$\delta_m = \frac{3}{4\pi R_m^3}\int_0^{R_m} dR\,4\pi R^2\frac{\delta\rho}{\rho_b}(R,t_H), \tag{D.12}$$

where the latter is given in term of the physical radial coordinate. We furthermore remind that, the density contrast is given as a function of the curvature fluctuation by

$$\begin{aligned}\delta(\hat{r},t) &= -\frac{4(1+\omega)}{5+3\omega}\left(\frac{1}{aH}\right)^2 e^{-5/2\zeta(\hat{r})}\nabla^2 e^{\zeta(\hat{r})/2},\\ &= -\frac{4}{3}\Phi(t)\left(\frac{1}{aH}\right)^2 e^{-5/2\zeta(\hat{r})}\nabla^2 e^{\zeta(\hat{r})/2},\end{aligned} \tag{D.13}$$

where, this time, $\hat{r}$ denotes the radial coordinate in comoving slicing gauge, $R = a(t)\hat{r}e^{\zeta(\hat{r})}$.

We first proceed to calculate $\delta_m$ at linear order, i.e for small enough perturbations. We get,

$$\delta_{\rm lin}(\hat{r},t) = -\frac{2}{3}\Phi(t)\left(\frac{1}{aH}\right)^2\nabla^2\zeta(\hat{r}). \tag{D.14}$$

In these coordinates, the linear expression for the volume averaged density contrast becomes,

$$\delta_l = \frac{3}{(\hat{r}_m e^{\zeta(\hat{r}_m)})^3}\int_0^{\hat{r}_m} d\hat{r}\,(\hat{r}e^{\zeta(\hat{r})})'(\hat{r}e^{\zeta(\hat{r})})^2\delta_{\rm lin}(\hat{r},t_H), \tag{D.15}$$

where $'$ denotes the derivative with respect to $\hat{r}$.
Inserting the expression for $\delta_{\rm lin}(\hat{r}, t_H)$ we obtain [221],

$$\delta_l = -2\Phi(t)\hat{r}_m\zeta(\hat{r}_m)'. \tag{D.16}$$

Accordingly, this last quantity is described by a Gaussian probability distribution.

The full non-linear relation for $\delta_m$ is obtained by inserting the full expression for $\delta(\hat{r}, t_H)$ in the radial integral. We get [221],

$$\begin{aligned}\delta_m &= \frac{3}{(\hat{r_m}e^{\zeta(\hat{r}_m)})^3}\int_0^{\hat{r}_m} d\hat{r}\,(\hat{r}e^{\zeta(\hat{r})})'(\hat{r}e^{\zeta(\hat{r})})^2\delta(\hat{r}, t_H),\\ &= -\frac{2}{3}\hat{r}_m\zeta(\hat{r}_m)'\left(2+\hat{r}_m\zeta(\hat{r}_m)'\right),\\ &= \delta_l - \frac{3}{8}\delta_l^2.\end{aligned} \tag{D.17}$$

Hence, although in the non-linear regime $\delta_m$ is not described by a Gaussian distribution, the latter can be described via $\delta_l$ which is Gaussian. This method will used in the main text when the Press-Schechter mechanism is introduced.

# Appendix E

# List of Bayesian Seach Parameters and Priors

## E.1 Detection Analysis

| Detection analysis | | | |
|---|---|---|---|
| Parameter | Description | Prior | Comments |
| **White Noise** | | | |
| $E_k$ | EFAC per backend/receiver system | Uniform $[0, 10]$ | single-pulsar only |
| $Q_k[s]$ | EQUAD per backend/receiver system | log-Uniform $[-8.5, -5]$ | single-pulsar only |
| $J_k[s]$ | ECORR per backend/receiver system | log-Uniform $[-8.5, -5]$ | single-pulsar only (NG12, NG9) |
| **Red Noise** | | | |
| $A_{\rm red}$ | Red noise power-law amplitude | log-Uniform $[-20, -11]$ | one parameter per pulsar |
| $\gamma_{\rm red}$ | Red noise power-law spectral index | Uniform $[0, 7]$ | one parameter per pulsar |
| **DM Variations Gaussian Process Noise** | | | |
| $A_{\rm DM}$ | DM noise power-law amplitude | log-Uniform $[-20, -11]$ | one parameter per pulsar (IPTADR2) |
| $\gamma_{\rm DM}$ | DM noise power-law spectral index | Uniform $[0, 7]$ | one parameter per pulsar (IPTADR2) |
| **scalar induced GW Background, w/ SMBHBs** | | | |
| $A_\zeta, \Delta = 1$ | Power spectrum amplitude | log-Uniform $[-3, -1.44]$ | one parameter for PTA |
| $A_\zeta, \Delta = 0.05$ | Power spectrum amplitude | log-Uniform $[-3, -1.57]$ | one parameter for PTA |
| $k_\star[\mathrm{Mpc}^{-1}]$ | Peak scale of the power spectrum | log-Uniform $[4, 9]$ | one parameter for PTA |
| **scalar induced GW Background, w/o SMBHBs** | | | |
| $A_\zeta, \Delta = 1$ | Power spectrum amplitude | log-Uniform $[-3, -1.52]$ | one parameter for PTA |
| $A_\zeta, \Delta = 0.05$ | Power spectrum amplitude | log-Uniform $[-3, -1.65]$ | one parameter for PTA |
| $k_\star[\mathrm{Mpc}^{-1}]$ | Peak scale of the power spectrum | log-Uniform $[4, 9]$ | one parameter for PTA |
| **scalar induced GW Background, w/o SMBHBs, w/ HD correlations** | | | |
| $A_\zeta$ | Power spectrum amplitude | log-Uniform $[-3, -1.22]$ | one parameter for PTA |
| $k_\star[\mathrm{Mpc}^{-1}]$ | Peak scale of the power spectrum | log-Uniform $[4, 9]$ | one parameter for PTA |
| $\Delta$ | Width of the power spectrum | log-Uniform $[\log_{10}(0.5), \log_{10} 3]$ | one parameter for PTA |
| **Supermassive Black Hole Binaries (SMBHBs)** | | | |
| $A_{\rm GWB}$ | Strain amplitude | log-Uniform $[-18, -13]$ | one parameter for PTA |

**Table E.1:** List of priors used in our Bayesian search (detection analysis). This table corresponds to Tab.1 in Ref.[179].

## E.2 Upper Limit analysis

| Upper limit analysis | | | |
|---|---|---|---|
| Parameter | Description | Prior | Comments |
| **White Noise** | | | |
| $E_k$ | EFAC per backend/receiver system | Uniform $[0, 10]$ | single-pulsar only |
| $Q_k[s]$ | EQUAD per backend/receiver system | log-Uniform $[-8.5, -5]$ | single-pulsar only |
| $J_k[s]$ | ECORR per backend/receiver system | log-Uniform $[-8.5, -5]$ | single-pulsar only (NG12, NG9) |
| **Red Noise** | | | |
| $A_{\rm red}$ | Red noise power-law amplitude | Linear-Exponent $[-20, -11]$ | one parameter per pulsar |
| $\gamma_{\rm red}$ | Red noise power-law spectral index | Uniform $[0, 7]$ | one parameter per pulsar |
| **DM Variations Gaussian Process Noise** | | | |
| $A_{\rm DM}$ | DM noise power-law amplitude | Linear-Exponent $[-20, -11]$ | one parameter per pulsar (IPTADR2) |
| $\gamma_{\rm DM}$ | DM noise power-law spectral index | Uniform $[0, 7]$ | one parameter per pulsar (IPTADR2) |
| **scalar induced GW Background** | | | |
| $A_\zeta$ | Power spectrum amplitude | Linear-Exponent $[-3, 0.]$ | one parameter for PTA |
| $k_\star[\mathrm{Mpc}^{-1}]$ | Peak scale of the power spectrum | Fixed, see text | one parameter for PTA |
| **Supermassive Black Hole Binaries (SMBHBs)** | | | |
| $A_{\rm SMBHBs}$, NG12 | Strain amplitude | Fixed to $-14.57$ $(-14.86)$ | one parameter for PTA |
| $A_{\rm SMBHBs}$, IPTA DR2 | Strain amplitude | Fixed to $-14.4$ $(-14.7)$ | one parameter for PTA |

**Table E.2:** List of priors used in our upper limit analysis. This table corresponds to Tab.2 in Ref.[179].

# Appendix F

# Gravitational Waves Induced by Axion Density Fluctuations

Few months after the publication of the study conducted on NANOGrav 12.5 years [179], the new data set (15 years) has been released. As discussed in the main, they confirmed some of the conclusion already made in the previous data set and brought even stronger evidence on the Hellings-Down correlation [37]. On the other hand, if some cosmological models have been ruled out in the process, numerous stay plausible (although the SMBHB explanation seems to stay one of the most statistical favored). It is, therefore, important to keep studying all possible cosmological sources of SGWB.
In this appendix, we consider the density fluctuations naturally produced within the random phase model (Sec.3.1.2). We recall that those are large, $\mathcal{O}(1)$, time-dependent over densities. Therefore, it can be, naively, thought that their time fluctuations can then be associated with GW production. We proceed to demonstrate that this GW production is extremely small (essentially zero) in the galaxy.

Let's start by considering an axion field, $a(\boldsymbol{x}, t)$, as a sum over momentum modes with for each a different phase. On average, it therefore reproduces the mean local density $\rho_{\rm DM}$, and specific realizations of the phases bring granular fluctuations in the density. Explicitly,

$$a(\boldsymbol{x}, t) = \frac{\sqrt{2\rho_{\rm DM}}}{m_a} \sum_{\boldsymbol{k}} \sqrt{\Delta^3 k f(k)} \cos\left(\omega_k t - \boldsymbol{k}.\boldsymbol{x} - \phi_{\boldsymbol{k}}\right), \tag{F.1}$$

where $\Delta^3 k = (2\pi)^3/V$ with $V$ the galaxy volume, $f(k)$ is the momentum distribution function, $\omega_k \approx m_a + k^2/(2m_a)$ and $\phi_{\boldsymbol{k}}$ are the random phases.
By definition, the gravitational waves produced by a source, i.e a non-zero energy-momentum tensor $T_{\mu\nu}$, is given by the usual formula,

$$h_{ij}(\boldsymbol{x}, t) = 4G \int_{\rm V_s} d^3x' \, \frac{T_{ij}(\boldsymbol{x'}, t - |\boldsymbol{x} - \boldsymbol{x'}|)}{|\boldsymbol{x} - \boldsymbol{x'}|}, \tag{F.2}$$

where the integral is performed over the volume of the source $\rm V_s$.
In this particular case, the energy momentum tensor can be written as

$$\begin{aligned} T_{ij}(\boldsymbol{x}, t) &= \partial_i a(\boldsymbol{x}, t) \partial_j a(\boldsymbol{x}, t), \\ &= \sum_{\boldsymbol{kq}} k_i q_j \alpha_{\boldsymbol{k}} \alpha_{\boldsymbol{q}} \cos\left(\omega_k t - \boldsymbol{k}.\boldsymbol{x} - \phi_{\boldsymbol{k}}\right) \cos\left(\omega_q t - \boldsymbol{q}.\boldsymbol{x} - \phi_{\boldsymbol{q}}\right), \end{aligned} \tag{F.3}$$

where in the last line we have defined $\alpha_{\boldsymbol{k}}$ as the Fourier coefficient of the modes. Note that we have not included the other terms of the energy tensor since they are vanishing when taking the TT gauge.

Let's now assume that we evaluate this field at large distances to the source, so that the denominator of the last expression can be approximated to $|\boldsymbol{x} - \boldsymbol{x'}| \approx r_s$. On the other hand, the same quantity appearing in the energy momentum tensor can not be approximated that way since

it would imply to neglect the fast oscillations of the axion field. If this is usually the assumption made for GWs produced by binary black holes, considering individual sources forces us to assume a volume in which many wavelengths are contained. Instead, we expand it as $|\boldsymbol{x}-\boldsymbol{x'}| \approx r_s - \hat{\boldsymbol{r}}_{\boldsymbol{s}}\boldsymbol{x'}$, with $\hat{\boldsymbol{r}}_{\boldsymbol{s}} = \boldsymbol{r_s}/r_s$.
The GW tensor becomes,

$$\begin{aligned} h_{ij}(\boldsymbol{x},t) &= 4G\sum_s \frac{1}{r_s}\int_{\mathrm{V_s}} d^3x'\, T_{ij}(\boldsymbol{x'}, t-(r_s-\hat{\boldsymbol{r}}_{\boldsymbol{s}}\boldsymbol{x'})), \\ &= 4G\sum_s \frac{1}{2r_s}\sum_{\boldsymbol{kq}} k_i q_j \alpha_{\boldsymbol{k}}\alpha_{\boldsymbol{q}} \int_{\mathrm{V_s}} d^3x'\, \cos\left[\omega_k(t-(r_s-\hat{\boldsymbol{r}}_{\boldsymbol{s}}\boldsymbol{x'})) - \boldsymbol{k}.\boldsymbol{x'} - \phi_{\boldsymbol{k}}\right] \\ &\qquad \times \cos\left[\omega_q(t-(r_s-\hat{\boldsymbol{r}}_{\boldsymbol{s}}\boldsymbol{x'})) - \boldsymbol{q}.\boldsymbol{x'} - \phi_{\boldsymbol{q}}\right] \end{aligned} \tag{F.4}$$

where the first sum goes over all the sources. Let's calculate explicitly the space integral,

$$\begin{aligned} \mathcal{I}(\boldsymbol{k},\boldsymbol{q},t) &= \int_{\mathrm{V_s}} d^3x'\, \cos\left[\omega_k(t-(r_s-\hat{\boldsymbol{r}}_{\boldsymbol{s}}\boldsymbol{x'})) - \boldsymbol{k}.\boldsymbol{x'} - \phi_{\boldsymbol{k}}\right]\cos\left[\omega_q(t-(r_s-\hat{\boldsymbol{r}}_{\boldsymbol{s}}\boldsymbol{x'})) - \boldsymbol{q}.\boldsymbol{x'} - \phi_{\boldsymbol{q}}\right], \\ &= \frac{1}{4}\int_{\mathrm{V_s}} d^3x'\, \left(\exp\left[i\left(\omega_k(t-(r_s-\hat{\boldsymbol{r}}_{\boldsymbol{s}}\boldsymbol{x'})) - \boldsymbol{k}.\boldsymbol{x'} - \phi_{\boldsymbol{k}}\right)\right] + c.c.\right) \\ &\qquad \times \left(\exp\left[i\left(\omega_q(t-(r_s-\hat{\boldsymbol{r}}_{\boldsymbol{s}}\boldsymbol{x'})) - \boldsymbol{q}.\boldsymbol{x'} - \phi_{\boldsymbol{q}}\right)\right] + c.c.\right). \end{aligned} \tag{F.5}$$

Since it has been assumed that many wavelengths are contained inside the source volume, the integral over space will lead to Dirac deltas. Explicitly,

$$\begin{aligned} \mathcal{I}(\boldsymbol{k},\boldsymbol{q},t) = \frac{1}{4}[&\exp(i((\omega_k+\omega_q)t - (\phi_{\boldsymbol{k}}+\phi_{\boldsymbol{q}}))\delta^{(3)}(\boldsymbol{k}+\boldsymbol{q}-(\omega_k+\omega_q)\hat{\boldsymbol{r}}_{\boldsymbol{s}}) \\ &+ \exp(i((-\omega_k+\omega_q)t - (-\phi_{\boldsymbol{k}}+\phi_{\boldsymbol{q}}))\delta^{(3)}(-\boldsymbol{k}+\boldsymbol{q}-(-\omega_k+\omega_q)\hat{\boldsymbol{r}}_{\boldsymbol{s}}) \\ &+ \exp(i((-\omega_k-\omega_q)t - (-\phi_{\boldsymbol{k}}-\phi_{\boldsymbol{q}}))\delta^{(3)}(-\boldsymbol{k}-\boldsymbol{q}-(-\omega_k-\omega_q)\hat{\boldsymbol{r}}_{\boldsymbol{s}}) \\ &+ \exp(i((\omega_k-\omega_q)t - (\phi_{\boldsymbol{k}}-\phi_{\boldsymbol{q}}))\delta^{(3)}(\boldsymbol{k}-\boldsymbol{q}-(\omega_k-\omega_q)\hat{\boldsymbol{r}}_{\boldsymbol{s}})]. \end{aligned} \tag{F.6}$$

Let's have a closer look at the delta functions. They would lead to two different conditions:

$$\begin{aligned} \boldsymbol{k}+\boldsymbol{q} &= 2m_a\hat{\boldsymbol{r}}_{\boldsymbol{s}}, \\ \boldsymbol{k}-\boldsymbol{q} &= \left(\frac{k^2}{2m_a} - \frac{q^2}{2m_a}\right)\hat{\boldsymbol{r}}_{\boldsymbol{s}}. \end{aligned} \tag{F.7}$$

The first one leads to the condition $|v_{\boldsymbol{k}}+v_{\boldsymbol{q}}| = 1$, with $v_{\boldsymbol{k}} = \boldsymbol{k}/m_a$, which implies that axions should be relativistic in order to fulfill it. However, in the galaxy it is known that the typical velocity is of the order $\mathcal{O}(10^{-3})$, so that the momentum distribution $f(k)$ is essentially zero when fulfilling the first Dirac delta condition.
The second condition implies the same large velocity constraint in addition to the trivial solution, $\boldsymbol{k} = \boldsymbol{q}$. Therefore, the latter indeed produces GWs, but it might be observed that applying the Dirac delta makes $h_{ij}$ time independent. Hence, the gravitational wave energy arising from this solution,

$$\rho_{\mathrm{gw}} = \frac{\langle \partial_t h_{ij}\partial_t h^{ij}\rangle}{32\pi G}, \tag{F.8}$$

would be zero as well.

We conclude here that no SGWB would be induced by the density fluctuations inherited by the random phase model. The interpretation of this result is the following: The retarded Green's function induces space oscillations with wavelengths given by the frequency $1/\omega_k$. Those are fast oscillations compared to the mode oscillations proportional to $1/k$. Hence, the multiplication of those two averages to zero expect in the limit of similar wavelengths, which is the condition given by the Dirac deltas. In the present situation, the velocity distribution with variance given by $\sigma_v \sim 10^{-3}$ makes it therefore impossible to obtain a sizeable GW spectrum.

# Bibliography


[1] T. Kuhn, *The structure of scientific revolutions*. The University of Chicago Press, 1970.

[2] J. Lexell, *Recherches sur la nouvelle planete, découverte par M. Herschel nominee Georgium Sidus*. Acta Academia Scientarum Imperialis Petropolitanae, 1783.

[3] U. Le Verrier, *Lettre de M. Le Verrier à M. Faye sur la théorie de Mercure et sur le mouvement du périhélie de cette planète, Comptes rendus hebdomadaires des séances de l'Académie des sciences* (1859).

[4] U. Le Verrier, *Lettre de M. Le Verrier à M. Faye sur la théorie de Mercure et sur le mouvement du périhélie de cette planète, Comptes rendus hebdomadaires des séances de l'Académie des sciences* (1859).

[5] A. Einstein, *The foundation of the general theory of relativity.*, *Annalen Phys.* **49** (1916), no. 7 769–822.

[6] F. Zwicky, *Die Rotverschiebung von extragalaktischen Nebeln*, *Helv. Phys. Acta* **6** (1933) 110–127.

[7] V. C. Rubin and W. K. Ford, Jr., *Rotation of the Andromeda Nebula from a Spectroscopic Survey of Emission Regions*, *Astrophys. J.* **159** (1970) 379–403.

[8] D. Clowe, A. Gonzalez, and M. Markevitch, *Weak lensing mass reconstruction of the interacting cluster 1E0657-558: Direct evidence for the existence of dark matter*, *Astrophys. J.* **604** (2004) 596–603, [astro-ph/0312273].

[9] M. Markevitch, A. H. Gonzalez, L. David, A. Vikhlinin, S. Murray, et al., *A Textbook example of a bow shock in the merging galaxy cluster 1E0657-56*, *Astrophys. J. Lett.* **567** (2002) L27, [astro-ph/0110468].

[10] **Planck**, N. Aghanim et al., *Planck 2018 results. VI. Cosmological parameters*, *Astron. Astrophys.* **641** (2020) A6, [1807.06209]. [Erratum: Astron.Astrophys. 652, C4 (2021)].

[11] S. P. Martin, *A Supersymmetry primer*, *Adv. Ser. Direct. High Energy Phys.* **18** (1998) 1–98, [hep-ph/9709356].

[12] **PandaX-II**, A. Tan et al., *Dark Matter Results from First 98.7 Days of Data from the PandaX-II Experiment*, *Phys. Rev. Lett.* **117** (2016), no. 12 121303, [1607.07400].

[13] **XENON**, E. Aprile et al., *Dark Matter Search Results from a One Ton-Year Exposure of XENON1T*, *Phys. Rev. Lett.* **121** (2018), no. 11 111302, [1805.12562].

[14] **ATLAS**, G. Aad et al., *Summary of the ATLAS experiment's sensitivity to supersymmetry after LHC Run 1 — interpreted in the phenomenological MSSM*, *JHEP* **10** (2015) 134, [1508.06608].

[15] R. D. Peccei and H. R. Quinn, *CP Conservation in the Presence of Instantons*, *Phys. Rev. Lett.* **38** (1977) 1440–1443.

[16] F. Wilczek, *Two Applications of Axion Electrodynamics*, *Phys. Rev. Lett.* **58** (1987) 1799.

[17] S. Weinberg, *The U(1) Problem*, *Phys. Rev. D* **11** (1975) 3583–3593.

[18] S. Weinberg, *A New Light Boson?*, *Phys. Rev. Lett.* **40** (1978) 223–226.

[19] M. Dine, W. Fischler, and M. Srednicki, *A Simple Solution to the Strong CP Problem with a Harmless Axion*, *Phys. Lett. B* **104** (1981) 199–202.

[20] M. Dine and W. Fischler, *The Not So Harmless Axion*, *Phys. Lett. B* **120** (1983) 137–141.

[21] J. Preskill, M. B. Wise, and F. Wilczek, *Cosmology of the Invisible Axion*, *Phys. Lett. B* **120** (1983) 127–132.

[22] M. S. Turner, *Coherent Scalar Field Oscillations in an Expanding Universe*, *Phys. Rev. D* **28** (1983) 1243.

[23] M. S. Turner, *Cosmic and Local Mass Density of Invisible Axions*, *Phys. Rev. D* **33** (1986) 889–896.

[24] L. Visinelli and P. Gondolo, *Dark Matter Axions Revisited*, *Phys. Rev. D* **80** (2009) 035024, [0903.4377].

[25] C. J. Hogan and M. J. Rees, *AXION MINICLUSTERS*, *Phys. Lett. B* **205** (1988) 228–230.

[26] E. W. Kolb and I. I. Tkachev, *Nonlinear axion dynamics and formation of cosmological pseudosolitons*, *Phys. Rev. D* **49** (1994) 5040–5051, [astro-ph/9311037].

[27] E. W. Kolb and I. I. Tkachev, *Axion miniclusters and Bose stars*, *Phys. Rev. Lett.* **71** (1993) 3051–3054, [hep-ph/9303313].

[28] K. M. Zurek, C. J. Hogan, and T. R. Quinn, *Astrophysical Effects of Scalar Dark Matter Miniclusters*, *Phys. Rev. D* **75** (2007) 043511, [astro-ph/0607341].

[29] M. Buschmann, J. W. Foster, and B. R. Safdi, *Early-Universe Simulations of the Cosmological Axion*, *Phys. Rev. Lett.* **124** (2020), no. 16 161103, [1906.00967].

[30] A. Vaquero, J. Redondo, and J. Stadler, *Early seeds of axion miniclusters*, *JCAP* **04** (2019) 012, [1809.09241].

[31] B. Eggemeier, J. Redondo, K. Dolag, J. C. Niemeyer, and A. Vaquero, *First Simulations of Axion Minicluster Halos*, *Phys. Rev. Lett.* **125** (2020), no. 4 041301, [1911.09417].

[32] L. Hui, *Wave Dark Matter*, *Ann. Rev. Astron. Astrophys.* **59** (2021) 247–289, [2101.11735].

[33] P. Sikivie, *Experimental Tests of the Invisible Axion*, *Phys. Rev. Lett.* **51** (1983) 1415–1417. [Erratum: Phys.Rev.Lett. 52, 695 (1984)].

[34] P. Sikivie, *Detection Rates for 'Invisible' Axion Searches*, *Phys. Rev. D* **32** (1985) 2988. [Erratum: Phys.Rev.D 36, 974 (1987)].

[35] J. Antoniadis et al., *The International Pulsar Timing Array second data release: Search for an isotropic gravitational wave background*, *Mon. Not. Roy. Astron. Soc.* **510** (2022), no. 4 4873–4887, [2201.03980].

[36] **NANOGrav**, M. F. Alam et al., *The NANOGrav 12.5 yr Data Set: Observations and Narrowband Timing of 47 Millisecond Pulsars*, *Astrophys. J. Suppl.* **252** (2021), no. 1 4, [2005.06490].

[37] **NANOGrav**, A. Afzal et al., *The NANOGrav 15 yr Data Set: Search for Signals from New Physics*, *Astrophys. J. Lett.* **951** (2023), no. 1 L11, [2306.16219].

[38] J. Antoniadis et al., *The second data release from the European Pulsar Timing Array: V. Implications for massive black holes, dark matter and the early Universe*, 2306.16227.

[39] H. Middleton, A. Sesana, S. Chen, A. Vecchio, W. Del Pozzo, et al., *Massive black hole binary systems and the NANOGrav 12.5 yr results*, *Mon. Not. Roy. Astron. Soc.* **502** (2021), no. 1 L99–L103, [2011.01246].

[40] S. Burke-Spolaor et al., *The Astrophysics of Nanohertz Gravitational Waves*, *Astron. Astrophys. Rev.* **27** (2019), no. 1 5, [1811.08826].

[41] S. Matarrese, O. Pantano, and D. Saez, *General relativistic dynamics of irrotational dust: Cosmological implications*, *Phys. Rev. Lett.* **72** (1994) 320–323, [astro-ph/9310036].

[42] S. Matarrese, S. Mollerach, and M. Bruni, *Second order perturbations of the Einstein-de Sitter universe*, *Phys. Rev. D* **58** (1998) 043504, [astro-ph/9707278].

[43] H. Noh and J.-c. Hwang, *Second-order perturbations of the Friedmann world model*, *Phys. Rev. D* **69** (2004) 104011.

[44] C. Carbone and S. Matarrese, *A Unified treatment of cosmological perturbations from super-horizon to small scales*, *Phys. Rev. D* **71** (2005) 043508, [astro-ph/0407611].

[45] K. Nakamura, *Second-order gauge invariant cosmological perturbation theory: Einstein equations in terms of gauge invariant variables*, *Prog. Theor. Phys.* **117** (2007) 17–74, [gr-qc/0605108].

[46] D. Baumann, P. J. Steinhardt, K. Takahashi, and K. Ichiki, *Gravitational Wave Spectrum Induced by Primordial Scalar Perturbations*, *Phys. Rev. D* **76** (2007) 084019, [hep-th/0703290].

[47] Y. B. Zel'dovich and I. D. Novikov, *The Hypothesis of Cores Retarded during Expansion and the Hot Cosmological Model*, *Soviet Astron. AJ (Engl. Transl. )*, **10** (1967) 602.

[48] B. J. Carr and S. W. Hawking, *Black holes in the early Universe*, *Mon. Not. Roy. Astron. Soc.* **168** (1974) 399–415.

[49] R. D. Peccei, *The Strong CP problem and axions*, *Lect. Notes Phys.* **741** (2008) 3–17, [hep-ph/0607268].

[50] W. A. Bardeen, *Anomalous Ward identities in spinor field theories*, *Phys. Rev.* **184** (1969) 1848–1857.

[51] S. L. Adler, *Axial vector vertex in spinor electrodynamics*, *Phys. Rev.* **177** (1969) 2426–2438.

[52] G. 't Hooft, *Symmetry Breaking Through Bell-Jackiw Anomalies*, *Phys. Rev. Lett.* **37** (1976) 8–11.

[53] R. J. Crewther, P. Di Vecchia, G. Veneziano, and E. Witten, *Chiral Estimate of the Electric Dipole Moment of the Neutron in Quantum Chromodynamics*, *Phys. Lett. B* **88** (1979) 123. [Erratum: Phys.Lett.B 91, 487 (1980)].

[54] C. A. Baker et al., *An Improved experimental limit on the electric dipole moment of the neutron*, *Phys. Rev. Lett.* **97** (2006) 131801, [hep-ex/0602020].

[55] D. B. Kaplan and A. V. Manohar, *Current Mass Ratios of the Light Quarks*, *Phys. Rev. Lett.* **56** (1986) 2004.

[56] W. H. Press and P. Schechter, *Formation of galaxies and clusters of galaxies by selfsimilar gravitational condensation*, *Astrophys. J.* **187** (1974) 425–438.

[57] O. Wantz and E. P. S. Shellard, *Axion Cosmology Revisited*, *Phys. Rev. D* **82** (2010) 123508, [0910.1066].

[58] D. J. Gross, R. D. Pisarski, and L. G. Yaffe, *Qcd and instantons at finite temperature*, *Rev. Mod. Phys.* **53** (Jan, 1981) 43–80.

[59] S. Borsanyi et al., *Calculation of the axion mass based on high-temperature lattice quantum chromodynamics*, *Nature* **539** (2016), no. 7627 69–71, [1606.07494].

[60] J. E. Kim, *Weak Interaction Singlet and Strong CP Invariance*, *Phys. Rev. Lett.* **43** (1979) 103.

[61] M. A. Shifman, A. I. Vainshtein, and V. I. Zakharov, *Can Confinement Ensure Natural CP Invariance of Strong Interactions?*, *Nucl. Phys. B* **166** (1980) 493–506.

[62] A. R. Zhitnitsky, *On Possible Suppression of the Axion Hadron Interactions. (In Russian)*, *Sov. J. Nucl. Phys.* **31** (1980) 260.

[63] M. Srednicki, *Axion Couplings to Matter. 1. CP Conserving Parts*, *Nucl. Phys. B* **260** (1985) 689–700.

[64] S. Chang and K. Choi, *Hadronic axion window and the big bang nucleosynthesis*, *Phys. Lett. B* **316** (1993) 51–56, [hep-ph/9306216].

[65] G. Grilli di Cortona, E. Hardy, J. Pardo Vega, and G. Villadoro, *The QCD axion, precisely*, *JHEP* **01** (2016) 034, [1511.02867].

[66] J. E. Kim, *Constraints on very light axions from cavity experiments*, *Phys. Rev. D* **58** (1998) 055006, [hep-ph/9802220].

[67] L. Di Luzio, F. Mescia, and E. Nardi, *Redefining the Axion Window*, *Phys. Rev. Lett.* **118** (2017), no. 3 031801, [1610.07593].

[68] L. Di Luzio, F. Mescia, and E. Nardi, *Window for preferred axion models*, *Phys. Rev. D* **96** (2017), no. 7 075003, [1705.05370].

[69] L. Di Luzio, M. Giannotti, E. Nardi, and L. Visinelli, *The landscape of QCD axion models*, *Phys. Rept.* **870** (2020) 1–117, [2003.01100].

[70] D. A. Dicus, E. W. Kolb, V. L. Teplitz, and R. V. Wagoner, *Astrophysical Bounds on the Masses of Axions and Higgs Particles*, *Phys. Rev. D* **18** (1978) 1829.

[71] **OSQAR**, R. Ballou et al., *New exclusion limits on scalar and pseudoscalar axionlike particles from light shining through a wall*, *Phys. Rev. D* **92** (2015), no. 9 092002, [1506.08082].

[72] C. O'Hare, "cajohare/axionlimits: Axionlimits." https://cajohare.github.io/AxionLimits/, July, 2020.

[73] **ADMX**, N. Du et al., *A Search for Invisible Axion Dark Matter with the Axion Dark Matter Experiment*, *Phys. Rev. Lett.* **120** (2018), no. 15 151301, [1804.05750].

[74] **ADMX**, T. Braine et al., *Extended Search for the Invisible Axion with the Axion Dark Matter Experiment*, *Phys. Rev. Lett.* **124** (2020), no. 10 101303, [1910.08638].

[75] **ADMX**, C. Bartram et al., *Axion dark matter experiment: Run 1B analysis details*, *Phys. Rev. D* **103** (2021), no. 3 032002, [2010.06183].

[76] **ADMX**, C. Bartram et al., *Search for Invisible Axion Dark Matter in the 3.3–4.2 $\mu$eV Mass Range*, *Phys. Rev. Lett.* **127** (2021), no. 26 261803, [2110.06096].

[77] **CAST**, V. Anastassopoulos et al., *New CAST Limit on the Axion-Photon Interaction*, *Nature Phys.* **13** (2017) 584–590, [1705.02290].

[78] **CAST**, S. Aune et al., *CAST search for sub-eV mass solar axions with 3He buffer gas*, *Phys. Rev. Lett.* **107** (2011) 261302, [1106.3919].

[79] **CAST**, M. Arik et al., *Search for Solar Axions by the CERN Axion Solar Telescope with $^3$He Buffer Gas: Closing the Hot Dark Matter Gap*, *Phys. Rev. Lett.* **112** (2014), no. 9 091302, [1307.1985].

[80] **CAST**, M. Arik et al., *New solar axion search using the CERN Axion Solar Telescope with $^4$He filling*, *Phys. Rev. D* **92** (2015), no. 2 021101, [1503.00610].

[81] A. Ayala, I. Domínguez, M. Giannotti, A. Mirizzi, and O. Straniero, *Revisiting the bound on axion-photon coupling from Globular Clusters*, *Phys. Rev. Lett.* **113** (2014), no. 19 191302, [1406.6053].

[82] C. P. Salemi et al., *Search for Low-Mass Axion Dark Matter with ABRACADABRA-10 cm*, *Phys. Rev. Lett.* **127** (2021), no. 8 081801, [2102.06722].

[83] J. L. Ouellet et al., *First Results from ABRACADABRA-10 cm: A Search for Sub-$\mu$eV Axion Dark Matter*, *Phys. Rev. Lett.* **122** (2019), no. 12 121802, [1810.12257].

[84] **IAXO**, E. Armengaud et al., *Physics potential of the International Axion Observatory (IAXO)*, *JCAP* **06** (2019) 047, [1904.09155].

[85] **MADMAX**, P. Brun et al., *A new experimental approach to probe QCD axion dark matter in the mass range above 40 $\mu$eV*, *Eur. Phys. J. C* **79** (2019), no. 3 186, [1901.07401].

[86] **MADMAX Working Group**, A. Caldwell, G. Dvali, B. Majorovits, A. Millar, G. Raffelt, et al., *Dielectric Haloscopes: A New Way to Detect Axion Dark Matter*, *Phys. Rev. Lett.* **118** (2017), no. 9 091801, [1611.05865].

[87] J. A. Grifols, E. Masso, and R. Toldra, *Gamma-rays from SN1987A due to pseudoscalar conversion*, *Phys. Rev. Lett.* **77** (1996) 2372–2375, [astro-ph/9606028].

[88] J. W. Brockway, E. D. Carlson, and G. G. Raffelt, *SN1987A gamma-ray limits on the conversion of pseudoscalars*, *Phys. Lett. B* **383** (1996) 439–443, [astro-ph/9605197].

[89] M. Baryakhtar, *Searching for the QCD axion with black holes and gravitational waves*. PhD thesis, Stanford U., 2015.

[90] A. Pargner, *Phenomenology of Axion Dark Matter*. PhD thesis, KIT, Karlsruhe, IKP, 2, 2019.

[91] P. Fox, A. Pierce, and S. D. Thomas, *Probing a QCD string axion with precision cosmological measurements*, hep-th/0409059.

[92] J.-c. Hwang and H. Noh, *Axion as a Cold Dark Matter candidate*, *Phys. Lett. B* **680** (2009) 1–3, [0902.4738].

[93] H. Noh, C.-G. Park, and J.-c. Hwang, *Axion as a Cold Dark Matter Candidate: Proof to Second order*, *Phys. Lett. B* **726** (2013) 559–563, [1309.5692].

[94] H. Noh, J.-c. Hwang, and C.-G. Park, *Axion as a cold dark matter candidate: Proof to fully nonlinear order*, *Astrophys. J.* **846** (2017), no. 1 1, [1707.08568].

[95] P. Sikivie and Q. Yang, *Bose-Einstein Condensation of Dark Matter Axions*, *Phys. Rev. Lett.* **103** (2009) 111301, [0901.1106].

[96] V. Desjacques, A. Kehagias, and A. Riotto, *Impact of ultralight axion self-interactions on the large scale structure of the Universe*, *Phys. Rev. D* **97** (2018), no. 2 023529, [1709.07946].

[97] L. Hui, J. P. Ostriker, S. Tremaine, and E. Witten, *Ultralight scalars as cosmological dark matter*, *Phys. Rev. D* **95** (2017), no. 4 043541, [1610.08297].

[98] L. F. Abbott and P. Sikivie, *A Cosmological Bound on the Invisible Axion*, *Phys. Lett. B* **120** (1983) 133–136.

[99] K. J. Bae, J.-H. Huh, and J. E. Kim, *Update of axion CDM energy*, *JCAP* **09** (2008) 005, [0806.0497].

[100] J. Enander, A. Pargner, and T. Schwetz, *Axion minicluster power spectrum and mass function*, *JCAP* **12** (2017) 038, [1708.04466].

[101] T. W. B. Kibble, *Topology of Cosmic Domains and Strings*, *J. Phys. A* **9** (1976) 1387–1398.

[102] A. Vilenkin, *Cosmic Strings and Domain Walls*, *Phys. Rept.* **121** (1985) 263–315.

[103] M. B. Hindmarsh and T. W. B. Kibble, *Cosmic strings*, *Rept. Prog. Phys.* **58** (1995) 477–562, [hep-ph/9411342].

[104] V. B. . Klaer and G. D. Moore, *The dark-matter axion mass*, *JCAP* **11** (2017) 049, [1708.07521].

[105] E. W. Kolb and I. I. Tkachev, *Large amplitude isothermal fluctuations and high density dark matter clumps*, *Phys. Rev. D* **50** (1994) 769–773, [astro-ph/9403011].

[106] E. W. Kolb and I. I. Tkachev, *Femtolensing and picolensing by axion miniclusters*, *Astrophys. J. Lett.* **460** (1996) L25–L28, [astro-ph/9510043].

[107] W. Kolb and S. Turner, *The early universe*, *Westview Press, Boulder, CO*, (1990).

[108] M. Fairbairn, D. J. E. Marsh, J. Quevillon, and S. Rozier, *Structure formation and microlensing with axion miniclusters*, *Phys. Rev. D* **97** (2018), no. 8 083502, [1707.03310].

[109] L. Dai and J. Miralda-Escudé, *Gravitational Lensing Signatures of Axion Dark Matter Minihalos in Highly Magnified Stars*, *Astron. J.* **159** (2020), no. 2 49, [1908.01773].

[110] J. F. Navarro, C. S. Frenk, and S. D. M. White, *The Structure of cold dark matter halos*, *Astrophys. J.* **462** (1996) 563–575, [astro-ph/9508025].

[111] D. Ellis, D. J. E. Marsh, and C. Behrens, *Axion Miniclusters Made Easy*, *Phys. Rev. D* **103** (2021), no. 8 083525, [2006.08637].

[112] W. H. Press and P. Schechter, *Formation of Galaxies and Clusters of Galaxies by Self-Similar Gravitational Condensation*, **187** (Feb., 1974) 425–438.

[113] V. Dandoy, T. Schwetz, and E. Todarello, *A self-consistent wave description of axion miniclusters and their survival in the galaxy*, *JCAP* **09** (2022) 081, [2206.04619].

[114] P. Tinyakov, I. Tkachev, and K. Zioutas, *Tidal streams from axion miniclusters and direct axion searches*, *JCAP* **01** (2016) 035, [1512.02884].

[115] V. I. Dokuchaev, Y. N. Eroshenko, and I. I. Tkachev, *Destruction of axion miniclusters in the Galaxy*, *Soviet Journal of Experimental and Theoretical Physics* **125** (Sept., 2017) 434–442, [1710.09586].

[116] B. J. Kavanagh, T. D. P. Edwards, L. Visinelli, and C. Weniger, *Stellar disruption of axion miniclusters in the Milky Way*, *Phys. Rev. D* **104** (2021), no. 6 063038, [2011.05377].

[117] X. Shen, H. Xiao, P. F. Hopkins, and K. M. Zurek, *Disruption of Dark Matter Minihaloes in the Milky Way environment: Implications for Axion Miniclusters and Early Matter Domination*, 2207.11276.

[118] J. Spitzer, Lyman, *Disruption of Galactic Clusters.*, **127** (Jan., 1958) 17.

[119] A. H. Guth, M. P. Hertzberg, and C. Prescod-Weinstein, *Do Dark Matter Axions Form a Condensate with Long-Range Correlation?*, *Phys. Rev. D* **92** (2015), no. 10 103513, [1412.5930].

[120] E. W. Lentz, T. R. Quinn, and L. J. Rosenberg, *Condensate Dynamics with Non-Local Interactions*, *Nucl. Phys. B* **952** (2020) 114937, [1808.06378].

[121] L. M. Widrow and N. Kaiser, *Using the Schrodinger equation to simulate collisionless matter*, *Astrophys. J. Lett.* **416** (1993) L71–L74.

[122] H.-Y. Schive, T. Chiueh, and T. Broadhurst, *Cosmic Structure as the Quantum Interference of a Coherent Dark Wave*, *Nature Phys.* **10** (2014) 496–499, [1406.6586].

[123] B. Schwabe, J. C. Niemeyer, and J. F. Engels, *Simulations of solitonic core mergers in ultralight axion dark matter cosmologies*, *Phys. Rev. D* **94** (2016), no. 4 043513, [1606.05151].

[124] B. Schwabe, M. Gosenca, C. Behrens, J. C. Niemeyer, and R. Easther, *Simulating mixed fuzzy and cold dark matter*, *Phys. Rev. D* **102** (2020), no. 8 083518, [2007.08256].

[125] X. Li, L. Hui, and G. L. Bryan, *Numerical and Perturbative Computations of the Fuzzy Dark Matter Model*, *Phys. Rev. D* **99** (2019), no. 6 063509, [1810.01915].

[126] P. Mocz, M. Vogelsberger, V. H. Robles, J. Zavala, M. Boylan-Kolchin, et al., *Galaxy formation with BECDM – I. Turbulence and relaxation of idealized haloes*, *Mon. Not. Roy. Astron. Soc.* **471** (2017), no. 4 4559–4570, [1705.05845].

[127] L. Hui, A. Joyce, M. J. Landry, and X. Li, *Vortices and waves in light dark matter*, *JCAP* **01** (2021) 011, [2004.01188].

[128] J. W. Foster, N. L. Rodd, and B. R. Safdi, *Revealing the Dark Matter Halo with Axion Direct Detection*, *Phys. Rev. D* **97** (2018), no. 12 123006, [1711.10489].

[129] S.-C. Lin, H.-Y. Schive, S.-K. Wong, and T. Chiueh, *Self-consistent construction of virialized wave dark matter halos*, *Phys. Rev. D* **97** (2018), no. 10 103523, [1801.02320].

[130] S. Knirck, A. J. Millar, C. A. J. O'Hare, J. Redondo, and F. D. Steffen, *Directional axion detection*, *JCAP* **11** (2018) 051, [1806.05927].

[131] H. A. Kramers, *Wellenmechanik und halbzahlige Quantisierung*, *Z. Phys.* **39** (1926), no. 10 828–840.

[132] G. Wentzel, *Eine Verallgemeinerung der Quantenbedingungen für die Zwecke der Wellenmechanik*, *Z. Phys.* **38** (1926), no. 6 518–529.

[133] X. Li, L. Hui, and T. D. Yavetz, *Oscillations and Random Walk of the Soliton Core in a Fuzzy Dark Matter Halo*, *Phys. Rev. D* **103** (2021), no. 2 023508, [2011.11416].

[134] T. D. Yavetz, X. Li, and L. Hui, *Construction of wave dark matter halos: Numerical algorithm and analytical constraints*, *Phys. Rev. D* **105** (2022), no. 2 023512, [2109.06125].

[135] N. Dalal, J. Bovy, L. Hui, and X. Li, *Don't cross the streams: caustics from Fuzzy Dark Matter*, *JCAP* **03** (2021) 076, [2011.13141].

[136] A. S. Eddington, *The distribution of stars in globular clusters*, *MNRAS* **76** (May, 1916) 572–585.

[137] J. Binney and S. Tremaine, *Galactic Dynamics*. Princeton University Press, Princeton, NJ USA, 2008.

[138] V. Dandoy, J. Jaeckel, and V. Montoya, *Using Axion Miniclusters to Disentangle the Axion-photon Coupling and the Dark Matter Density*, 2307.11871.

[139] D. Ellis, D. J. E. Marsh, B. Eggemeier, J. Niemeyer, J. Redondo, et al., *Structure of axion miniclusters*, *Phys. Rev. D* **106** (2022), no. 10 103514, [2204.13187].

[140] L. Hernquist, *An Analytical Model for Spherical Galaxies and Bulges*, *Astrophys. J.* **356** (1990) 359.

[141] J. Binney, O. Gerhard, and D. Spergel, *The photometric structure of the inner galaxy*, *Mon. Not. Roy. Astron. Soc.* **288** (1997) 365–374, [astro-ph/9609066].

[142] L. J.Spitzer, *Disruption of Galactic Clusters.*, *Astrophys. J.* **127** (1958), no. 17.

[143] A. M. Green and S. P. Goodwin, *On mini-halo encounters with stars*, *Mon. Not. Roy. Astron. Soc.* **375** (2007) 1111–1120, [astro-ph/0604142].

[144] A. Schneider, L. Krauss, and B. Moore, *Impact of Dark Matter Microhalos on Signatures for Direct and Indirect Detection*, *Phys. Rev. D* **82** (2010) 063525, [1004.5432].

[145] M. S. Delos, *Evolution of dark matter microhalos through stellar encounters*, *Phys. Rev. D* **100** (2019), no. 8 083529, [1907.13133].

[146] L. A. Martinez-Medina, M. Gieles, O. Y. Gnedin, and H. Li, *On the response of a star cluster to a tidal perturbation*, *Monthly Notices of the Royal Astronomical Society* **516** (aug, 2022) 1237–1249.

[147] V. I. Dokuchaev, Y. N. Eroshenko, and I. I. Tkachev, *Destruction of axion miniclusters in the Galaxy*, *J. Exp. Theor. Phys.* **125** (2017), no. 3 434–442, [1710.09586].

[148] S. Wang, *Generalization of the thomas-reiche-kuhn and the bethe sum rules*, *Phys. Rev. A* **60** (Jul, 1999) 262–266.

[149] M. Belloni and R. W. Robinett, *Quantum mechanical sum rules for two model systems*, *American Journal of Physics* **76** (sep, 2008) 798–806.

[150] M. Gieles and F. Renaud, *If it does not kill them, it makes them stronger: collisional evolution of star clusters with tidal shocks*, *Monthly Notices of the Royal Astronomical Society: Letters* **463** (Aug, 2016) L103–L107.

[151] E. Seidel and W.-M. Suen, *Formation of solitonic stars through gravitational cooling*, *Phys. Rev. Lett.* **72** (1994) 2516–2519, [gr-qc/9309015].

[152] H.-Y. Schive, M.-H. Liao, T.-P. Woo, S.-K. Wong, T. Chiueh, et al., *Understanding the Core-Halo Relation of Quantum Wave Dark Matter from 3D Simulations*, *Phys. Rev. Lett.* **113** (2014), no. 26 261302, [1407.7762].

[153] B. Eggemeier and J. C. Niemeyer, *Formation and mass growth of axion stars in axion miniclusters*, *Phys. Rev. D* **100** (2019), no. 6 063528, [1906.01348].

[154] D. G. Levkov, A. G. Panin, and I. I. Tkachev, *Gravitational Bose-Einstein condensation in the kinetic regime*, *Phys. Rev. Lett.* **121** (2018), no. 15 151301, [1804.05857].

[155] J. Chen, X. Du, E. W. Lentz, D. J. E. Marsh, and J. C. Niemeyer, *New insights into the formation and growth of boson stars in dark matter halos*, *Phys. Rev. D* **104** (2021), no. 8 083022, [2011.01333].

[156] P.-H. Chavanis, *Mass-radius relation of newtonian self-gravitating bose-einstein condensates with short-range interactions. i. analytical results*, *Physical Review D* **84** (aug, 2011).

[157] L. Visinelli, S. Baum, J. Redondo, K. Freese, and F. Wilczek, *Dilute and dense axion stars*, *Phys. Lett. B* **777** (2018) 64–72, [1710.08910].

[158] H. Xiao, I. Williams, and M. McQuinn, *Simulations of axion minihalos*, *Phys. Rev. D* **104** (2021), no. 2 023515, [2101.04177].

[159] M. Fairbairn, D. J. E. Marsh, and J. Quevillon, *Searching for the QCD Axion with Gravitational Microlensing*, *Phys. Rev. Lett.* **119** (2017), no. 2 021101, [1701.04787].

[160] A. Katz, J. Kopp, S. Sibiryakov, and W. Xue, *Femtolensing by Dark Matter Revisited*, *JCAP* **12** (2018) 005, [1807.11495].

[161] F. Nesti and P. Salucci, *The Dark Matter halo of the Milky Way, AD 2013*, *JCAP* **07** (2013) 016, [1304.5127].

[162] F. C. van den Bosch, G. F. Lewis, G. Lake, and J. Stadel, *Substructure in dark halos: orbital eccentricities and dynamical friction*, *Astrophys. J.* **515** (1999) 50, [astro-ph/9811229].

[163] N. Bissantz and O. Gerhard, *Spiral arms, bar shape and bulge microlensing in the milky way*, *Mon. Not. Roy. Astron. Soc.* **330** (2002) 591, [astro-ph/0110368].

[164] T. Bensby, S. Feltzing, I. Lundstrom, and I. Ilyin, *Alpha-, r-, and s-process element trends in the Galactic thin and thick disks*, *Astron. Astrophys.* **433** (2005) 185–203, [astro-ph/0412132].

[165] **SDSS**, M. Juric et al., *The Milky Way Tomography with SDSS. 1. Stellar Number Density Distribution*, *Astrophys. J.* **673** (2008) 864–914, [astro-ph/0510520].

[166] W. Dehnen and J. Binney, *Mass models of the Milky Way*, *Mon. Not. Roy. Astron. Soc.* **294** (1998) 429, [astro-ph/9612059].

[167] R. Diehl et al., *Radioactive Al-26 and massive stars in the galaxy*, *Nature* **439** (2006) 45–47, [astro-ph/0601015].

[168] J. Alvey, M. Escudero, N. Sabti, and T. Schwetz, *Cosmic neutrino background detection in large-neutrino-mass cosmologies*, *Phys. Rev. D* **105** (2022), no. 6 063501, [2111.14870].

[169] A. A. Dutton and A. V. Macciò, *Cold dark matter haloes in the Planck era: evolution of structural parameters for Einasto and NFW profiles*, *Mon. Not. Roy. Astron. Soc.* **441** (2014), no. 4 3359–3374, [1402.7073].

[170] J. W. Foster, Y. Kahn, R. Nguyen, N. L. Rodd, and B. R. Safdi, *Dark Matter Interferometry*, *Phys. Rev. D* **103** (2021), no. 7 076018, [2009.14201].

[171] C. A. J. O'Hare and A. M. Green, *Axion astronomy with microwave cavity experiments*, *Phys. Rev. D* **95** (2017), no. 6 063017, [1701.03118].

[172] L. Krauss, J. Moody, F. Wilczek, and D. E. Morris, *Calculations for Cosmic Axion Detection*, *Phys. Rev. Lett.* **55** (1985) 1797.

[173] J. D. Jackson, *Classical Electrodynamics*. Wiley, 1998.

[174] A. A. Melcón et al., *Axion Searches with Microwave Filters: the RADES project*, *JCAP* **05** (2018) 040, [1803.01243].

[175] A. S. Eddington, *The distribution of stars in globular clusters*, *MNRAS* **76** (May, 1916) 572–585.

[176] A. Berlin, R. T. D'Agnolo, S. A. R. Ellis, C. Nantista, J. Neilson, et al., *Axion Dark Matter Detection by Superconducting Resonant Frequency Conversion*, *JHEP* **07** (2020), no. 07 088, [1912.11048].

[177] A. A. Clerk, M. H. Devoret, S. M. Girvin, F. Marquardt, and R. J. Schoelkopf, *Introduction to quantum noise, measurement, and amplification*, *Rev. Mod. Phys.* **82** (2010), no. 2 1155–1208, [0810.4729].

[178] M. Blennow, J. Herrero-Garcia, and T. Schwetz, *A halo-independent lower bound on the dark matter capture rate in the Sun from a direct detection signal*, *JCAP* **05** (2015) 036, [1502.03342].

[179] V. Dandoy, V. Domcke, and F. Rompineve, *Search for scalar induced gravitational waves in the International Pulsar Timing Array Data Release 2 and NANOgrav 12.5 years dataset*, 2302.07901.

[180] **LIGO Scientific, Virgo**, B. P. Abbott et al., *Observation of Gravitational Waves from a Binary Black Hole Merger*, *Phys. Rev. Lett.* **116** (2016), no. 6 061102, [1602.03837].

[181] M. Rajagopal and R. W. Romani, *Ultralow frequency gravitational radiation from massive black hole binaries*, *Astrophys. J.* **446** (1995) 543–549, [astro-ph/9412038].

[182] A. H. Jaffe and D. C. Backer, *Gravitational waves probe the coalescence rate of massive black hole binaries*, *Astrophys. J.* **583** (2003) 616–631, [astro-ph/0210148].

[183] A. Sesana, F. Haardt, P. Madau, and M. Volonteri, *Low - frequency gravitational radiation from coalescing massive black hole binaries in hierarchical cosmologies*, *Astrophys. J.* **611** (2004) 623–632, [astro-ph/0401543].

[184] S. T. McWilliams, J. P. Ostriker, and F. Pretorius, *Gravitational waves and stalled satellites from massive galaxy mergers at $z \leq 1$*, *Astrophys. J.* **789** (2014) 156, [1211.5377].

[185] M. C. Begelman, R. D. Blandford, and M. J. Rees, *Massive black hole binaries in active galactic nuclei*, *Nature* **287** (1980) 307–309.

[186] M. C. Guzzetti, N. Bartolo, M. Liguori, and S. Matarrese, *Gravitational waves from inflation*, *Riv. Nuovo Cim.* **39** (2016), no. 9 399–495, [1605.01615].

[187] G. Domènech, *Scalar Induced Gravitational Waves Review*, *Universe* **7** (2021), no. 11 398, [2109.01398].

[188] C. Caprini et al., *Science with the space-based interferometer eLISA. II: Gravitational waves from cosmological phase transitions*, *JCAP* **04** (2016) 001, [1512.06239].

[189] A. Vilenkin, *Gravitational radiation from cosmic strings*, *Phys. Lett. B* **107** (1981) 47–50.

[190] **KAGRA, Virgo, LIGO Scientific**, R. Abbott et al., *Upper limits on the isotropic gravitational-wave background from Advanced LIGO and Advanced Virgo's third observing run*, *Phys. Rev. D* **104** (2021), no. 2 022004, [2101.12130].

[191] **NANOGrav**, Z. Arzoumanian et al., *The NANOGrav 12.5 yr Data Set: Search for an Isotropic Stochastic Gravitational-wave Background*, *Astrophys. J. Lett.* **905** (2020), no. 2 L34, [2009.04496].

[192] B. Goncharov et al., *On the Evidence for a Common-spectrum Process in the Search for the Nanohertz Gravitational-wave Background with the Parkes Pulsar Timing Array*, *Astrophys. J. Lett.* **917** (2021), no. 2 L19, [2107.12112].

[193] S. Chen et al., *Common-red-signal analysis with 24-yr high-precision timing of the European Pulsar Timing Array: inferences in the stochastic gravitational-wave background search*, *Mon. Not. Roy. Astron. Soc.* **508** (2021), no. 4 4970–4993, [2110.13184].

[194] R. Flauger, N. Karnesis, G. Nardini, M. Pieroni, A. Ricciardone, et al., *Improved reconstruction of a stochastic gravitational wave background with LISA*, *JCAP* **01** (2021) 059, [2009.11845].

[195] M. Maggiore et al., *Science Case for the Einstein Telescope*, *JCAP* **03** (2020) 050, [1912.02622].

[196] S. Kawamura et al., *Current status of space gravitational wave antenna DECIGO and B-DECIGO*, *PTEP* **2021** (2021), no. 5 05A105, [2006.13545].

[197] K. Inomata and T. Terada, *Gauge Independence of Induced Gravitational Waves*, *Phys. Rev. D* **101** (2020), no. 2 023523, [1912.00785].

[198] V. De Luca, G. Franciolini, A. Kehagias, and A. Riotto, *On the Gauge Invariance of Cosmological Gravitational Waves*, *JCAP* **03** (2020) 014, [1911.09689].

[199] C. T. Byrnes, P. S. Cole, and S. P. Patil, *Steepest growth of the power spectrum and primordial black holes*, *JCAP* **06** (2019) 028, [1811.11158].

[200] J. Martin, H. Motohashi, and T. Suyama, *Ultra Slow-Roll Inflation and the non-Gaussianity Consistency Relation*, *Phys. Rev. D* **87** (2013), no. 2 023514, [1211.0083].

[201] H. Motohashi, A. A. Starobinsky, and J. Yokoyama, *Inflation with a constant rate of roll*, *JCAP* **09** (2015) 018, [1411.5021].

[202] G. Franciolini, *Primordial Black Holes: from Theory to Gravitational Wave Observations*. PhD thesis, Geneva U., Dept. Theor. Phys., 2021. 2110.06815.

[203] R. w. Hellings and G. s. Downs, *UPPER LIMITS ON THE ISOTROPIC GRAVITATIONAL RADIATION BACKGROUND FROM PULSAR TIMING ANALYSIS*, *Astrophys. J. Lett.* **265** (1983) L39–L42.

[204] V. Vaskonen and H. Veermäe, *Did NANOGrav see a signal from primordial black hole formation?*, *Phys. Rev. Lett.* **126** (2021), no. 5 051303, [2009.07832].

[205] V. De Luca, G. Franciolini, and A. Riotto, *NANOGrav Data Hints at Primordial Black Holes as Dark Matter*, *Phys. Rev. Lett.* **126** (2021), no. 4 041303, [2009.08268].

[206] Z.-C. Chen, C. Yuan, and Q.-G. Huang, *Pulsar Timing Array Constraints on Primordial Black Holes with NANOGrav 11-Year Dataset*, *Phys. Rev. Lett.* **124** (2020), no. 25 251101, [1910.12239].

[207] M. Maggiore, *Gravitational wave experiments and early universe cosmology*, *Phys. Rept.* **331** (2000) 283–367, [gr-qc/9909001].

[208] J. R. Espinosa, D. Racco, and A. Riotto, *A Cosmological Signature of the SM Higgs Instability: Gravitational Waves*, *JCAP* **09** (2018) 012, [1804.07732].

[209] J.-O. Gong, *Analytic Integral Solutions for Induced Gravitational Waves*, *Astrophys. J.* **925** (2022), no. 1 102, [1909.12708].

[210] K. Kohri and T. Terada, *Semianalytic calculation of gravitational wave spectrum nonlinearly induced from primordial curvature perturbations*, *Phys. Rev. D* **97** (2018), no. 12 123532, [1804.08577].

[211] S. Pi and M. Sasaki, *Gravitational Waves Induced by Scalar Perturbations with a Lognormal Peak*, *JCAP* **09** (2020) 037, [2005.12306].

[212] K. N. Ananda, C. Clarkson, and D. Wands, *The Cosmological gravitational wave background from primordial density perturbations*, *Phys. Rev. D* **75** (2007) 123518, [gr-qc/0612013].

[213] **EROS-2**, P. Tisserand et al., *Limits on the Macho Content of the Galactic Halo from the EROS-2 Survey of the Magellanic Clouds*, *Astron. Astrophys.* **469** (2007) 387–404, [astro-ph/0607207].

[214] D. Croon, D. McKeen, N. Raj, and Z. Wang, *Subaru-HSC through a different lens: Microlensing by extended dark matter structures*, *Phys. Rev. D* **102** (2020), no. 8 083021, [2007.12697].

[215] **Macho**, R. A. Allsman et al., *MACHO project limits on black hole dark matter in the 1-30 solar mass range*, *Astrophys. J. Lett.* **550** (2001) L169, [astro-ph/0011506].

[216] K. Griest, A. M. Cieplak, and M. J. Lehner, *Experimental Limits on Primordial Black Hole Dark Matter from the First 2 yr of Kepler Data*, *Astrophys. J.* **786** (2014), no. 2 158, [1307.5798].

[217] M. Oguri, J. M. Diego, N. Kaiser, P. L. Kelly, and T. Broadhurst, *Understanding caustic crossings in giant arcs: characteristic scales, event rates, and constraints on compact dark matter*, *Phys. Rev. D* **97** (2018), no. 2 023518, [1710.00148].

[218] G. Hütsi, M. Raidal, V. Vaskonen, and H. Veermäe, *Two populations of LIGO-Virgo black holes*, *JCAP* **03** (2021) 068, [2012.02786].

[219] P. D. Serpico, V. Poulin, D. Inman, and K. Kohri, *Cosmic microwave background bounds on primordial black holes including dark matter halo accretion*, *Phys. Rev. Res.* **2** (2020), no. 2 023204, [2002.10771].

[220] Y. Ali-Haïmoud and M. Kamionkowski, *Cosmic microwave background limits on accreting primordial black holes*, *Phys. Rev. D* **95** (2017), no. 4 043534, [1612.05644].

[221] S. Young, *The primordial black hole formation criterion re-examined: Parametrisation, timing and the choice of window function*, *Int. J. Mod. Phys. D* **29** (2019), no. 02 2030002, [1905.01230].

[222] I. Musco, *Threshold for primordial black holes: Dependence on the shape of the cosmological perturbations*, *Phys. Rev. D* **100** (2019), no. 12 123524, [1809.02127].

[223] S. Young, I. Musco, and C. T. Byrnes, *Primordial black hole formation and abundance: contribution from the non-linear relation between the density and curvature perturbation*, *JCAP* **11** (2019) 012, [1904.00984].

[224] J. C. Niemeyer and K. Jedamzik, *Near-critical gravitational collapse and the initial mass function of primordial black holes*, *Phys. Rev. Lett.* **80** (1998) 5481–5484, [astro-ph/9709072].

[225] J. C. Niemeyer and K. Jedamzik, *Dynamics of primordial black hole formation*, *Phys. Rev. D* **59** (1999) 124013, [astro-ph/9901292].

[226] A. D. Gow, C. T. Byrnes, P. S. Cole, and S. Young, *The power spectrum on small scales: Robust constraints and comparing PBH methodologies*, *JCAP* **02** (2021) 002, [2008.03289].

[227] V. De Luca, G. Franciolini, A. Kehagias, M. Peloso, A. Riotto, et al., *The Ineludible non-Gaussianity of the Primordial Black Hole Abundance*, *JCAP* **07** (2019) 048, [1904.00970].

[228] M. Kawasaki and H. Nakatsuka, *Effect of nonlinearity between density and curvature perturbations on the primordial black hole formation*, *Phys. Rev. D* **99** (2019), no. 12 123501, [1903.02994].

[229] T. Harada, C.-M. Yoo, T. Nakama, and Y. Koga, *Cosmological long-wavelength solutions and primordial black hole formation*, *Phys. Rev. D* **91** (2015), no. 8 084057, [1503.03934].

[230] C.-M. Yoo, T. Harada, J. Garriga, and K. Kohri, *Primordial black hole abundance from random Gaussian curvature perturbations and a local density threshold*, *PTEP* **2018** (2018), no. 12 123E01, [1805.03946].

[231] S. Young and M. Musso, *Application of peaks theory to the abundance of primordial black holes*, *JCAP* **11** (2020) 022, [2001.06469].

[232] A. Escrivà, E. Bagui, and S. Clesse, *Simulations of PBH formation at the QCD epoch and comparison with the GWTC-3 catalog*, *JCAP* **05** (2023) 004, [2209.06196].

[233] T. Harada, C.-M. Yoo, and K. Kohri, *Threshold of primordial black hole formation*, *Phys. Rev. D* **88** (2013), no. 8 084051, [1309.4201]. [Erratum: Phys.Rev.D 89, 029903 (2014)].

[234] A. Escrivà, C. Germani, and R. K. Sheth, *Universal threshold for primordial black hole formation*, *Phys. Rev. D* **101** (2020), no. 4 044022, [1907.13311].

[235] I. Musco, V. De Luca, G. Franciolini, and A. Riotto, *Threshold for primordial black holes. II. A simple analytic prescription*, *Phys. Rev. D* **103** (2021), no. 6 063538, [2011.03014].

[236] J. I. Juan, P. D. Serpico, and G. Franco Abellán, *The QCD phase transition behind a PBH origin of LIGO/Virgo events?*, *JCAP* **07** (2022), no. 07 009, [2204.07027].

[237] C. T. Byrnes, M. Hindmarsh, S. Young, and M. R. S. Hawkins, *Primordial black holes with an accurate QCD equation of state*, *JCAP* **08** (2018) 041, [1801.06138].

[238] K. Kohri and T. Terada, *Solar-Mass Primordial Black Holes Explain NANOGrav Hint of Gravitational Waves*, *Phys. Lett. B* **813** (2021) 136040, [2009.11853].

[239] B. Carr, M. Raidal, T. Tenkanen, V. Vaskonen, and H. Veermäe, *Primordial black hole constraints for extended mass functions*, *Phys. Rev. D* **96** (2017), no. 2 023514, [1705.05567].

[240] J. M. Bardeen, J. R. Bond, N. Kaiser, and A. S. Szalay, *The Statistics of Peaks of Gaussian Random Fields*, *Astrophys. J.* **304** (1986) 15–61.

[241] J. P. W. Verbiest, S. Oslowski, and S. Burke-Spolaor, *Pulsar Timing Array Experiments*, 2101.10081.

[242] J. M. Cordes, *Limits to PTA sensitivity: spin stability and arrival time precision of millisecond pulsars*, *Class. Quant. Grav.* **30** (2013) 224002.

[243] M. T. Lam et al., *The NANOGrav Nine-Year Data Set: Excess Noise in Millisecond Pulsar Arrival Times*, *Astrophys. J.* **834** (2017), no. 1 35, [1610.01731].

[244] M. L. Jones et al., *The NANOGrav Nine-year Data Set: Measurement and Analysis of Variations in Dispersion Measures*, *Astrophys. J.* **841** (2017), no. 2 125, [1612.03187].

[245] L. Lentati, P. Alexander, M. P. Hobson, S. Taylor, J. Gair, et al., *Hyper-efficient model-independent Bayesian method for the analysis of pulsar timing data*, *Phys. Rev. D* **87** (2013), no. 10 104021, [1210.3578].

[246] R. Kato and J. Soda, *Search for ultralight scalar dark matter with NANOGrav pulsar timing arrays*, *JCAP* **09** (2020) 036, [1904.09143].

[247] S. Detweiler, *Pulsar timing measurements and the search for gravitational waves*, **234** (Dec., 1979) 1100–1104.

[248] E. Thrane and J. D. Romano, *Sensitivity curves for searches for gravitational-wave backgrounds*, *Phys. Rev. D* **88** (2013), no. 12 124032, [1310.5300].

[249] C. Caprini and D. G. Figueroa, *Cosmological Backgrounds of Gravitational Waves*, *Class. Quant. Grav.* **35** (2018), no. 16 163001, [1801.04268].

[250] J. A. Ellis, X. Siemens, and R. van Haasteren, *An Efficient Approximation to the Likelihood for Gravitational Wave Stochastic Background Detection Using Pulsar Timing Data*, *Astrophys. J.* **769** (2013) 63, [1302.1903].

[251] R. van Haasteren and M. Vallisneri, *Low-rank approximations for large stationary covariance matrices, as used in the Bayesian and generalized-least-squares analysis...*, *Mon. Not. Roy. Astron. Soc.* **446** (2015) 1170–1174, [1407.6710].

[252] B. B. P. Perera et al., *The International Pulsar Timing Array: Second data release*, *Mon. Not. Roy. Astron. Soc.* **490** (2019), no. 4 4666–4687, [1909.04534].

[253] J. A. Ellis, M. Vallisneri, S. R. Taylor, and P. T. Baker, "ENTERPRISE: Enhanced Numerical Toolbox Enabling a Robust PulsaR Inference SuitE." Astrophysics Source Code Library, record ascl:1912.015, Dec., 2019.

[254] J. Ellis and R. van Haasteren, *jellis18/ptmcmcsampler: Official release*, Oct., 2017.

[255] A. Lewis, *GetDist: a Python package for analysing Monte Carlo samples*, 1910.13970.

[256] E. S. Phinney, *A Practical Theorem on Gravitational Wave Backgrounds*, *arXiv e-prints* (Aug., 2001) astro–ph/0108028, [astro-ph/0108028].

[257] D. J. Fixsen, E. S. Cheng, J. M. Gales, J. C. Mather, R. A. Shafer, et al., *The Cosmic Microwave Background spectrum from the full COBE FIRAS data set*, *Astrophys. J.* **473** (1996) 576, [astro-ph/9605054].

[258] B. Carr, K. Kohri, Y. Sendouda, and J. Yokoyama, *Constraints on primordial black holes*, *Rept. Prog. Phys.* **84** (2021), no. 11 116902, [2002.12778].

[259] Z. Yi and Q. Fei, *Constraints on primordial curvature spectrum from primordial black holes and scalar-induced gravitational waves*, *Eur. Phys. J. C* **83** (2023), no. 1 82, [2210.03641].

[260] Z.-C. Zhao and S. Wang, *Bayesian Implications for the Primordial Black Holes from NANOGrav's Pulsar-Timing Data Using the Scalar-Induced Gravitational Waves*, *Universe* **9** (2023), no. 4 157, [2211.09450].

[261] **NANOGrav**, G. Agazie et al., *The NANOGrav 15 yr Data Set: Evidence for a Gravitational-wave Background*, *Astrophys. J. Lett.* **951** (2023), no. 1 L8, [2306.16213].

[262] P. J. McMillan, *Mass models of the milky way*, *Monthly Notices of the Royal Astronomical Society* **414** (apr, 2011) 2446–2457.